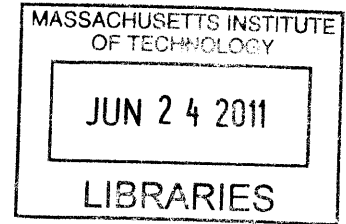


The Effect of Complex Inclusion Geometries on Fracture and Crack Coalescence Behavior in Brittle Material

By

Stephen Philip Morgan

B.S., Civil Engineering (2009)
University of New Hampshire



Submitted to the Department of Civil and Environmental Engineering
in Partial Fulfillment of the Requirements for the Degree of
Master of Science in Civil and Environmental Engineering

ARCHIVES

at the

Massachusetts Institute of Technology

June 2011

© 2011 Massachusetts Institute of Technology
All rights reserved

Signature of Author.....
Department of Civil and Environmental Engineering
May 19, 2011

Certified by.....
Herbert H. Einstein
Professor of Civil and Environmental Engineering
Thesis Supervisor

Accepted by.....
Heidi M. Nepf
Chair, Departmental Committee for Graduate Students

The Effect of Complex Inclusion Geometries on Fracture and Crack Coalescence Behavior in Brittle Material

By

Stephen Morgan

Submitted to the Department of Civil and Environmental Engineering
on May 19, 2011 in Partial Fulfillment of the
Requirements for the Degree of Master of Science
in Civil and Environmental Engineering

ABSTRACT

This research study investigates the cracking processes in a brittle material associated with inclusions of varying shape, orientation and materials. Specifically, this study summarizes a series of uniaxial compression tests on gypsum specimens with varying inclusion materials, shapes and pair configurations using high speed imagery to determine cracking behavior. The inclusions in the study consisted of differing materials, of contrasting Young's Modulus (higher and lower than the matrix), shapes (hexagon, diamond, ellipse), and relative pair orientations (bridging angle). In addition, single ellipse inclusions were tested to investigate the cracking behavior associated with an ellipse inclusion in a brittle material.

Similar to previous research regarding the coalescence of cracks propagating from inclusion pairs, the inclusion material did not affect the coalescence patterns. The coalescence behavior trended from indirect or no coalescence, to direct shear coalescence, to combined direct tensile-shear coalescence as the inclusion bridging angle was increased, similar to past studies on circular and square inclusion pairs, as well as flaw pairs. An analogy was proposed relating the debonded inclusion interfaces to corresponding flaw pairs to compare coalescence behavior. Although the general coalescence trends regarding the effect of bridging angle on inclusion pairs were comparable to those of flaw pairs, the coalescence based on a debonded interface representation did not appear to be similar to that of corresponding flaw pairs. Along with previous work conducted by the MIT rock mechanics group, this research provides detailed experimental observations regarding both the cracking and coalescence behaviors of inclusions in a brittle material.

Thesis Supervisor: Herbert Einstein

Title: Professor of Civil and Environmental Engineering

ACKNOWLEDGEMENTS

First of all I want to thank everyone that has always been there for me. The amazing people in my life are the reason for my success and they fuel my determination. My relationships with people are the most important things in my life and I want to thank you all for putting up with me and helping me out over the years.

I want to thank my family (Mom, Dad, Jamie and Brandon), you mean everything to me and I know that no matter what I will always have you in my life. I also want to thank all of my friends that have stuck it out with me, through the best and worst of times. This includes all of my friends from home (Brandyn, Jarred) and also my friends from UNH. Living close enough to visit you all, on random occasions, has been my secret to success here and I think it has always kept me true to what matters most in my life (my friends and family).

Secondly, I absolutely must thank Professor Einstein for being an awesome advisor. This past year has been very hectic with a lot of unexpected events happening, but regardless he has remained more dedicated and resilient than anyone I have ever met in my life. It is a testament to how driven he is and his determination motivates me to continue working harder each day. I would like to thank Dr. Germaine for being an amazing mentor. He has been there on many occasions for me and now I know why he is in everyone's acknowledgement section. I must thank Stephen Rudolph for helping out and always being available with random things in the lab, even if I'm constantly being let down when someone tells me they are looking for "The Other Steve".

There is no way I was going to write this acknowledgement without specifically referencing Brendan Casey and Amy Adams. I am in a life debt to them for all the times they were there to explain something I didn't understand in a book or class. They have been there to listen to me rant on for hours about classes, research, etc. There is absolutely no question that they are two of the smartest and kindest people I have ever known and I'm just glad I've become close with them before they became famous.

Thank you so much Catherine and Julie for helping me out with your UROP projects. Julie went above and beyond the call of duty and some of her work can be seen in this thesis. I have no doubt she will become an amazing engineer. I have to thank Zenzi and Yvonne for being such awesome mentors and excellent role models for me to look up to. Also, thanks to Aiden and Jana for being awesome and bringing a different sense of humor to the department this year.

I have to thank last year's Meng class for being some of the best friends I have ever met and making my transition to MIT so smooth. I must specifically mention Geoff, John, Charles and Patty for being some of my best friends ever, even though we were in the same school for only months. You're truly amazing people and MIT misses you greatly.

TABLE OF CONTENTS

Abstract.....	3
Acknowledgments	5
Table of Contents	7
CHAPTER 1 – Introduction	11
1.1 Motivation	11
1.2 Approach	12
1.3 Organization of Thesis	13
CHAPTER 2 – Background	14
2.1 Introduction	14
2.2 Fracture Theory	14
2.2.1 Crack Interaction Theory	19
2.3 Fracture Experiments.....	22
2.3.1 Single Flaw Experiments	24
2.3.2 Double Flaw Experiments.....	25
2.4 Inclusions.....	35
2.3.1 Inclusion Theory	35
2.3.2 Experimental Inclusion Research.....	42
CHAPTER 3 – Experimental Setup	53
3.1 Introduction	53
3.2 Material Properties.....	53
3.3 Inclusion Geometries	54
3.4 Specimen Preparation	56
3.4.1 Introduction	56
3.4.2 Matrix Casting.....	56
3.4.3 Inclusion Casting.....	59
3.4.4 Sanding.....	60
3.4.5 Pre-Test Preparation.....	60

3.5 Uniaxial Compression Tests	61
3.5.1 Test Setup	61
3.5.2 Loading Regime and Data Acquisition	62
3.5.3 Failure Detection	63
3.6 Analysis Procedure	63
3.6.1 Introduction	63
3.6.2 Real Time Video	64
3.6.3 High Speed Video	64
3.6.4 Synchronization	66
3.6.5 Visual Analysis	67
3.6.6 Stress-Strain Analysis	68
3.6.7 Compilation	69
CHAPTER 4 – Results: Single Ellipse Inclusions	71
4.1 Introduction	71
4.2 Single Ellipse Inclusions	71
4.3 Cracking Behavior	72
4.3.1 Introduction	72
4.3.2 Cracking Sequence	73
4.3.3 Debonding	73
4.3.4 Primary Tensile Cracking	74
4.3.5 Secondary Cracking	74
4.3.6 Spalling	75
4.4 Stress Behavior	76
4.4.1 Introduction	76
4.4.2 Maximum Stress	76
4.3.3 Tensile Crack Initiation	77
4.5 Summary	78
CHAPTER 5 – Results: Inclusion Pairs	79

5.1 Introduction	79
5.2 Hexagon Inclusion Pairs.....	82
5.2.1 Debonding	82
5.2.2 Cracking.....	83
5.2.3 Surface Spalling	84
5.2.4 Coalescence	85
5.2.5 Stress Behavior	87
5.3 Diamond Inclusion Pairs	91
5.3.1 Debonding	91
5.3.2 Cracking.....	92
5.3.3 Surface Spalling	94
5.3.4 Coalescence	94
5.3.5 Stress Behavior	96
5.4 Ellipse Inclusion Pairs	99
5.3.1 Debonding	99
5.3.2 Cracking.....	101
5.3.3 Surface Spalling.....	102
5.3.4 Coalescence	103
5.3.5 Stress Behavior	104
5.5 Summary	108
5.5.1 Introduction.....	108
5.5.2 Debonding	108
5.5.3 Cracking.....	109
5.5.4 Surface Spalling.....	109
5.5.5 Coalescence	110
5.5.6 Stress Behavior	112
 CHAPTER 6 – Results: Inclusion Pairs	 116
6.1 Introduction	116
6.2 Comparison to Previous Inclusion Studies	116
6.2.1 Debonding	116

6.2.2 Cracking Sequence.....	119
6.2.3 Coalescence.....	120
6.2.4 Stress Behavior	121
6.3 Comparison to Previous Flaw Studies	123
6.3.1 Crack Patterns	123
6.3.2 Coalescence Behavior	128
CHAPTER 7 – Conclusions	132
7.1 Conclusions.....	132
7.1.1 Introduction	132
7.1.2 Debonding	132
7.1.3 Cracking Sequence.....	133
7.1.4 Coalescence.....	133
7.2 Summary	134
7.3 Future Research	137
CHAPTER 8 – References	139
APPENDIX A – Poisson’s Ratio Determination Procedure	144
APPENDIX B – Gypsum Preparation Caveats	152
APPENDIX C – Half-Inch Single Ellipse Inclusion Analysis	172
APPENDIX D – Half-Inch Hexagon Inclusion Pair Analysis	190
APPENDIX E – Half-Inch Diamond Inclusion Pair Analysis	237
APPENDIX F – Half-Inch Ellipse Inclusion Pair Analysis	284

CHAPTER 1 – Introduction

1.1 Motivation

The fracturing behavior of brittle materials containing inclusions is important for both natural material, such as pebbles embedded in conglomerates and large rock masses, as well as synthetic composite materials such as concrete consisting of a cement-matrix with aggregate inclusions. The inclusions found in composite materials can directly affect the composite strength by either weakening or strengthening the material as a whole,

The cracking processes (initiation, propagation, and coalescence) are directly associated with the strength (failure) of the composite material. In order to fully understand and predict the strength of different composite materials with varying inclusion size, shapes, materials, and orientations, the effects of these inclusions parameters on the cracking processes must be fully investigated experimentally.

1.2 Approach

The cracking processes in brittle materials, which contain inclusions have been studied both analytically (Zaitsev and Wittmann, 1981; Tasdemir et al. 1990) and experimentally (Zaitsev and Wittmann, 1981; Maji and Shah, 1989; Janeiro and Einstein, 2010). Only recently have experiments been performed with the technology capable of capturing high speed imagery to fully describe the crack propagation with a focus on the coalescence behavior associated with inclusions (Janeiro and Einstein, 2010). Although inclusions may be elliptical or angular in shape, the majority of the previous research performed on brittle materials with inclusions investigated the fracturing patterns associated with circular or rectangular (square) inclusions.

By identifying and varying the key inclusion parameters the corresponding effects on fracturing processes can be investigated. The present research was conducted to develop a more detailed description of the cracking and coalescence patterns of uniaxially loaded

gypsum specimens with inclusion pairs of varying shape, stiffness and orientation. Emphasis was placed on the coalescence behavior associated with the effects of varying these inclusion pair configurations. The goals of the current study, which will be addressed, are as followed:

- Perform experiments on inclusion pairs of varying shape, orientation and material; specifically to study the effect of inclusion shapes (hexagon, diamond, and ellipse) on cracking processes in gypsum specimens.
- Perform experiments on single ellipse inclusions of varying material to determining the cracking processes associated with single elliptical shaped inclusions in gypsum specimens.
- Use a high speed camera, in both the single and double inclusion experiments, to detect the high speed cracking sequencing and coalescence in gypsum specimens with inclusions.
- Determine the patterns and trends associated with the cracking sequence (debonding, initiation, and propagation) and coalescence associated with various inclusions in a brittle material.
- Integrate and compare the current study with previous studies, specifically with work conducted by the MIT rock mechanics group regarding flaws and inclusions in a brittle material.

1.3 Organization of Thesis

The thesis will be organized as followed:

- Chapter 2 – A background review. This review includes the key research studies regarding general fracture theory and experimental flaw testing as well as the general

theory regarding inclusions in a material and the previous experimental studies conducted on inclusions in brittle materials.

- Chapter 3 – The experimental setup of the current study. This includes the procedure for preparing specimens as well as the test setup used to conduct uniaxial compression tests on prismatic gypsum specimens. This is followed by an explanation of the data analysis procedures.
- Chapter 4 & 5 – The results of the single ellipse inclusions and double hexagon-, diamond-, and ellipse inclusion pairs tested conducted. The single ellipse inclusion results are divided into the cracking processes and stress behavior. The results of the inclusion pairs are subdivided by inclusion shape and discuss the corresponding cracking processes (debonding, crack sequence, spalling), coalescence and stress behavior.
- Chapter 6 – The discussion and comparison of results to previously conducted studies. This discussion is divided into two parts: the comparisons of the current research to previous research regarding inclusions and the comparisons to previous studies on flaws.
- Chapter 7 – The conclusions drawn from the results and comparisons sections. This chapter summarizes and draws conclusions from both the results and discussion chapters. Future research recommendations are also discussed in this section.

CHAPTER 2 – Background

2.1 Introduction

This following review of the previous research on inclusions in a brittle material is preceded by a brief discussion of crack initiation and propagation theory as well as a summary of the experimental work regarding cracking and coalescence in brittle homogenous materials containing flaws (pre-existing cracks).

2.2 Fracture Theory

The basis of stress concentrations around pre-existing cracks (flaws) was first approximated mathematically by Inglis in 1913 (See Figure 2.1). A flaw was represented by an elliptical hole within an infinite plate having a major axis ($2a$) much larger than its minor axis ($2b$). From this model, Inglis developed the tangential stress concentration at the flaw tip (σ_{tip}) of a sharp elliptical hole ($a \gg b$) subjected to a far field tensile stress (σ_v):

$$\sigma_{\theta\theta} = \sigma_{tip} = 2\sigma_v \sqrt{\frac{a}{\rho}} \quad (2.1)$$

Where a is the flaw half length and $\rho (= \frac{b^2}{a})$ is the radius of curvature of the flaw tip. From this derivation, the stress concentration at the flaw tip increase as either the flaw half length (a) increases or the radius of curvature decreases. The radius of curvature decreases if the flaw becomes “sharper” having a smaller minor axis (b) in comparison to the major axis (e.g. the flaw half length, a). This relationship can be intuitively understood since a circular hole should have lower stress concentrations than an extremely thin crack. Inglis postulated that once the local stress exceeds the strength of the material, this flaw expands (crack initiation). This is the basis of the **stress-based criterion** for crack initiation.

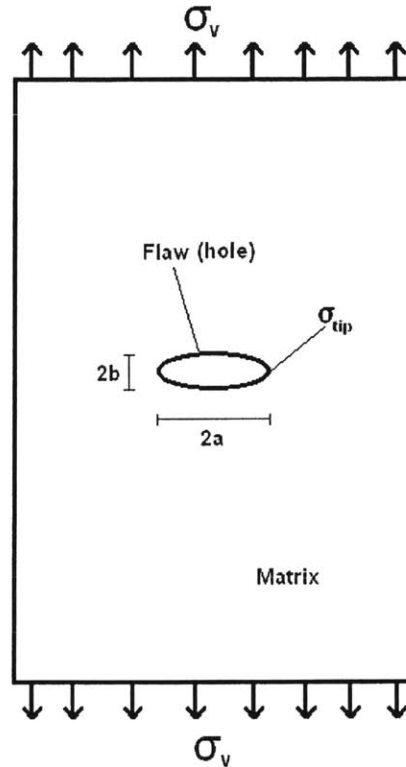


Figure 2.1 – Approximation of Tangential Stress at a Flaw Tip

Since crack initiation was observed at a much lower stress than the actual strength of the atomic bonds in materials it was determined that other mechanisms are controlling the initiation of cracks. Griffith (1920) extended on the theory of stress concentrations developed by Inglis (1913) and applied laws of thermodynamics and energy conservation to determine the stress required to initiate a crack at the flaw tip. This is the basis of the **energy-based criterion** for crack initiation. Griffith expressed the change in strain work and potential energy of creating a surface crack in a plate (Refer to Figure 2.1) as

$$d(W-\Pi) = \frac{d(W_{\text{elastic}})}{da} - \frac{d(W_{\text{surface}})}{da} = 0 \quad (2.2)$$

$$\text{Where, } W = W_{\text{elastic}} = \text{Stored elastic strain energy} = \frac{\pi a^2 \sigma_v}{E} \quad (2.3)$$

$$\Pi = W_{\text{surface}} = \text{Potential Surface energy created by a crack} = 4\gamma a \quad (2.4)$$

where a is the crack half length, E is the Young's Modulus of the plate and γ is the specific surface energy of the material. Substituting equations 2.3 and 2.4 into equation 2.2 the

increment of stored elastic strain energy to the surface energy required to create a crack at the flaw tip and can be expressed as

$$\frac{d}{da} \left(\frac{\pi a^2 \sigma_v}{E} \right) = \frac{d}{da} (4\gamma a) \quad (2.5)$$

Therefore, by integrating and solving for the stress (σ_v), the necessary stress to produce crack initiation can be defined as followed:

$$\sigma_{v, \text{ crack}} = \sqrt{\frac{2E\gamma}{\pi a}} \quad (2.6)$$

Along with in plane tensile cracking (Mode I), there are two other modes of cracking which can occur; in-plane shear cracking (Mode II) and out-of-plane shear cracking (Mode III) (See Figure 2.2).

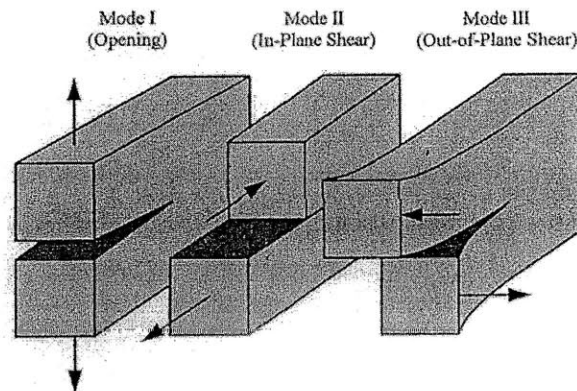


Figure 2.2 – Modes of Cracking (Anderson, 2005)

Extending on the energy-based criterion developed by Griffith (1920), Irwin (1957) proposed an energy release rate concept which expressed the displacement and stresses around a flaw tip by a stress concentration factor, K .

$$K = -\sigma_v Q \sqrt{\pi a} \quad (2.7)$$

where Q is a geometric factor ($Q = 2/\pi$ for penny shape crack, $Q = 1$ for an infinitely thin crack) and σ_v is the far field stress at which the crack initiates. There are three different stress concentration factors differentiated by mode of cracking in a material (K_I , K_{II} , K_{III}). The

inclination of the crack can be expressed by determining the crack orientation corresponding to the critical stress concentration factor.

An extensively used model describing the cracking of an inclined flaw is called the sliding wing crack model (e.g. Brace and Bombolakis, 1963; Gramberg, 1965; Moss & Gupta, 1982; Germanovich & Dyskin, 2000). This model describes the curvilinear tensile wing crack which initiates at the tips of an inclined flaw (open or closed) and propagates toward the direction of applied compressive loading (Figure 2.3). As these tensile wing cracks initiate and propagate, the top and bottom surfaces of the flaw must slide relative to each other; thus it is named the sliding wing crack model.

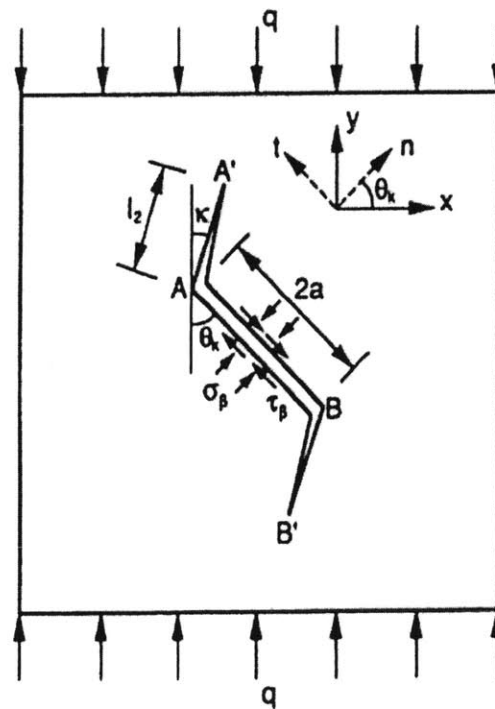


Figure 2.3 – Sliding Crack Model (Tasdemir et al., 1990)

Mellville (1973) applied stress intensity factors to a sliding compressive closed-crack model. In this scenario, any closed-flaw under uniaxial compression will experience a friction

resistance along the sliding surface (Figure 2.3). From the equilibrium at the interface, the resultant normal and shear stresses on the sliding crack surface can be determined as

$$\sigma_{\beta} = -q \sin^2 \theta_k \quad (2.8)$$

$$\tau_{\beta} = -q \sin \theta_k \cos \theta_k \quad (2.9)$$

Where θ_k is the angle of the flaw with the direction of loading and q is the far field compressive stress. These stresses on the closed flaw can be used to determine the stress intensity factor of initiating a shear (mode II) crack at the flaw tip as

$$K_{II} = -q \sqrt{\pi a} (\sin \theta_k \cos \theta_k - \mu \sin^2 \theta_k) \quad (2.10)$$

Where μ is the coefficient of friction and a is the half flaw length. Since this criterion of sliding is based on the components of normal (σ_n) and shear stress ($\mu|\sigma_n|$), the critical flaw angle initiating sliding can be related to the frictional coefficient as $\theta_{kc} = \text{arccot}(\mu)$.

As the load is increased an additional kink crack will initiate at the flaw tip (labeled A-A' on Figure 2.3) and can occur as either a shear or tensile crack. Based on equation 2.7, the intensity factors for a kink crack (A-A' in figure 2.3) initiating at the flaw tip (A-B in figure 2.3) in a different direction (κ), by either mode I tensile opening or mode II shearing, can be determined as

$$K_I^{Kink} = \frac{1}{4} K_{II} \left[\cos \left(\frac{\kappa}{2} \right) + 3 \cos \left(\frac{3\kappa}{2} \right) \right] \quad (2.11)$$

$$K_{II}^{Kink} = -\frac{3}{4} K_{II} \left[\sin \left(\frac{\kappa}{2} \right) + \sin \left(\frac{3\kappa}{2} \right) \right] \quad (2.12)$$

Where K_{II} is the stress intensity factor calculated in eq. 2.10 and κ is the angle between the kink crack initiating at the flaw tip and the direction of compressive loading. This sliding crack model will be discussed later on in relation to a crack initiating at an inclusion interface.

Although early research assumed that linear elastic fracture mechanics (LEFM) was applicable in describing the brittle behavior of rock, more recent research has discovered that the behavior of cracking in rock is actually quasi-brittle (Irwin, 1961; Dugdale, 1960; Barenblatt, 1962). It has been shown that there is a plastic area (process zone) ahead of the

propagating crack tip which is characterized by tractional bridging and microcracking (See Figure 2.4). This plastic zone can affect the stress concentrations predicted at the crack tip. As a result of these findings, there has been much research conducted in order to determine the existence these process zones ahead of crack tips brittle material (Friedman et al., 1972; Segall & Pollard, 1983; Maji and Wang, 1992; Anderson, 2005).

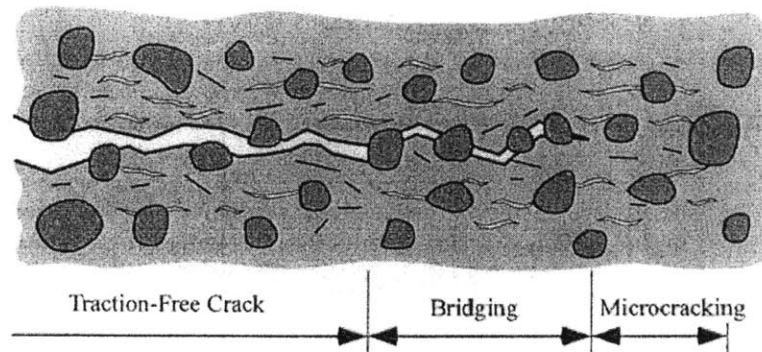


Figure 2.4 –Fracture-process zone ahead of a crack in concrete. The process zone consists of the bridging and microcracking areas at the crack tip (Anderson, 2005).

2.2.1 Crack Interaction Theory

Although predicting crack initiation and propagation in a brittle material can be used to estimate the strength of a body containing a flaw, the interaction and interconnection (referred to as coalescence) between cracks also plays an important role in the failure of a material with multiple flaws. There have been several analytical studies conducted to predict the interaction of cracks in a brittle material.

One of the initial studies which theoretically predicted crack interaction was conducted by Horii and Nemat-Nasser (1985). That research super-imposed a series of sub-scenarios consisting of homogenous material as well as multiple scenarios with single crack in the matrix in order to model the interaction of multiple cracks in a homogenous material (Figure 2.5). Unknown quantities from interacting cracks, referred to as “pseudo-tractions”, are

determined by solving the superimposed scenarios simultaneously (Refer to Figure 2.5). That study served as the basis for several other analytical models of crack interaction.

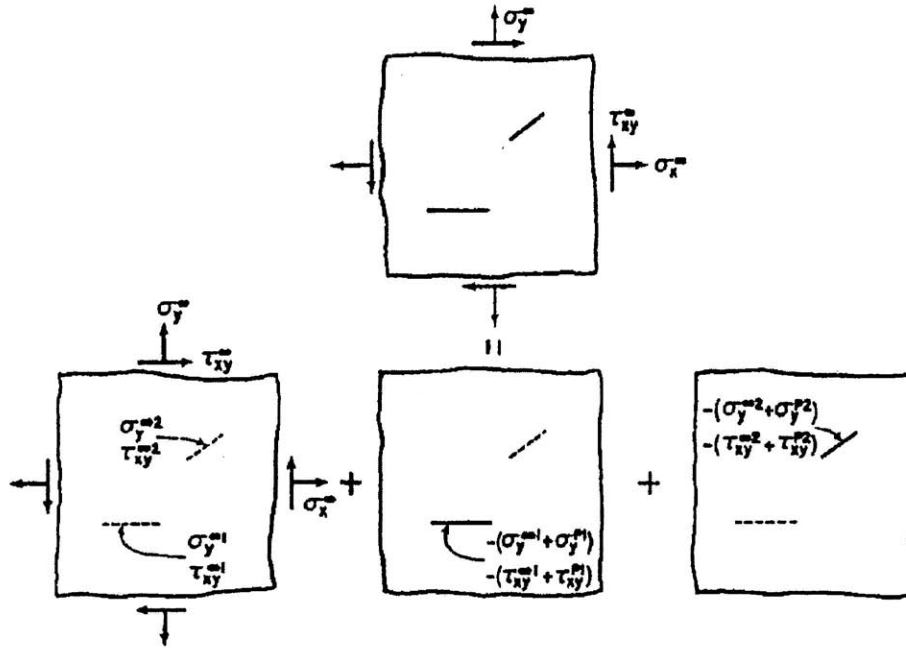


Figure 2.5 – An illustration crack interaction model using super-position of three sub-scenarios (From left to right: homogenous, a single horizontal crack, and a single slanted crack). The stress on the cracks include both far field and “pseudo-tractions” from the interaction of adjacent cracks (Horii and Nemat-Nasser, 1985)

Costin (1985) proposed a model in which a body contains a series of pre-existing cracks, oriented along the direction of loading (Figure 2.6). As these cracks propagate along the direction of loading the distance between the cracks decrease and an interaction occurs based on the local tensile stress fields at the crack tips. Similar to the study conducted by Horii and Nemat-Nasser (1985), this model also used sub-scenarios with unknown pseudo-tractions representing the interaction of other cracks in the system. These sub-scenarios are used to simultaneously solve the system of cracks numerically and determine the stress intensity factor K_I .

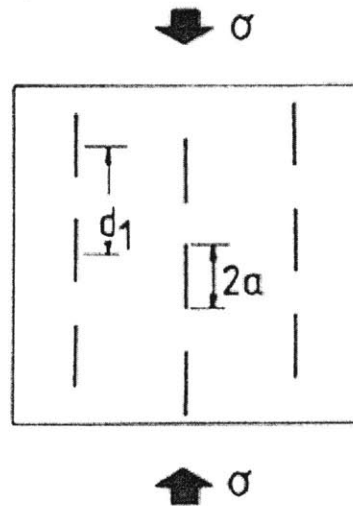


Figure 2.6 – An illustration of a series of vertical cracks (length $2a$) in a material with a distance between cracks d_1 after Costin, 1985. (Wong, 2008)

A series of studies by Ashby & Hallam (1986) and Hallam & Ashby (1990) proposed an alternative crack interaction model in which a series of inclined pre-existing cracks propagate at the crack tips in the direction of compressive loading. As these cracks propagate the area between the cracks creates a “column” of material which will be subject to buckling affect under the compressive load (Figure 2.7). This buckling effect changes the stress intensity factor K_I in the cracks, thus representing the crack interaction.

Finally, a model proposed by Kemeny & Cook (1987) expanded on the previous model from Ashby & Hallam (1986) by incorporating a curve-linear shape to the kink cracks that initiate from the pre-existing flaws as described in the sliding wing crack model. Similar to the previous model by Ashby & Hallam (1986), the crack interaction is related to effective “columns” which form between cracks (Refer to Figure 2.7). The crack interaction can be expressed by the failure of these “columns” in either axial compression (one column) or shear (multiple columns).

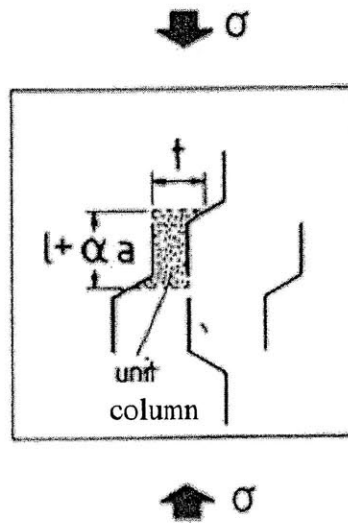


Figure 2.7 – An illustration of a series of sliding wing cracks in a material which form “columns” that can be modeled to determine crack interaction after Ashby & Hallam, 1986, and Hallam & Ashby, 1990. (Wong, 2008)

Numerical modeling of cracks has been done by the MIT rock mechanics group starting in 1986 by Chan. Chan (1986) developed the code 'FROCK' (which stands for fractured rock). This is a Displacement Discontinuity Method (DDM) which incorporates Linear Elastic Fracture Mechanics principles and stress intensity factors to model crack initiation and initial crack propagation. The code FROCK was later improved by Bobet (1997), who incorporated a stress based criterion to better model crack initiation, propagation and coalescence.

2.3 Fracture Experiments

Some of the first experimental tests on the fracturing in brittle materials were conducted by Brace & Bombolakis (1963). Since then there have been many experimental studies regarding the cracking processes in various natural and composite brittle materials. The following list of experimental research done on rock-like and natural rock brittle materials can be found in Wong (2008):

Rock-like brittle/semi-brittle materials

- **Columbia Resin 39** - (Brace & Bombolakis, 1963; Nemat-Nasser & Horii, 1982; Horii & Nemat-Nasser, 1985)
- **Glass** - (Hoek & Bieniawski, 1965; Bieniawski, 1967)
- **Plaster of Paris** - (Lajtai, 1970; Nemetova & Lajtai, 1973)
- **Polymethylmethacrylate, or PMMA** - (Petit & Barquins, 1988; Chaker & Barquins, 1996)
- **Molded Gypsum** - (Reyes, 1991; Reyes & Einstein, 1991; Shen et al., 1995; Bobet, 1997; Bobet & Einstein, 1998; Sagong, 2001; Sagong & Bobet, 2002; Wong & Einstein, 2009)
- **Sandstone-like Molded Barite** - (Wong, 1997; Wong & Chau, 1997, 1998; Wong et al., 2001)
- **Sandstone-like Concrete Mix** - (Mughieda & Alzo'ubi, 2004)

Natural rocks

- **Sandstone** - (Petit & Barquins, 1988)
- **Granodiorite** - (Ingraffea & Heuze, 1980)
- **Limestone** - (Ingraffea & Heuze, 1980)
- **Granite** - (Martinez, 1999; Miller, 2008)
- **Marble** - (Huang et al., 1990; Chen et al., 1995; Martinez, 1999; Li et al., 2005; Wong 2008)
- **Ice** - (Wang & Shrive, 1995)

It should be noted that these experimental tests were conducted on specimens of different sizes with various flaw lengths, orientations and apertures. The specimen parameters should be taken into account when comparing the observed cracking mechanisms from these different studies.

2.3.1 Single Flaw Experiments

One of the major inconsistencies in many of the previous studies conducted on single flaw specimens is the terminology associated with primary and secondary crack types. Primary cracking refers to the first crack to initiate from the flaw and is usually a tensile wing crack. Secondary cracking includes any cracks which occur after primary cracking and in many cases are shear in nature. Due to this trend in chronology and cracking mode, many studies use shear and secondary cracking interchangeably. This makes it difficult to interpret different research studies which use different terminology for the same types of cracking. However, in most of the previous studies which uses the terms secondary and shear cracking interdependently, the author correctly refers to secondary cracks in which shearing cannot be determined solely as secondary cracking.

There have been many studies regarding the brittle cracking processes associated with a single flaw. Most of the early research in this field focused on the cracking order (Primary, Secondary) and mode (Tensile, Shear) associated with different flaw sizes and inclinations. Although similar cracking order occurred in all studies (Primary tensile wing cracking and secondary tensile or shear cracking at the tips), some discrepancies existed regarding the areas and shape of shear crack zones or banding which occurred near the tips of the flaw and extended to the edges of the specimen (Figure 2.8).

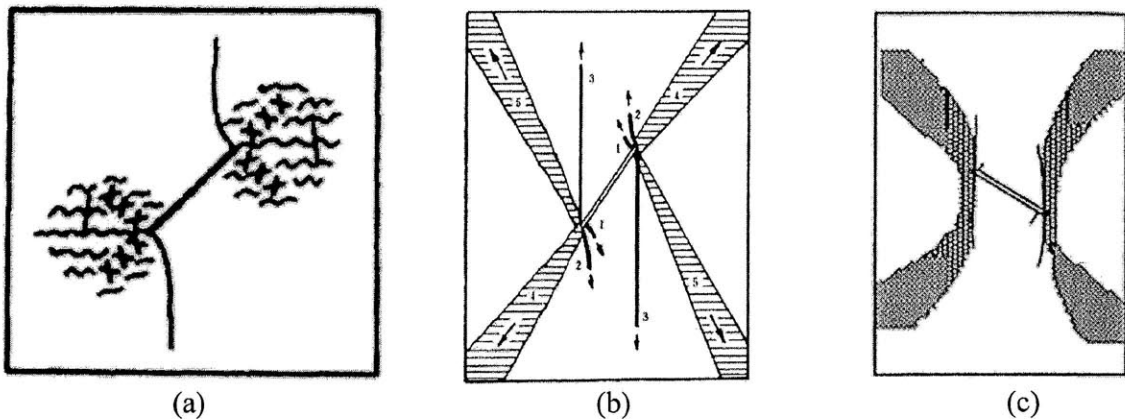


Figure 2.8 – Shear crack zone shapes (a) Lajtai, 1974 (b) Huang et al. 1990 (c) Chen et al., 1995. Shear zones are shaded or cross-hatched. Tensile cracks are shown as darker lines extending from the flaw tips toward the direction of loading (top/bottom).

Recently, Wong and Einstein (2009) conducted a series of single and double flaw uniaxial compression tests on molded gypsum and Carrara marble using a high speed camera to track the cracking processes. From these tests a set of crack types were proposed (See Figure 2.9).

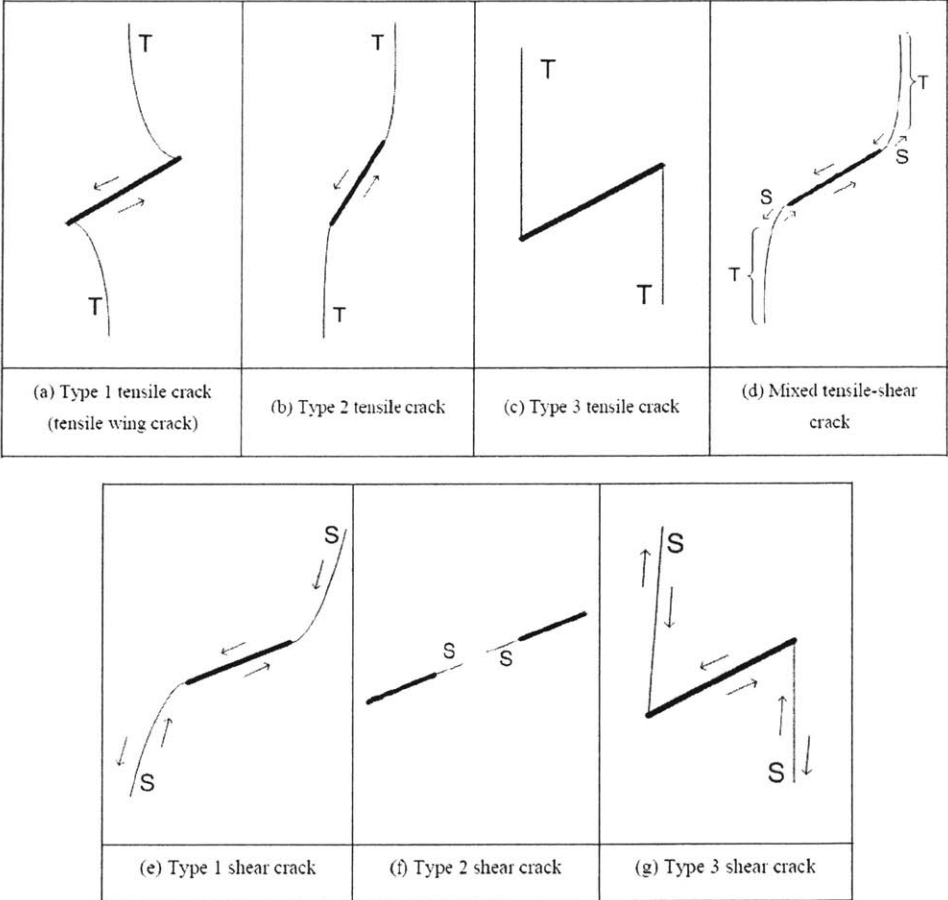


Figure 2.9 – Crack Types Proposed by Wong and Einstein (2009) T = Tensile Crack, S = Shear Crack

2.3.2 Double Flaw Experiments

As previously stated, the interaction between cracks plays a key role in the strength and behavior of a brittle material. In order to represent the interaction of multiple cracks in a material an additional flaw can be introduced and these flaws are referred to as a flaw pair.

Flaw pairs can be geometrically varied by changing the ligament length between the flaws (L), the inclination of the flaw (β) and the bridging angle between the two flaws (α) (Figure 2.10a). An important distinction between different studies testing flaw pairs is the terminology and definition of the flaw pair geometries. There are currently two different geometric definitions used in the research; ligament length and bridging angle or spacing and continuity (Figure 2.10).

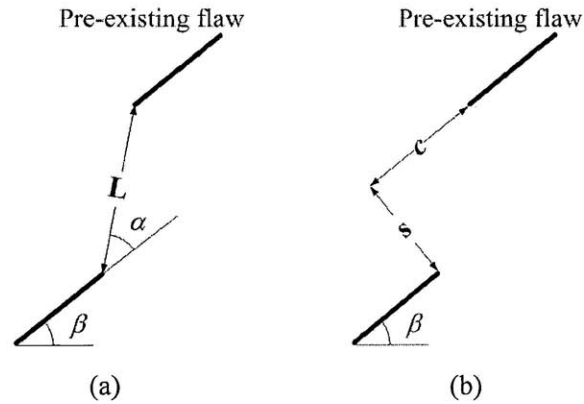


Figure 2.10 – Definition of Flaw Pairs Geometries by (a) flaw inclination angle [β], bridging angle [α] and ligament length [L], or (b) flaw inclination angle [β], continuity [c] and spacing [s] (Wong, 2009).

The ligament length (L) and bridging angle (α) can be easily determined from a flaw pair defined by spacing (s) and continuity (c) by using the simple geometry relations

$$L = \sqrt{s^2 + c^2} \quad (2.13)$$

$$\alpha = \arctan(s/c) \quad (2.14)$$

Conversely, the spacing (s) and continuity (c) can be determined from the ligament length (L) and flaw inclination by

$$s = L \sin(\alpha) \quad (2.15)$$

$$c = L \cos(\alpha) \quad (2.16)$$

The behavior of flaw pairs has been tested experimentally as early as 1963 by Brace and Bombolakis. Since then many other experiments have been conducted regarding the coalescence patterns of different flaw length, flaw inclinations and flaw bridging angles (e.g. Horii and Nemat-Nasser, 1985; Reyes and Einstein, 1991; Chen et al., 1995). For the purpose of this literature review, only the most recent and relevant studies will be discussed.

In 1995 Shen et al. conducted a series of uniaxial compression tests on molded gypsum with various geometric flaw (open and closed) configurations (bridging angle, flaw angle, ligament length). From these tests the cracking initiation process and the cracking mode of coalescence cracks were recorded (Figure 2.11)

Shen et al. divided the coalescence into three different classifications based on the mode of the coalescence cracking; shearing, mixed shearing and tensile, and tensile. One of the most important conclusions from this study was the trend in varying bridging angles (α) between flaws (with a constant ligament length, L):

Small positive bridging angles and small negative bridging angles

Coalescence generally occurred as a **shear** crack between the inner flaw tips

Intermediate bridging angles

Coalescence generally occurred by both **shear** and **tensile** cracks.

Large bridging angles

Coalescence generally occurred by a **tensile** crack




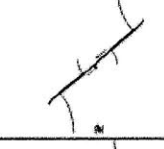

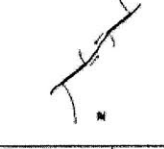

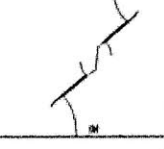


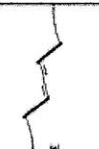



Number	Specimen	Critical Load at Coalescence, MPa	Schematic Path of Coalescence		Description of Coalescence	Mode of Coalescence
			(a) frictional	(b) nonfrictional		
1	30°/15° (2 specimens with friction fractures + 1 specimen with nonfrictional fractures)	No coalescence (frictional fractures) 17.2 MPa (nonfrictional fractures)			Type of coalescing fracture: secondary fracture. Initiation position: preexisting fracture tips. Surface characterization: rough, with many small kink steps; containing crushed gypsum.	Shearing
2	45°/0° (2 + 2)	21.9, 22.2 MPa (frictional fractures) 19.4, 17.9 MPa (nonfrictional fractures)			Type of coalescing fracture: secondary fracture. Initiation position: preexisting fracture tips. Surface characterization: rough, with many small kink steps; containing crushed gypsum.	Shearing
3	45°/15° (1 + 1) [†]	17.8 MPa (frictional fractures) 14.1 MPa (nonfrictional fractures)			Type of coalescing fracture: secondary fracture. Initiation position: preexisting fracture tips. Surface characterization: rough, with several large kink steps. Noticeable crushed gypsum presented.	Shearing
4	45°/30° (1 + 1) [†]	19.2 MPa (frictional fractures) 14.1 MPa (nonfrictional fractures)			Type of coalescing fracture: secondary fracture. Initiation position: unclear. Surface characterization: rough, with two big kink steps. No noticeable crushed gypsum.	Shearing + tension
5	45°/45° (2 + 1)	(a) 17.8, MPa (a') 16.8* MPa (frictional fractures) (b) 16.4 MPa (nonfrictional fractures)			Type of coalescing fracture: (a) wing fracture + secondary fracture; (a') and (b) secondary fracture. Initiation position: (a) preexisting fracture tips; (a') and (b) intact material. Surface characterization: some parts are clean and smooth while other parts are rough with crushed gypsum.	Shearing + tension
6	45°/60° (2 + 1)	17.8, 16.8 MPa (frictional fractures) 16.4 MPa (nonfrictional fractures)			Type of coalescing fracture: wing fracture. Initiation position: preexisting fracture tips. Surface characterization: smooth and clean. Note: additional secondary fractures occur from the outer tips in case (b).	Tension
7	45°/75° (2 + 1)	(a) 21.0 MPa (a') 23.1 MPa (frictional fractures) (b) 17.6 MPa (nonfrictional fractures)			Type of coalescing fracture: wing fracture. Initiation position: preexisting fracture tips. Surface characterization: smooth and clean. Note additional coalescence by secondary fractures occurs in case (b).	Tension

Figure 2.11 – Coalescence patterns recorded for uniaxial compression tests of molded gypsum with two flaws. (Shen et al., 1995)

Number	Specimen	Critical Load at Coalescence MPa	Schematic Path of Coalescence		Description of Coalescence	Mode of Coalescence
			(a) frictional	(b) nonfrictional		
8	60°/-15° (2 + 1)	22.4, 21.4 MPa (frictional fractures) 17.8 MPa (nonfrictional fractures)			Type of coalescing fracture: secondary fracture. Initiation position: preexisting fracture tips. Surface characterization: rough, with many small kink steps; containing crushed gypsum.	Shearing
9	60°/0° (4 + 1)	20.5, 17.8, 20.3, 20.9 MPa (frictional fractures) 15.2 MPa (nonfrictional fractures)			Type of coalescing fracture: secondary fracture. Initiation position: preexisting fracture tips. Surface characterization: rough, with several large kink steps. Noticeable crushed gypsum presented.	Shearing
10	60°/15° (1 + 1)†	18.5 MPa (frictional fractures) 13.7 MPa (nonfrictional fractures)			Type of coalescing fracture: (a) secondary fracture ; (b) secondary fracture + wing fracture. Initiation position: pre-existing fracture tips. Surface characterization: rough, with a few kink steps. No noticeable crushed gypsum.	Shearing + tension
11	60°/30° (1 + 1)†	19.2 MPa (frictional fractures) 14.2 MPa (nonfrictional fractures)			Type of coalescing fracture: (a) wing fracture ; (b) wing fracture + secondary fracture. Initiation position: preexisting fracture tips; Surface characterization: most parts are clean and smooth.	Tension + shearing
12	60°/45° (2 + 1)	19.9, 22.2 MPa (frictional fractures) 18.0 MPa (nonfrictional fractures)			Type of coalescing fracture: wing fracture. Initiation position: preexisting fracture tips. Surface characterization: smooth and clean.	Tension
13	60°/60° (1 + 1)†	23.5 MPa (frictional fractures) 21.0 MPa (nonfrictional fractures)			Type of coalescing fracture: secondary fracture. Initiation position: preexisting fracture tips. Surface characterization: very rough, coated with a lot of crushed gypsum.	Shearing

† Only two of the three specimens produced useful results, the other specimen failed due to mismanipulation of the loading machine.

* The frictional fractures in this specimen have weaker contact than other frictional fractures. The polyethylene sheets were left longer (45 min) by mistake before they were pulled out. As a result, the created fractures did not close firmly.

Figure 2.11 – Coalescence patterns recorded for uniaxial compression tests of molded gypsum with two flaws. (Shen et al., 1995) (continued)

In similar tests conducted by Bobet and Einstein in 1998, gypsum specimens with flaw pairs were tested under uniaxial and biaxial compression. In this test series, which used spacing and continuity geometric definitions, the effect of geometric orientation as well as ligament length was investigated. A series of general coalescence types were proposed based on both cracking type and shape (Figure 2.12). Bobet and Einstein (1998a) concluded that the

coalescence trends in regard to bridging angle are similar to those observed by Shen et al. (1995).

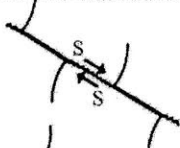
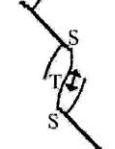
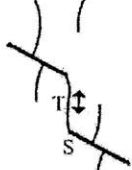
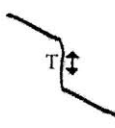
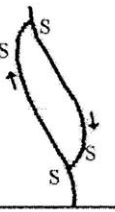
Type	Schematic path of Coalescence	Description of Coalescence	Mode of Coalescence
I		Type of coalescing fracture: secondary shear crack. Initiation position: preexisting flaw tips. Crack surface characterization: rough, with many small kink steps; contains crushed gypsum	Shearing
II		Type of coalescing fracture: secondary shear and tensile cracks. Initiation position: preexisting flaw tips. Crack surface characterization: some parts are clean and smooth while other parts are rough with crushed gypsum	Shearing + tension
III		Type of coalescing fracture: secondary shear crack and wing crack. Initiation position: preexisting flaw tips. Crack surface characterization: some parts are clean and smooth while other parts are rough with crushed gypsum	Shearing + tension
IV		Type of coalescing fracture: wing crack. Initiation position: preexisting flaw tips. Crack surface characterization: smooth and clean.	Tension
V		Type of coalescing fracture: secondary crack. Initiation position: preexisting flaw tips. Crack surface characterization: very rough, coated with a lot of crushed gypsum	Shearing?

Figure 2.12 – Coalescence types proposed by Bobet and Einstein (1998a) in molded gypsum specimen. T = Tensile cracking, S = Shear cracking

In 1998 Wong and Chau performed a series of uniaxial compression tests on a sandstone type specimen with double flaw pairs. The observed coalescence patterns were divided into shear, mixed (shear and tensile), and wing tensile. All of the flaws were closed and the coefficient of friction (μ) was varied. From these tests Wong and Chau were able to plot each geometric configuration as a test point and define zones for each coalescence type as bridging angle and flaw angle vary (Figures 2.13-2.15).

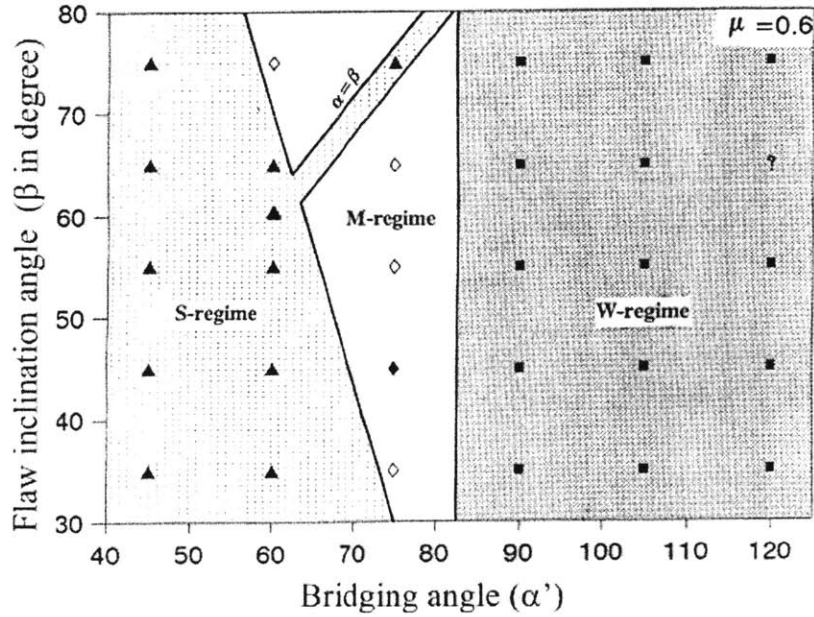


Figure 2.13 – Coalescence zones based on bridging angle and flaw inclination angle for a coefficient of friction $\mu = 0.6$. S-regime represents geometric configurations in which shear coalescence occur. M-regime represents geometric configurations in which mixed (shear and tensile) coalescence occur. W-regime represents geometric configurations in which tensile wing coalescence occurs. Points labeled “?” showed no coalescence. (Wong and Chau, 1998)

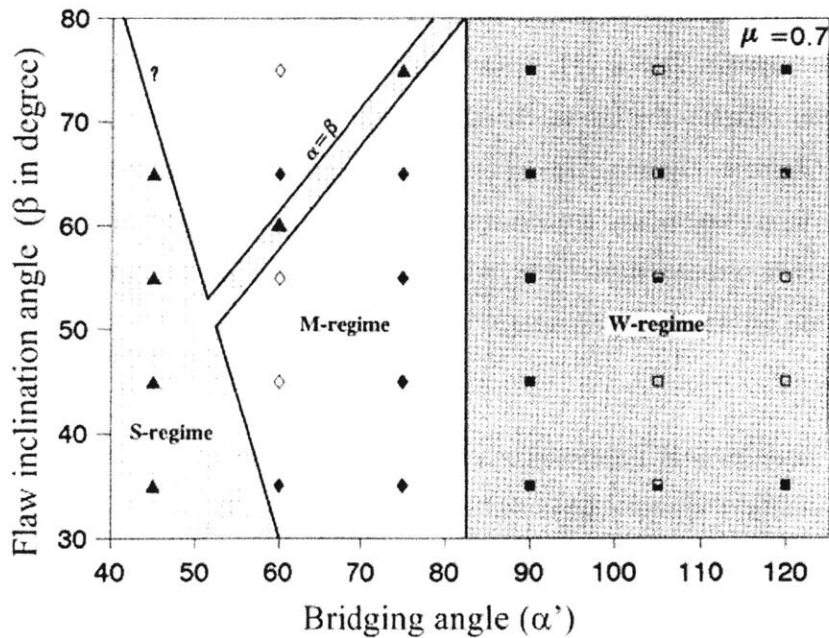


Figure 2.14 – Coalescence zones based on bridging angle and flaw inclination angle for a coefficient of friction $\mu = 0.7$. All other captions are the same as those for figure 2.13 (Wong and Chau, 1998)

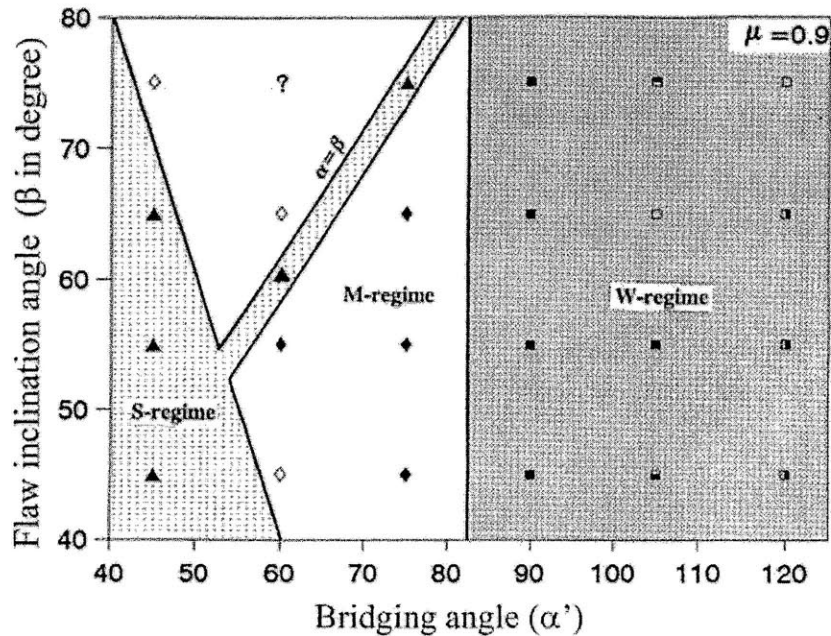


Figure 2.15 – Coalescence zones based on bridging angle and flaw inclination angle for a coefficient of friction $\mu = 0.9$. All other captions are the same as those for figure 2.13 (Wong and Chau, 1998)

The coalescence regimes defined by Wong and Chau (1998) showed a trend in coalescence with regard to increasing bridging angle that was similar to previous research by Shen et al. (1995) (Refer to Figures 2.13-2.15). These coalescence regimes also showed that as the friction coefficient between the closed flaws decreases, shear coalescence occurred at higher bridging angles (Refer to Figures 2.13-2.15). It should be noted though that Wong and Chau (1998) used the terms secondary cracks and shear cracks interchangeable. Therefore, it is unknown whether a proper distinction was made between coalescence occurring from secondary cracking and shear coalescence.

More recently, experimental coalescence research was conducted by Wong and Einstein (2009) on both natural Carrara marble and molded gypsum. This research was one of the first studies regarding cracking and coalescence to incorporate the use of a high-speed camera to properly determine shear cracking and follow crack propagation. Four different test series were conducted on each of the two materials (Table 2.1).

<u>Test Series</u>	<u>Description</u>	<u>Ligament Length, L</u>	<u>Bridging Angle, α</u>	<u>Inclination Angle, β</u>
1	coplanar	2a	0	0, 30, 45, 60, 75
2	stepped	2a	-60, -30, 0, 30, 60, 90, 120	30
3	coplanar	4a	0	0, 30, 45, 60, 75
4	stepped	4a	-60, -30, 0, 30, 60, 90, 120	30

Table 2.1 – The four test series conducted by Wong and Einstein (2009). Divided by ligament length and then coplanar (bridging angle of 0 degrees) and stepped flaws. All stepped flaws were oriented at an inclination of 30 degrees.

From the tests conducted on these flaw geometries Wong and Einstein (2009) proposed a set of nine different coalescence patterns (Figure 2.16). The following conclusions were drawn:

Bridging Angle (α) – The effect of bridging angle was determined based on the stepped flaws test series with a constant flaw inclination angle of 30 degrees. It was concluded that at small bridging angles shear coalescence occurred. As the bridging angle increased mixed shear and tensile coalescence was observed. At higher bridging angles tensile coalescence was observed. This matched the previous conclusions made by Shen et al. (1995) and Bobet and Einstein (1998).

Inclination Angle (β) – The effect of inclination angle was determined from the coplanar test series (constant 0 bridging angle). As the inclination increased, a trend from indirect or no coalescence, to shear coalescence, to tensile coalescence was reported.

Ligament Length (L) – Increasing the ligament length reduced the amount of coalescence (e.g. a higher number of no-coalescence), especially in the coplanar flaw geometries.

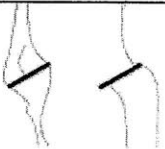
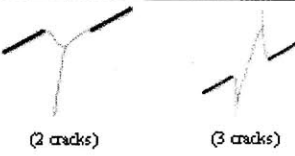

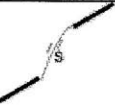





Category	Coalescence patterns	Crack types involved
1		No coalescence
2		Indirect coalescence by two or multiple cracks (crack types vary)
3		Type 2 S crack(s)
4		Type 1 S crack(s)
5		One or more type 2 S crack(s) and type 2 T crack segments between inner flaw tips
6		Type 2 T crack(s). There may be occasional short S segments present along the coalescence crack.
7		Type 1 T crack(s)
8		Flaw tips of the same side linked up by T crack(s) not displaying wing appearance (crack type not classified). There may be occasional short S segments present along the coalescence crack.
9		Type 3 T crack(s) linking right tip of the top flaw and left tip of the bottom flaw. There may be occasional short S segments present along the coalescence crack.

Figure 2.16 – Nine coalescence patterns proposed by Wong and Einstein (2009), determined from uniaxial compression tests on Carrara marble and molded gypsum. T= Tensile Cracks, T = Shear Cracks. Types 1 and 2 show indirect or no coalescence. Types 3 and 4 show shear coalescence. Type 5 shows mixed coalescence. Types 6 through 9 show tensile coalescence.

2.4 Inclusions

The fracturing behavior of brittle materials which contain inclusions is important for both natural material such as pebbles embedded in conglomerates (Eidelman and Reches, 1992) and large rock masses (Reches, 1998) as well as composite materials such as concrete which contains a cement-matrix and aggregate inclusions (e.g. Zhang and Gjrv, 1990; Lo and Cui, 2004; Aulia, 2000). By identifying the key parameters and assumptions regarding inclusions in a matrix, the fracturing of brittle material containing inclusions can be predicted theoretically.

2.4.1 Inclusion Theory

There are many important parameters which affect the behavior of heterogeneous material consisting of a matrix body and inclusions. The most important properties in a composite material are the inclusion and matrix strength, the shape changing parameters (bulk and shear modulus), and the bond strength of the interface between the inclusion and matrix. The strengths of the inclusion and matrix in brittle materials (e.g. rocks and concrete) are typically represented by a large compressive strength and a very low tensile strength. The elastic constants can be represented by the Young's modulus (E) and the Poisson's ratio (ν) of the material. The strength of the interface bond and persistence of the bond contact between the inclusion and matrix material are much more difficult to measure and predict.

In general, a body containing inclusions consists of three parts; a matrix body, inclusion material, and an interface zone (Figure 2.17). The interface, or transition zone, between the inclusion and matrix is typically considered the weakest part of a composite material (Taylor and Broms, 1964). This interface zone can have various thicknesses and typically has lower strength properties. The interface zone is an important topic in concrete research since it controls the bonding between cement and aggregate. In concrete (cement and aggregate composite), this lower strength at the transition zone is due to an increase in voids (referred to as wall effects), which are created during bonding (bleeding at the aggregate interface in concrete). The bonding between cement paste and aggregates can be affected by several

different factors such as aggregate size and porosity (e.g. light weight concrete). It has been shown that the interface is stronger and this transition zone is smaller in concrete using lightweight aggregate due to interlocking of cement with porous aggregate (Zhang and Gjrv, 1990; Lo and Cui, 2004).

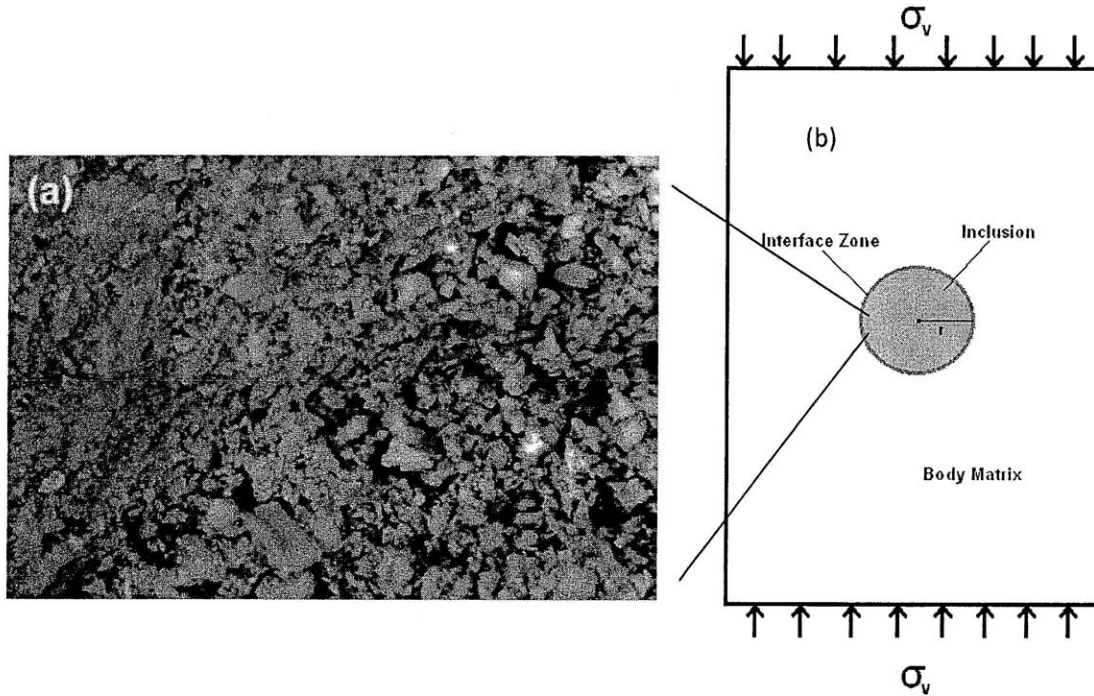


Figure 2.17 – (a) Microscopic view of the interface zone of gypsum specimens similar to those in the current study (Janeiro, 2009) (b) Components of a body containing an inclusion.

In order to fully understand the stress concentrations (change in elastic stress field) created by introducing an inclusion, consider a simplified scenario of a circular inclusion in a plate. Two basic cases are assumed; a circular hole ($E_{inc}=0$) or a circular rigid inclusion ($E_{inc}=\infty$), both subjected to a far-field compressive stress (σ_v) in an infinite plate (See Figure 2.17). Using the derivation of the stress fields associated with a cylindrical hole in a plate by Kirsch (1898) the stress concentration factors around this hole can be determined.

$$\sigma_{\theta\theta} = \sigma \cdot \frac{1}{2} \left\{ \left(\frac{a}{r} \right)^2 + \left[1 + 3 \left(\frac{a}{r} \right)^4 \right] \cos 2\theta + 1 \right\} \quad (2.17)$$

$$\sigma_{rr} = \sigma \cdot \frac{1}{2} \left\{ \left(\frac{a}{r} \right)^2 - \left[1 - 4 \left(\frac{a}{r} \right)^2 + 3 \left(\frac{a}{r} \right)^4 \right] \cos 2\theta + 1 \right\} \quad (2.18)$$

Where a is the distance from the center of the hole, r is the radius of the hole, σ is the far field stress, and θ is the angle with the horizontal. From these equations the σ_{rr} (radial stress) and $\sigma_{\theta\theta}$ (tangential stress) can be determined at any location using polar coordinates (a, θ) (Figure 2.18a).

In order to develop the stress concentration factors for an infinitely rigid inclusion ($E_i \approx \infty$), solutions by Goodier (1933) were used (Figure 2.18b)

$$\sigma_{\theta\theta} = \sigma \cdot \frac{1}{2} \left\{ -(1 - 2\nu_m) \left(\frac{a}{r}\right)^2 + \left[-1 + \frac{3}{3-4\nu_m} \left(\frac{a}{r}\right)^4 \right] \cos 2\theta + 1 \right\} \quad (2.19)$$

$$\sigma_{rr} = \sigma \cdot \frac{1}{2} \left\{ -(1 - 2\nu_m) \left(\frac{a}{r}\right)^2 + \left[1 + \frac{2}{3-4\nu_m} \left(\frac{a}{r}\right)^2 + \frac{3}{3-4\nu_m} \left(\frac{a}{r}\right)^4 \right] \cos 2\theta + 1 \right\} \quad (2.20)$$

where ν_m is the Poisson's ratio of the matrix material.

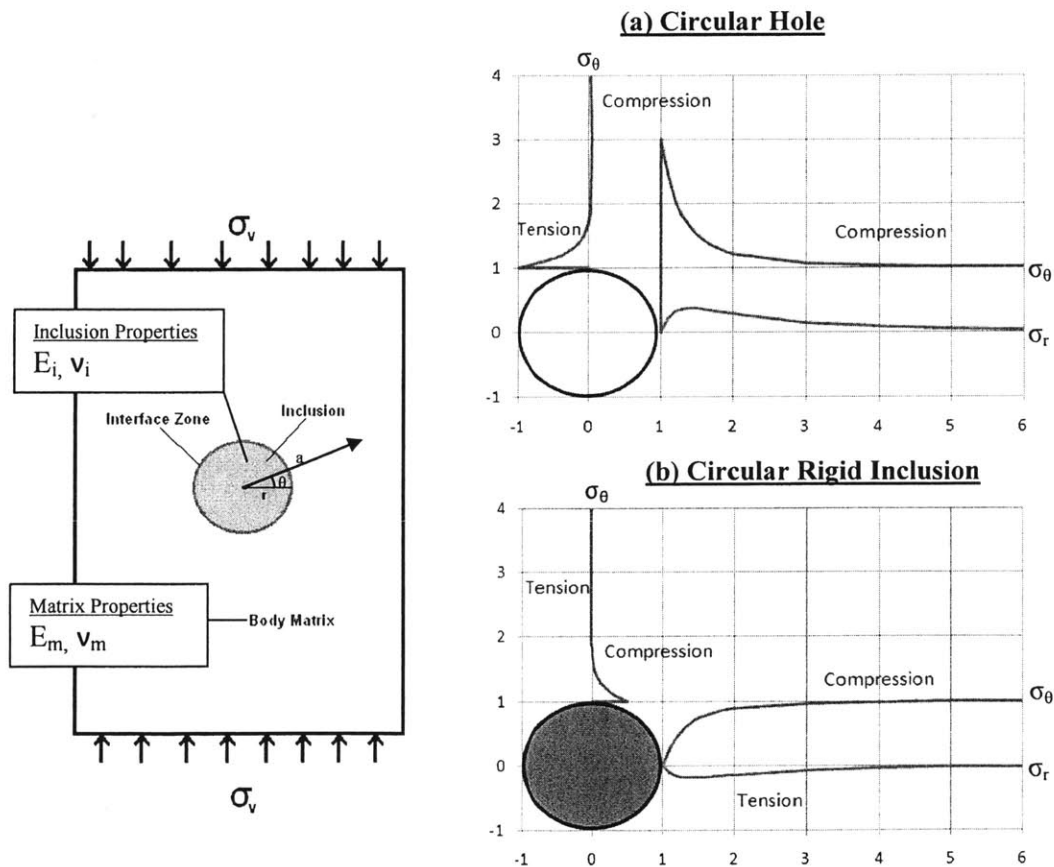


Figure 2.18 – Comparison of a stress concentration factors for a circular hole (a) and rigid inclusion (b) in an infinite plate ($\nu = 0.25$).

In reality, an inclusion material has some elastic modulus that is between these two scenarios ($0 < E_{inc} < \infty$) and therefore the stress concentrations developed fall somewhere between these two cases.

Due to low tensile strengths in brittle materials (concrete especially), the critical stress state is typically tensile. When a hole is introduced into a homogenous brittle material tensile cracks will appear at the locations of maximum tensile stress around that hole. When loaded in compression, high tensile stresses develop at the top and bottom of the holes and cracking will occur first at the edges of the hole in the direction of loading (top and bottom) (Figure 2.18a).

In contrast, when a rigid inclusion is introduced tangential compression is observed on the edges of the inclusion in the direction of loading (top and bottom) (Figure 2.18b). A much smaller tensile tangential stresses will occur at approximately 1.75 radius lengths in the direction of loading. This area of tensile stress in the matrix is a possible location of tensile crack initiation in the matrix above and below the rigid inclusion. A tensile radial stress perpendicular to the loading direction (left and right edges) will occur. Depending on the material and interface properties, tensile debonding may occur at the left and right edges due to the radial tension. Also, since the top and bottom edges of the rigid inclusion are in compression, any debonding which occurs here before matrix crack initiation must be shear in nature.

In order to analytically represent inclusion fracture Zaitsev and Wittmann (1981) used the principle of a sliding wing crack model with stress concentration factors to predict the initiation of a crack in a material containing an inclusion (Figure 2.19). This model assumes that a crack initiates at the interface (A-B) of an inclusion which then propagates in the direction of loading (A-A', B-B').

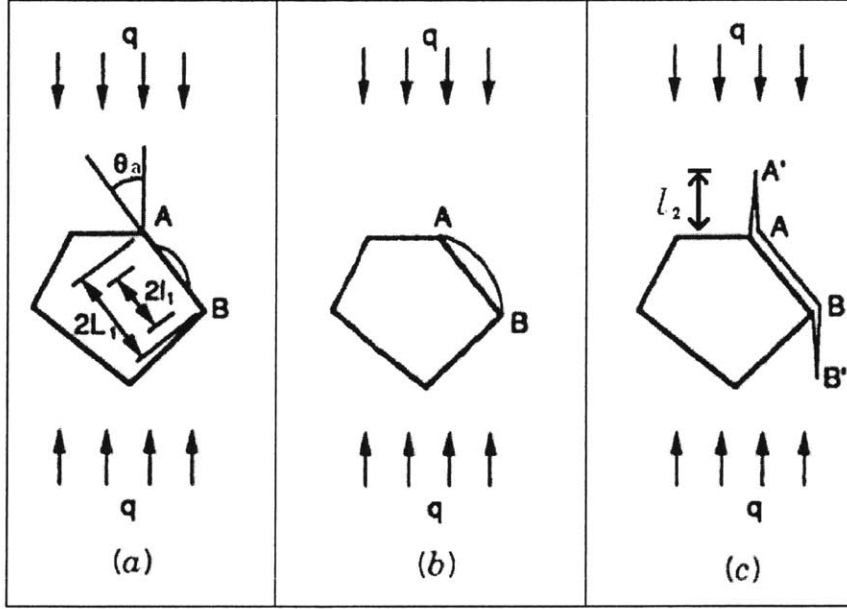


Figure 2.19—Sliding crack model at an inclusion interface (a) Crack initiation at the interface (b) Extension of crack along interface (c) Crack propagation into the matrix (Zaitsev and Wittmann, 1981)

The critical far field compressive stress (q) at which a mode II shear crack (sliding) will initiate along the surface A-B (Refer to figure 2.19) can be expressed as

$$q_{II}^{INF} = - \frac{K_{IIC}^{INF}}{\sqrt{\pi l_1} (k_s \sin \theta_a \cos \theta_a - k_n \mu \sin^2 \theta_a)} \quad (2.21)$$

Where q_{II}^{INF} is the far field stress initiating a shear crack at the interface, K_{IIC}^{INF} is the critical stress intensity factor for mode II shear at the interface, k_s and k_n are the shear and normal stress concentration factors on the interface, l_1 is the length of the crack, μ is the coefficient of friction and θ_a is the inclination. This model assumes some initial discontinuity along the interface ($l_1 > 0$). In addition the far field stress can be determined as a function of the stable tensile crack which initiates in the matrix along the direction of loading (A-A' in figure 2.19) as

$$q = - \frac{\sqrt{\pi l_2}}{2L_1} \frac{K_{IC}^M}{(k_s \sin \theta_a \cos \theta_a - k_n \mu \sin^2 \theta_a) \sin \theta_a} \quad (2.22)$$

Where l_2 is the length of crack in the matrix, K_{IC}^M is the stress intensity factor of tensile cracking in the matrix and L_1 is the total length of the interface where the crack initiated.

This study also incorporated a double inclusion model to predict the propagation of a tensile crack from one inclusion interface to the interface of a second inclusion (See Figure 2.19).

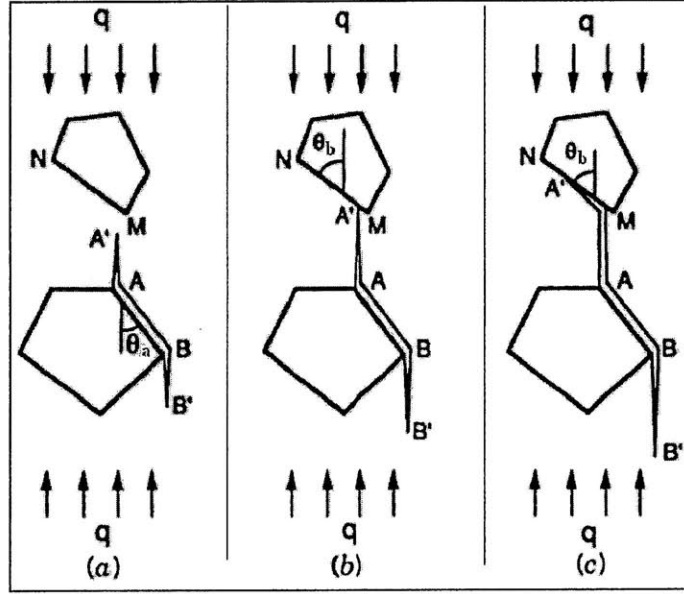


Figure 2.20 –Model in Figure 2.19 with multiple inclusions (a) Initial crack in Figure 2.18c (b) Crack propagation upward to the second inclusion interface (c) Coalescence of crack to the second inclusion interface. (Zaitsev and Wittmann, 1981)

As the crack propagates through the matrix and reaches the interface (M-N) of a new inclusion (Figure 2.20), there are three possible cracking scenarios which can occur; tensile cracking through the inclusion, tensile cracking along the interface, or shear cracking along the interface. The far field stresses (q) are represented by the corresponding stress intensity factors (K) as

$$q_I^{INCL} = -\frac{\sqrt{\pi l_2}}{2L_1} \frac{K_{IC}^M}{D_{IF}(\theta_a, \mu) \cdot \sin \theta_a} \quad (2.23)$$

$$q_I^{INT} = -\frac{2\sqrt{\pi l_2} K_{IC}^M / L_1}{D_{IF}(\theta_a, \mu) \cdot \sin \theta_a \left[3 \cos\left(\frac{\theta_b}{2}\right) + \cos\left(\frac{3\theta_b}{2}\right) \right] - 3D_{IF}(\theta_a, \mu) \cdot \cos \theta_a \left[\sin\left(\frac{\theta_b}{2}\right) + \sin\left(\frac{3\theta_b}{2}\right) \right]} \quad (2.24)$$

$$q_{II}^{INT} = -\frac{2\sqrt{\pi l_2} K_{II}^M / L_1}{D_{IF}(\theta_a, \mu) \cdot \sin \theta_a \left[\sin\left(\frac{\theta_b}{2}\right) + \sin\left(\frac{3\theta_b}{2}\right) \right] + D_{IF}(\theta_a, \mu) \cdot \cos \theta_a \left[\cos\left(\frac{\theta_b}{2}\right) + 3 \cos\left(\frac{3\theta_b}{2}\right) \right]} \quad (2.25)$$

Where,

$$D_{IF}(\theta_a, \mu) = (k_s \sin \theta_a \cos \theta_a - k_n \mu \sin^2 \theta_a) \quad (2.26)$$

where K is the stress intensity factor for the corresponding mode of cracking, and θ_b is the inclination of the second inclusion interface with the vertical.

In 1990, Tasdemir et al. used the sliding wing crack model based on the relations developed by Mellville (1973) (Refer to equations 2.8-2.12) to model a crack along an inclusion interface (Figure 2.21). Similar to the model by Zaitsev and Wittmann (1981), this model assumed a shear crack forming on the interface of an inclined inclusion and propagating as a tensile crack into the matrix. The model accounted for the initial inclination (κ) of the kink crack (wing effect) forming at the crack tip. Tasdemir et al. (1990) used equation 2.11 (Refer to Section 2.2) to show that, for all flaw angles (θ_k), the critical tensile stress intensity factor occurs when the kink inclination (κ) is approximately 71° (κ when $\frac{\delta K_I}{\delta \kappa} = 0$). Unlike the model proposed by Zaitsev and Wittman (1981), this model does not need to incorporate the stress concentrations at the crack interface because it uses the stress intensity factors at the crack tip.

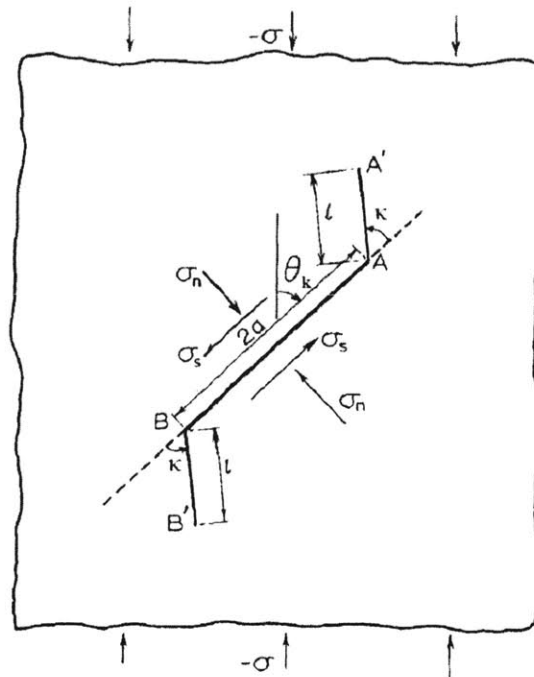


Figure 2.21 – Sliding Crack Model defined by Tasdemir et al. (1990)

2.4.2 Experimental Inclusion Research

In order to verify the assumptions of their model, Zaitsev and Wittmann (1981) conducted a series of uniaxial compression tests on prismatic mortar specimens (40mm x 40mm x 160 mm) with steel inclusions. These inclusions were rounded with one flat inclined face. The inclusions were aligned vertically along the direction of loading (Similar to Figure 2.19) and the faces were either inclined in the same direction or opposite directions (See Figure 2.22).

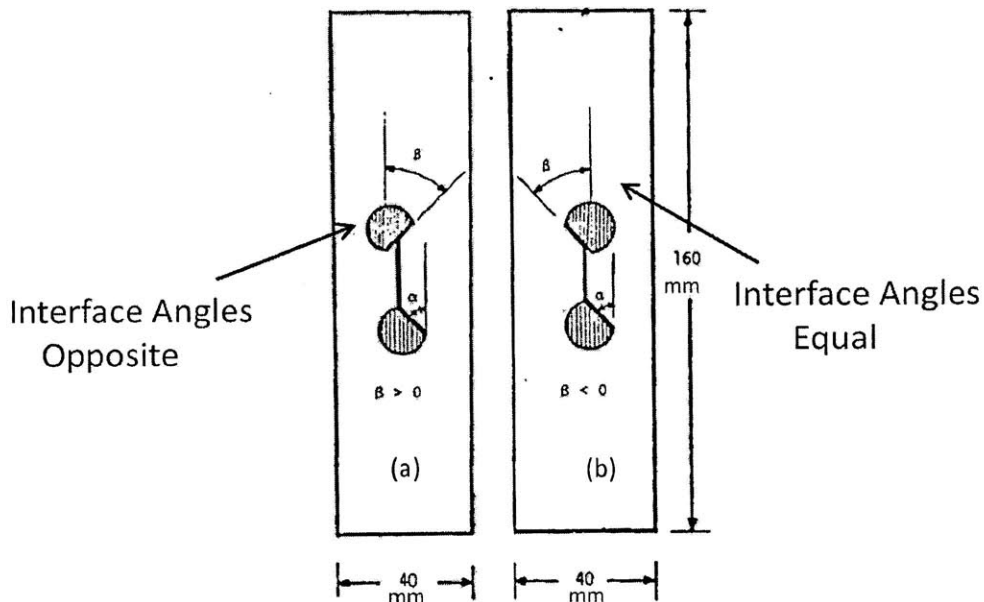


Figure 2.22 – Experiments performed by Zaitsev and Wittmann (1981). Uniaxial compression tests on mortar specimens with steel inclusions. (a) Inclusion interfaces oppositely aligned (b) Inclusion interfaces equally aligned.

These experiments led to the conclusion that inclusions that were oppositely aligned required a higher load to propagate cracking (Zaitsev and Wittmann, 1981). This result showed that the inclinations of the inclusion interfaces (θ_a and θ_b) were very important in determining the far field stresses required to propagate a crack along an inclusion interface and reaffirmed what the derived equations had predicted (Refer to equations 2.21 to 2.26).

Maji and Shah (1989) conducted an experimental study on the cracking of prismatic concrete specimens with either circular limestone inclusions or holes. The holes or inclusions were either 1 inch or 1/2 inch in diameter. (See Figure 2.23) These specimens were loaded in uniaxial compression and holographic interferometry was used to detect cracks down to a 0.3 micron level.

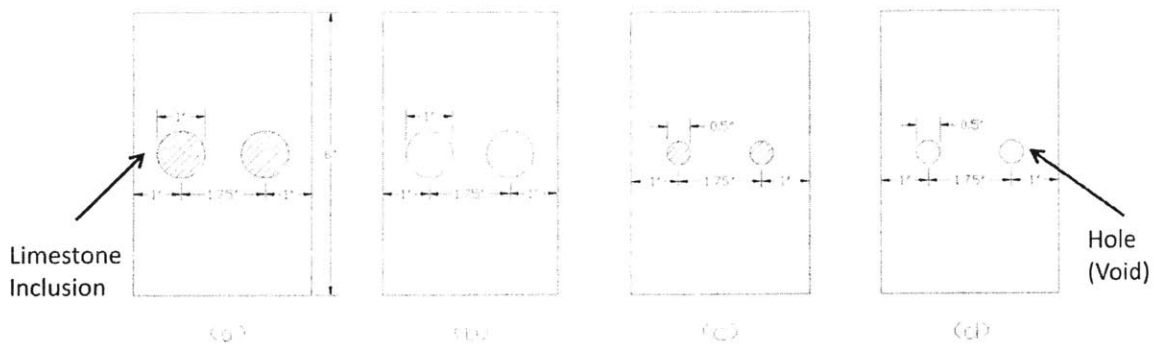


Figure 2.23 – Prismatic specimens tested by Maji and Shah (1989). (a) 1 inch limestone inclusions (b) 1 inch holes (c) 1/2 inch limestone inclusions (d) 1/2 inch holes.

Maji and Shah (1989) reported that cracking typically occurred around the interface of the 1 inch limestone inclusion (debonding) before propagating into the matrix (Figure 2.24b). Debonding cracks were observed at points all around the inclusion. Since debonding occurred on the top and bottom inclusion interfaces, which are in compression due to the direction of compressive loading, it appears that those debonding cracks must have been shear in nature.

Cracking occurring in the matrix initiated at the top and bottom of the inclusions and propagated in the direction of loading (Refer to figure 2.24c). Prior to failure, diagonal cracks connecting the cracks from each inclusion were observed (coalescence). Fewer debonding cracks were observed in the 1/2 inch limestone compared to 1 inch limestone specimens. Slightly non-linear stress-strain behavior was observed for the specimens containing the limestone inclusions.

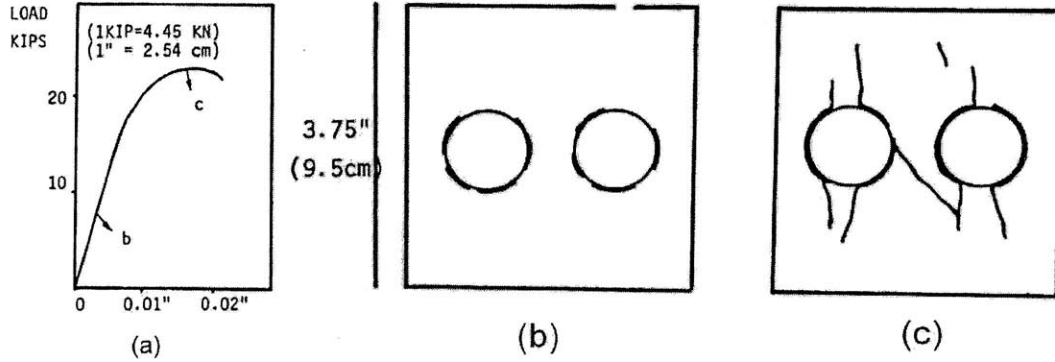


Figure 2.24 – 1 inch limestone inclusion tested by Maji and Shah (1989) (a) Load–Strain curve with the corresponding locations of sketches of (b) and (c)

Different results were observed for the specimens with holes. A more linear stress-strain behavior occurred in the specimens with holes compared to that of the specimens with inclusions. Cracking always initiated at the top and bottom of the holes. Diagonal cracking also occurred between the holes, similar to the inclusions. Although Maji and Shah (1989) concluded that the stress resulting in initiation of cracks depended on the size of the holes, theoretically the stress is not dependent on the size of the hole (Refer to Equations 2.17 and 2.18 by Kirsch, 1898).

In 1990, Tasdemir et al. conducted an additional experimental study based on the derivations of the sliding wing crack model initiation at an inclusion interface (Refer to Section 2.3.1). This study consisted of a series of uniaxial compression tests on prismatic cement specimens (8in x 6in x 3in) which were cast around rectangular limestone inclusions (2in x 0.3in x 3in) oriented at different angles with respect to the direction of loading ($\beta = 18^\circ, 36^\circ, 54^\circ, 72^\circ$) (Figure 2.25).

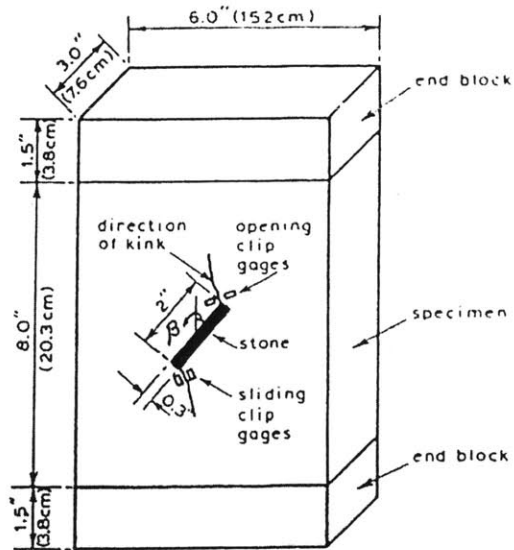


Figure 2.25 – Prismatic cement specimen with an inclined limestone inclusion tested by Tasdemir et al. (1990). The end blocks were limestone to reduce constraining effects. β is the inclusion inclination with respect to the vertical.

The ends were capped with limestone to reduce the constraining effects associated with unconfined compression tests. The first test was conducted without clip gages to determine the locations of sliding and opening cracks at the tips of the stone inclusion. Using holographic interferometry to detect cracking, debonding was always observed to occur before crack propagation in the matrix. This reaffirmed previous assumptions of a crack initiating at an inclusion interface and propagating into the matrix (Zaitsev and Wittmann, 1981; Tasdemir et al. 1990). This debonding typically initiated at very low stress, in some cases at approximately half the stress at crack initiation in the matrix (Figure 2.26) (Table 2.2).

B	<u>Stresses (psi)</u>				Compressive Strength
	Debonding	Crack Initiation ($l = 0''$)	$l = 0.5''$	$l = 1.0''$	
18°	293	573	1057	1478	4657
36°	327	550	983	1200	5380
54°	366	851	1187	1524	-
76°	1450	2986	3560	-	-

Table 2.2 – Tests performed by Tasdemir et al. (1990). Stress levels corresponding to interface cracking (debonding), cracking in the matrix (length, l) and the ultimate compressive strength.

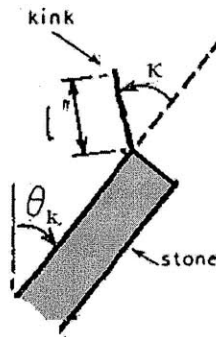


Figure 2.26 – Crack imitation into the matrix (kink) from Tasdemir et al. (1990)

More recently a series of tests on inclusions of different materials and shapes was conducted by Janeiro and Einstein (2009). Extending on the macro-scale flaw testing techniques used in the MIT rock mechanics lab (e.g. Shen et al., 1995; Bobet, 1997; Wong and Einstein; 2009), inclusions were incorporated into molded gypsum and uniaxially loaded. Similar to the work done by Wong and Einstein (2009), the study also used a high-speed camera to record the cracking sequence and nature. Both single and double inclusion pairs of various inclusion shapes (square, diamond, hexagon, circle) (See Figure 2.27), sizes (1/2", 1"), and materials (plaster, Ultracal) were tested.

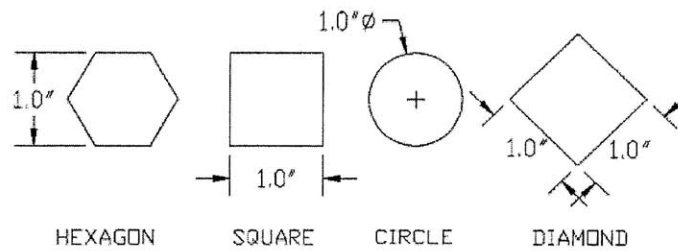


Figure 2.27 – 4 Single Inclusions Tested (Janeiro and Einstein, 2010)

The study tested 1" single square-, circle-, diamond-, and hexagon inclusion shapes as well as 1/2" circular and square inclusions. Pre-test surface cracks due to shrinkage were seen in a considerable number of the single inclusions and occurred more frequently in the 1" inclusions. From these single inclusion tests four tensile crack types were proposed, defined by their initiation point and shape (See Figure 2.28):

Type I – A tensile crack that initiates at the interface and propagates straight upward.

Type II – A tensile crack that initiates at the interface and propagates upward with curvature

Type III – A tensile crack that initiates at a pre-test surface crack (in the inclusion).

Type IV – A tensile crack that initiates within the matrix.

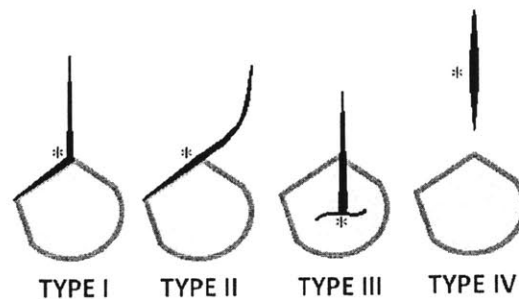


Figure 2.28 – A schematic illustration of the four tensile crack types defined by Janeiro and Einstein (2010) on an arbitrary inclusion shape. * Denotes the point of initiation

Although the cracking type and crack initiation point varied with inclusion size, shape, and stiffness the cracking sequences generally started with a (primary) tensile crack at the inclusion interface (See Figures 2.29 and 2.30). It was shown that the initial tensile cracking was usually followed by a secondary shear crack which propagated into the matrix near the lateral extremity of the inclusion. Also, that study showed that debonding of Ultracal circle inclusions (both 1/2" and 1") and 1/2" square inclusions (both plaster and Ultracal) occurred before cracking in the matrix. Shear debonding was never observed as the initial crack in any of the test series. This is in contrast to previous research, which always observed debonding (usually shear) initially at the inclusion interface and then crack propagation into the matrix.

1" Inclusion Shape & Material		Initial Geometry	Typical Fracturing Sequence and Relative Stress Levels		
Circle	Plaster		 (71%) 3/3 (94%)	 (83%) 3/3 (97%)	 (98%) 2/3 (99%)
	Ultracal		 2/3 (63%)	 2/3 (93%)	 3/3 (99%)
Hexagon	Plaster		 3/3 (81%)	 3/3 (89%)	 3/3 (99%)
	Ultracal	 2/3	 3/3	 3/3	 3/3
Diamond	Plaster		 (82%) 3/3 (99%)	 (92%) 2/3 (99%)	 (94%) 3/3 (99%+)
	Ultracal		 3/3	 3/3 2/3	 3/3
Square	Plaster		 (67%) 2/3 (65%)	 (75%) 2/3 (69%)	 (93%) 2/3 (92%)
	Ultracal	 3/3	 2/3	 1/3 one side 1/3 both sides	 1/3 one side 1/3 both sides

Figure 2.29 – Crack Sequencing for 1" Single Inclusions. The relative stress level, with respect to the maximum stress, is shown in the top right corner (Janeiro, 2009)

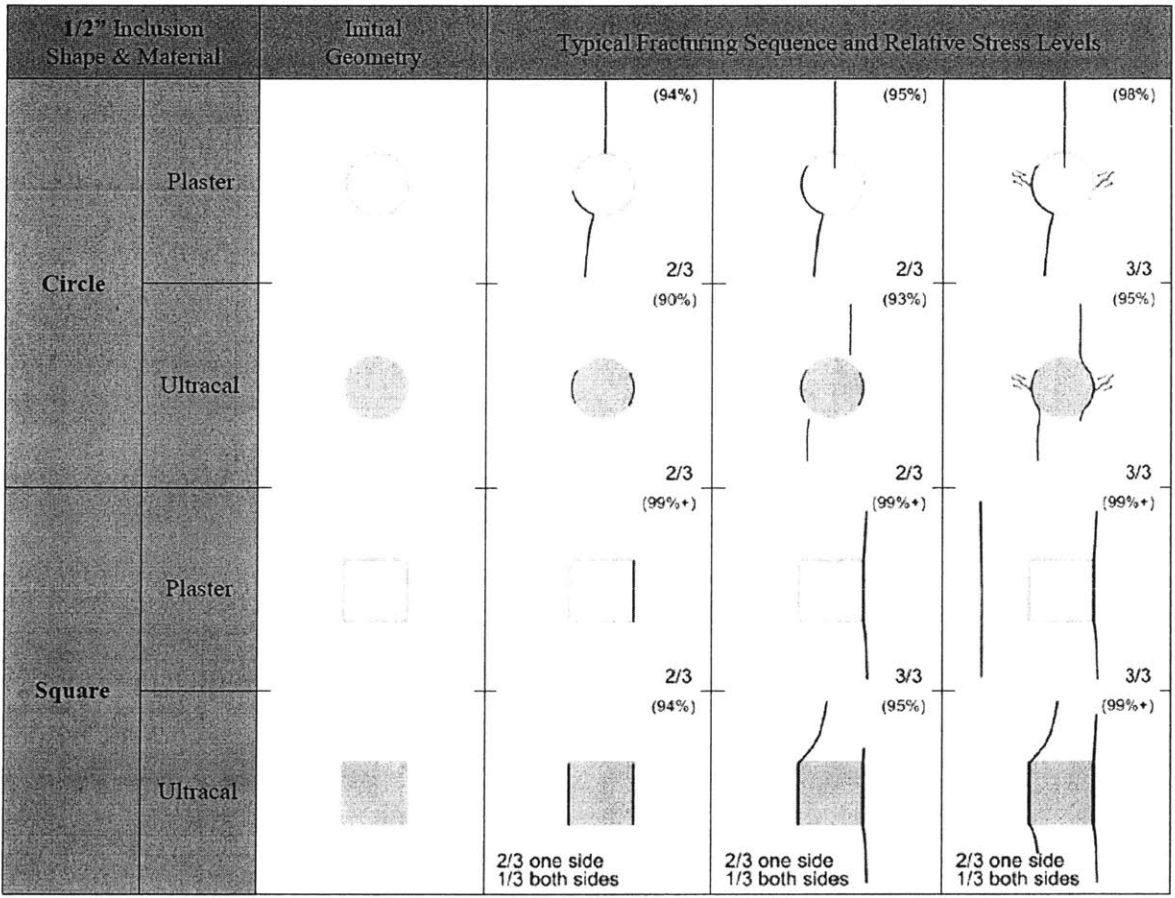


Figure 2.30 – Crack Sequencing for 1/2" Single Inclusions. The relative stress level, with respect to the maximum stress, is shown in the top right corner (Janeiro, 2009)

In addition to testing single inclusions, that study also tested circle and square inclusion pairs with varying bridging angles between the inclusions. Bridging angles for circles were defined relative to their center point, and squares from the top-right of one to the bottom-left of the corresponding square (See Figure 2.31). The coalescence patterns observed for the square and circle inclusion pairs trended from indirect to direct shear coalescence, to a combined tensile and shear crack coalescence (mixed-mode) as bridging angles were increased (See Figure 2.32). There appeared to be no difference in coalescence patterns for inclusion pairs of different material. From that study, Janeiro and Einstein (2010) were able to make comparisons between the coalescence of inclusion pairs and the coalescence patterns in flaws observed by Wong (Refer to Figure 2.16).

Shape		
Sizes	1/2"	1/2"
Materials	Ultracal, plaster	Ultracal, plaster
Bridging Angle (β)	0°, 30°, 60°	0°, 30°, 60°, 75°
Inclusion Angle(α)*	0°	0°

Figure 2.31 – Circle and Square Inclusion Pairs and Orientation Definition (Janeiro, 2009)

* α is the angle between the I.A. (Inclusion Axis) and the horizontal

	PLASTER INCLUSIONS	ULTRACAL INCLUSIONS		PLASTER INCLUSIONS	ULTRACAL INCLUSIONS	Wong (2008)
$\beta = 0^\circ$	 2/3	 3/3	$\beta = -45^\circ$	 2/3	 3/3	
$\beta = 30^\circ$	 3/3	 3/3	$\beta = 30^\circ$	 1/3 (2/3 no coal.)	 3/3	
			$\beta = 60^\circ$	 1/3 (1/3 no coal.)	 2/3	
$\beta = 60^\circ$	 3/3	 2/3	$\beta = 75^\circ$	 2/3	 2/3	

Figure 2.32 – Double Circle and Double Square Inclusion Coalescence (Janeiro and Einstein, 2010) compared with coalescence patterns in flaws as proposed by Wong and Einstein (2009) in the top right (T=Tensile Crack, S=Shear Crack). The number of test repetitions showing this behavior is in the bottom-right.

2.4 Literature Review Summary

It has been shown in previous research that the relative orientation of flaw pairs (flaw inclination and relative pair bridging angle) are key factors affecting coalescence behavior (Shen et al. 1995; Bobet and Einstein, 1998; Wong and Einstein, 2009). As the flaw angle (of co-planar flaws), or bridging angle (of flaws with equivalent flaw angles), increases observed coalescence trends from no coalescence, to shear coalescence, to tensile coalescence (e.g. Wong and Einstein, 2009).

Previous research conducted by Zaitsev and Wittmann (1981), Maji and Shah (1989) and Tasdemir et al. (1990) regarding fracturing in a material containing inclusions assumed a shear debonding crack forming at the interface of the inclusion and propagating into the matrix (similar to a sliding wing crack). This assumption was confirmed by a series of experimental compression tests by Zaitsev and Wittmann (1981), Maji and Shah (1989), and Tasdemir et al. (1990). However, in series of recent experimental tests conducted by Janeiro (2009), which used a high speed camera to detect cracking, both tensile and shear debonding crack types were observed at the interfaces of various inclusion shapes and sizes (refer to figure 2.29 and 2.30). Also in contrast to the previous experimental research regarding inclusions, the initial cracking in the study by Janeiro (2009) did not always occur at an inclusion interface (as debonding) and in some cases initial cracking occurred in the matrix body.

Although there has been a large amount of experimental research conducted on the coalescence patterns between pre-existing cracks (flaws) in a brittle material, little experimental work has been done on coalescence between inclusions. Janeiro and Einstein (2010) conducted a series of compression tests containing inclusions pairs and preliminary results led to similar coalescence patterns that were observed in flaw pairs.

Due to the fact that many previous research studies have shown that initial cracking typically occurs at the interface of an inclusion, the behavior of coalescence between inclusions may be related to the cracks initiating at these interfaces. Inclusion pairs with inclined surfaces, such as those tested by Zaitsev and Wittmann (1981), may clarify the similarities and differences between coalescence patterns of inclined flaw pairs and those observed between inclusions.

CHAPTER 3 – Experimental Setup

3.1 Introduction

To describe the cracking and coalescence patterns in brittle materials containing inclusions a series of uniaxial compression tests were performed on prismatic cast gypsum specimens containing different inclusions. These inclusions were varied in shape (hexagon, diamond, and ellipse), orientation and material. In this research single ellipse inclusions as well as hexagon-, diamond-, and ellipse pairs were tested. A high speed camera was used to determine the cracking processes and coalescence patterns observed. The following sections describe the experimental setup including the materials used, specimen preparation, testing procedures and data analysis.

3.2 Material Properties

Three different gypsum based materials were used in this study; HYDROCAL B-11™, Ultracal™ 30, and white molding plaster. The matrix of the gypsum specimens consisted of HYDROCAL B-11™ gypsum. The two different inclusion materials were chosen to represent a stiffer (with respect to the matrix) and less stiff inclusion. The stiffer inclusion was cast from Ultracal™ 30 and the less stiff inclusion cast from white molding plaster. The difference between the materials' stiffness is represented in their Young's modulus (See Table 3.1). It should be noted that the Young's modulus for Ultracal was determined in a separate test conducted by the researcher and is approximately 74% higher than the 7,500 MPa previously stated by Janeiro (2009) (Appendix A). Also, the Poisson's ratio of the inclusion materials was determined (Refer to Table 3.1) from an additional experiment by the researcher (See Appendix A). Chemically the Hydrocal gypsum and Ultracal Inclusions consist of calcium sulfate hemihydrates ($\text{CaSO}_4 \cdot 1/2\text{H}_2\text{O}$) (~85%) and Portland cement (~15%). The molding plaster only consists of sulfate hemihydrates.

		Material		
		Hydrocal™	Ultracal™	plaster
Young's Modulus, E	[MPa]	5960 ^a	13,020	3330
Ratio to Hydrocal-E		1.00	2.18	0.56
Compressive Strength, σ_C	[MPa]	37.2 ^c	91.1 ^c	28.6 ^c
Tensile Strength, σ_T	[MPa]	2.4 ^b	2.9 ^b	2.9 ^b
Poisson's Ratio, ν		0.24 ^b	0.38	0.20
Density		1.54 ^c	1.69 ^c	1.12 ^c
MSDS # (material safety data sheet)		52-140-047	52-140-018	52-100-016
Portland Cement	[WT%]	>85	>85	~100
CaSO₄ · 1/2H₂O	[WT%]	<10	<10	~0
Crystalline Silica	[WT%]	>5	>5	<1

a:From Bobet, 1997

b:From Nelson, 1968

c:From Janeiro and Einstein, 2010

Table 3.1 – Material Properties of Specimen Matrix and Inclusions

3.3 Inclusion Geometries

This study includes specimens with single ellipse inclusions oriented at 45° (Table 3.2) and specimens with hexagon-, diamond-, and ellipse shaped inclusion pairs (Table 3.3) [Note: One inch and half inch single hexagon-, diamond-, circle- and square inclusions, as well as half inch circle and square inclusion pairs, were previously tested by Janeiro (2009)]. All inclusions were prepared with either Ultracal or plaster. The orientation of the inclusion (α) is defined as the angle between the inclusion axis (I.A.) and the horizontal (Refer to the figures in Tables 3.2 and 3.3). For the hexagon and diamond inclusion geometries the inclusion angle (α) was always 0°. The elliptical geometries were oriented at an inclusion angle (α) of 45°. The orientation of the bridging angles (β) corresponds to the angle between the interior tips of the inclusion shapes of an inclusion pair. In order to ensure consistency in the test results, three tests on each type of inclusion shape, orientation, and material were conducted. For the inclusion pairs, three bridging angles ($\beta = 0^\circ, 30^\circ, 60^\circ$) and two materials were used for each geometric shape, resulting in a total of 54 specimens tested (3 shapes x 2 materials x 3 angles

x 3 test repetitions). In addition, 6 tests were conducted on single ellipse inclusions oriented at 45° (1 shape x 2 material x 1 angle x 3 test repetitions).

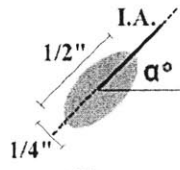
Shape	 Ellipse
Sizes	1/2"
Materials	Ultracal, Plaster
Inclusion Angle(α)*	45°

Table 3.2 – Single geometric inclusions tested in the current study.
* α is the angle between the I.A. (Inclusion Axis) and the horizontal

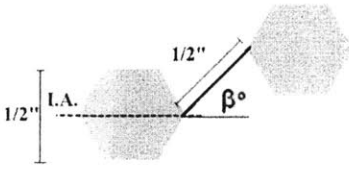
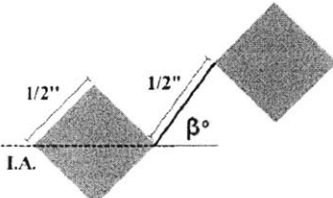
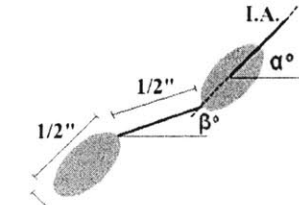
Shape	 Hexagon	 Diamond	 Ellipse
Sizes	1/2"	1/2"	1/2"
Materials	Ultracal, Plaster	Ultracal, Plaster	Ultracal, Plaster
Bridging Angle (β)	0°, 30°, 60°	0°, 30°, 60°	0°, 30°, 60°
Inclusion Angle(α)*	0°	0°	45°

Table 3.3 – Geometric inclusion pairs tested in the current study.
* α is the angle between the I.A. (Inclusion Axis) and the horizontal

3.4 Specimen Preparation

3.4.1 Introduction

The preparation techniques used in this study to cast the gypsum specimens were similar to methods previously used by the MIT rock mechanics group (e.g. Wong, 2008; Janeiro, 2009) [preparation caveats are explained in detail in Appendix B]. The specimen matrix was cast in a special steel mold and nylon bars were used to create the inclusion voids. After the matrix cured, the inclusion material was mixed and poured into the voids. Finally, the specimens were sanded down to a standard size. The final size of the specimens was approximately 6"x3"x1.25" [$\sim 152\text{mm} \times 77\text{mm} \times 32\text{mm}$] (Height x Width x Thickness) (Figure 3.1).

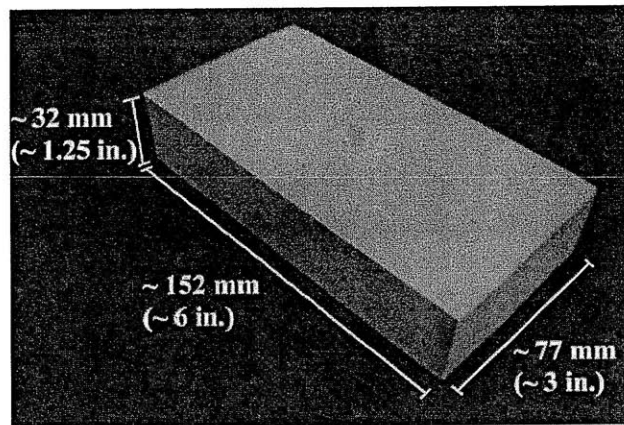


Figure 3.1 – A picture of a final specimen with the average dimensions labeled.

3.4.2 Matrix Casting

Steel molds were used to cast the matrix paste consisting of Hydrocal powder, celite and water at a 175:2:70 mass ratio (Figure 3.2). Celite powder was added to the Hydrocal mix to prevent bleeding when casting the matrix. Nylon bars were used to create the inclusion voids in the matrix. Cardboard stencil forms held the nylon bars in place, perpendicular to the base of the steel mold (Figure 3.3). The Hydrocal was mixed in a common kitchen blender

(KitchenAid™ model k5-A). After removing the cast specimen from the steel molds, the nylon bars were removed and the specimens were hand sanded to smooth out jagged edges. The specimens were then placed in an oven at approximately 40°C for curing. The casting procedure used in this study is depicted in Figure 3.4.

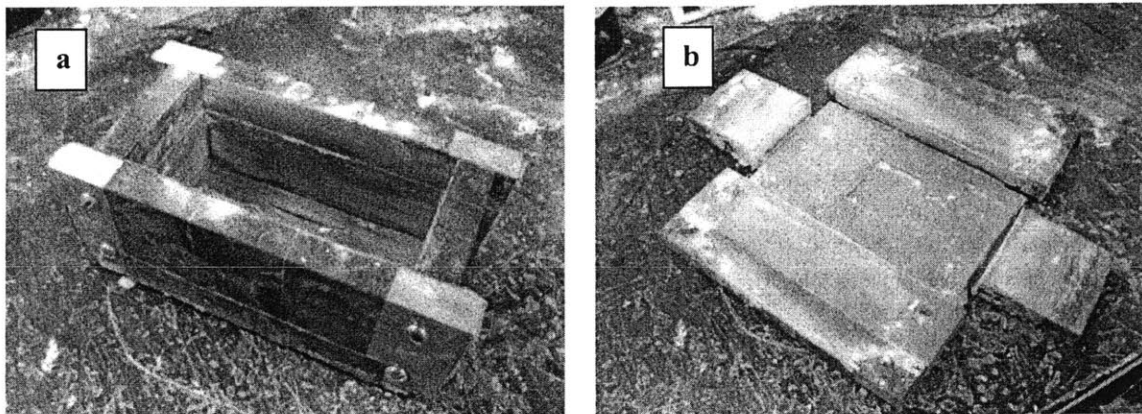


Figure 3.2 – The steel mold used to cast the matrix of the specimens. a) Closed mold b) Open mold

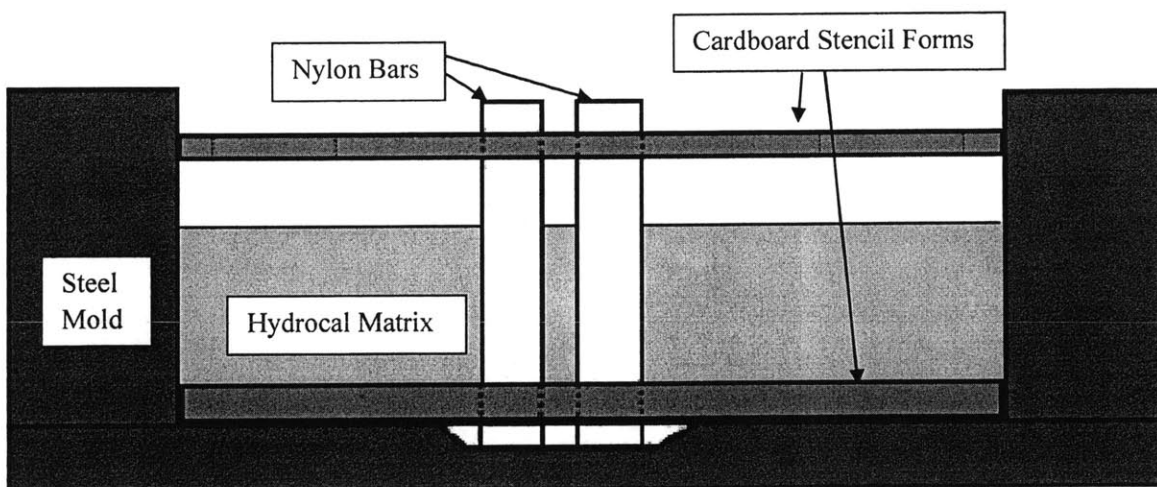


Figure 3.3 – A cross sectional illustration of the steel mold with the top and bottom cardboard stencil forms, nylon bars, and Hydrocal matrix.

Procedure for Specimen Matrix Fabrication

1. Assemble the steel mold with the geometric forms. Grease the nylon bar(s) and place them into the bottom form.
2. Measure **6.4 grams** of celite powder and **560 grams** Hydrocal B-11® (gypsum) powder.
3. Measure **224 mL** of water.
4. Pour the celite powder into the mixing bowl.
5. Pour the water into the mixing bowl.
6. Put the bowl back in the mixer and switch on the mixer at the lowest setting.
7. Switch off the mixer after **20 seconds**.
8. Remove the bowl from the mixer.
9. **Gently** pour the gypsum powder into the bowl.
10. Put the bowl back into the mixer and switch on the mixer at the lowest setting.
11. Switch off the mixer after **four minutes**.
12. Remove the bowl from the mixer.
13. Pour the paste into the steel mold. (Figure 1)
14. Place the bowl and all utensils into the settling bucket to wash later.
15. Put the top form on the mold.
16. Vibrate the mold for **two minutes**.
17. Record the time when the vibration is completed and put the mold on top of a **level** horizontal bench. (Figure 2)
18. Clean the mixing bowl and utensils in the settling bucket.
19. After **one hour**, remove the specimen from the mold
20. Using a screwdriver or hammer **gently** tap out the nylon bars from the specimen. (Figure 3)
19. Label the specimen on its edge.
20. Lightly sand down the specimen edges and inclusion void edges using the hand sander.
21. Place the specimen into the oven set at 40°C.
22. Measure the mass of the specimen after 7 days.
23. Continue to mass the specimen until the mass reaches a constant value.

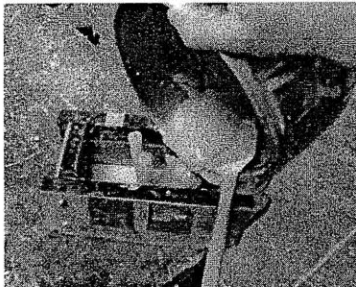


Figure 1

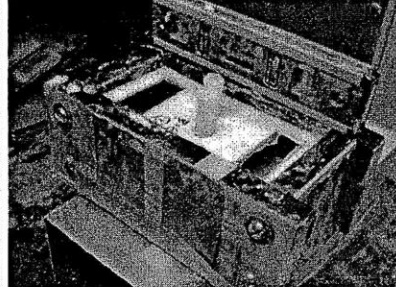


Figure 2



Figure 3

Figure 3.4 – Matrix fabrication procedures [Some parts taken from Janeiro (2009) and Wong (2008)]

3.4.3 Inclusion Casting

Once the specimen reached constant mass the inclusion material was cast into the void (approximately 7 days after casting) (Figure 3.5). The submerging technique developed by Janeiro (2009) was used to prevent the occurrence of surface cracks. After the matrix was submerged the inclusion material was mixed and poured into the voids. The plaster inclusions were mixed at a powder to water mass ratio of 120:81, respectively and the Ultracal inclusions were mixed at a powder to water mass ratio of 59:19, respectively. After the inclusions were cast, the specimen was placed back into the oven until constant mass was reached (approximately 7 days).

Procedure for Inclusion Fabrication

1. Remove the specimen from the oven and submerge it in water at room temperature for **15-20 minutes**. (Figure 1)
2. Remove the specimen from the water and place tape around specimen, over the inclusion voids. (Figure 2)
3. Cut out holes in the tape on one side of the specimen. (Figure 3)
4. Mix the inclusion material as follows:

For Plaster Inclusions

4a. Measure 60 grams of plaster powder, and 40.5 mL of water.

For Ultracal Inclusions

4b. Measure 56 grams of Ultracal® 30 powder, and 19.0 mL of water.
5. Pour the powder into a mixing bowl, and add water.
6. Hand mix for 45 seconds.
7. Pour the paste into the inclusion void and vibrate for 1 ½ minutes. (Figure 4)

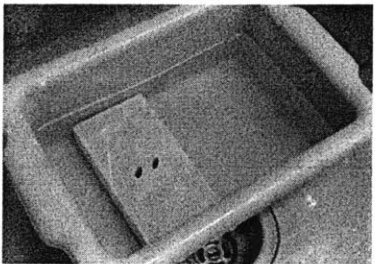


Figure 1

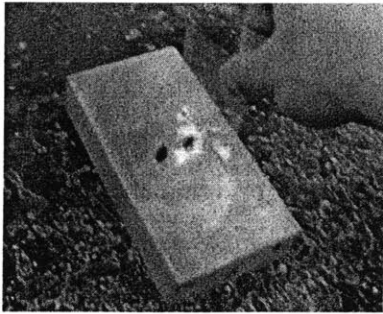


Figure 2

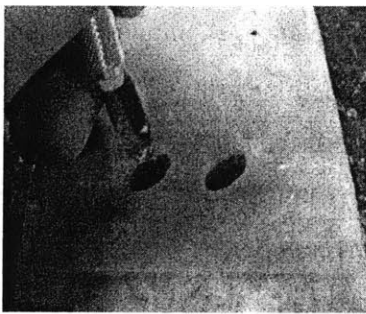


Figure 3

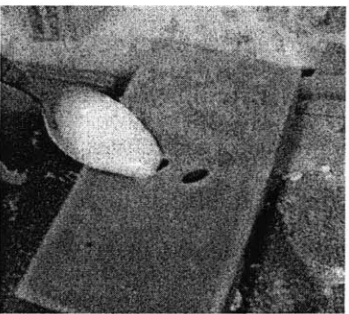


Figure 4

Figure 3.5 – Inclusion fabrication procedures [Some parts taken from Janeiro (2009)]

3.4.4 Sanding

Once the matrix and inclusion had completely cured, the specimen needed to be sanded down to a standard size. Sanding was conducted in a specially constructed sanding box to control particulate dust. A 5 inch circular orbital sander (Figure 3.6a) and steel guide blocks were used to sand the specimen to the desired dimensions (Figure 3.6b). Finer grit sand paper was used as a final stage to polish the front surface of the specimen.

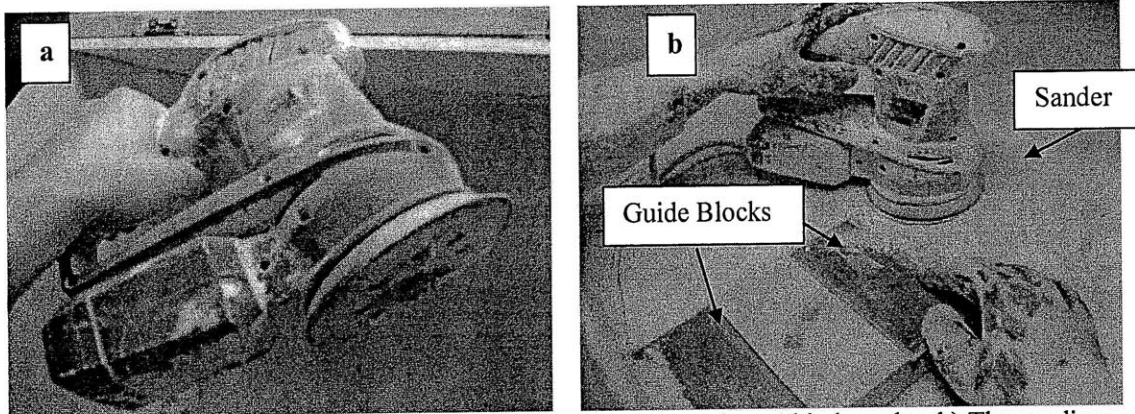


Figure 3.6 – The sanding tools used in the current study. a) A random orbital sander. b) The sanding box including the orbital sander with two steel guide blocks on each side of a specimen.

3.4.5 Pre-Test Preparation

Before testing, each specimen was labeled using the following convention: (Shape)-(Inclusion Angle)-(Bridging Angle)-(Test Repetition)-(Material). If the inclusion angle was zero then the inclusion angle was omitted from the label (such as in diamond- and hexagon- pairs). For example, an ellipse inclusion pair (E) inclined at 45° angle (45) with a 30° bridging angle (30) that was tested as the second test repetition (B) with plaster (p) inclusions would be labeled as (E-45-30-Bp). All specimen dimensions were measured using electronic calipers (0.01 mm accuracy) and then each specimen was massed.

3.5 Uniaxial Compression Tests

3.5.1 Test Setup

The specimens were uniaxially loaded with a 200-KIP Baldwin™ hydraulic loading frame. The data were collected with a program called MTestW, which recorded the load, displacement and time electronically. Dimensions measured prior to testing were used to approximate the stress corresponding to the recorded load. High speed imagery was captured using a Phantom™ V-series high speed camera controlled by a separate laptop computer and the test was also videotaped at real time with a Sony™ Camcorder. Steel brush platens developed by Bobet (1997) were used on the specimen boundaries to reduce end effects (Refer to Bobet, 1997). A photograph of the test setup is shown in Figure 3.7 and a schematic of the test setup is shown in Figure 3.8.

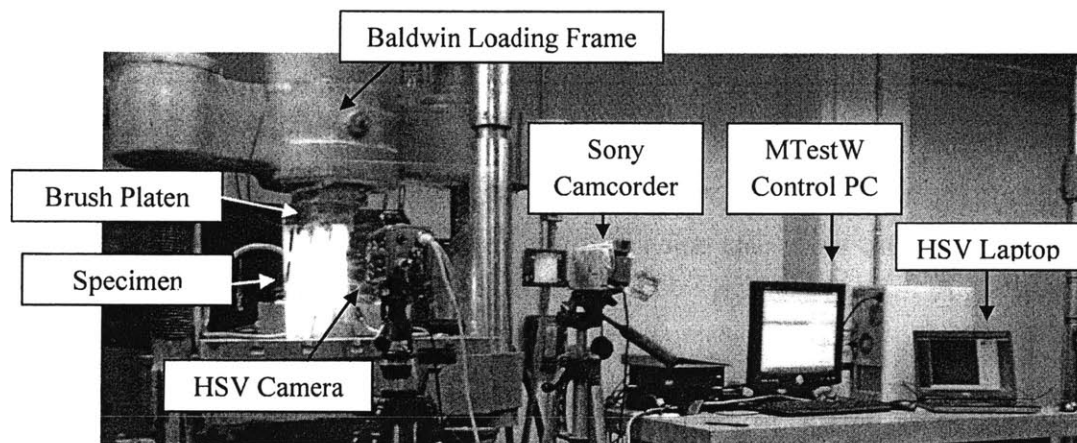


Figure 3.7 – Photograph of the test setup in the current study.

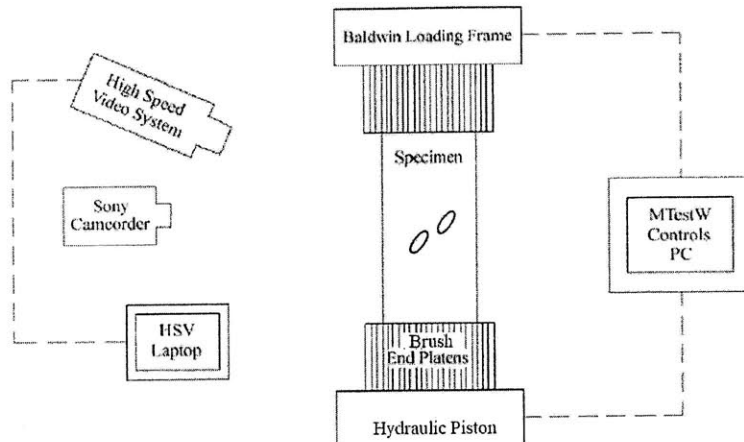


Figure 3.8 – Schematic illustration of the test setup used in the current study.

3.5.2. Loading Regime and Data Acquisition

The loading frame was operated by MTestW (Version M 9.0.7i created by ADMET) and was controlled by either specified position rates or loading rates. These rates could be adjusted and varied over the course of the compression test based on applicable ranges of load. For the current test the control varied from a position controlled rate to a load controlled rate as the specimen was loaded to higher loads (Table 3.4). The amount of data logged (data per second) could also be adjusted specifically for each of the loading regimes. This data logging control was used to record fewer data points at lower loads where cracking and coalesce are less likely to occur (Refer to Table 3.4).

<u>Control</u>	<u>Rate</u>	<u>Load</u>	<u>Data Logging</u>
Position	0.0017 in/sec	0-1,000 lbs.	1.0 sec
Position	0.0003 in/sec	1,000-2,500 lbs.	0.5 sec
Load	38.3333 lb/sec	2,500 – 30,000 lbs	0.1 sec

Table 3.4 – Machine rates and data acquisition regimes for the test setup.

3.5.3 Failure Detection

MTestW automatically stops loading the specimen when a failure is detected. The criterion for failure detection could be adjusted by the program and was based on a drop in load. For the current test setup, failure was determined by any drop in load below 70% of the peak load (Figure 3.9). This setting could be adjusted to determine the high speed processes of different events such as tensile crack initiation, which is typically associated with slight drops in load, by using a higher sample break peak load to detect tensile cracking as “failure”. One drawback to this technique is that any pieces breaking off of the edges or surface spalling, potentially before primary tensile cracking has occurred, would cause the test to stop and the camera to trigger.

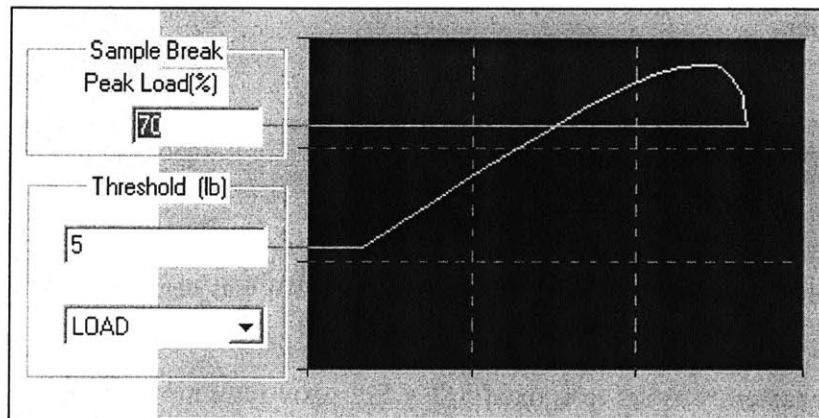


Figure 3.9 - Failure criteria set in MTestW for the current test setup.

3.6 Analysis Procedure

3.6.1 Introduction

For each test both real time and high speed video were recorded. Still images were taken by the high speed camera periodically during the test as well as at key events (crack initiation,

spalling, breaking etc.). From the MTestW load, displacement, and time data were recorded automatically for each test and stress-strain results were determined. Finally, the data was compiled together by synchronizing the key visual images with the stress-strain data.

3.6.2 Real Time Video

For each test real time video was recorded by a Sony Handycam™ (DCR-HC65) and saved to a digital format. This camera recorded at approximately 30 frames per second. This digital format was transferred to a computer and stored electronically. Each video included a label marker indicating the specimen number and a close up recording of the real time cracking events that occurred. When necessary the real time video can be used to determine the real time cracking order.

3.6.3 High Speed Video

A Phantom V-Series (v7.1) high speed camera (Figure 3.10) was centered on the middle of the specimen to capture the cracking and coalescence patterns around the area of the inclusions. The camera was set to a fixed 512 x 512 pixel resolution with the sides of the specimen on the edges of the images. Therefore, the camera recorded a square section of the specimen center about 75 mm x 75 mm (specimen width). The areas above and below the high speed imagery are assumed to behave the same as the top and bottom edges of the images.

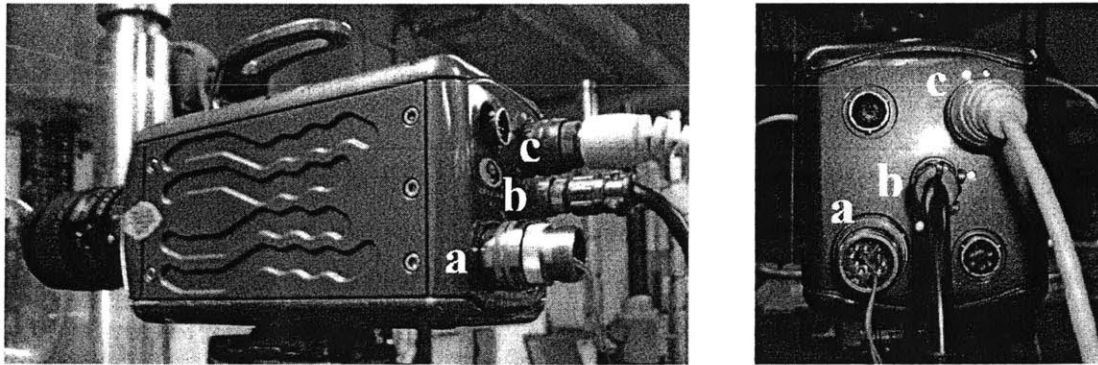


Figure 3.10 – The Phantom V-Series high speed camera used in the test: side view (left) and back view (right). The three connections are labeled (a) Trigger connection to the computer controlled by MWTEST (b) Power cable to the camera (c) Ethernet connection to control the camera with the laptop.

The high speed video for these tests captured about 5,404 image frames over a 1.081 second time period (~5,000 frames per second). In order to capture the high speed video (HSV) the high speed camera needed to be “triggered” by the laptop controlling the camera. The camera was constantly recording and when the camera was triggered the last 1.081 seconds (5404 images) of high speed footage was stored. The camera did have a setting called a “post-trigger”, which allowed the user to set an amount of frames to be captured after the camera has been triggered. The camera operated this way so that the operator could respond to an event (in this case failure) and initiate the trigger.

In the current study, the camera triggering system was upgraded by directly connecting the control box run by MTestW to the camera. An electronic “switch”, which closed when the machine detected failure, allowed the camera to be automatically triggered when the test stopped (capturing failure). This prevented any human error associated with initiating the trigger too late but it did have some drawbacks. In some cases the trigger occurred almost instantaneously with the machine detecting failure and some cracks may have formed after the trigger had occurred. This problem was easily solved by adjusting the post-trigger on the camera to allow for more frames to be recorded after the machine detected failure. Also the automatic trigger only captured failure events, although coalescence may have occurred well

before failure. Regardless, the trigger was a reliable form of capturing high speed imagery with an extremely quick response time.

One of the unique capabilities of the high speed camera is that it was able to capture still images before the high speed imagery has occurred. While the camera was operating, the user had the ability to store still images at any point in the test with the laptop controlling the camera. These still frame images were taken periodically during the test (about every 3,000 lbs load) as reference images to determine changes such as spalling, white patching or debonding. The still images were also captured during any cracking or spalling events and the load was recorded. Since the images were taken from the same visual reference point as the high speed video, the still images were primarily used to describe pre-high speed video events.

3.6.4 Synchronization

In order to relate the events in the videos with stress-strain data, the videos and images need to be synchronized to reference points (Figure 3.11). The real time video was synchronized by relating the point of initial tensile cracking since it was a very distinct point in each test. High speed imagery was referenced by relating the failure point in the high speed footage to the peak stress in the stress-strain data.

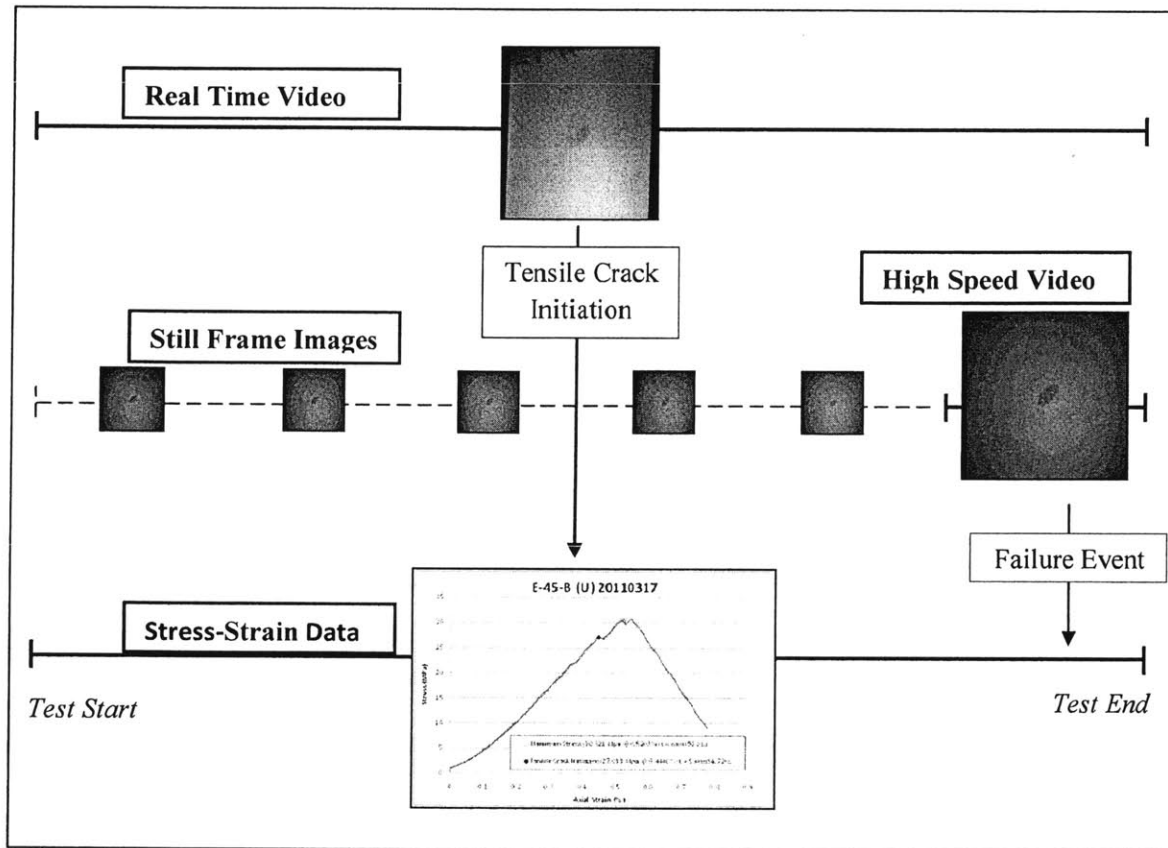


Figure 3.11 – A schematic illustration of the data synchronization in chronological order. Not to scale. Solid lines indicate continuous record and dashed lines indicate periodic still frames taken.

3.6.5 Visual Analysis

Although real-time video was taken for all tests, the analysis used the higher resolution still images manually taken by the high speed camera along with the high speed footage of failure. The real time video was used as an alternative reference to determine general cracking order or to investigating discrepancies in the still images, which were manually captured.

From the images captured by the high speed camera during the test, the cracking sequences and progressions could be presented visually using Adobe Photoshop CS4™ (Figure 3.12). Each test was sub-divided into specific events according to key points such as crack initiation,

coalescence or failure. Cracks were identified and labeled corresponding to their mode; “T” for tensile cracks or “S” for shear cracks. Arrows were included with shear cracks to indicate the direction of shearing. Spalling occurring on the surface of the specimen was designated by a lightly shaded area. Cracks were labeled in the order which they occurred by numeric sub-scripts. Any event frame which had multiple cracks occurring had each crack labeled chronologically if the order could be determined, otherwise the cracks were numbered arbitrarily from left to right (this was explicitly stated in each frame of the data analysis).

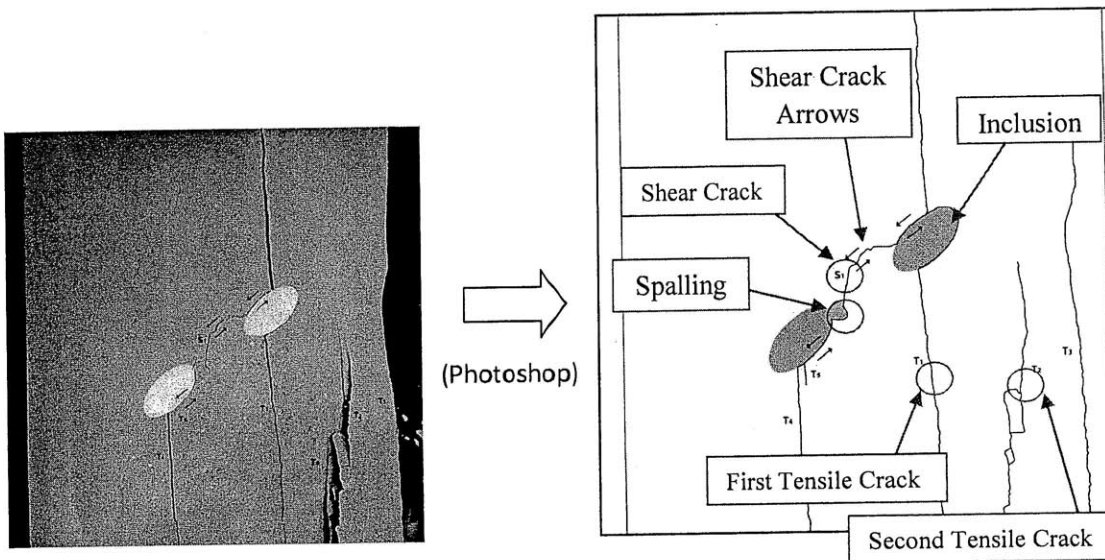


Figure 3.12 – An example of a high speed image of the visual analysis from E-45-30-Cp. T = Tensile crack, S = Shear crack. The arrows indicate the direction of shearing. The lighter colored shading is an area of spalling.

3.6.6 Stress Strain Analysis

The stress-strain results were determined from the load, displacement and time data automatically collected by MTestW (Figure 3.13). The approximate stress applied was determined by dividing the load cell output (load) by the initial specimen cross sectional dimensions (per area) (engineering stress). The strain was calculated by dividing the initial specimen length by the displacement of the loading frame (engineering strain). Using the synchronized event frames from each test, three key points in each test were identified on the

stress-strain curve; tensile crack initiation, coalescence, and failure. In some tests coalescence did not occur and thus “no coalescence” appears on the analysis legend.

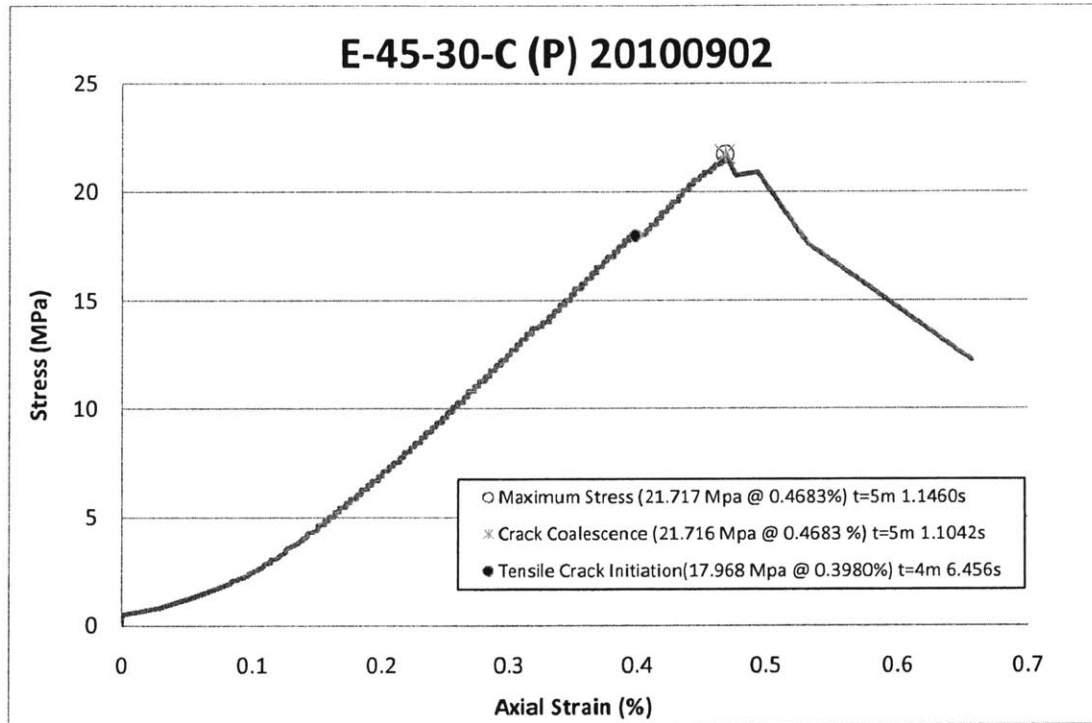


Figure 3.13 – An example of the stress-strain summary for a test conducted on plaster ellipse pairs with an inclination angle of 45 and a bridging angle of 30 (E-45-30-Cp). Maximum stress, crack coalescence and tensile crack initiation in the legend are shown on the curve.

3.6.7 Compilation

Both the interpreted visual results and the synchronized stress-strain data were combined into a final compiled analysis of the event frame (Figure 3.14). The analysis included a description of the processes (cracking, spalling, breaking, etc.), which occurred in that frame as well as their order. Any frame that had a key event (tensile crack initiation, coalescence, failure) occurring was labeled accordingly. A full test analysis included multiple event frames which explain the cracking progression and state (stress/strain) at key points of the test.

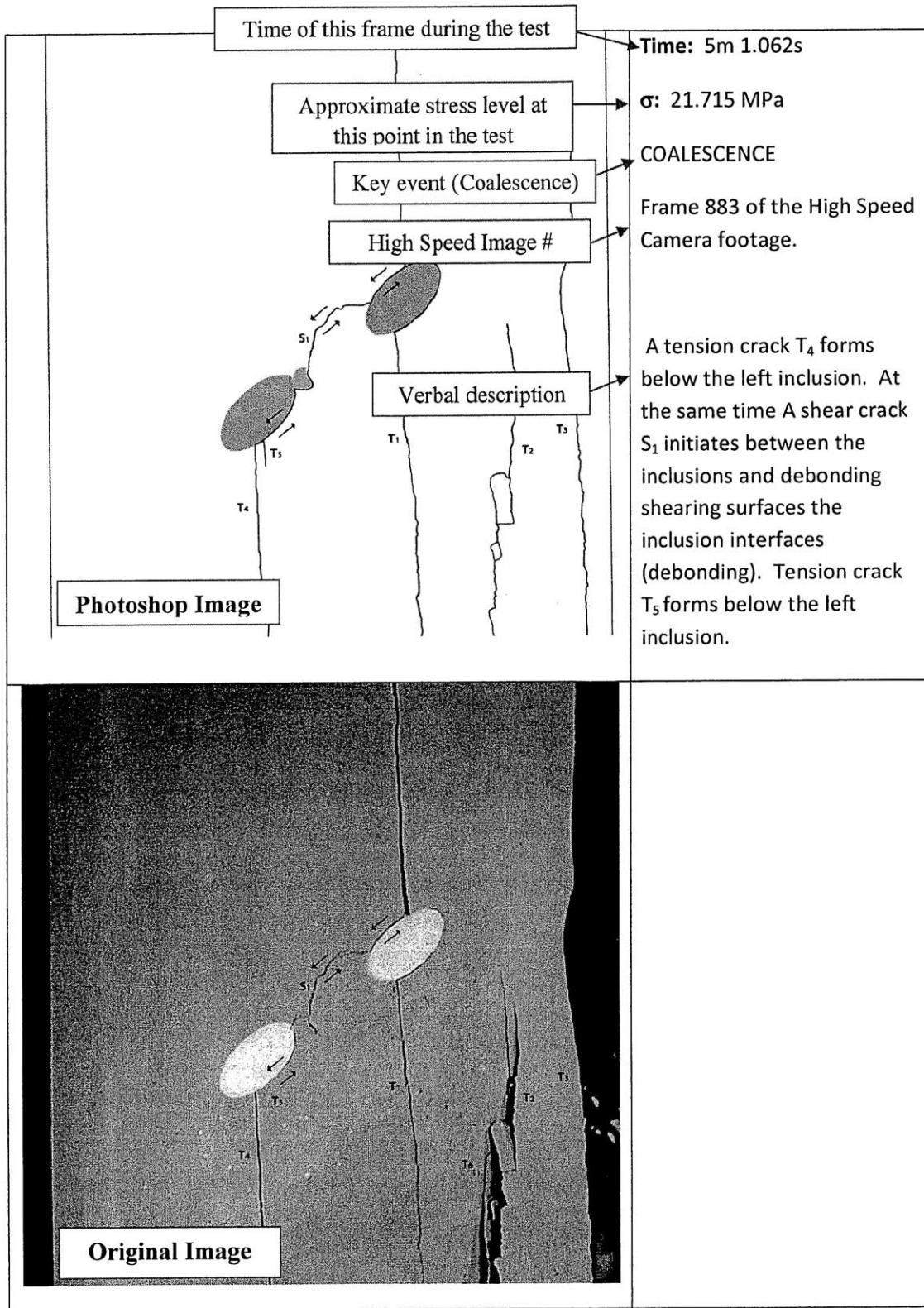


Figure 3.14 – An example of a combined data analysis which includes both visual data as well as stress/time data of a specific uniaxial compression test (E-45-30-Cp).

CHAPTER 4 – Results: Single Ellipse Inclusions

4.1 Introduction

In order to better compare the fracturing behavior of a brittle material with inclusions to a brittle material with flaws, elliptical shaped inclusions were introduced into gypsum specimens. Specimens with single ellipse inclusions were cast and a series of uniaxial compression tests were conducted to determine the fracturing behavior. The detailed analysis of these single ellipse tests can be found in appendix C.

4.2 Single Ellipse Inclusions

Half-inch single ellipse inclusions (quarter-inch minor axis) were incorporated into the gypsum specimens to compare the previous research regarding both inclusions and flaws in brittle material (See Figure 4.1). These elliptical inclusions were oriented at a 45° angle (α) from the horizontal (Refer to Figure 4.1). Two gypsum based inclusion materials were used to represent a stiff (Ultracal) and less stiff (molding plaster) inclusion compared to the matrix stiffness. Three test repetitions were conducted for inclusion material, for a total of 6 tests.

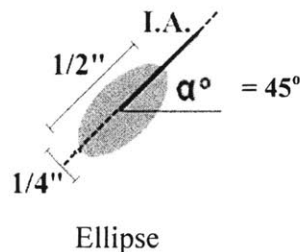


Figure 4.1 – Single ellipse inclusions tested in this study. α is defined as the angle between the inclusion axis (I.A.) along the major axis and the horizontal. α was always 45° for the single ellipse test series.

4.3 Cracking Behavior

4.3.1 Introduction

For each material the cracking sequences (order) and patterns (shape) were determined. The cracking progression was determined for ellipse inclusions of each inclusion material (Figure 4.2). The number in the top left is the number of test repetitions exhibiting the shown behavior and the number in the top right is the average percentage of the peak stress when the behavior occurred. All of the tests had tensile cracking occur before the high speed imagery was taken. Therefore, the point of primary tensile crack initiation and the direction of propagation are not shown.




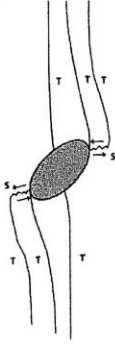


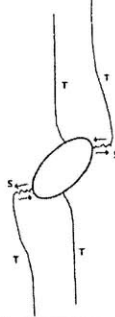
Material	Initial	Primary		Secondary	
		Tensile	Tensile	Tensile	Shear-Tensile
Ultracal		(3/3) 85% 	(3/3) 89% 	(3/3) 99% 	
Plaster		(2/3) 91% 	(3/3) ~100% 		

Figure 4.2 – Fracturing sequence for single 45° ellipse inclusions with either a) Ultracal or b) Plaster inclusion material. T = Tensile Cracking, S = Shear Cracking. Arrows indicate the direction of shearing.

4.3.2 Cracking Sequence

The cracking sequences of elliptical inclusion depended on the inclusion material (Refer to Figure 4.2). In both inclusion materials, primary tensile cracking typically occurred along the inclusion interface (debonding). Primary tensile cracking was followed by secondary tensile cracking in specimens with Ultracal inclusions. Both inclusion materials exhibited secondary shear cracking occurring at the exterior “tips” of the inclusion with a tensile crack propagating toward the direction of loading.

4.3.3 Debonding

When primary tensile cracking initiated, significant debonding of the elliptical inclusions was observed. In many cases there was complete debonding occurring from the primary tensile crack (Figure 4.3a). It should be noted that both initial tensile cracking and debonding occur before high speed imagery was recorded. Therefore, the sequence and cracking mode (tensile or shear) in which the debonding occurred could not easily be determined using high speed techniques. However, using the still frame images, taken before failure, the majority of debonding appeared to occur from a single primary crack which appeared to be tensile in nature. In one test case the inclusion did not completely debond from primary tensile cracking and shear debonding was observed when the secondary shear cracking occurred (Figure 4.3b).

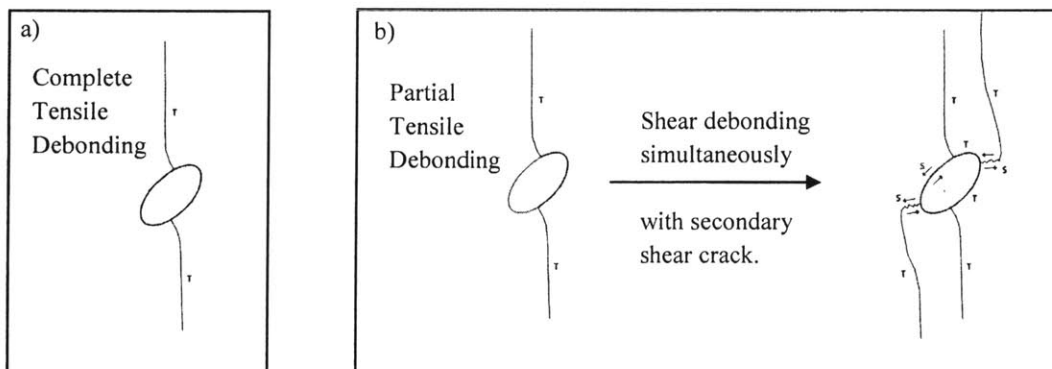


Figure 4.3 – Typical debonding occurring in the single ellipse inclusions tested for **both** materials. a) The typical tensile debonding observed. b) Shear debonding occurring in one of the test repetitions.

4.3.4 Primary Tensile Cracking

Primary tensile cracking occurred initially in both Ultracal and plaster inclusion specimens (Refer to figure 4.2). However, there were some slight differences in the shape and location of this tensile cracking. Specifically, there was a difference in the point at which the primary tensile cracks intersected the inclusion interface depending on the inclusion materials (Figure 4.4). In specimens with Ultracal inclusions primary tensile cracking occurred close to the mid-point of the inclusion interface (Refer to Figure 4.4). In specimens with plaster inclusions primary tensile cracking occurred closer toward the exterior “tips” of the inclusion interface. The primary tensile cracks in specimens with plaster inclusions also had slightly more curvature (Refer to Figure 4.4). Specimens with Ultracal inclusions had primary tensile cracks with very little curvature and typically propagated more linearly toward the direction of loading.

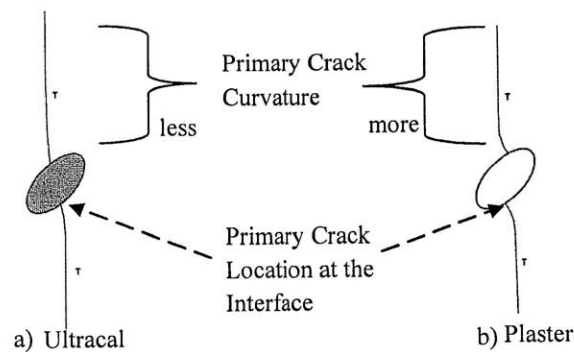


Figure 4.4 – Primary tensile crack location and shape for a) Ultracal and b) Plaster single ellipse inclusion specimens tested.

4.3.5 Secondary Cracking

Cracks which occurred after primary tensile cracking are referred to as secondary cracks. Secondary cracks always occurred on the left-hand or right-hand exterior tips of the inclusion. All secondary cracks showed propagation in either direction (up or down), toward the direction of loading. In specimens with Ultracal inclusions, the primary tensile crack was followed by secondary tensile cracking at the exterior tips of the inclusions (See Figure 4.5).

Both inclusion materials exhibited secondary shear cracking typically occurring at the exterior tips of the inclusion at stresses near the maximum failure stress (Refer to Figure 4.5).

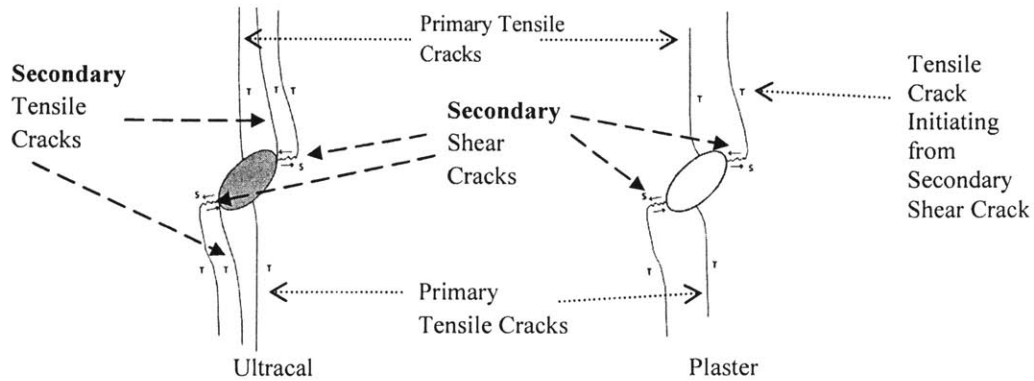


Figure 4.5 – Secondary shear cracks observed at the exterior “tips” of the single ellipse inclusions tested. S = Shear crack. The arrows indicate the direction of shearing.

4.3.6 Spalling

The surface spalling was also determined for the ellipse specimens in the current test series. Regardless of inclusion material, spalling typically occurred at the “tips” of the ellipse simultaneously with secondary shear cracking (Figure 4.6). Since surface spalling is one of the indicators of shear cracking, spalling occurring near these exterior secondary shear cracks should be expected.

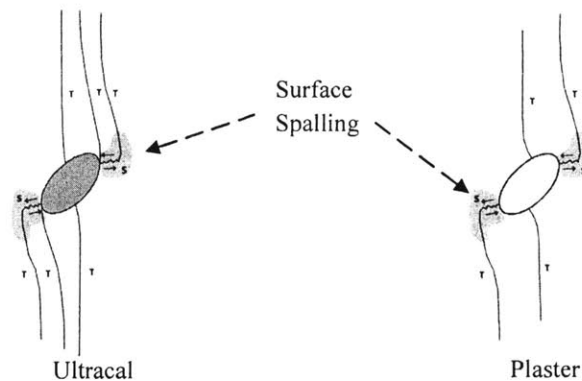


Figure 4.6 – Areas of spalling occurring near the exterior “tips” of the single ellipse inclusions tested. Shaded areas near shear cracking indicate locations of surface spalling.

4.4 Stress Behavior

4.4.1 Introduction

From the Stress-Strain data recorded during each test specific key stress values were determined and calculated. The maximum and tensile crack initiation stresses were calculated. The ratio of tensile crack initiation to maximum stress was also calculated as well.

4.4.2 Maximum Stress

For each specimen the maximum stress exhibited during the test was determined (Figure 4.7). In this study the maximum stress was defined as the peak stress at failure. All of the specimens with ellipse inclusions had a lower maximum stress than the compressive strength of the Hydrocal matrix (Refer to Figure 4.7). A slightly higher average maximum stress was exhibited in the ellipse specimens with Ultracal in comparison to those of plaster.

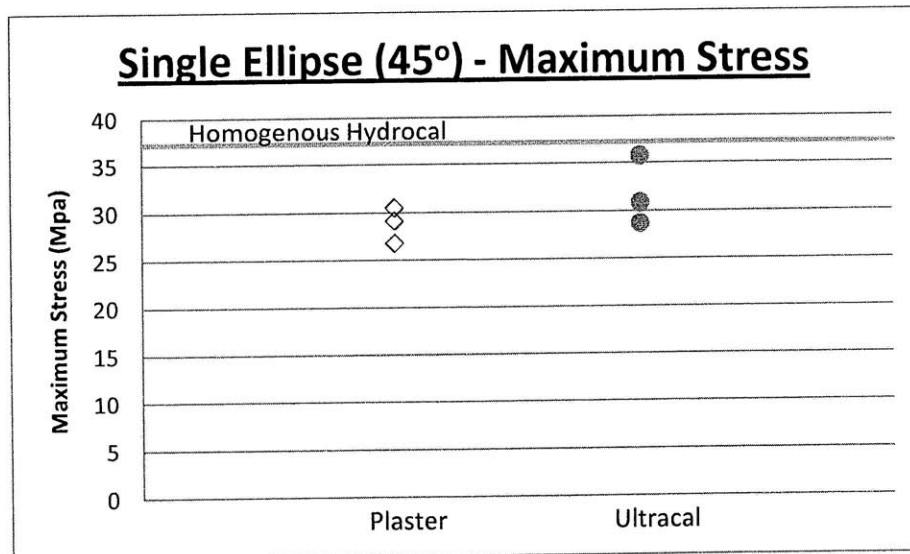


Figure 4.7 – **Maximum stress** of specimens with single **ellipse** inclusions. Blue = Ultracal (solid circles), Red = Plaster (hollow diamonds). The compressive strength of the homogenous Hydrocal matrix was plotted as a green line.

4.4.3 Tensile Crack Initiation

Along with the maximum stress of each test specimen, the stress when primary tensile crack initiated was also determined (Figure 4.8). Slightly higher tensile crack initiation stresses were observed for Ultracal inclusions compared to plaster.

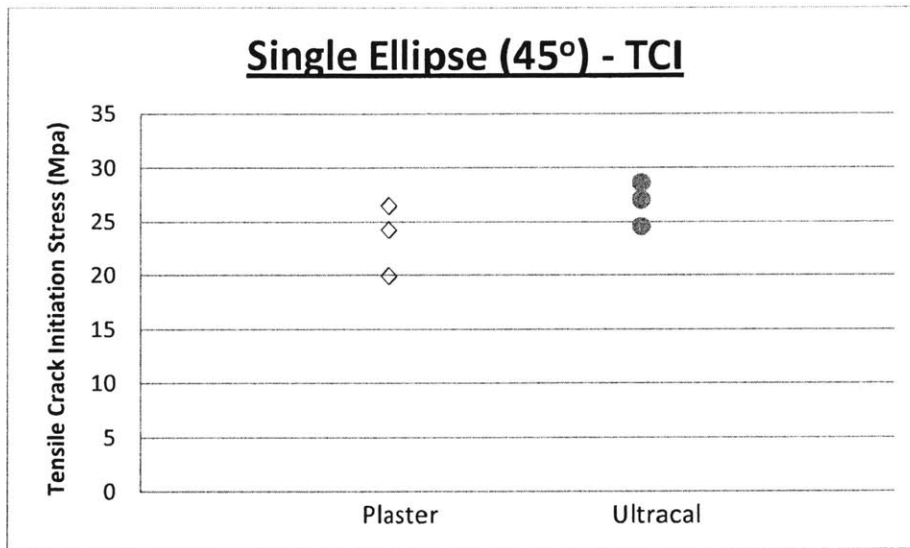


Figure 4.8 – **Tensile crack initiation (TCI) stress** of specimens with single **ellipse** inclusions. Blue = Ultracal (solid circles), Red = Plaster (hollow diamonds).

To determine the relative stress at which primary tensile cracks initiated in each specimen, the tensile crack initiation stress was normalized by the maximum stress in each test as

$$\text{TCI Ratio} = \frac{\text{Tensile Crack Initiation Stress}}{\text{Maximum Stress}} \quad (4.1)$$

The tensile crack initiation ratio (TCI Ratio) was calculated for each test and is presented in Figure 4.9. There was a large spread in the TCI ratio between the test repetitions, for both Ultracal and plaster ellipse inclusions (Refer to Figure 4.9). The average TCI ratios of the two inclusion materials appeared to be similar with the average values approximately between 80 to 90 % (0.80-0.90) of the maximum load.

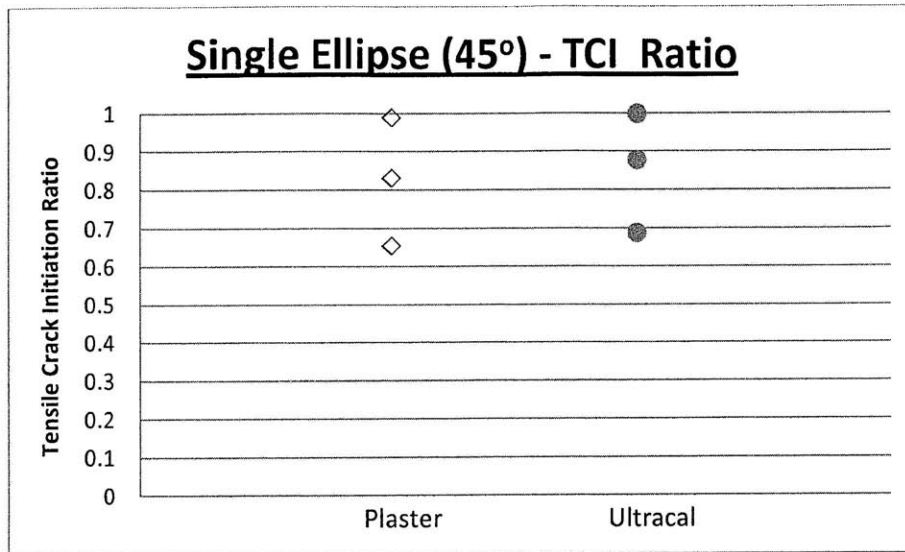


Figure 4.9 – **Tensile crack initiation (TCI) ratio** of specimens with single **ellipse** inclusions. Blue = Ultracal (solid circles), Red = Plaster (hollow diamonds).

4.5 Summary

The cracking sequence of inclined elliptical inclusions was similar for both Ultracal and plaster inclusion materials. Primary tensile cracking, typically resulting in complete debonding, was followed by secondary shear cracking and surface spalling near the exterior tips of the inclusion interface. Ultracal inclusions showed secondary tensile cracks occurring at the exterior tips of the inclusion before secondary shear cracks formed.

Slightly higher maximum stresses and tensile crack initiation stresses were observed in ellipse inclusions of Ultracal compared to those of plaster. However, the normalized tensile crack initiation stresses were similar for both inclusion materials.

CHAPTER 5 – Results: Inclusion Pairs

5.1 Introduction

In addition to testing half-inch single ellipse inclusions, half-inch inclusion pairs were tested with hexagon-, diamond- and ellipse (oriented at 45°) shapes as well (Figure 5.1). Similar to the previous tests, the inclusion material was varied between Ultracal (stiffer) and plaster (less stiff). Also, the orientation angle between the inclusions (the bridging angle, β) was varied between three angles; 0° , 30° , 60° (Refer to Figure 5.1). Three repetitions were conducted for each geometric configuration and inclusion material, resulting in 54 total tests (3 shapes x 2 materials x 3 angles x 3 test repetitions). A fourth test repetition was conducted if there was a testing error in one of the test repetitions or if the patterns of the three previous test repetitions were not conclusive.

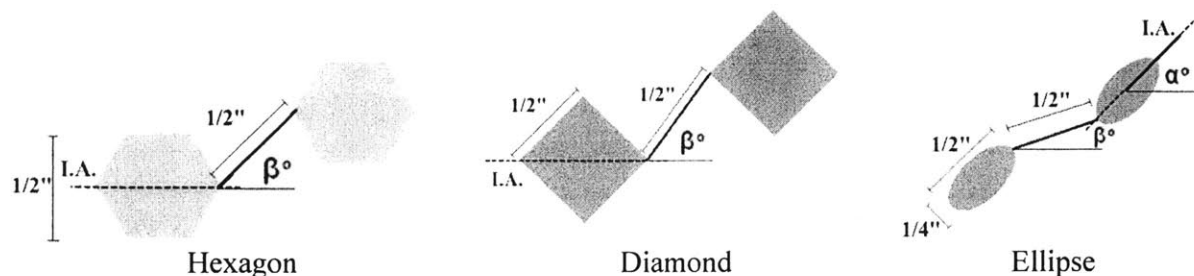


Figure 5.1 – Inclusion pairs geometries tested in this study. β is the angle between the interior reference tips of the inclusions and the horizontal. α is the angle between the inclusion axis (I.A.) defined for each inclusion and the horizontal.

Each test specimen was given a specific label based on the geometric configuration, material and test repetition. The labels consisted of the first letter of the shape (E – ellipse, D – diamond, H – hexagon) followed by the inclusion angle (α) (Refer to Figure 5.1). Tests with 0° inclusion angles, such as the specimens with hexagon- and diamond pairs, omitted the inclusion angle (α) part of the label. The following number on the label was the bridging angle (β) between the inclusion pairs. This was followed by the test repetition (A, B, C, or D for a fourth test repetition). Finally, the last letter was the inclusion material, either “u” for Ultracal or “p” for plaster. The label for the first test repetition (“A”) of each geometric series

can be seen in Table 5.1. The visual representation of the geometric configurations (independent of inclusion material) can be seen in Figure 5.2.

Inclusion		Bridging Angle, β		
		0°	30°	60°
Hexagon	Ultracal	H-0-Au	H-30-Au	H-60-Au
	Plaster	H-0-Ap	H-30-Ap	H-60-Ap
Diamond	Ultracal	D-0-Au	D-30-Au	D-60-Au
	Plaster	D-0-Ap	D-30-Ap	D-60-Ap
Ellipse ($\alpha=45^\circ$)	Ultracal	E-45-0-Au	E-45-30-Au	E-45-60-Au
	Plaster	E-45-0-Ap	E-45-30-Ap	E-45-60-Ap

Table 5.1 – Labeling notation for the first test repetition (“A”) of the tested inclusions pairs. Additional test repetitions would have the “A” replaced with B, C, etc.




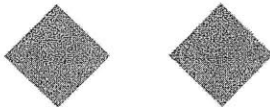
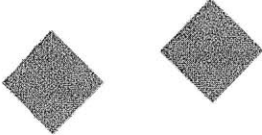
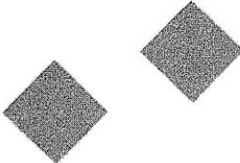



Inclusion	Bridging Angle, β		
	0°	30°	60°
Hexagon			
Diamond			
Ellipse ($\alpha=45^\circ$)			

Figure 5.2 – A visual representation of geometric series tested in this study. The inclusion material is not shown because these geometric series are the same for specimens with different inclusion material.

In the following sections, the results are divided into the observed behavior of each shape. The observed debonding, cracking sequences, surface spalling, coalescence patterns and stress behaviors of each shape will be discussed. Lastly, the behavior of all the tested inclusion pairs will be summarized and compared.

When presenting the debonding and cracking types observed in the inclusion pairs a particular convention was used to represent the symmetry of the cracks. If the debonding or cracking type was typically observed on either inclusion (left or right), as well as on either side of both inclusions (left or right), a single inclusion was used to represent all of these configurations (symmetry) (Figure 5.3). If the cracking or debonding type was associated with the inclusion pair’s orientation then an inclusion pair was presented.

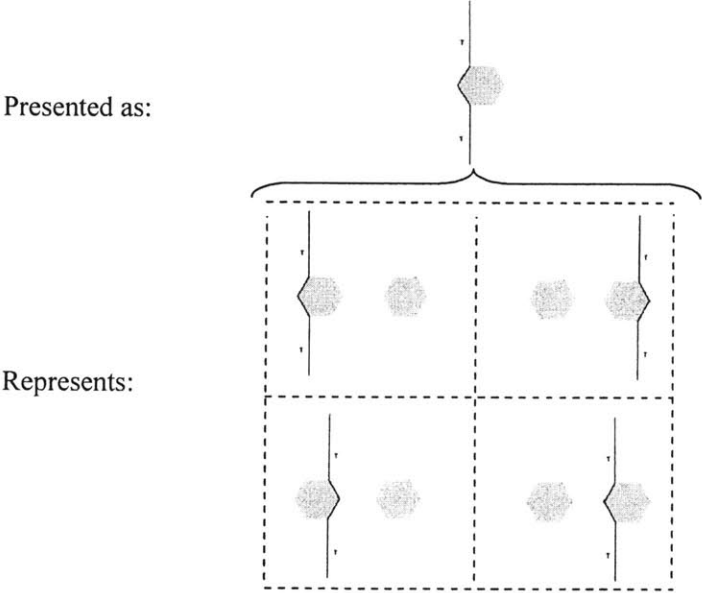


Figure 5.3 – A visual representation of the symmetric convention used in this study for debonding and cracking observed in the inclusion pairs. Although this is presented for an example crack in a hexagon inclusion, the convention applies for all cracking and debonding types in all inclusion shapes and materials.

5.2 Hexagon Inclusion Pairs

5.2.1 Debonding

Similar debonding behavior was observed for both Ultracal and plaster hexagon inclusions (location and shape). Debonding in hexagon inclusion pairs occurred either simultaneously with tensile cracking initiation or after tensile crack initiation had occurred. The debonding generally occurred on the sides of the hexagon inclusions (Figure 5.4) and complete inclusion debonding rarely occurred. On rare occasions shear debonding occurred when secondary shear cracks formed (Refer to Figure 5.4).

The amount of interface debonding was estimated for each test and the average values are presented in Table 5.2. It should be noted that because the hexagon pairs were analyzed before diamond- and ellipse pairs the debonding amount and mode (shearing or tensile) was more carefully studied in the analysis of diamond and ellipse pairs. Therefore, the amount of debonding (especially shear debonding) observed in the analysis of hexagon inclusion pairs may have been slightly under-estimated.

The amount of debonding in hexagon pairs appeared to be similar between all bridging angles and between both materials (Refer to Table 5.2). However, slightly more post-failure debonding appeared to occur at lower bridging angles.

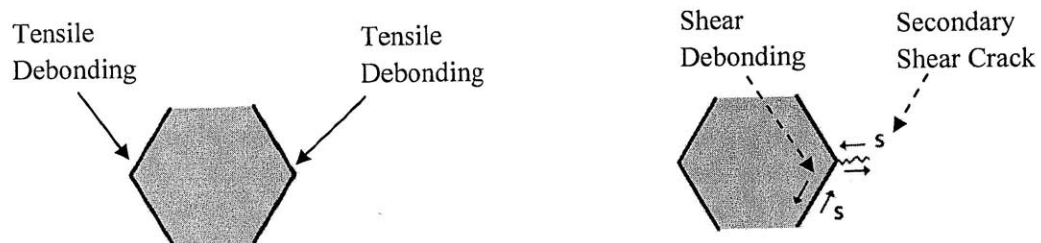


Figure 5.4 – Characteristic debonding occurring in specimens containing hexagon pairs (same for Ultracal and Plaster). Occurred typically as tensile cracks (left) but also occurred as shear cracks (right).

Material	Bridging Angle, β	Hexagon Debonding					
		Primary Tensile Crack			At Failure		
		Tensile	Shear	Total	Tensile	Shear	Total
Plaster	0	10%	0%	10%	55%	0%	55%
	30	35%	0%	35%	45%	5%	50%
	60	20%	0%	20%	45%	0%	45%
Ultracal	0	30%	0%	30%	55%	0%	55%
	30	20%	0%	20%	40%	0%	40%
	60	25%	0%	25%	40%	0%	40%

Table 5.2 – Estimated average debonding of hexagon interfaces due to primary tensile cracking occurring at each inclusion and when failure had occurred. The debonding percentage was estimated based on the total interface length for each inclusion shape and rounded to the nearest 5%.

5.2.2 Cracking

Two distinct types of primary tensile cracking were observed in the specimens with hexagon inclusion pairs (Figure 5.5). There were both primary tensile cracks initiating at the interface and propagating straight (Figure 5.5a) and primary tensile cracks initiating at the interface and propagating with curvature (Figure 5.5 b & c). The primary tensile cracks which propagated with curvature could be divided into those which curved along the direction of the inclusion interface (Figure 5.5b) and those which curved opposite the inclusion interface (Figure 5.5c).

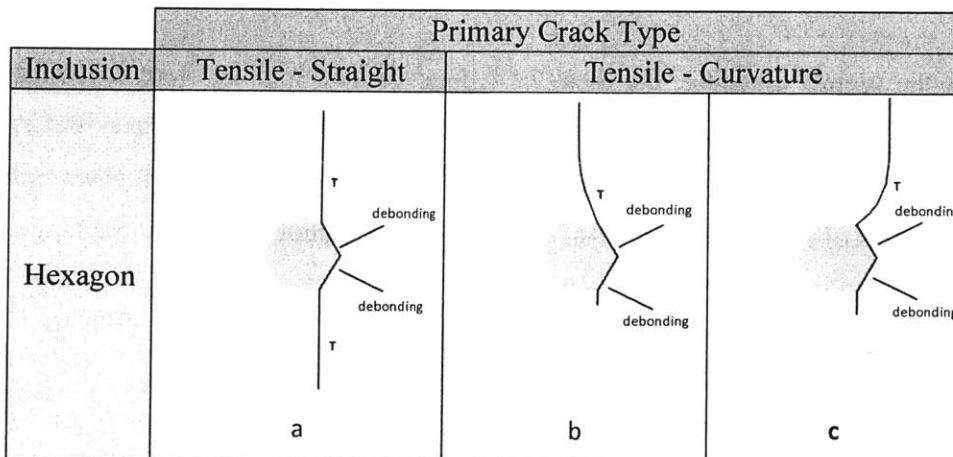


Figure 5.5 - Primary cracking types observed in hexagon pair specimens. T = tensile crack. Tensile crack initiating at the interface and propagating a) straight b) curvature along interface direction c) curvature opposite interface direction). Cracking shown on single inclusions was symmetric and not affected by the location of the other inclusion (left or right side).

Primary tensile cracking in the hexagon inclusion pairs was followed by secondary shear cracking at the exterior (left or right) edges of the inclusion (Figure 5.6). A tensile crack typically initiated at the end of the secondary shear cracks and propagated toward the direction of loading.

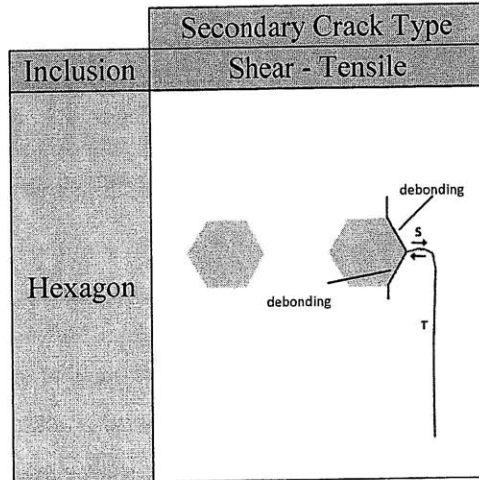


Figure 5.6 - Secondary cracking types observed in hexagon pair specimens. T = tensile crack, S = shear crack. There was no effect of bridging angle.

5.2.3 Surface Spalling

Along with the typical cracking, the areas of typical surface spalling were determined for specimens with hexagon pairs (Figure 5.7). Spalling generally occurred near the exterior edges of the hexagon inclusion. This spalling was generally associated with shear cracking. The shape and size of the spalling area was dependent on the amount of shear cracking.

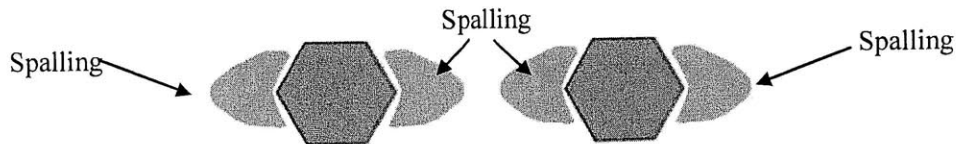


Figure 5.7 – Locations of typical spalling occurring in specimens with hexagon inclusion pairs. Spalling at the interior tips of an inclusion pair followed the direction of shear cracking (coalescence).

5.2.4 Coalescence

For this current study coalescence was divided into two categories. Indirect coalescence was defined as coalescence, which occurred from multiple cracks. Direct coalescence was defined as coalescence which had only one crack connecting between the inclusions (See Figure 5.8).

The coalescence behavior of the tested hexagon inclusion pairs was visually analyzed and the results were organized by inclusion material and bridging angle in Figure 5.8. The effect of primary tensile cracking on the coalescence of hexagon inclusion pairs is presented in Table 5.3 (See Figure 5.9 for a visual explanation of the classifications used to differentiate the primary tensile crack “effect” on coalescence). Debonding surfaces related to coalescence were shown as cracks and were labeled accordingly (Refer to Figure 5.8). At lower bridging angles (0° and 30°) either indirect or no coalescence was observed in both Ultracal and plaster inclusion pairs (Refer to Figure 5.8). At 30° bridging angles the indirect coalescence point occurred between the two inclusions. This resulted in one of the coalescence cracks propagating a longer distance from the furthest inclusion (The “left” inclusion coalescence crack at $\beta=30^\circ$ in Figure 5.8). At high bridging angles (60°) mixed (both shear and tensile) direct shear coalescence was observed. Shear cracks propagated from both of the inclusion interfaces in Ultracal hexagon specimens at 60° . This is in contrast to the plaster hexagon pairs at a 60° bridging angle which only had one shear crack propagating from one of the inclusion interfaces.

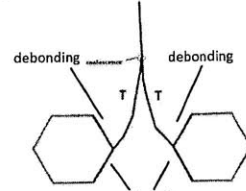
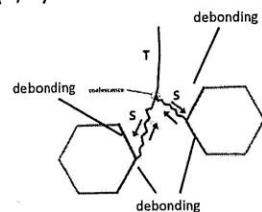
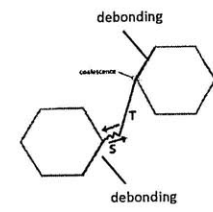
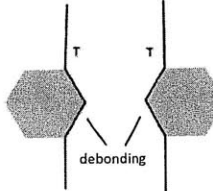
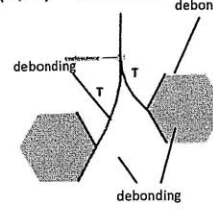
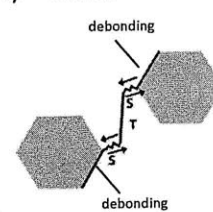
Hexagon Inclusion	Inclusion Angle (β)		
	$\beta = 0^\circ$	$\beta = 30^\circ$	$\beta = 60^\circ$
Plaster	(1/3) Indirect  [1/3 No Coal]	(2/3) Indirect  [1/3 No Coal]	(3/3) Direct  [1/3 No Coal]
Ultracal	(3/3) No Coalescence  [3/3 No Coal]	(1/3) Indirect  [1/3 No Coal]	(2/4) Direct  [1/3 No Coal]

Figure 5.8 – The coalescence patterns observed in hexagon inclusion pairs. The number in the top left is the amount of test repetitions showing this behavior. The number in the bottom left is the amount of test repetitions showing no coalescence. T = tensile crack, S = shear crack.

Classification of Primary Tensile Crack Effect on Coalescence

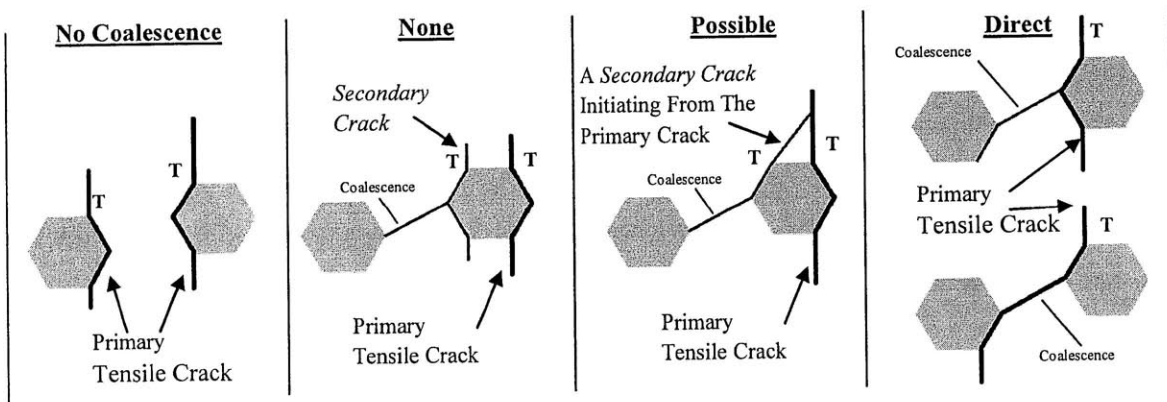


Figure 5.9 – The determination of primary tensile crack effect on coalescence patterns observed in hexagon inclusion pairs. This criterion was used to describe primary tensile cracking effect on coalescence for all inclusion shapes. Thick lines = primary tensile cracks, Thin Lines = secondary/coalescence cracks. “Possible” designates when coalescence occurred from a secondary crack initiating from a primary crack, or if the primary crack was unknown. “Direct” corresponds to any coalescence involving the primary tensile crack of each inclusion; this includes debonded interfaces created by primary tensile cracking.

Bridging Angle, β	Primary Tensile Crack Effect on Coalescence Hexagon Pairs	
	Material	
	Plaster	Ultracal
0	None (2/3) Possible (1/3)	No Coalescence (3/3)
30	None (1/3) Possible (1/3) No Coalescence (1/3)	None (1/3) Direct (1/3) No Coalescence (1/3)
60	Direct (3/3)	None (1/3) Possible (1/3) No Coalescence (1/3)

Table 5.3 – The effect of primary tensile cracking on hexagon coalescence. “Direct” corresponds to any coalescence involving the primary tensile crack of each inclusion, this included debonded interfaces created by primary tensile cracking. “Possible” designates when coalescence occurred from a secondary crack initiating from a primary crack, or if the primary crack was unknown. (Refer to Figure 5.9 for an illustration of the notation)

5.2.5 Stress Behavior

For each inclusion pair, the maximum stress was determined from the stress-strain data. In this study the maximum stress was defined as the peak failure stress. The maximum stress for the hexagon inclusion pairs is shown in Figure 5.10. Similar maximum stresses occurred in both Ultracal and plaster inclusions, with the exception of Ultracal hexagon pairs at 30° bridging angle, which experienced higher maximum stress compared to the corresponding plaster hexagon pair (Refer to Figure 5.10). With the exception of a higher maximum stress for the 30° Ultracal hexagon pairs, there was a general trend toward a lower maximum stress as the bridging angle was increased.

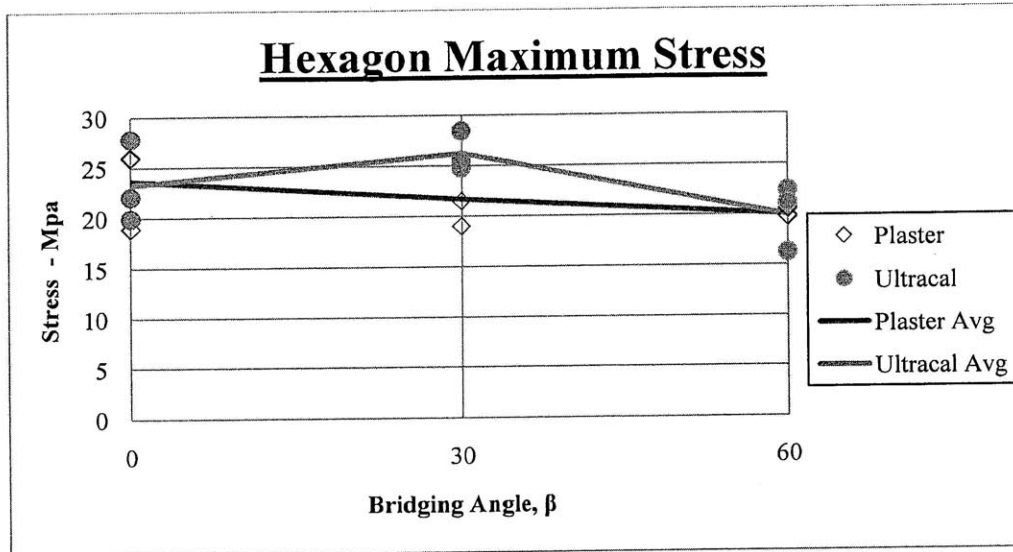


Figure 5.10 – **Maximum stress** of specimens with **hexagon** inclusion pairs. Blue = Ultracal (solid circles), Red = Plaster (hollow diamonds). Lines are the average values of the test repetitions.

Along with maximum stress, the stress when primary tensile cracks initiated was determined for each hexagon pair test. The corresponding tensile crack initiation stress of hexagon inclusions pairs can be seen in Figure 5.11. Similar to the maximum stresses there was a peak tensile crack stress in the 30° Ultracal pairs (Refer to Figure 5.11). Also with the exception of very low tensile crack initiation stresses for 0° Ultracal pairs, the tensile crack initiation stress trended downward as the bridging angle increased.

From the tensile crack initiation (TCI) stress the tensile crack initiation ratio (tensile crack initiation normalized by the maximum stress, See Equation 4.1) was determined for inclusion pair. For the hexagon pairs the average tensile crack initiation was approximately between 80% (0.80) to 95% (0.95) of the maximum stress (Figure 5.12). There was no clear trend in the TCI ratio for hexagon pairs of either inclusion material.

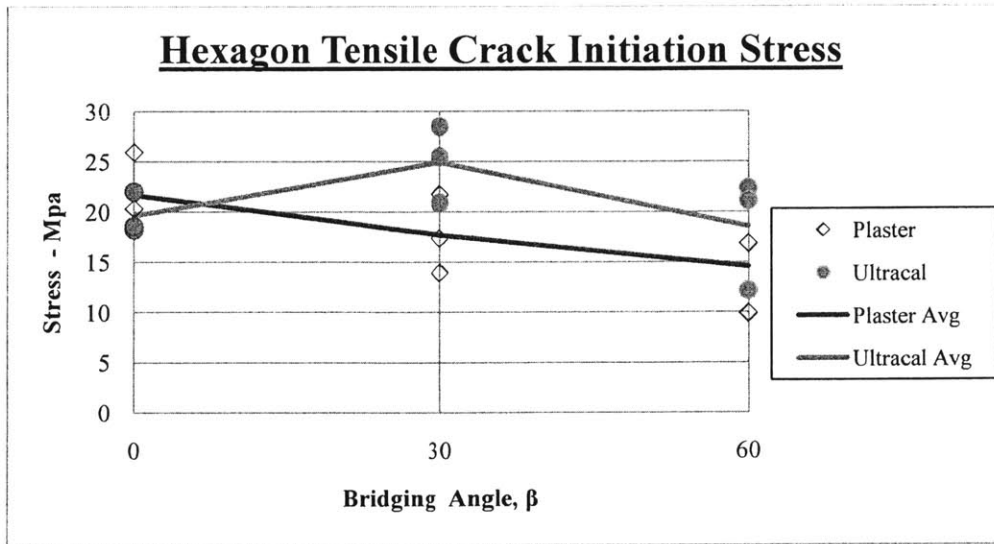


Figure 5.11 – **Tensile crack initiation stress** of specimens with **hexagon** inclusion pairs. Blue = Ultracal (solid circles), Red = Plaster (hollow diamonds). Lines are the average values of the test repetitions.

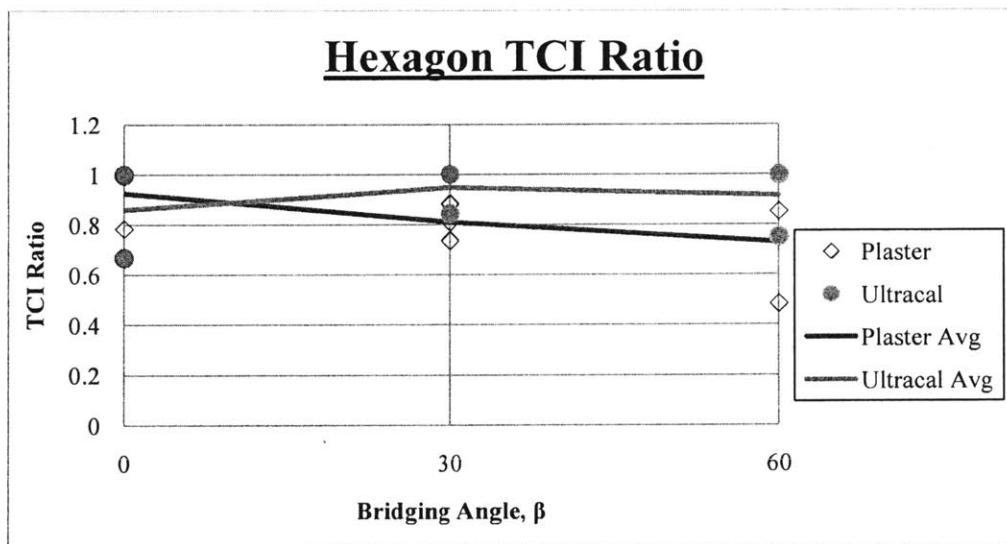


Figure 5.12 – **Tensile crack initiation ratio** of specimens with **hexagon** inclusion pairs. Blue = Ultracal (solid circles), Red = Plaster (hollow diamonds). Lines are the average values of the test repetitions.

From the point at which coalescence occurred the stress in the specimen could be determined for each test. The coalescence stresses for the hexagon inclusion pairs can be seen in Figure 5.13. Some tests did not show any coalescence, such as the 0° Ultracal hexagon pair, and no data points are shown on the plots (Refer to Figure 5.13). The coalescence stress of Ultracal

hexagon pairs appeared to be slightly higher than corresponding plaster pairs. There was no clear trend in coalescence stress with bridging angle.

The coalescence stress was also normalized by the maximum stress to determine the relative percentage of load when coalescence occurs (coalescence stress ratio)

$$\text{Coalescence Stress Ratio} = \frac{\text{Coalescence Stress}}{\text{Maximum Stress}} \quad (5.1)$$

The coalescence stress ratios for hexagon pairs are shown in Figure 5.14. The coalescence appeared to occur very close to failure in almost all of hexagon inclusion pair specimens (Refer to Figure 5.14).

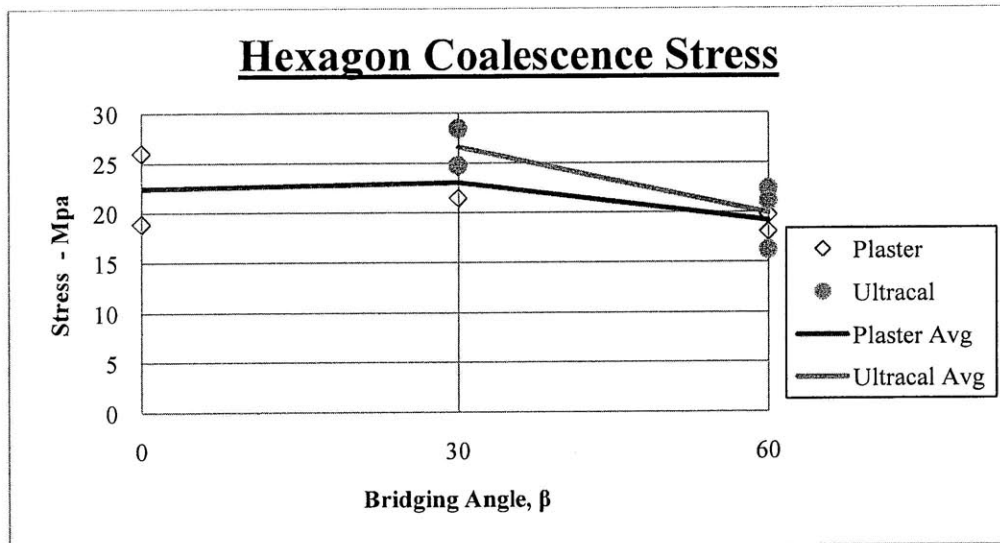


Figure 5.13 – Coalescence Stress of specimens with hexagon inclusion pairs. Blue = Ultracal (solid circles), Red = Plaster (hollow diamonds). Lines are the average values of the test repetitions.

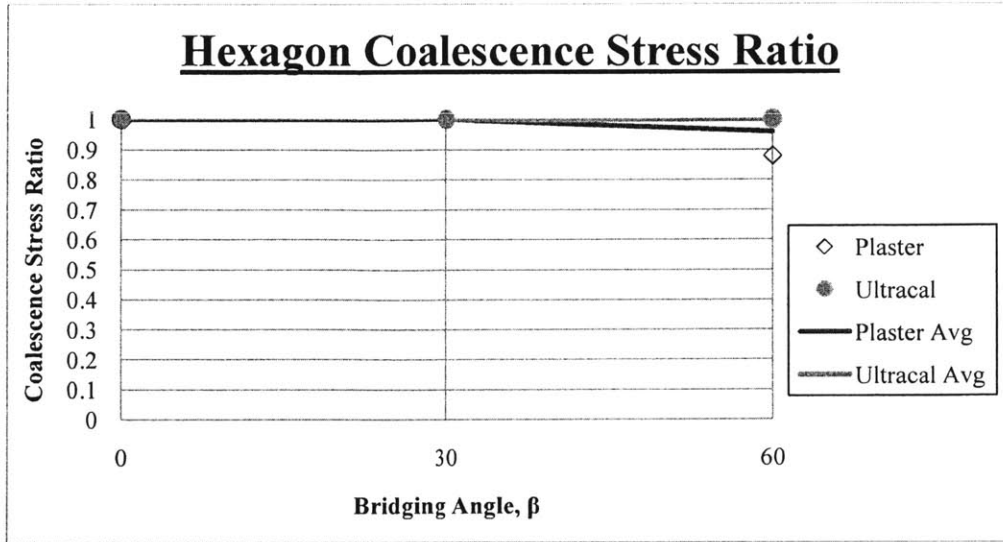


Figure 5.14 – Coalescence Stress Ratio of specimens with hexagon inclusion pairs. Blue = Ultracal (solid circles), Red = Plaster (hollow diamonds). Lines are the average values of the test repetitions.

5.3 Diamond Inclusion Pairs

5.3.1 Debonding

In contrast to the hexagon inclusions, diamond inclusions typically exhibited complete debonding (Figure 5.15). The debonding of the diamond inclusion interfaces occurred either as tensile cracks or shear cracks (Refer to Figure 5.15).

From the average amount of debonding in the diamond inclusion pairs (Table 5.4), there appeared to be slightly more primary tensile debonding which occurred at lower bridging angles for both materials. Also, there was a high amount of debonding at primary tensile cracking (almost 70% in some test series) as well as a large percentage of interface debonding at the occurrence of failure (over 70% in all tests) (Refer to Table 5.4). Typically more shear debonding occurred at higher bridging angles where direct coalescence between the inclusions resulted in debonding.

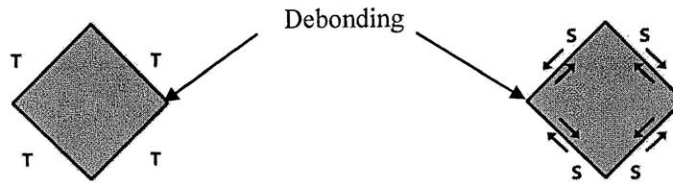


Figure 5.15 – Characteristic debonding occurring in specimens containing diamond pairs (same for Ultracal and Plaster). Debonding usually occurred as complete debonding by either tensile cracks (left) or shear cracks (right) regardless of bridging angle.

Material		Bridging Angle, β		Diamond Debonding					
				Primary Tensile Crack			At Failure		
				Tensile	Shear	Total	Tensile	Shear	Total
Plaster	0	40%	30%	70%	50%	40%	90%		
	30	45%	5%	50%	70%	5%	75%		
	60	40%	5%	45%	80%	15%	90%		
Ultracal	0	50%	0%	50%	85%	0%	85%		
	30	0%	25%	25%	10%	65%	70%		
	60	10%	35%	40%	15%	75%	90%		

Table 5.4 – Estimated average debonding of diamond interfaces due to primary tensile cracking occurring in each inclusion and when failure had occurred.

5.3.2 Cracking

Primary tensile cracking in diamond inclusions was sub-divided into straight cracks (Figure 5.16a) and cracks with curvature (Figure 5.16 b & c). Primary tensile cracks with curvature were observed to propagate either in the same direction as the inclusion interface (Figure 5.16b) or in the opposite direction of the interface (Figure 5.16c).

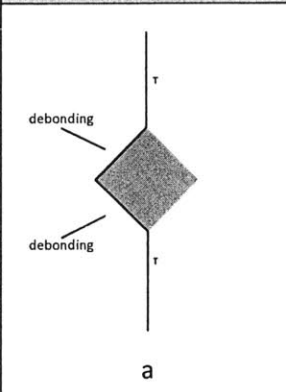
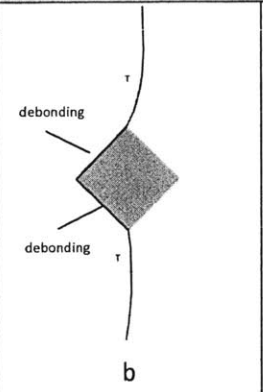
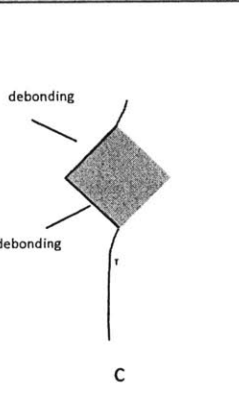
Inclusion	Primary Crack Type		
	Tensile - Straight	Tensile - Curvature	
Diamond	 <p>a</p>	 <p>b</p>	 <p>c</p>

Figure 5.16 - Primary cracking types observed in diamond pair specimens. T = tensile crack. Primary tensile crack propagating in the direction of loading either a) straight, b) with curvature in the direction of the inclusion interface, or c) with curvature opposite the direction of the inclusion interface.

Similar to hexagon pairs secondary shear cracks were observed at the exterior edges (left or right) of the diamond inclusion (See Figure 5.17a). At the end of the secondary shear crack a tensile crack propagated toward the direction of loading (either up or down). Also, secondary tensile cracks were observed in diamonds initiating near the exterior edge of the inclusion and propagating up (or down) to connect with the primary tensile crack in the matrix (Figure 5.17b).

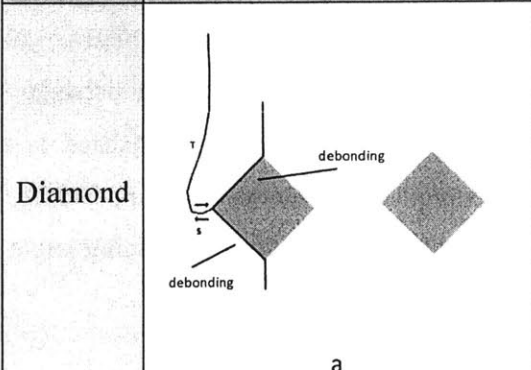
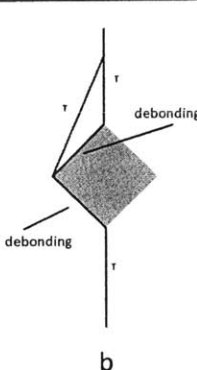
Inclusion	Secondary Crack Type	
	Shear - Tensile	Tensile
Diamond	 <p>a</p>	 <p>b</p>

Figure 5.17 - Secondary cracking types observed in diamond pair specimens. T = tensile crack, S = shear crack. a) Secondary shear crack propagating out from the exterior edge of the inclusion b) Secondary tensile crack propagating from the edge of the inclusion and connecting with the primary tensile crack. Bridging angle had no effect. Cracking shown on single inclusions was symmetric and not affected by the location of the other inclusion (left or right side).

5.3.3 Spalling

Surface spalling was observed near the edges of the diamond inclusions, typically where ever secondary shear cracks formed (Figure 5.18). Spalling between diamond inclusions was usually based on the amount of shear coalescence cracking.

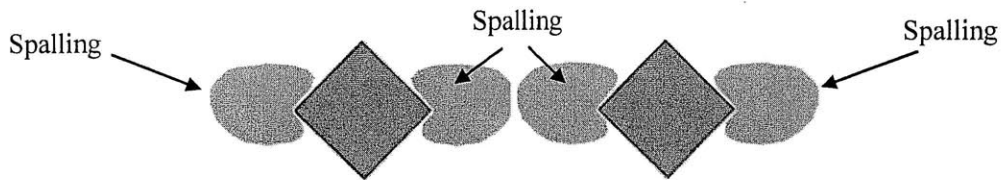


Figure 5.18 – Locations of typical surface spalling occurring in specimen with diamond inclusion pairs.

5.3.4 Coalescence

The coalescence behavior of the diamond inclusion pairs was organized by inclusion material and bridging angle in Figure 5.19. The effect of primary tensile cracking occurring in each diamond inclusion on the coalescence is presented in Table 5.5. At very low bridging angles (0°) indirect coalescence occurred in both inclusion materials (Refer to Figure 5.19). At moderate bridging angles (30°) a single direct shear crack occurred between plaster diamond inclusions and a direct mixed (shear and tensile) crack occurred between corresponding Ultracal inclusions. Coalescence at high bridging angles (60°) consisted of a direct mixed tensile-shear crack in both inclusions materials. In general, there appeared to be a trending from indirect, to direct shear, to direct mixed coalescence as the bridging angle was increased in the diamond inclusion pairs tested.

Diamond Inclusion	Inclusion Angle (β)		
	$\beta = 0^\circ$	$\beta = 30^\circ$	$\beta = 60^\circ$
Plaster	(3/3) Indirect [2] 	(2/3) Direct [3] 	(2/3) Direct [5]
Ultracal	(2/3) Indirect [2] [1/3 No Coal]	(2/3) Direct [5] 	(3/3) Direct [5]

Figure 5.19 – The coalescence patterns observed in diamond inclusion pairs. The number in the top left is the amount of test repetitions showing this behavior. The number in the bottom left is the amount of test repetitions showing no coalescence. T = tensile crack, S = shear crack.

Bridging Angle, β	<u>Primary Tensile Crack Effect on Coalescence</u>	
	Diamond Pairs	
	Material	
	Plaster	Ultracal
0	Direct (3/3)	None (1/3) Possible (1/3) Direct (1/3)
30	Direct (3/3)	None (1/3) Direct (2/3)
60	Direct (3/3)	None (1/3) Direct (2/3)

Table 5.5 – The effect of primary tensile cracking on diamond coalescence. “Direct” corresponds to any coalescence involving the primary tensile crack of each inclusion; this included debonded interfaces created by primary tensile cracking. “Possible” designates when coalescence occurred from a secondary crack initiating from a primary crack, or if the primary crack was unknown. (Refer to Figure 5.9 for an illustration of the notation)

5.3.5 Stress Behavior

For all bridging angles, the Ultracal specimens showed higher maximum stresses compared to corresponding plaster diamond inclusions (Figure 5.20). With the exception of a slightly lower maximum stress of Ultracal diamond pairs at 0° bridging angles, there was a general trending from higher to lower maximum stress as bridging angle increased (Refer to Figure 5.20).

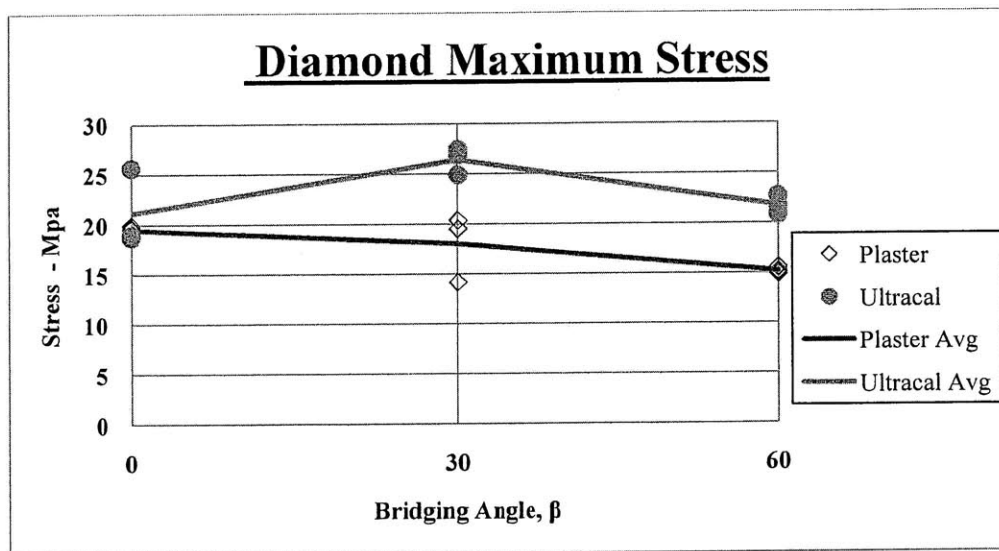


Figure 5.20 – **Maximum stress** of specimens with **diamond** inclusion pairs. Blue = Ultracal (solid circles), Red = Plaster (hollow diamonds). Lines are the average values of the test repetitions.

The stress initiating tensile cracking for specimens with diamond inclusions pairs is presented in Figure 5.21. Similar to the maximum stresses, tensile crack initiation occurred at higher stresses in Ultracal specimens and there was a general trend toward decreasing tensile crack initiation stress as bridging angle increased (Refer to Figure 5.21).

The tensile crack initiation (TCI) ratio for the diamond inclusion pair specimens is shown in Figure 5.22. Specimens with Ultracal diamond inclusions appeared to have slightly higher tensile crack initiation ratio than corresponding tests with plaster inclusions (Refer to Figure

5.22). There was no clear trend in the normalized tensile crack initiation observed, which typically ranged between 80% (0.80) to 100% (1.0) of the maximum stress.

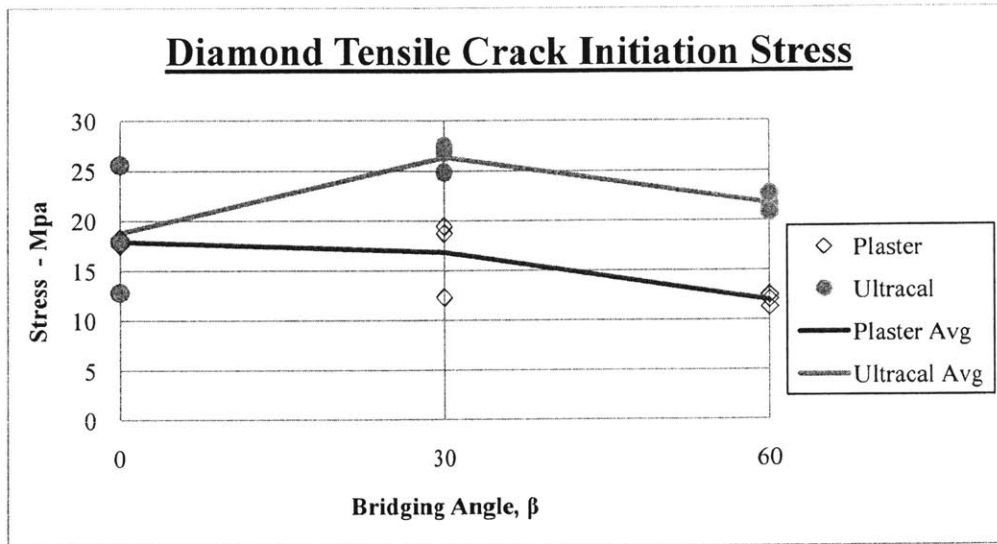


Figure 5.21 – Tensile crack initiation stress of specimens with **diamond** inclusion pairs. Blue = Ultracal (solid circles), Red = Plaster (hollow diamonds). Lines are the average values of the test repetitions.

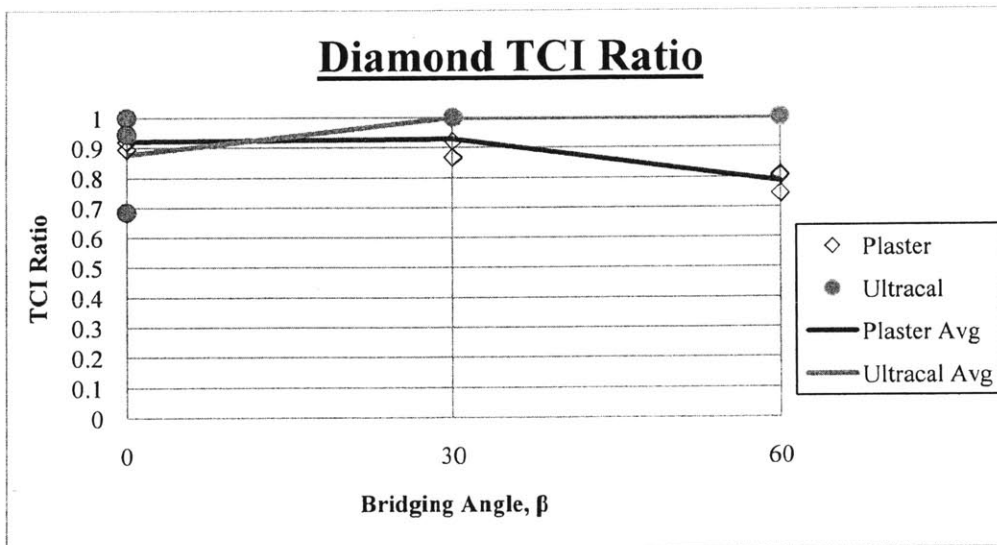


Figure 5.22 – Tensile crack initiation ratio of specimens with **diamond** inclusion pairs. Blue = Ultracal (solid circles), Red = Plaster (hollow diamonds). Lines are the average values of the test repetitions.

The coalescence stress of the diamond geometries was also determined (Figure 5.23). The trends in coalescence stresses of diamonds were similar to maximum and tensile initiation stresses. Coalescence occurred at higher stresses in specimens with Ultracal inclusions and there was a general trend in lower coalescence stresses at higher bridging angles (Refer to Figure 5.23).

The coalescence stresses were normalized for the tests performed on diamond inclusion pairs (Figure 5.24). Coalescence occurred approximately near the failure stress for all diamond specimens, except for plaster diamond inclusions with a 60° in which coalescence typically occurred at 80% (0.80) of the maximum stress (Refer to Figure 5.24).

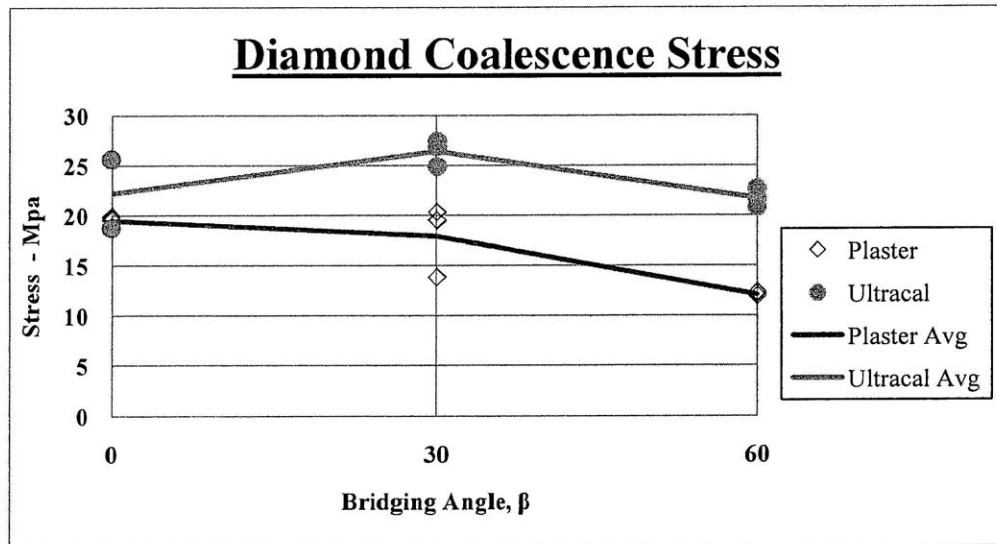


Figure 5.23 – **Diamond coalescence stress** of specimens with **diamond** inclusion pairs. Blue = Ultracal (solid circles), Red = Plaster (hollow diamonds). Lines are the average values of the test repetitions.

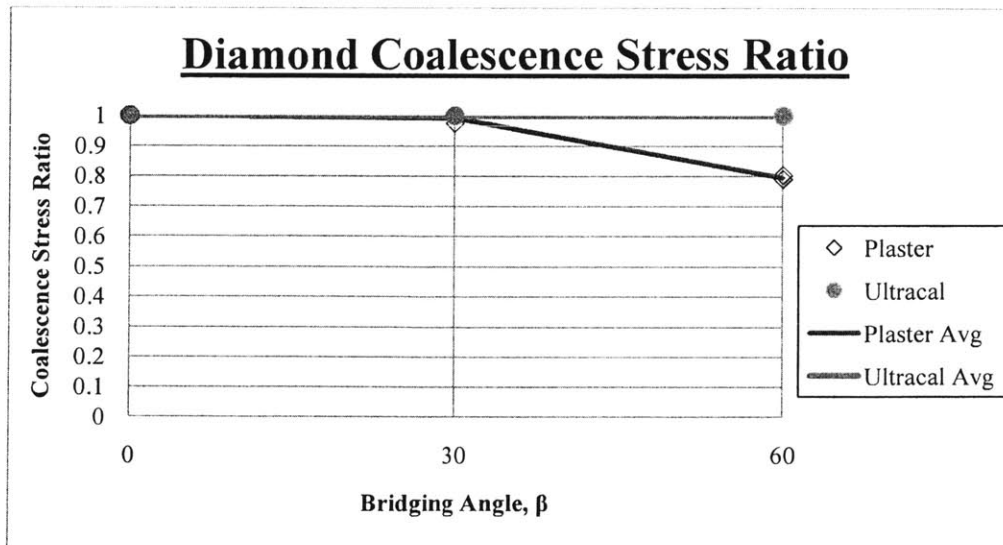


Figure 5.24 – **Diamond coalescence stress ratio** of specimens with **diamond** inclusion pairs. Blue = Ultracal (solid circles), Red = Plaster (hollow diamonds). Lines are the average values of the test repetitions.

5.4 Ellipse Inclusion Pairs

5.4.1 Debonding

Debonding in elliptical pairs occurred as either tensile or shear debonding (Figure 5.25). Ellipse inclusions experienced a significant amount of debonding at primary tensile crack initiation as well as at the occurrence of failure (Table 5.6). In contrast to single ellipse inclusions, the inclusion pairs typically showed only partial debonding during primary tensile cracking (Refer to Table 5.6). However, some ellipse inclusion pairs exhibited complete debonding at the occurrence of coalescence and failure.

At higher bridging angles, where direct coalescence occurred, shear debonding typically occurred (Refer to Table 5.6). One significant difference between the interface debonding in the ellipse pairs and the debonding in the other inclusions is the difference in debonding between inclusion materials. Specifically, there appeared to be slightly more total debonding in plaster pairs compared to corresponding Ultracal pairs (Refer to Table 5.6). There was also a significantly higher percentage of shear debonding in plaster pairs compared to Ultracal

pairs. This difference was typically due to the fact that at higher bridging angles, where shear debonding occurred due to shear coalescence cracks, tensile debonding occurred before direct shear coalescence in the Ultracal inclusions. This tensile debonding behavior is similar to the secondary tensile cracks forming at the exterior tips of a single Ultracal ellipse inclusion, as discussed in Chapter 4.

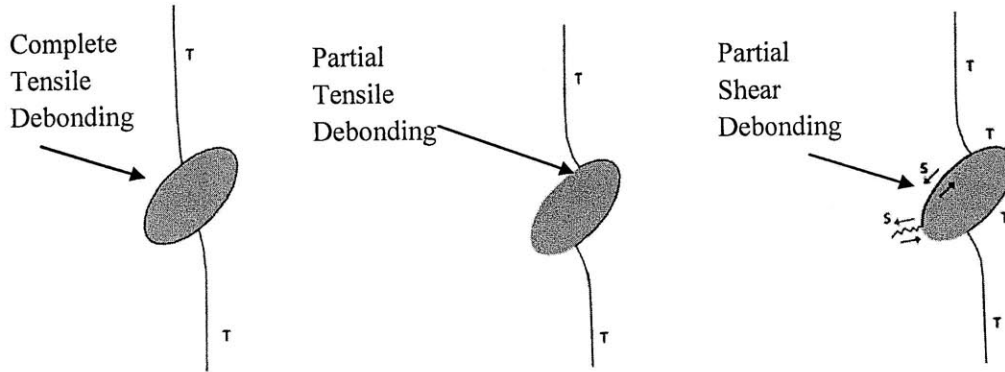


Figure 5.25 – Characteristic debonding occurring in specimens containing ellipse pairs (same for Ultracal and Plaster). In most cases debonding occurred as complete tensile debonding (left) or partial tensile debonding (middle). In some cases when complete tensile debonding did not occur, shear debonding occurred as shear cracks developed between inclusions (right). Debonding shown on single inclusions was symmetric and not affected by the location of the other inclusion.

Material	Bridging Angle, β	Ellipse Debonding					
		Primary Tensile Crack			Failure		
		Tensile	Shear	Total	Tensile	Shear	Total
Plaster	0	50%	0%	50%	70%	0%	70%
	30	15%	35%	45%	40%	40%	75%
	60	0%	40%	40%	50%	40%	90%
Ultracal	0	25%	0%	25%	50%	0%	50%
	30	25%	5%	30%	65%	5%	70%
	60	35%	0%	35%	55%	0%	55%

Table 5.6 – Estimated average debonding of ellipse interfaces due to primary tensile cracking occurring in each inclusion and when failure had occurred. The debonding percentage was estimated based on the total interface length for each inclusion shape and rounded to the nearest 5%.

5.4.2 Cracking

Similar to hexagon and diamond inclusion pairs, primary tensile cracks occurring in ellipse pairs were divided into primary tensile cracks with or without curvature (Figure 5.26). Primary tensile cracks curving along the inclusion interface and opposite the inclusion interface were also seen in ellipse pairs (Figure 5.26 b & c, respectively). There was also a unique primary tensile crack occurring in ellipse pairs which had a distinct “bend” (Figure 5.26 d)

Secondary shear cracks also occurred in ellipse pairs (Figure 5.27a). In contrast to the other inclusion pairs tested the secondary cracks did not occur at the mid-height edges of the inclusion. Secondary shear cracks typically occurred at the most exterior edges (left and right) of the inclined ellipse inclusions (Refer to Figure 5.27a). Also, secondary tensile cracks were observed in ellipse pairs initiating at the inclusion interface and terminating in the matrix (Figure 5.27b).

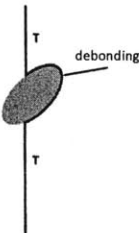
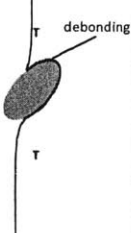
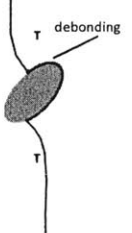
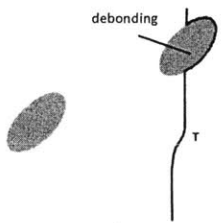
Inclusion	Primary Crack Type			
	Tensile - Straight	Tensile - Curvature		
Ellipse	 <p>a</p>	 <p>b</p>	 <p>c</p>	 <p>d</p>

Figure 5.26 - Primary cracking types observed in ellipse pair specimens. T = tensile crack. Primary tensile crack: a) straight b) curvature along inclusion interface c) curvature opposite inclusion interface d) bent curvature. Cracking shown on single inclusions was symmetric and not affected by the location of the other inclusion.

Inclusion	Secondary Crack Type	
	Shear - Tensile	Tensile
Ellipse		

Figure 5.27 - Secondary cracking types observed in ellipse pair specimens. T = tensile crack, S = shear crack. No effect of bridging angle. Cracking shown on single inclusions was symmetric and not affected by the location of the other inclusion.

5.4.3 Spalling

Surface spalling also occurred at the inclusion tips in specimens with ellipse pairs (Figure 5.28). Similar to previously discussed inclusion spalling, this spalling typically occurred near shear cracking and the amount of spalling between inclusions was dependent on the amount of shear coalescence cracking.

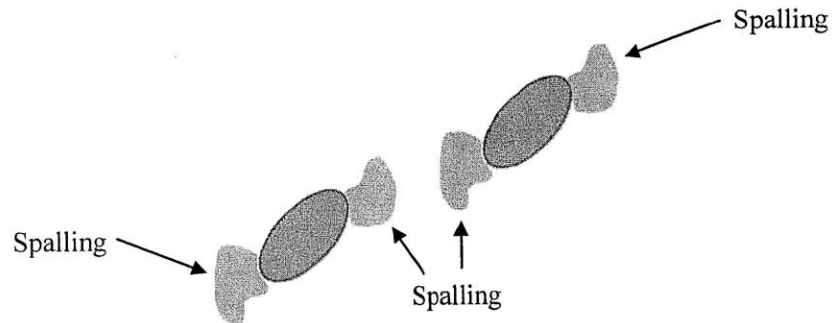


Figure 5.28 – Locations of typical spalling occurring in specimen with ellipse inclusion pairs.

5.4.4 Coalescence

From the tests conducted on the inclined ellipse inclusions, the resulting coalescence behavior was organized by material type and bridging angle (Figure 5.29). The effect of primary tensile cracking occurring in each ellipse inclusion on the coalescence is presented in Table 5.7. At a low bridging angle (0°) plaster ellipse inclusion pairs showed indirect coalescence and corresponding Ultracal inclusions showed no coalescence (Refer to Figure 5.29). For both inclusion materials, direct single shear crack coalescence occurred at moderate bridging angles (30°) and direct mixed mode (tensile and shear) coalescence occurred at a high bridging angles (60°).

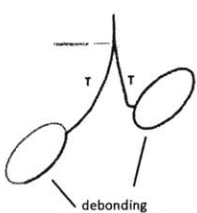
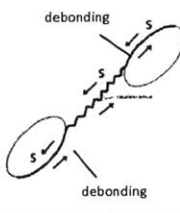
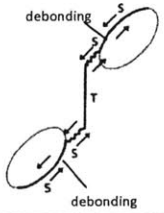
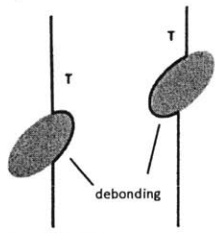
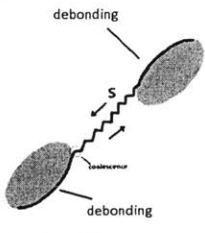
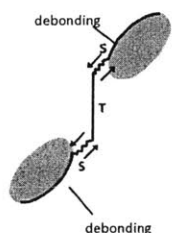
Ellipse ($\alpha = 45^\circ$) Inclusion	Inclusion Angle (β)		
	$\beta = 0^\circ$	$\beta = 30^\circ$	$\beta = 60^\circ$
Plaster	(2/3) Indirect [2] 	(3/3) Direct [3] 	(3/3) Direct [5] 
Ultracal	(2/3) No Coal [1]  [2/3 No Coal]	(1/3) Direct [3]  [1/3 No Coal]	(3/3) Direct [5] 

Figure 5.29 – The coalescence patterns observed in ellipse inclusion pairs. The number in the top left is the amount of test repetitions showing this behavior. The number in the bottom left is the amount of test repetitions showing no coalescence. T = tensile crack, S = shear crack.

Primary Tensile Crack Effect on Coalescence		
Ellipse Pairs		
Material		
Bridging Angle, β	Plaster	Ultracal
0	Possible (1/3) Direct (2/3)	No Coalescence (2/3) Direct (1/3)
30	Direct (3/3)	No Coalescence (1/3) Direct (2/3)
60	Direct (3/3)	Direct (3/3)

Table 5.7 – The effect of primary tensile cracking on ellipse coalescence. “Direct” corresponds to any coalescence involving the primary tensile crack of each inclusion; this includes debonded interfaces created by primary tensile cracking. “Possible” designates when coalescence occurred from a secondary crack initiating from a primary crack, or if the primary crack was unknown. (Refer to Figure 5.9 for an illustration of the notation)

5.4.5 Stress Behavior

From the maximum stresses calculated for ellipse pairs (Figure 5.30), slightly higher maximum stresses were observed in Ultracal ellipse pairs compared to corresponding plaster inclusions. There was not a clear trend between maximum stresses and bridging angle in either Ultracal or plaster elliptical inclusion pairs (Refer to Figure 5.30).

The tensile crack initiation stresses were also higher in Ultracal ellipse inclusions compared to corresponding plaster inclusions (Figure 5.31). Although there was no clear trend in tensile crack initiation and bridging angle in Ultracal inclusions, there was a slight decrease in tensile crack initiation stress as bridging angle was increased with plaster inclusions (Refer to Figure 5.31).

The tensile crack initiation (TCI) ratios for ellipse pairs were typically above 80% (0.80) of the maximum load (Figure 5.32). There were slightly higher TCI ratios for Ultracal

inclusions compared to corresponding plaster inclusions (Refer to Figure 5.32). There was a slight decrease in TCI ratio for plaster inclusion as bridging angles were increased.

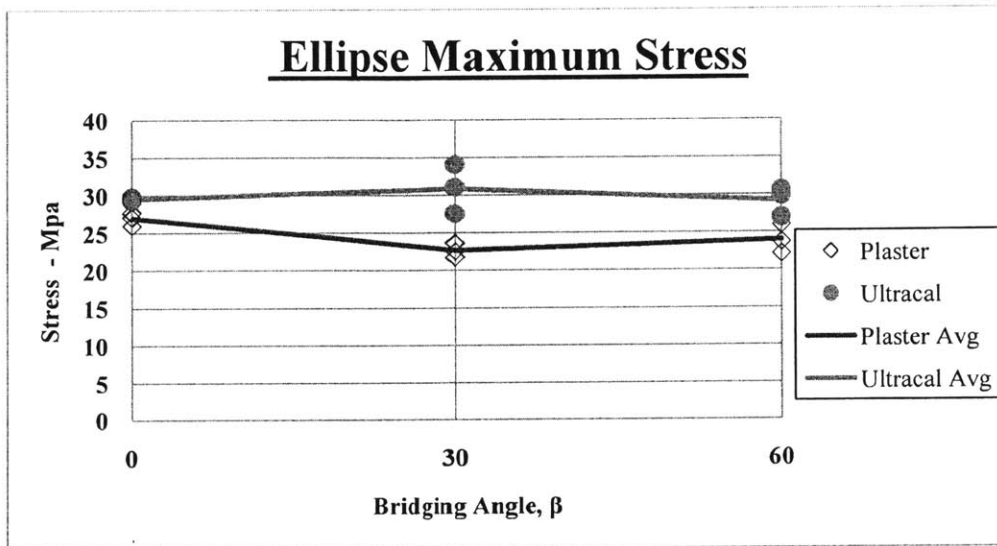


Figure 5.30 – **Maximum stress** of specimens with **ellipse** inclusion pairs. Blue = Ultracal (solid circles), Red = Plaster (hollow diamonds). Lines are the average values of the test repetitions.

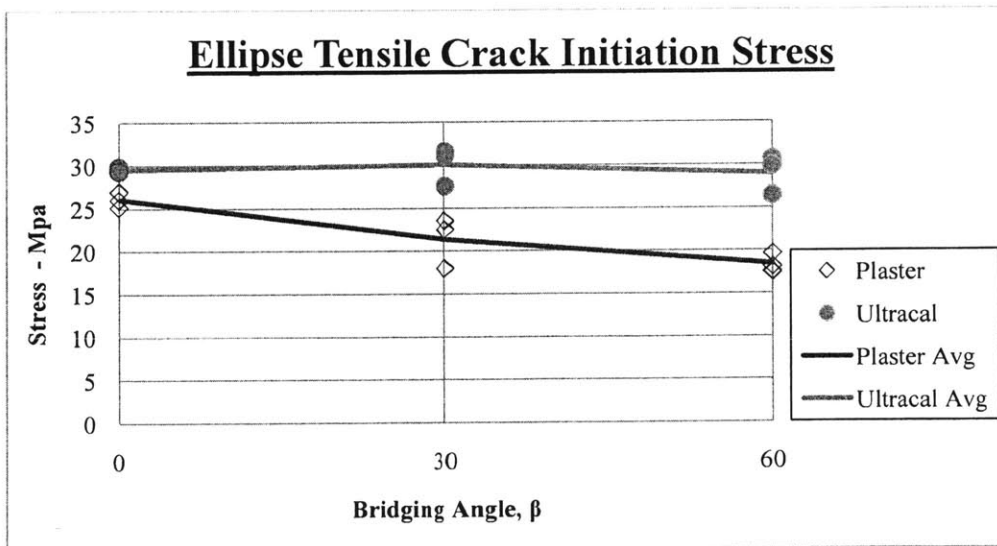


Figure 5.31 – **Tensile crack initiation stress** of specimens with **ellipse** inclusion pairs. Blue = Ultracal (solid circles), Red = Plaster (hollow diamonds). Lines are the average values of the test repetitions.

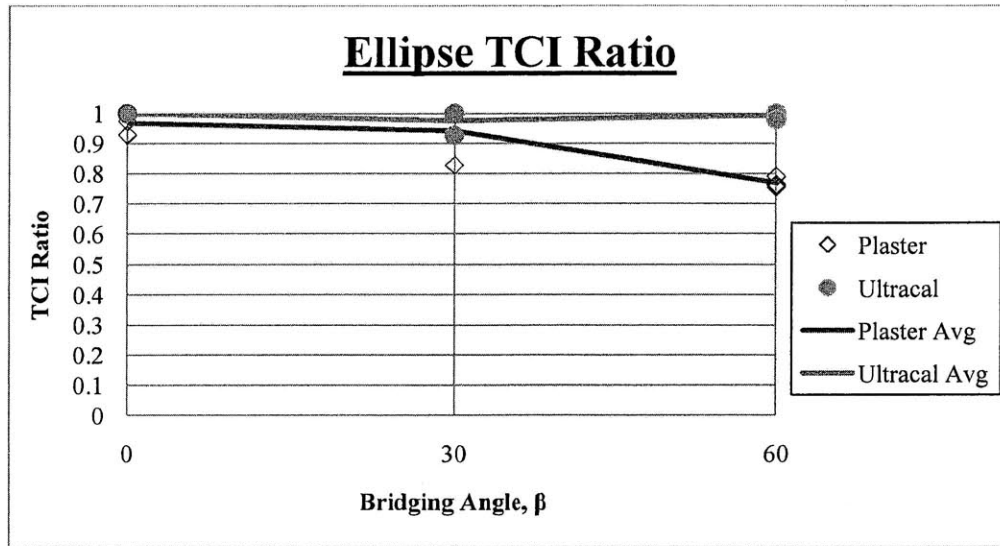


Figure 5.32 – Tensile crack initiation ratio of specimens with ellipse inclusion pairs. Blue = Ultracal (solid circles), Red = Plaster (hollow diamonds). Lines are the average values of the test repetitions.

Coalescence stress in ellipse inclusion pairs was typically higher for Ultracal inclusions compared to corresponding plaster inclusions (Figure 5.33). There was a decrease in coalescence stress of specimens with the plaster ellipse inclusions as bridging angle was increased (Refer to Figure 5.33).

Typically the ellipse pair specimens exhibited coalescence close to the maximum failure stress, with the exception of the plaster inclusion pairs at 60° bridging angles (Figure 5.34). This decrease in relative coalescence stress ratio was associated with a much lower coalescence stress for plaster ellipse inclusions at higher bridging angles (Refer to Figure 5.33).

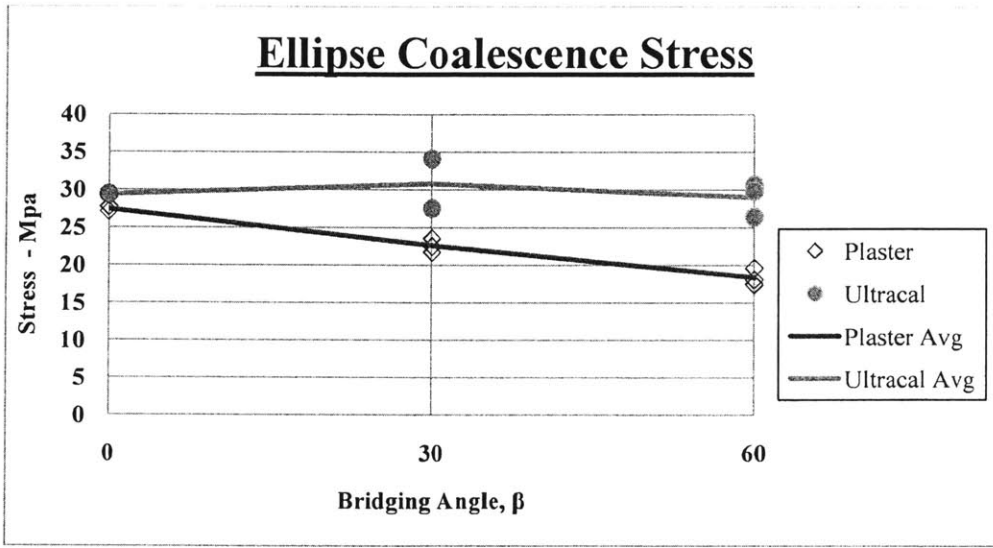


Figure 5.33 – Coalescence stress of specimens with ellipse inclusion pairs. Blue = Ultracal (solid circles), Red = Plaster (hollow diamonds). Lines are the average values of the test repetitions.

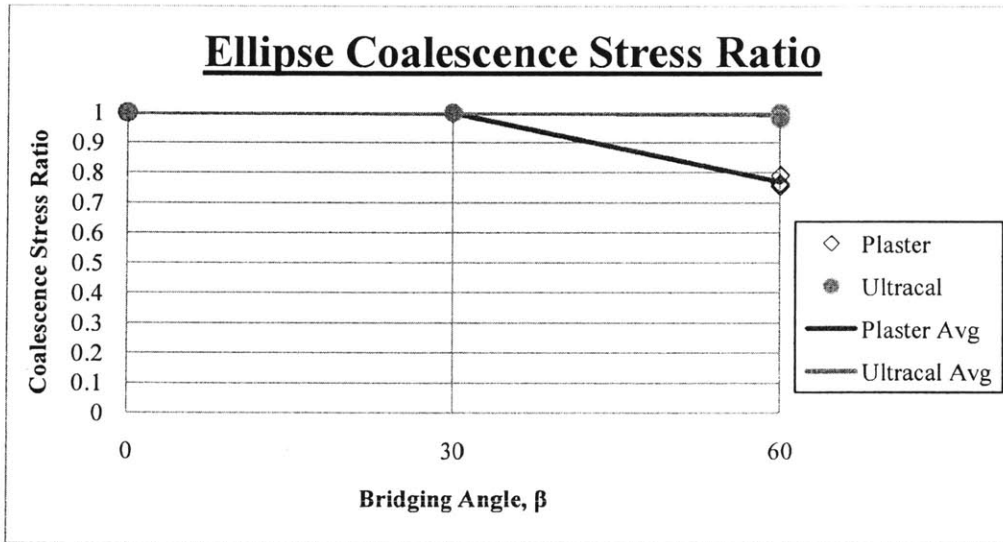


Figure 5.34 – Coalescence stress ratio of specimens with ellipse inclusion pairs. Blue = Ultracal (solid circles), Red = Plaster (hollow diamonds). Lines are the average values of the test repetitions.

5.5 Summary

5.5.1 Introduction

A better understanding can be gained by looking at the effect of inclusion shape on the cracking and coalescence patterns for the three differently shaped inclusion pairs (hexagon, diamond, and ellipse), with different inclusion materials (Ultracal and Plaster) and bridging angles (0° , 30° , and 60°).

5.5.2 Debonding

For all inclusion geometries, debonding was generally observed along the sides of the inclusions and occurred either after or simultaneously with primary tensile crack initiation. Debonding was never observed before primary tensile cracking initiation. Slightly more debonding was observed in diamond and ellipse inclusion shapes compared to hexagon inclusions (Table 5.8 and Table 5.9). This reduction in total interface debonding is likely due to the horizontally “flat” top and bottom sides of the hexagon which usually did not debond.

Slightly more debonding, both at primary tensile crack initiation and at failure, occurred in specimens with plaster inclusions compared to corresponding specimens with Ultracal inclusions (Refer to Tables 5.8 and 5.9). A considerably lower amount of shear debonding occurred in Ultracal ellipse inclusion pairs compared to the plaster inclusion pairs. This reduction in shear debonding shown in Ultracal ellipse inclusion pairs was likely due to the fact that most Ultracal inclusions exhibited tensile debonding before direct shear coalescence occurred, which typically caused shear debonding in corresponding plaster inclusions. This increase in shear debonding shown in plaster could also be due to higher amounts of debonding occurring for plaster inclusions during high speed imagery, where shear cracking can be determined much easier.

Average Primary Tensile Debonding						
<u>Shape</u>	Plaster			Ultracal		
	Tensile	Shear	Total	Tensile	Shear	Total
Hexagon	20%	0%	20%	25%	0%	25%
Diamond	40%	15%	55%	20%	20%	40%
Ellipse	20%	25%	45%	30%	0%	30%

Table 5.8 – Estimated average debonding of inclusion interfaces due to primary tensile cracking over all bridging angles.

Average Debonding at Failure						
<u>Shape</u>	Plaster			Ultracal		
	Tensile	Shear	Total	Tensile	Shear	Total
Hexagon	50%	0%	50%	45%	0%	45%
Diamond	65%	20%	85%	35%	45%	80%
Ellipse	55%	25%	80%	55%	0%	60%

Table 5.9 – Estimated average debonding of inclusion interfaces due to failure over all bridging angles.

5.5.3 Cracking

Initial (primary) cracking generally occurred as a tensile crack along the interface of the inclusion which resulted in a debonded interface. Primary tensile cracks were typically followed by secondary shear cracks which occurred at the exterior edges of the inclusion pairs. Secondary cracking (typically shear) also occurred at the interior edges of the inclusion sometimes resulting in coalescence. All inclusion shapes showed both straight and curved tensile cracking as well as secondary shear cracks at the edges of the inclusion (refer to Figures 5.5-5.6, 5.16-5.17, 5.26-5.27) . All inclusions also experience some tensile cracks which curved at the same inclination as the inclusion interface and some tensile which curved opposite to the inclination of the inclusion interface.

5.5.4 Spalling

For all inclusion shapes and materials, surface spalling usually occurred at the left and right edges, near areas of secondary shear cracking. Surface spalling occurred more frequently,

and in larger areas, in specimens with more shear cracking such as inclusion pairs with low or moderate bridging angles (Figure 5.35).

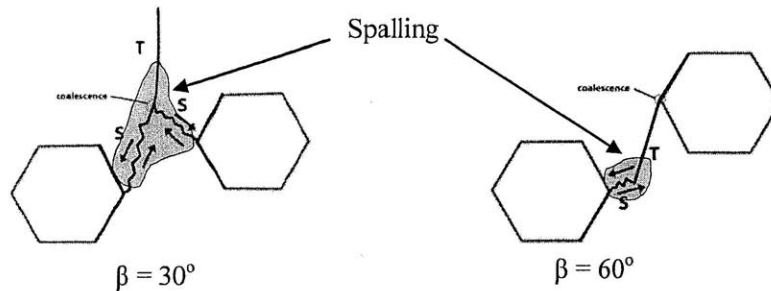


Figure 5.35 – The area of surface spalling observed due to the amount of shear cracking observed. This is shown for hexagon inclusion pairs of two different bridging angles, but this trend applied for all inclusion shapes and materials.

5.5.5 Coalescence

By combining the coalescence behaviors of all of the different geometric shapes and inclusion materials and organizing them in terms of bridging angle, a general trend can be observed (Figure 5.36). For all geometric shapes, either indirect or no coalescence was observed at 0° bridging angles (β) (refer to Figure 5.36). In many of the inclusion series with indirect coalescence, no coalescence was also observed in one of the other test repetitions. All of the shapes showed some interior shear crack at 30° and 60° bridging angles, and direct coalescence at a 60° bridging angle. A difference in the coalescence patterns was observed between the shapes in the 30° bridging angle. There appeared to be indirect coalescence in both of the 30° -hexagon specimens and direct coalescence in all of the 30° -diamond- and ellipse specimens. Therefore, regardless of the inclusion material or shape, as the bridging angle increased, there was a trend from indirect or no coalescence, to direct shear coalescence, to direct combined tensile-shear coalescence.

This general coalescence trend is visualized in Figure 5.37 for a pair of arbitrarily shaped inclusions. In all cases, the coalescence at a low bridging angle (horizontal) was either indirect or no coalescence. As the bridging angle increases, one of the crack's length (ω_1) decreases until the coalescence is characterized by a single direct shear crack. As the bridging

angle increases further this single shear crack splits into two separate shear cracks, extending from the interior edges of the inclusions, connected by a single tensile crack (crack length ω_2). As the bridging angle increases further the crack length (ω_2) increases, potentially extending to a single tensile crack between the two inclusions at very high angles.

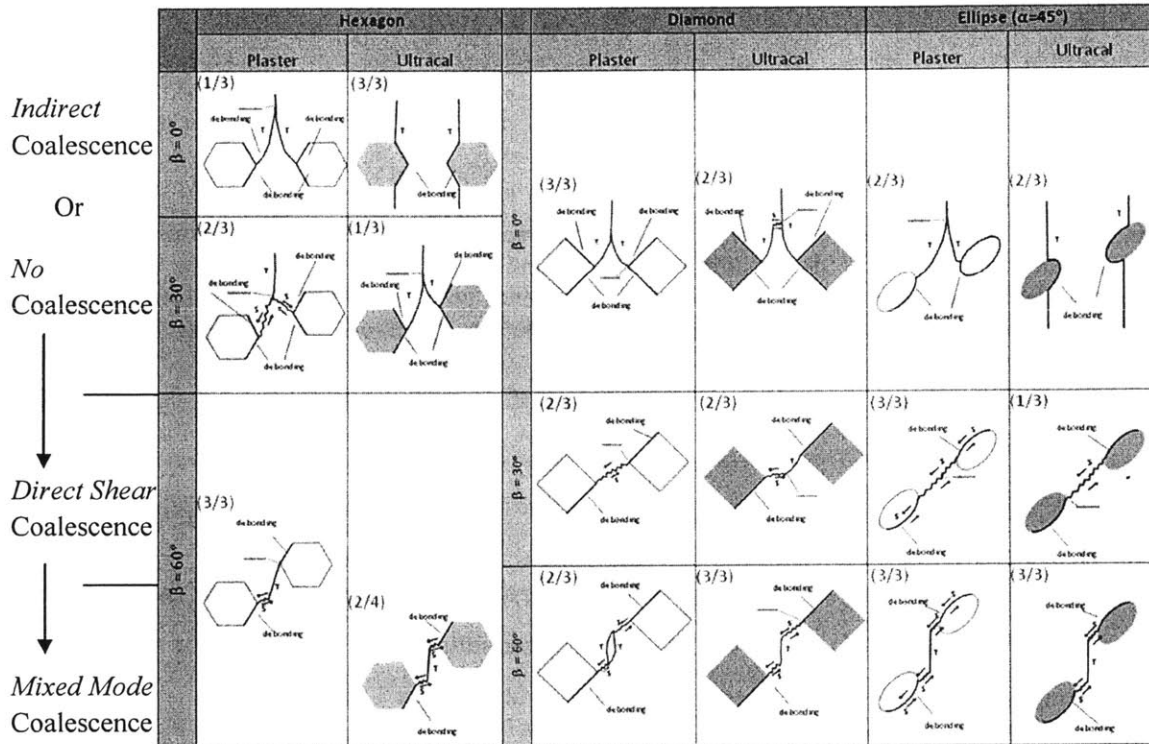


Figure 5.36 The double inclusion coalescence observed for all inclusion pairs tested in this study, organized by bridging angle and inclusion material. T = Tensile Cracking, S = Shear Cracking. The arrows near the shear cracks indicate the direction of shearing. The fraction in the top-left corner is the number of test repetitions with the shown behavior out of the number of specimens tested.

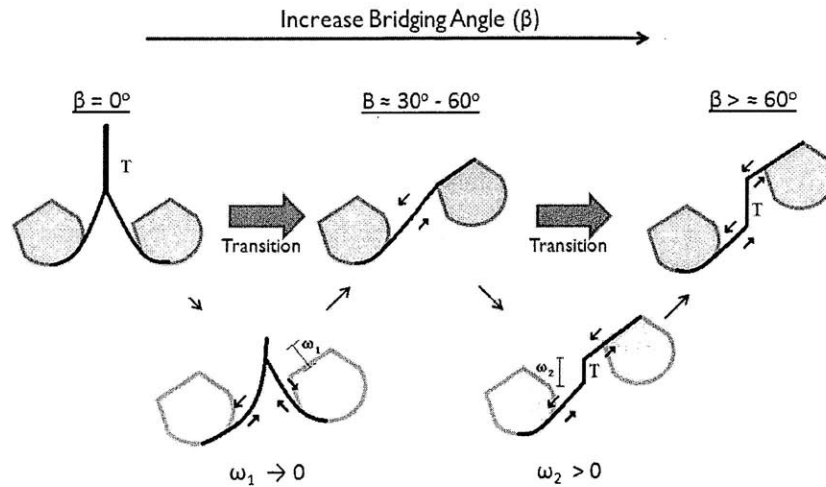


Figure 5.37 – Double inclusion coalescence observed between arbitrarily shaped inclusions with an increasing bridging angle (β). T denotes tensile cracking and arrows along a crack denote the shear direction. ω_1 denotes the crack length between the coalescence point and the inclusion interface. ω_2 denotes the crack length of the tensile crack between the two shear cracks extending from the inclusion interfaces.

5.5.6 Stress Behavior

From the compiled stress behavior of each geometric test series, average values of maximum stress, tensile crack initiation ratio, and coalescence stress ratio can be compared for different inclusion shapes and materials in regard to bridging angle (Figures 5.38-5.40).

On average the maximum stress of Ultracal inclusion pairs were higher than those of corresponding plaster inclusion material for all of the geometric shapes (Refer to Figure 5.38). Also, for all of the inclusion shapes consisting of plaster, there was a general decrease in maximum stress as the bridging angle increased. For all inclusion shapes consisting of Ultracal there were higher maximum stresses at 30° bridging angles and similar maximum stresses at 0° and 60°.

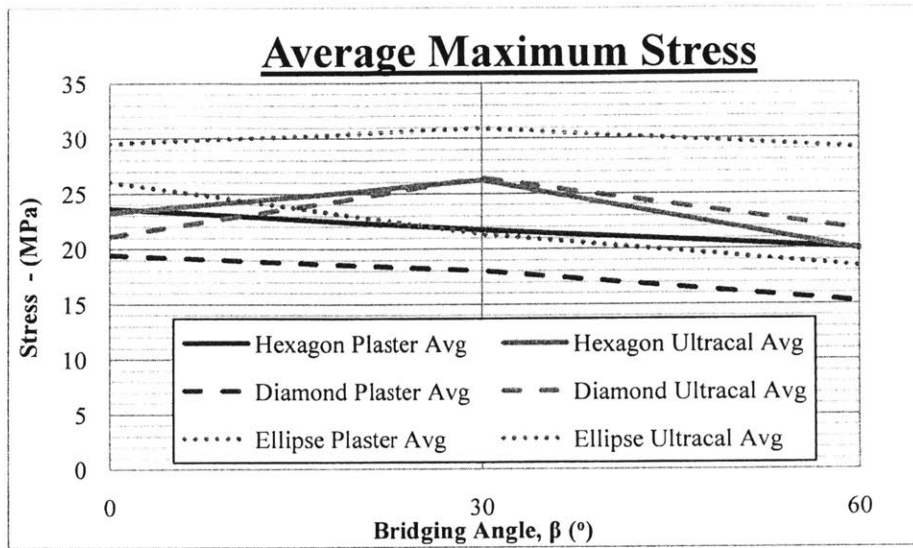


Figure 5.38 – The average **maximum stress** of all the inclusion pairs tested in regards to inclusion material and bridging angle. The lines are the average values of the test repetitions. Blue Lines = Ultracal, Red Lines = Plaster. Solid Lines = Hexagon Inclusions, Dashed Lines = Diamond Inclusions, Dotted Lines = Ellipse Inclusions.

Similar tensile crack initiation ratios were observed for all inclusion shapes and materials of corresponding bridging angle (Refer to Figure 5.39). However, both Ultracal and plaster ellipse pairs had slightly higher TCI ratios at a 0° bridging angle. There did not appear to be any general trend in TCI ratio at a 0° bridging angle. However, the inclusion material seemed to have an effect at moderate (30°) and high (60°) bridging angles because tensile crack initiation in Ultracal inclusions appeared to occur at higher relative stresses compared to corresponding plaster inclusions.

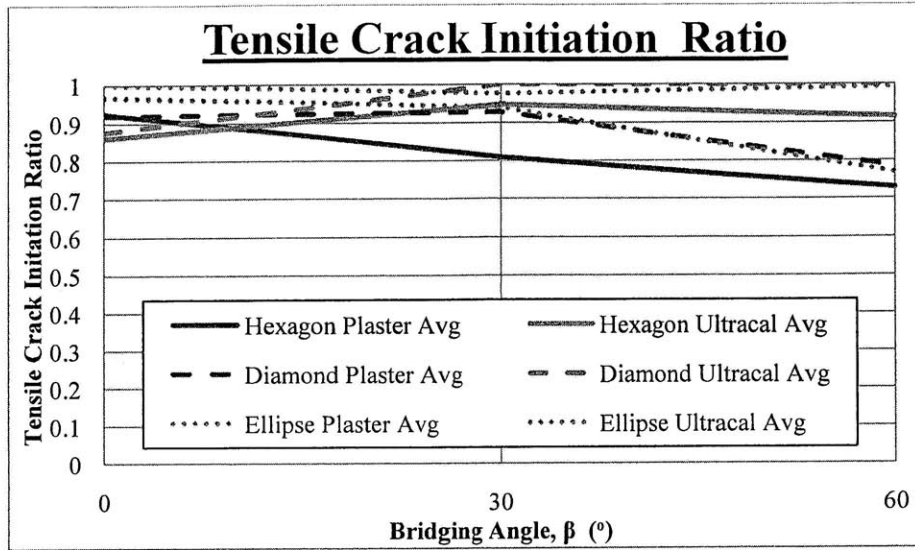


Figure 5.39 – The average **tensile crack initiation ratio** of all the inclusion pairs tested in regard to inclusion material and bridging angle. The lines are the average values of the test repetitions. Blue Lines = Ultracal, Red Lines = Plaster. Solid Lines = Hexagon Inclusions, Dashed Lines = Diamond Inclusions, Dotted Lines = Ellipse Inclusions.

Along with TCI ratio, the coalescence stress ratio also appeared to be similar for all inclusion shapes of similar inclusion material (Refer to Figure 5.40). However, there was a difference with regards to inclusion material. Almost all of the test specimens with Ultracal inclusions showed coalescence occurring approximately at the same stress as failure. At higher bridging angles (60°) the relative coalescence stress was much lower for plaster inclusions compared to corresponding Ultracal inclusions. Although plaster hexagons at a 60° bridging angle observed a high coalescence stress ratio (greater than 0.95), corresponding plaster diamond and ellipse inclusion pairs experienced a much lower coalescence stress ratio (~ 0.80). This difference in shape coalescence stress ratio could be due to the fact that more shear debonding occurred in diamond and ellipse inclusions which was associated with coalescence and failure (Refer to Tables 5.8 and 5.9).

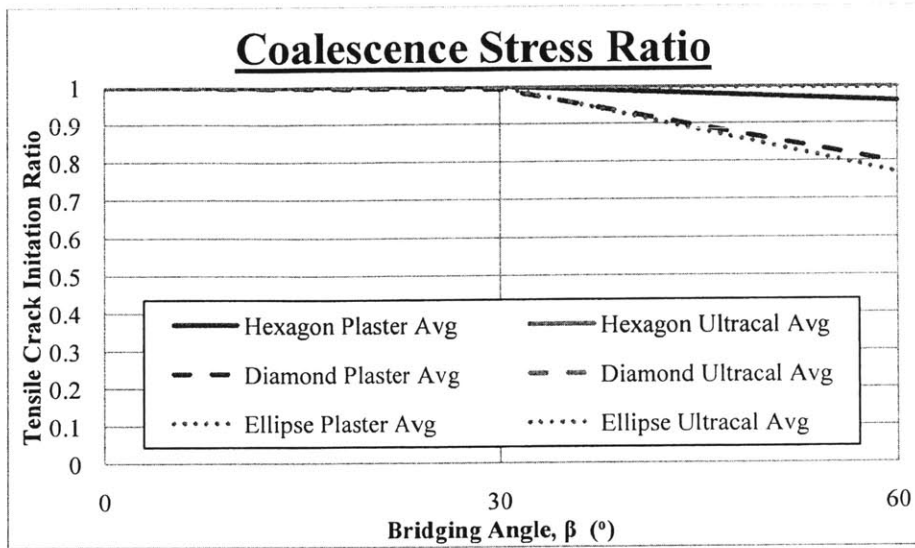


Figure 5.40 – The average **coalescence stress ratio** of all the inclusion pairs tested in regards to inclusion material and bridging angle. The lines are the average values of the test repetitions. Blue Lines = Ultracal, Red Lines = Plaster. Solid Lines = Hexagon Inclusions, Dashed Lines = Diamond Inclusions, Dotted Lines = Ellipse Inclusions.

CHAPTER 6 – Discussion and Comparisons to Previous Research

6.1 Introduction

With the observed high speed imagery, comparisons could be made to the previous experimental coalescence research done on inclusions and on flaws. The debonding and cracking processes as well as the coalescence patterns were compared to the previous work done on inclusions. The observed cracking and coalescence patterns were compared to previous research on single and double flaw pairs.

6.2 Comparison to Previous Inclusion Studies

The major studies regarding inclusions discussed in the following section were conducted by Maji and Shah (1989), Tasdemir et al. (1990) and Janeiro and Einstein (2010). The extent of debonding, the sequence and patterns of cracking, and the coalescence patterns which were applicable to each individual study is compared. The relevance of each research study compared to the currently presented results will be discussed in chronological order in regards to when each study was conducted.

6.2.1 Debonding

In a study conducted by Maji and Shah (1989) the debonding of circular limestone inclusions was observed before tensile crack initiation. Maji and Shah used holographic interferometry to detect debonding at a very high resolution level (almost 0.3 microns). The results showed debonding on the sides, top and bottoms of these inclusions before tensile crack initiation in

the matrix (Figure 6.1). Debonding was also detected at a very low relative loads, almost one-third of the maximum load (Refer to Figure 6.1)

These results are much different than the debonding results seen in this study. Debonding in the current study was never observed before tensile cracking in the matrix and was typically observed at the same time as primary tensile crack initiation. The tensile crack initiation ratio, and in the case of the current study, the debonding stress level, were relatively much higher for all geometric series (TCI ratio > 0.70, Refer to Figure 5.39) than the relative debonding stress level observed by Maji and Shah (1989) of almost 33% of the maximum load (Refer to Figure 6.1). This difference could be due to the resolution of holographic interferometry compared to the high speed camera still-frame imagery. Since the high speed imagery's main object is to detect high speed processes, the resolution of the captured images is not maximized for detecting inclusion interface debonding.

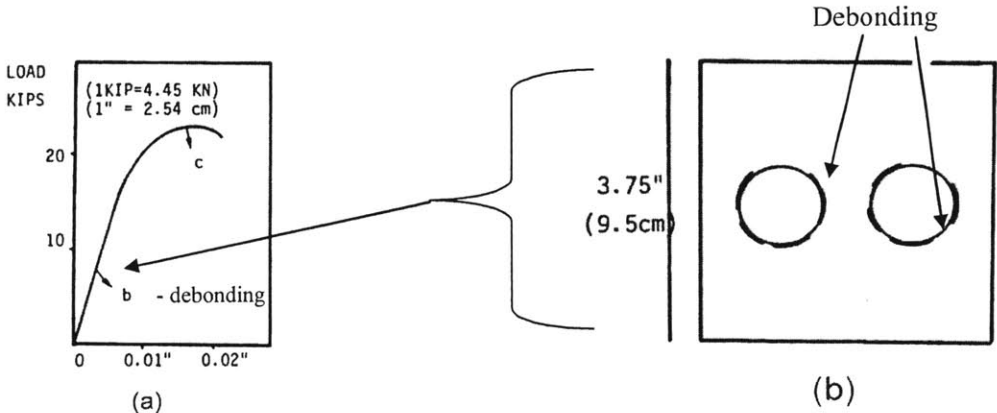


Figure 6.1 – Debonding locations as well as relative debonding load of 1 inch diameter circular limestone inclusions tested by Maji and Shah (1989)

In a similar study conducted by Tasdemir et al. (1990), which also used holographic interferometry on a single rectangular limestone inclusion, debonding was also detected at very low relative stress levels as well (Refer to Table 2.2). Debonding was detected at loads as low as 6% of the maximum loading and tensile crack initiation occurred in the matrix as low as 10% of the maximum load. Although the interface angle and material properties (fracture toughness) control the initiation stress and propagation of a crack, these values are significantly lower than the relative stress levels of debonding and tensile crack initiation

observed in the current study. The resolution of the holographic interferometry technique used to detect debonding and tensile crack initiation in the study by Tasdemir et al. (1990) could also be part of the reason for this large discrepancy in debonding and tensile crack initiation compared to the current research study.

In the study conducted by Janeiro and Einstein (2010), single inclusions of similar shape (hexagon, diamond) and material (Ultracal, plaster) were tested, similar to the current study. From the cracking sequences presented by Janeiro (2009), similar debonding was observed for hexagon and diamond inclusions (Figure 6.2). Debonding was also observed at similar stress levels compared to inclusions pairs at 0° bridging angle tested in the current study (debonding, or tensile crack initiation at 0° bridging angles, occurred between approximately 85 to 100% of the maximum stress) (Refer to Figures 5.39 and 6.2).

Also the amount of debonding, along with the type of each debonding (tensile or shear), occurring at primary tensile crack initiation and at failure can be determined by the single inclusion crack sequences observed by Janeiro (2009). Single hexagon inclusions appeared to have the same amount of debonding at primary tensile cracking and at failure, approximately 50% (3/6 sides) (Refer to Figure 6.2). This is slightly higher than the amount of average debonding at primary tensile cracking (20-25%) but was very similar to the amount of debonding at failure (40-55%) for the hexagon inclusion pairs tested in the current study (Refer to Tables 5.8 and 5.9). Similar amounts of debonding were seen in diamond inclusions pairs tested in the current study at both primary tensile cracking (40-55%) and at failure (80-85%). Also, the amount of tensile and shear debonding appears to be similar in the previously tested single diamond inclusions (50% tensile/shear for Ultracal in the study by Janeiro [2009]) compared to the diamond inclusion pairs tested (35% tensile, 45% shear for Ultracal in the current study). It appears that the debonding behavior observed by Janeiro (2009) in single inclusions was very similar to the debonding observed in corresponding inclusion pairs tested in the current study.

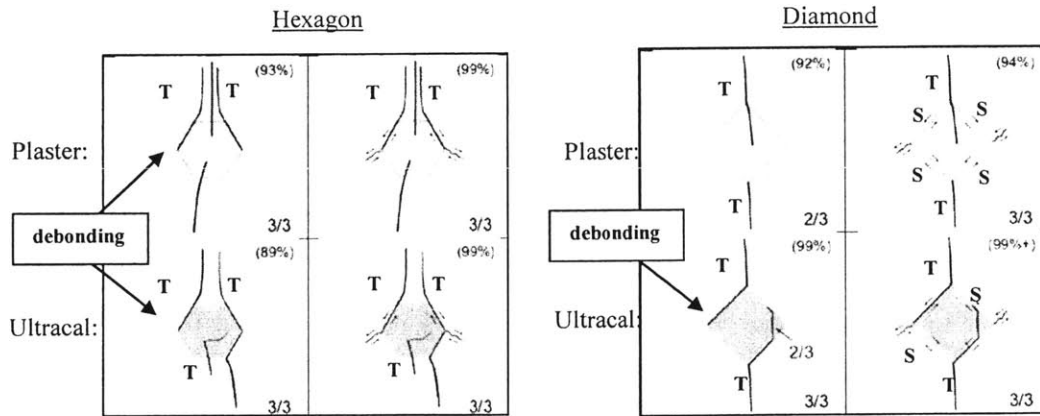


Figure 6.2 – Adapted figure of the debonding sequences in 1/2 inch single inclusions tested by Janeiro and Einstein (2010)

6.2.2 Cracking Sequence

Although the previous studies by Maji and Shah (1989) did not identify cracking nature (tensile or shear) or secondary exterior cracking (such as exterior shear cracks), the general cracking sequence can be compared to the inclusions in the current study. In general, a similar cracking sequence was observed. This included debonding and primary tensile cracking in the matrix, above and below the inclusions, which led to diagonal cracks connecting both inclusion cracks (coalescence) (Figure 6.3). However as previously stated, debonding was observed before tensile cracking by Maji and Shah (1989), which does differ from the current study, where debonding was never observed before tensile crack initiation in the matrix.

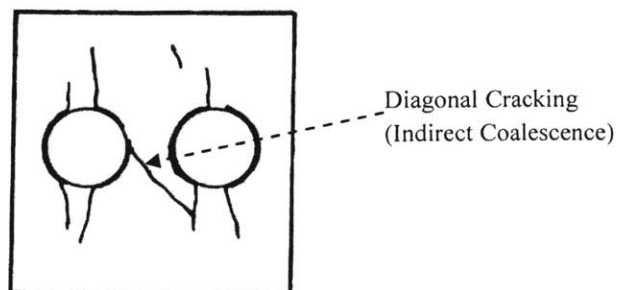


Figure 6.3 – Cracking of 1 inch diameter circular limestone inclusions tested by Maji and Shah (1989)

Similar to the previous work done on corresponding single inclusions, the initiation of primary tensile cracks was followed by shear cracking at the lateral (left-right) edges of the inclusions, especially in hexagon and diamond geometries. Also, three out of the four tensile crack types defined by Janeiro and Einstein (2010) were observed (Type I, II and IV) (Refer to Figure 2.28). Tensile cracks which initiated from a surface crack (Type III) were not observed (Refer to Figure 2.28). In contrast to the previous study conducted by Janeiro (2009), significantly lower amounts of pre-test surface cracks in the inclusions were observed in the current study. Since the previous study by Janeiro (2009) observed much less surface cracking in 1/2" single inclusions compared to the 1" single inclusions, the reduced amount of surface cracks seen in this study is likely due to the fact that all of the newly introduced inclusions pairs consisted of 1/2" inclusions only.

6.2.3 Coalescence

The study conducted by Maji and Shah (1989) tested horizontally aligned circular inclusion pairs (bridging angle = 0°). Although the coalescence behaviors were not specifically investigated in that study, the tests showed either no coalescence or diagonal cracks coalescing the two inclusions. These results are very similar to the coalescence patterns of the inclusions pairs at low bridging angles (0° and 30°) tested in the current study (Refer to Figure 5.36). Even though the study by Maji and Shah (1989) does not focus on the coalescence patterns of inclusion pairs, the coalescence patterns with respect to low bridging angles appear to be similar.

The study done by Janeiro and Einstein (2010) extensively investigated the coalescence behavior of inclusion pairs. In comparing the coalescence behavior of hexagon-, diamond- and ellipse pairs tested in this research to the circle- and square pairs previously tested by Janeiro and Einstein (2010), the coalescence patterns seemed to be quite similar (Refer to Figures 2.32 and 5.36). The coalescence in square- and circle pairs showed a trend from indirect coalescence, to shear coalescence, to combined tensile-shear coalescence as the bridging angle was increased. This trend is similar to the previously stated coalescence trend

of hexagon-, diamond- and ellipse pairs in regard to bridging angle (Refer to Section 5.5.5). Also, the coalescence of hexagon-, diamond-, and ellipse inclusion pairs typically initiated from a primary tensile crack along an inclusion interface (debonded side), which was also observed in the coalescence results of square and circular inclusion pairs.

6.2.4 Stress Behavior

One considerable difference between the inclusion pairs tested in the current study and the results of circular and square inclusion pairs tested by Janeiro and Einstein (2010) was the difference in the stress behavior observed, especially in regard to inclusion material. In contrast to the current study, higher maximum stresses were observed in plaster circle- and square inclusion pairs compared to the Ultracal inclusions. For the present test series on diamond-, hexagon- and ellipse inclusion pairs, higher peak stresses were almost always observed in the Ultracal inclusions (Figure 6.4). Also, the maximum stress of plaster circle- and square inclusion pairs appears to have the highest maximum stress at a 30° bridging angle (Refer to Figure 6.4). The trend for Ultracal circle- and square inclusions appears to decrease with an increase in bridging angle. In contrast, the trend of the currently tested inclusion geometries appears to be the opposite, with plaster inclusions having a decrease in maximum stress as bridging angle increases and Ultracal inclusions having the highest maximum stress at a 30° bridging angle.

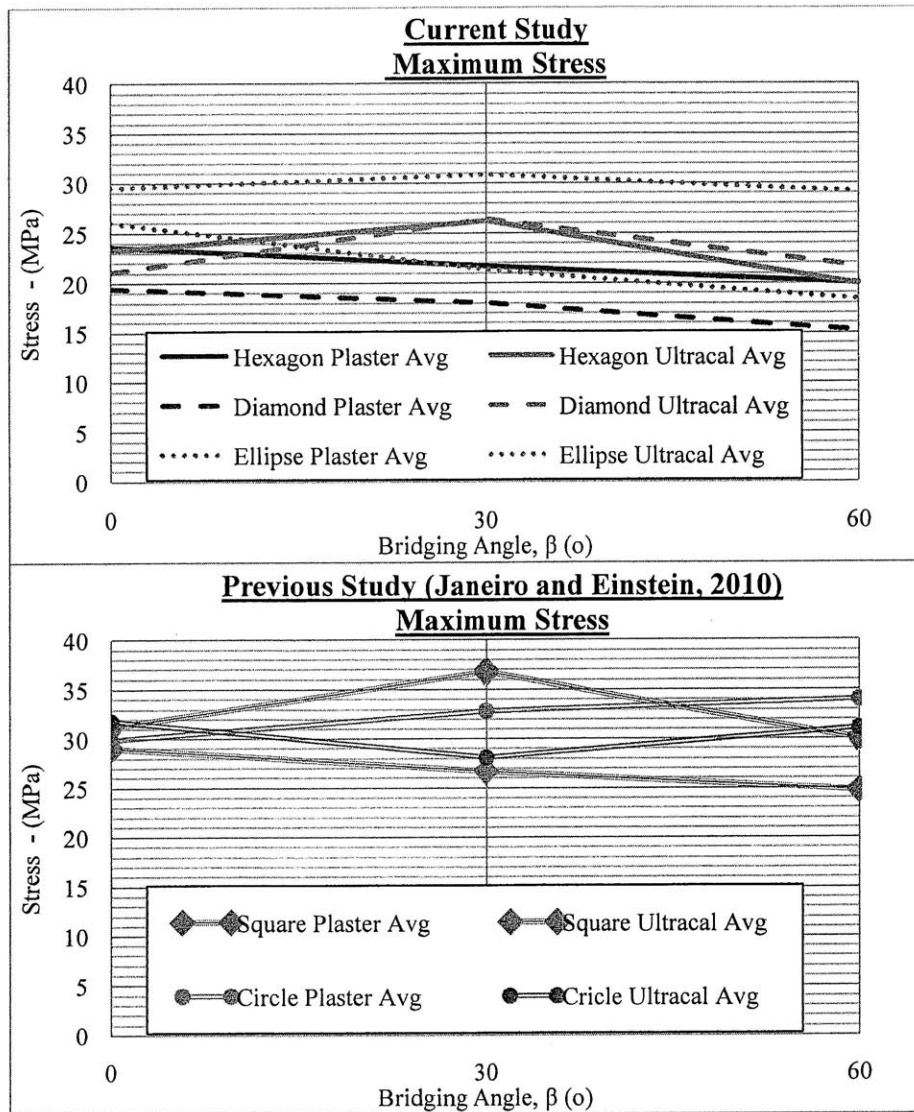


Figure 6.4 – A comparison of the average **maximum stress** of all the inclusion pairs tested in regards to inclusion material and bridging angle (including the inclusion pairs tested by Janeiro and Einstein [2010]). The lines are the average values of the test repetitions. Blue Lines = Ultracal, Red Lines = Plaster. Solid Lines = Hexagon Inclusions, Dashed Lines = Diamond Inclusions, Dotted Lines = Ellipse Inclusions, Double Lines with Circle Points = Circle Inclusions, Double Lines with Diamond Points = Square Inclusions.

The tensile crack initiation ratio from Janeiro and Einstein (2010) also differs from the inclusion pairs tested in the current study (Figure 6.5). The plaster circle- and square inclusions tested by Janeiro and Einstein (2010) have similar TCI ratios compared to the plaster inclusions tested in the current study but the TCI ratio of Ultracal inclusions differ

significantly (Refer to Figure 6.5). The TCI ratio for both the circle- and square Ultracal inclusions appears to be much lower than the corresponding plaster inclusions and decreases significantly as the bridging angle is increased. It appears that these differences in maximum stress and tensile crack initiation ratios are related to the geometric shape and/or coalescence behavior of the corresponding geometry.

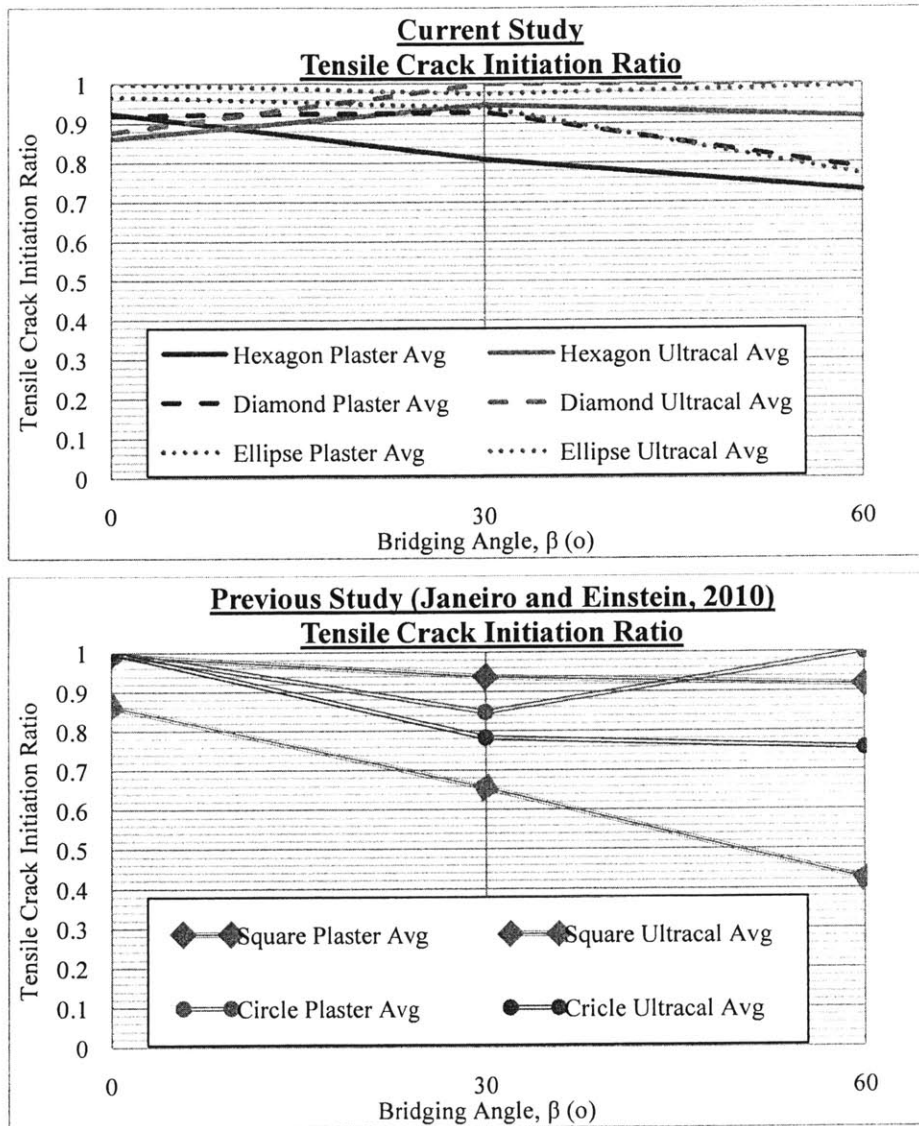


Figure 6.5 – A comparison of the average **tensile crack initiation ratio** of all the inclusion pairs tested in regards to inclusion material and bridging angle (including the inclusion pairs tested by Janeiro and Einstein [2010]). The lines are the average values of the test repetitions. Blue Lines = Ultracal, Red Lines = Plaster. Solid Lines = Hexagon Inclusions, Dashed Lines = Diamond Inclusions, Dotted Lines = Ellipse Inclusions, Double Lines with Circle Points = Circle Inclusions, Double Lines with Diamond Points = Square Inclusions.

6.3 Comparison to Previous Flaw Studies

Along with a comparison to previous inclusions research, the cracking and coalescence patterns in both single and double inclusion pairs tested in the current study were compared to previous research regarding flaws. The cracking types observed in both the single and double inclusions pairs are also compared to the set of crack types proposed by Wong and Einstein (2009). Lastly, the observed inclusion coalescence patterns are compared to the coalescence behaviors observed in flaw pairs tested by Shen et al. (1995), Bobet (1997), and Wong and Einstein (2009).

6.3.1 Crack Patterns

The crack types observed in the inclusions tested in the current study appeared to be very similar to the crack types defined by Wong and Einstein (2009) observed in flaws (Figure 6.6). This included the three types of tensile cracking observed as well as the secondary shear cracks which initiated at the inclusion or flaw edges and propagated toward the direction of loading as a tensile crack (Refer to Figure 6.6). Although figure 6.6 only depicts the similarities between these crack types proposed for flaws and those observed in hexagon inclusions, these crack types were also observed in diamond (Refer Figures 5.16 and 5.17) and ellipse (Refer to Figures 5.26 and 5.27) inclusions as well.

In order to compare the cracking patterns observed in the single ellipse inclusions tested in this study, flaws at a similar flaw inclination angle (45°) can be compared. The study by Wong (2008) tested open flaws (narrow and wide) at several flaw inclination angles (including 45°) in cast gypsum specimens, similar to the matrix used in the current study, as well as Carrara marble (Figure 6.7). Similar to the cracking patterns in both Ultracal and plaster single ellipse inclusions, tensile wing cracks (Type 1 Tensile, Refer to Figure 6.6) were the first crack to appear (Refer to Figures 4.2 and 6.7). After tensile cracking, secondary Type 2 tensile cracking (Refer to Figure 6.6) and/or secondary shear-tensile cracks occurred at the tips. Both Ultracal and plaster single ellipse inclusions showed secondary mixed shear-tensile cracks occurring at the inclusions tips. Ultracal single ellipse inclusions showed

tensile cracks with curvature in the same direction as the inclusion interface (Referred to as Type 2 tensile shown in Figure 6.6, by Wong [2008]).

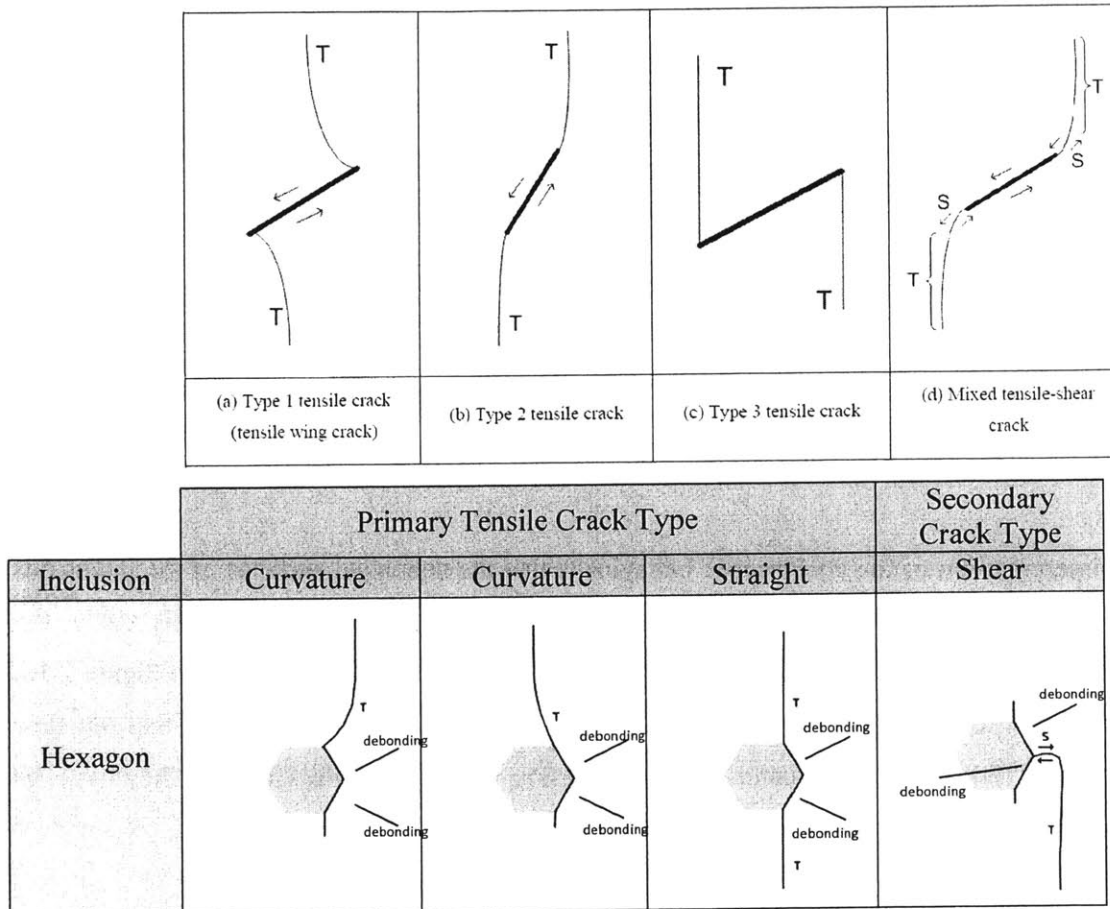


Figure 6.6 – A comparison between the crack types occurring in hexagon inclusion and the crack types in flaws defined by Wong and Einstein (2009). T = Tensile Cracking, S = Shear Cracking Hexagon crack types are used as an example here, but these crack types also occurred in diamond and ellipse inclusions as well (Refer to Figures 5.16, 5.17, 5.26, and 5.27).

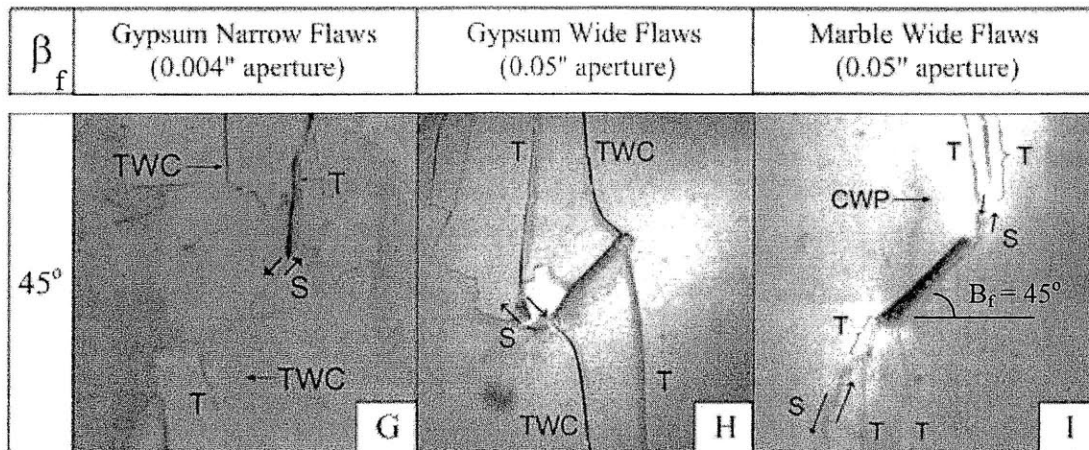


Figure 6.7 – Fracturing behavior in gypsum and marble specimens containing flaws at different flaw inclination angles (β_f). The length of the pre-existing flaws was 0.5". (TWC – tensile wing crack, CWP – curvilinear white patch, T – tensile crack, S – shear crack). (Wong, 2008)

6.3.2 Coalescence Behavior

One interpretation of the coalescence behavior is that the debonded surfaces of the inclusions are potentially behaving like flaw pairs (Figure 6.8). For the purpose of this study, the bridging-inclination angle flaw notation, discussed in section 2.3.2 and shown in Figure 2.10, will be used to represent flaw pairs (refer to Figure 6.8). It should be noted that the flaw inclination (β_f) is not the same as the inclusion bridging angle (β) and they will be differentiated by the subscript f for “flaw”.

Assuming that these debonded interfaces are behaving similar to flaws is a reasonable assumption used in many analytical studies on fracture propagation regarding inclusions, which are based on a debonded region of the interface occurring first and acting as a flaw which propagates into the matrix (e.g. Zaitsev and Wittmann, 1981 and Tasdemir et al., 1990). Since hexagon inclusions have a higher interface inclination angle ($\eta = 60^\circ$) than the diamonds ($\eta = 45^\circ$) and ellipses ($\eta \approx 45^\circ$) (See Figure 6.9), the potential effect of inclusion interface angle can be seen by the difference between the coalescence behavior of hexagon inclusion pairs to that of diamond- and ellipse inclusion pairs, specifically at a 30° bridging angle. As these interface sides have a lower inclination, at the same bridging angle, the

coalescence appears to trend from indirect or no coalescence [hexagon] to direct shear coalescence [diamond and ellipse] (Refer to $\beta=30^\circ$ on Figure 5.36).

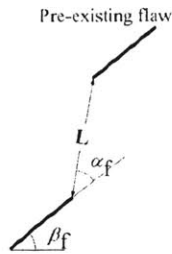


Figure 6.8 – Geometric representation of Stepped Flaws (where α_f is the “bridging” angle between the flaws and β_f is the angle of the flaw with the horizontal).

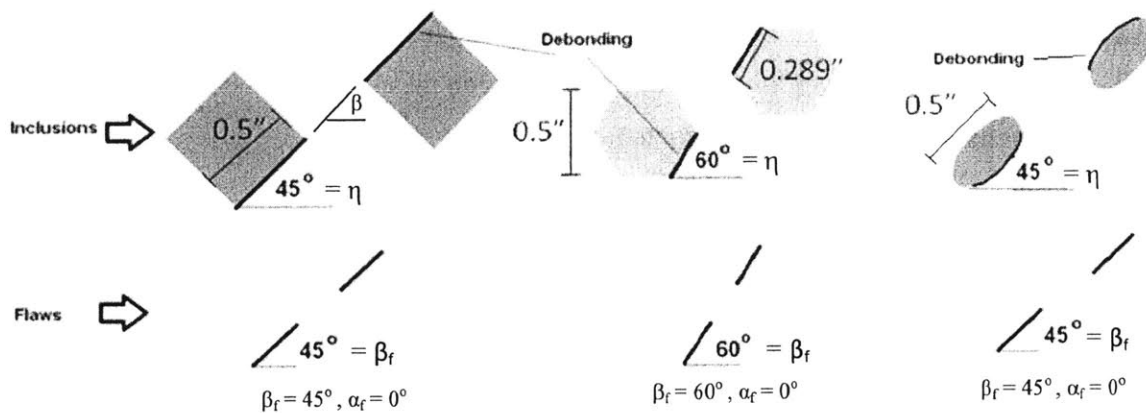


Figure 6.9 – A representation of the debonded interface sides to stepped flaws (where α_f is the angle between the flaws and β_f is the angle of the flaw with the horizontal). η is the angle between the horizontal and a debonded interface of an inclusion (interface angle). β is the bridging angle between the inclusion inner tips and the horizontal.

Previous research has shown that the relative orientation (inclination and bridging angle) of flaw pairs is a key factor affecting coalescence behavior (Shen et al., 1995; Bobet and Einstein, 1998; Wong and Einstein, 2009). As the flaw angle (of co-planar flaws), or bridging angle between flaws increases, coalescence trends from no coalescence, to shear coalescence, to tensile coalescence. From these findings, the coalescence trends of flaw pairs can be compared to the coalescence trends of inclusion pairs.

If the inclusion interface is compared to a flaw, the interface inclination (η) represents the flaw angle (β_f) and the inclusion bridging angle (β) between inclusions represents the bridging

angle between flaws (α_f) (refer to figure 6.8). As a preliminary observation, the coalescence trends of inclusion interfaces and flaws in regard to bridging angle are quite similar. A proper comparison between flaw angles and interface inclinations is difficult because the effects of flaw angles have only been compared for coplanar flaws while these inclusion interfaces are not always coplanar. In general, the trend in inclusion coalescence in regard to bridging angle is comparable to flaw pairs.

This representation of inclusion interfaces as flaw pairs also explains the similarity between inclusion coalescence with the coalescence types proposed by Wong and Einstein (2009) for flaws (Refer to Figure 2.16). Similar to the findings of Janeiro and Einstein (2010), flaw coalescence patterns all appear to match quite closely with the coalescence patterns observed in the present inclusion test series (Figure 6.9).

	Hexagon		Diamond		Ellipse ($\alpha=45^\circ$)		Flaw Coalescence (Wong and Einstein, 2009)
	Plaster	Ultracal	Plaster	Ultracal	Plaster	Ultracal	
$\beta = 0^\circ$	(1/3) [2] debonding	(3/3) [1] debonding	(3/3) [2] debonding	(2/3) [2] debonding	(2/3) [2] debonding	(2/3) [1] debonding	(no coalescence)
$\beta = 30^\circ$	(2/3) [2] debonding	(1/3) [2] debonding	(2/3) [3] debonding	(2/3) [5] debonding	(3/3) [3] debonding	(1/3) [3] debonding	(2 cracks)
$\beta = 60^\circ$	(3/3) [5] debonding	(2/4) [5] debonding	(2/3) [5] debonding	(3/3) [5] debonding	(3/3) [5] debonding	(3/3) [5] debonding	(1 crack)
			(2/3) [5] debonding	(3/3) [5] debonding	(3/3) [5] debonding	(3/3) [5] debonding	(3/3) [5] debonding

Figure 6.9 – Comparison of coalescence observed in inclusion pairs tested in the current study with coalescence patterns in flaws as proposed by Wong and Einstein (2009). The number in the top right is the coalescence category proposed by Wong and Einstein (2009). The number in the top left is the amount of test repetitions which exhibited this behavior. T = Tensile Cracking, S = Shear Cracking. The arrows indicate the direction of shearing.

Based on the similarity between the coalescence patterns of flaws proposed by Wong and Einstein (2009) and the coalescence pattern of the currently tested inclusion pairs, an investigation was conducted between coalescence of inclusions pairs and the actual coalescence behaviors observed for flaw pairs in gypsum tested by Shen et al. (1995) and Bobet (1997). For this comparison, the flaws were represented by the debonded inclusion interfaces (Refer to Figure 6.8). In this case 60° flaw angles (flaw angle, $\beta_f = 60^\circ$), correspond to hexagon interface sides ($\eta = 60^\circ$) and 45° flaw angles ($\beta_f \approx 45^\circ$) correspond to diamond- and ellipse interface sides ($\eta = 45^\circ$) (Refer to Figure 6.8).

From the tests conducted by Shen et al. (1995) on flaw pairs in gypsum, the recently tested inclusion pairs at a 60° bridging can be compared to corresponding flaw pairs. Both Shen et al. (1995) and Bobet (1997) used the flaw inclination (β_f)-bridging angle (α_f) notation to define the flaw pair geometry. Converting this flaw pair geometry to the inclusion interfaces for an inclusion bridging angle of 60° (β) would result in flaw bridging angles (α_f) of 0° for hexagon pairs and 15° for diamond- and ellipse pairs (See Figure 6.10). Both Shen et al. (1995) and Bobet (1997) were also not able to determine the mode of cracking (shear or tensile) and therefore only the order of cracking (primary or secondary) is distinguished. As previously stated in Chapter 2, secondary cracks may or may not be shear cracks.

The actual flaw pair coalescence results observed by Shen et al. (1995) show different coalescence behaviors compared to the coalescence observed between inclusions with corresponding inclined interfaces (Figure 6.10). Although most inclusion pairs showed some amount of mixed tensile-shear coalescence, the flaw pairs corresponding to the interfaces of the inclusions observed very distinct single secondary cracks between the interior tips of the flaws (Refer to Figures 6.10). It appears that secondary cracks initiated at the inner tips of the flaw pairs which are aligned with the inclination of the flaw bridging angle (greater than or equal to the flaw angle) and then propagated toward each other to coalescence as a single crack. In contrast, the secondary shear cracks initiating from the inner tips of the inclusions are inclined at an angle either equal or slightly lower than the inclusion interface angle and as

these shear cracks propagate toward each other they coalesce by a single vertical tensile crack. In summary, although the trend of coalescence with respect to bridging angle is similar in flaws and inclusions, the coalescence patterns between inclusions are not exactly the same as corresponding preexisting flaw pairs tested by Shen et al. (1995).

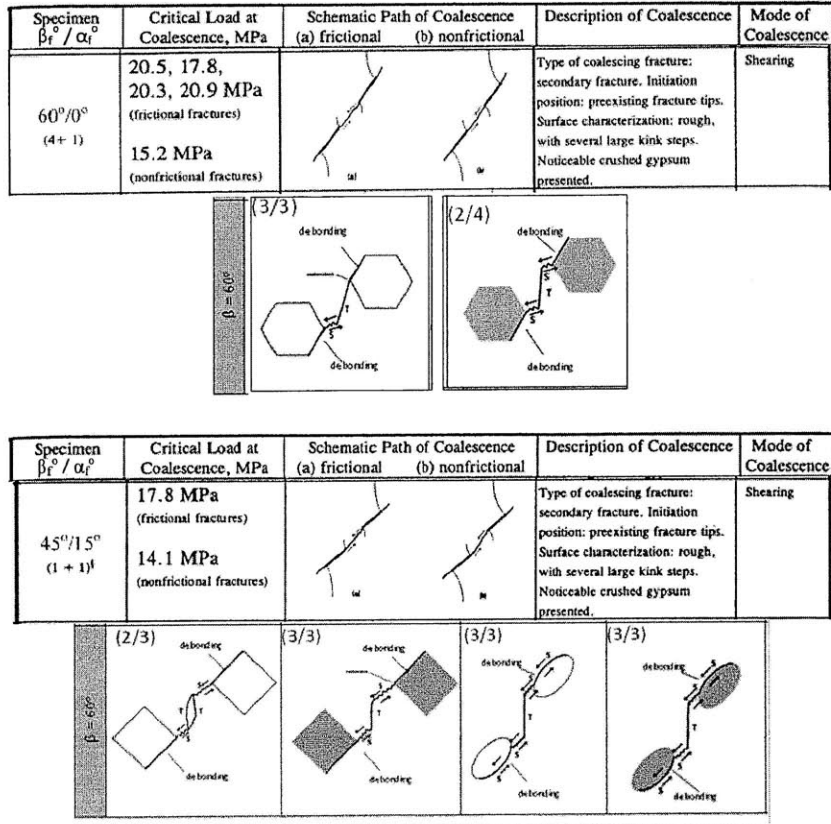
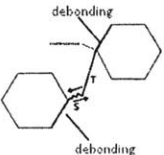
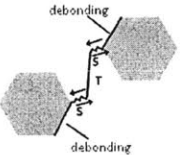



Figure 6.10 – A comparison of the coalescence patterns in specific inclusion series based on interface angles compared to corresponding flaw pairs tested by Shen et al. (1995). T = Tensile Cracking, S = Shear Cracking. The arrows indicate the direction of shearing

Also, these specific inclusion pair tests at 60° bridging angles were compared to a series of tests performed by Bobet (1997) on corresponding flaw pairs. As previously stated, these test results presented by Bobet (1997) make no distinction between shear or tensile cracking types (or direction of shearing). Similar to the comparison to the pairs tested by Shen et al. (1995), a difference can be seen between the coalescence of the 45° inclined (β_f) flaws with an approximate bridging angle (α_f) of 15° observed by Bobet (1997) (Refer to Figures 6.11).

Based on the comparisons of the coalescence patterns observed between inclusions pairs and these studies conducted on corresponding flaw pairs, it appears that the coalescence behavior of inclusions cannot be completely predicted simply from the interface angle. If the inclusion interface inclination and bridging angle were the only deciding factors regarding coalescence behavior, the observed coalescence would be expected to be the same as the flaw pairs of corresponding inclination and bridging angle.

	Plaster Hexagon – $\beta=60^\circ$	Ultracal Hexagon – $\beta=60^\circ$	Flaw - $\beta_f = 60^\circ, \alpha_f = 0^\circ$ (Bobet)		
Coalescence Behavior	(3/3) Direct 	(2/4) Direct 			
Coalescence Stress (MPa)	19.2	19.9	25.1 (open) 28.7 (closed)		
Maximum Stress (MPa)	20.0	19.9	≈26.0 (open) ≈28.6 (closed)		

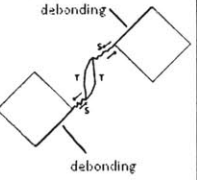
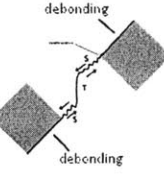
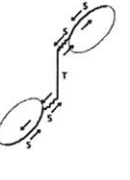
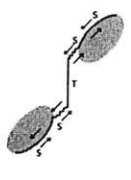
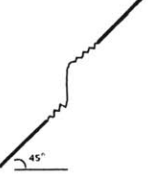
	Plaster Diamond – $\beta=60^\circ$	Ultracal Diamond – $\beta=60^\circ$	Plaster Ellipse – $\alpha=45^\circ \beta=60^\circ$	Ultracal Ellipse – $\beta=45^\circ \alpha=60^\circ$	Flaw - $\beta_f = 45^\circ, \alpha_f = 18^\circ$ (Bobet)
Coalescence Behavior	(3/3) Direct 	(1/3) Direct 	(3/3) Direct 	(3/3) Direct 	(2/3) Direct 
Coalescence Stress (MPa)	12.1	21.7	18.4	28.9	22.1 (open) ≈31.9 (closed)
Maximum Stress (MPa)	15.2	21.7	23.9	29.1	≈22.1 (open) ≈31.9 (closed)

Figure 6.11 – A comparison to stepped flaws tested by Bobet (1997). T = Tensile Cracking, S = Shear Cracking. The arrows indicate the direction of shearing. The number in the top left of the frame is the amount of test repetitions showing this behavior (Where α_f is the angle between the flaws and β_f is the angle of the flaw with the horizontal)

CHAPTER 7 – Conclusions and Future Research

7.1 Conclusions

7.1.1 Introduction

In order to expand on previous inclusion research investigating cracking behavior and coalescence patterns on square and circular geometries, inclusion pairs with other shapes (hexagon, diamond, and ellipse) were tested in uniaxial compression with the use of a high speed camera to detect the crack progression. In addition, the cracking behavior of single ellipse inclusions was also investigated. Specifically, debonding (tensile and shear), crack propagation (tensile and shear) and the details of crack coalescence were investigated.

7.1.2 Debonding

For all inclusion series tested, some amount of debonding occurred at the inclusion-matrix interface. Initial debonding was observed along the lateral (left-right) sides of the inclusions (as primary tensile cracking initiated in the matrix). On average more total interface debonding occurred for diamond- and ellipse inclusions compared to hexagon inclusions. Slightly more debonding occurred in specimens containing plaster (less stiff than the matrix) inclusions compared to Ultracal (stiffer than the matrix) inclusions. Also, more shear debonding occurred at higher bridging angles, which was likely due to the fact that more direct shear (or mixed shear-tensile) coalescence occurred.

Similar debonding nature (tensile or shear) and locations were observed in hexagon- and diamond inclusion pairs when compared to the previous studies conducted by Janeiro and

Einstein (2010) on single hexagon- and diamond inclusions. Also, similar relative debonding stresses were observed for hexagon- and diamond inclusion pairs compared to the single inclusions tested by Janeiro and Einstein (2010). In contrast to tests conducted by Maji and Shah (1998) and Tasdemir et al. (1990), interface debonding was never observed before tensile crack initiation and was typically observed at much higher relative stresses (in regard to both tensile crack initiation and maximum stress) compared to the specimens tested in their studies. These variations could be due to differences in testing techniques, such as measurement resolution and loading rates, and material properties.

7.1.3 Cracking Sequence

Similar to many previous studies on inclusions, primary tensile cracking was observed at the top and bottom of the inclusion (Maji and Shah, 1989; Tasdemir, 1990; Janeiro and Einstein, 2010). Also, similar to the research conducted by Janeiro and Einstein (2010) on inclusions, as well as many studies conducted on flaws, primary tensile cracks were typically followed by secondary shear cracks at the exterior edges (or tips) of the inclusions. In some cases, such as in single Ultracal ellipse inclusions, distinct secondary tensile cracks were observed, similar to the observations made by Wong (2008) on the cracking processes of flaws in gypsum and Carrara marble. The cracking processes associated with the inclusions in this study appeared to compare very well with previous studies regarding the cracking processes of inclusions and of flaws.

7.1.4 Coalescence

Similar to previous research conducted on the coalescence of inclusion pairs by Janeiro and Einstein (2010), a general trend from indirect or no coalescence, to direct shear coalescence, to mixed tensile-shear coalescence was observed as the bridging angle between inclusions was increased. Preliminary observations showed that the coalescence appeared to trend from indirect to direct shear coalescence as the debonded interface angle decreased. There

appeared to be no difference in the coalescence behavior of two geometrically similar inclusion pairs of different material (inclusions stiffer or less stiff than the matrix). At higher bridging angles, where direct coalescence between the two inclusions occurred commonly, coalescence occurred more frequently from primary tensile cracking.

These general coalescence trends in regard to bridging angle are comparable to the trends observed in flaw pairs as well. However, although coalescence generally occurred between two debonded interfaces of the inclusions, the actual coalescence behaviors between the debonded inclusions interfaces are not exactly equivalent to corresponding flaw pairs. Flaw pairs, corresponding to inclusion interfaces at moderate (45°) to high (60°) interface angles and high inclusion bridging angles (60°), showed direct coalescence consisting of a single shear crack whereas the corresponding inclusions typically showed direct mixed tensile-shear coalescence. As a preliminary observation, although the trend of coalescence behavior regarding bridging angle is similar to that of flaw pairs, the cracks initiating at debonded inclusion interfaces do not completely represent and predict the observed coalescence behavior.

7.2 Summary

The ultimate goal of this study was to determine the effects of several inclusion parameters on the cracking and coalescence behavior in brittle materials. From the results of the test series studied in this research, the effects of various inclusion properties (Shape, Material, and Interface Angle) and pair orientations (Bridging Angle) in regard to debonding, cracking sequence, and coalescence were determined and are summarized in the following table (Table 7.1).




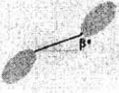

Inclusion Parameter:		Cracking Behavior		
		Debonding	Cracking Sequence	Coalescence
Shape	Hexagon 	Rare occurrences of complete debonding, less shear debonding observed compared to diamond and ellipse inclusions.	All shapes show the same cracking sequence: Primary tensile cracking (debonding) to lateral secondary shear cracking.	No direct correlation (See Interface Angle)
	Diamond 	More occurrences of complete debonding, More shear debonding observed compared to Hexagon inclusions.		
	Ellipse 			
Material	Plaster (Less Stiff)	More debonding was observed compared to Ultracal inclusions.	Primary tensile cracking (debonding) to secondary shear cracks.	No apparent effect
	Ultracal (Stiff)	Less debonding was observed compared to corresponding plaster inclusions.	Primary tensile cracking (debonding) to secondary shear cracks. Secondary tensile cracking in ellipses.	
Bridging Angle (β) 	Low (0°)	More debonding occurring from primary tensile debonding and less shear debonding compared to higher bridging angles	No apparent effect	Indirect or No Coalescence
	Moderate (30°)			Direct Shear or Mixed Tensile-Shear Coalescence
	High (60°)	Less debonding occurring due to primary tensile cracking and more shear debonding		Mixed Tensile-Shear Coalescence
Interface Angle (η) 	Moderate (45°) (Diamond, Ellipse)	No direct correlation (See Shape Effect)	No apparent effect	At moderate bridging angles (30°) - Direct Coalescence
	High (60°) (Hexagon)			At moderate bridging angles (30°) - Indirect Coalescence

Table 7.1 - A summary table of the inclusion parameters affecting the fracturing and coalescence patterns in a brittle material.

Focusing on the most important comparison aspects from the study, the following conclusions can be drawn;

- **General**

- (i) Cracking sequences occurring for *all* inclusion shapes and materials were similar to those of corresponding *single inclusions* in previous research conducted by Janeiro and Einstein (2010). (Initial tensile cracking, along with debonding, then secondary shear cracking at the lateral edges of the inclusions).

- **Shape**

- (ii) Interface debonding occurred more frequently for diamond- and ellipse inclusion pairs compared to hexagon inclusion pairs.

- **Material**

- (iii) Inclusion material does not seem to affect the *coalescence pattern*, similar to previous coalescence studies by Janeiro and Einstein (2010).

- (iv) Peak stresses observed in inclusion pairs containing *Ultracal inclusions* were higher than those with corresponding *plaster inclusions*, in contrast to previous research by Janeiro and Einstein (2010).

- **Bridging Angle**

- (v) Coalescence patterns ranged from indirect (or none) to direct as the *bridging angle* (β) between inclusions was increased, similar to previous research (Shen et al., 1995; Bobet, 1997; Janeiro and Einstein, 2010).

- **Interface Angle**

- (vi) Coalescence patterns at the same bridging angle trended from indirect to direct as the *inclusion interface angle* (η) was decreased.

7.3 Future Research

Additional experimental work should be performed to clarify some of the uncertainties regarding the effect of inclusion interface angle on the coalescence behavior between similar inclusion shapes. Further testing on inclusions with various interface inclination angles (η , such as 15° or 30°) could better explain the effect of inclusion interface angles on coalescence patterns. This could be achieved by performing additional testing on elliptical inclusions. Further testing on specimens with ellipse inclusions, specifically at horizontal or vertical inclinations, could be used compare the behavior of elliptical inclusion cracking and coalescence to that of circular inclusions.

Since debonding appears to be associated with all of the observed coalescence patterns, a microscopic investigation of the interface would provide further insight on the microscopic mechanisms affecting interface debonding, and thus coalescence. An experimental procedure similar to the technique used by Wong (2008), to determine the micro-cracking and processes zones in gypsum and marble, could be used to do a microanalysis of the inclusion-matrix interface. This would involve SEM (or ESEM) images of the interface at various loading stages of a test. Since previous studies (Maji and Shah, 1989; Tasdemir, 1990) have detected debonding at much lower stresses compared to tensile crack initiation, debonding, which may not be visible on a macro-scale by the imagery used in this study, may be observable on a micro-scale.

One of the limitations of high speed imagery as a research technique is the capacity of the camera, which was used to detect the fracturing processes. As previously discussed, the resolution of other crack detection techniques (e.g. holographic interferometry) could explain earlier detection of debonding. Using higher resolution images, by changing the camera settings or using a newer camera, could aid in the visual detection of debonding and crack initiation. Also, determining the sequence of debonding (before or after tensile cracking) was difficult in this research due to lack of high speed imagery recorded at tensile crack initiation.

It could be valuable to study initial cracking sequences by manually triggering the high speed camera at the occurrence of tensile crack initiation in order to determine the sequencing of debonding and initial matrix cracking. One drawback of triggering the camera when primary tensile cracking occurs is that, since the camera can only be triggered once per test, the high speed processes of coalescence would not be captured. Either performing additional tests simply comparing the initial cracking processes or using an additional high speed camera to capture tensile crack initiation and debonding are both potential options.

From the cracking behavior and coalescence patterns, a model framework should eventually be developed to describe and predict the cracking and coalescence of brittle material with various inclusion geometries and material properties. More importantly, along with additional experimental testing, theoretical solutions should be developed in order to compare to the cracking and coalescence processes observed in the tests. This would include elastic solutions and potentially a FEM analysis of the matrix-inclusion body. The ultimate goal of this research should be to implement a matrix-inclusion body in a model such as FROCK in order to simulate the cracking and coalescence occurring in a heterogeneous brittle material

Since all solutions are based on the estimated material properties (Elastic modulus, Poisson's ratio, interface bond strength, etc.), additional experiments should be performed to accurately determine the material properties of both the matrix and inclusion materials. The Poisson's ratio of the inclusion material should be investigated using a more accurate method than the testing procedure describe in the Appendix A. Also, an experimental test setup should be developed to estimate the bond strength. Although previous studies (e.g. Zaitsev and Wittmann, 1981; Tasdemir et al., 1990) assumed a crack developing at the interface, in order to accurately predict the occurrence of debonding, and crack propagation, the bond strength of the interface should be included in the model of crack initiation at an interface and the crack coalescence between inclusions in a brittle material.

CHAPTER 8 – References

Anderson, T.L. (2005) *Fracture Mechanics: Fundamentals and Applications*, Edition 3, CRC Press, Boca Raton, FL.

Ashby, M.F. and Hallam, S.D. (1986) the failure of brittle solids containing small cracks under compressive stress states. *Acta Metall.*, 34, pp. 497-510.

Ashby, M.F. and Sammis. (1990) The damage mechanics of brittle solids in compression, *Pure Appl. Geophys.*, 133, pp 489-521.

Aulia, T.B. (2000) Strain localization and fracture energy of high-strength concrete under uniaxial compression, *LACER* No. 5, pp. 221-240.

Barenblatt, G.I. (1962) The mathematical theory of equilibrium cracks in brittle fracture. *Advances in Applied Mechanics*, Vol. VII, Academic Press, NY, pp. 55-109.

Bienawski. (1967) Mechanisms of brittle fracture of rock, part II – experimental studies, *Int. J. Rock Mech. Min. Sci.*, Vol. 4, pp. 407-423.

Bobet, A. (1997) *Fracture Coalescence in Rock Materials: Experimental Observations and Numerical Predictions*, Sc.D. Thesis, Massachusetts Institute of Technology.

Bobet, A. and Einstein, H.H. (1998a) Fracture coalescence in rock-type materials under uniaxial and biaxial compression. *Int. J. Rock Mech Min Sci*, 35(7), pp. 863-88.

Bobet, A. and Einstein, H.H. (1998b) Numerical modeling of fracture coalescence in a model rock material. *Int. J. Fracture*, 92, pp. 221-252.

Brace, W.F. and Bombolakis, E.G. (1963) A note on brittle crack growth in compression, *J. Geophys Res*, 68(12), pp. 3709-3713.

Chaker and Barquins. (1996) Sliding effect on branch cracks, *Phys. Chem. Earth*, 21(4), pp. 319-323.

Chan, M. *Automatic Two-Dimensional Multi-Fracture Propagation Modeling of Brittle Solids with Particular Application to Rock*. Ph.D. Thesis, Massachusetts Institute of Technology, Cambridge. U.S.A. 1986.

Costin, L.S. (1985) Damage mechanics in the post-failure region. *Mech. Mat.* 4, pp. 149-160.

- Dugdale, D.S. (1960) Yielding in steel sheets containing slits, *Journal of the Mechanics and Physics of Solids*, 8, pp. 100-104.
- Eidelman A, Reches Z (1992) Fractured pebbles—a new stress indicator. *Geology* 20:307–310
- Friedman, M., Handin, J. and Alani, G. (1972) Fracture energy of rocks. *Int. J. Rock. Mech. Min. Sci.*, 9, pp. 757-766.
- Germanovich, L.N. and Dyskin, A.V. (2000) Fracture mechanisms and instability of openings in compression, *Int. J. Rock. Mech. Min. Sci.*, 37, pp. 263-284.
- Goodier, J.N. (1933) Concentration of stress around spherical and cylindrical inclusions and flaws, *J. Appl. Mech.*, 1, pp. 39-44.
- Gramberg, J. (1965) Axial cleavage fracturing, a significant process in mining and geology, *Engineering Geology*, 1(1), pp. 31-72.
- Griffith, A.A. (1920) The phenomenon of rupture and flow in solids. *Philosophical Transactions*, Series A, 221, pp. 163-198.
- Hallam, S.D. and Ashby, M.F. (1990) Compressive brittle fracture and the construction of multi-axial failure maps. In D.J. Barber and Meredith, P.G. (eds) *Deformation Processes in Minerals, Ceramics and Rocks*. London: Unwin Hyman, pp. 84-108.
- Hoek and Bieniawski. (1965) Brittle fracture propagation in rock under compression, *Int. J. of Fracture Mechanics*, Vol. 1, pp 137-155.
- Horii, H. & Nemat-Nasser, S. (1985) Compression-induced microcrack growth in brittle solids: Axial splitting and shear failure. *Journal of Geophysical Research*, 90 (B4), pp.3105-3125.
- Huang J.F., Chen G.L., Zhao Y.H. and Wang R. (1990) An experimental study of the strain field development prior to failure of a marble plate under compression. *Tectonophysics*, Vol. 175, pp. 283-290.
- Inglis, C.E. (1913) Stresses in a plate due to the presence of cracks and sharp corners. *Inst. Naval Architecture*, London, 55, pp. 219-230.

- Ingraffea, A. and Wawrzynek, P.A. (2001) *Encyclopedia of Materials: Science and Technology*, pp. 1745-1750.
- Irwin, G.R. (1957) Analysis of stresses and strains near the end of a crack traversing a plate. *Journal of Applied Mechanics*, 24, pp. 361-364.
- Janeiro, R. P. (2009) *The Effect of Inclusions in Brittle Material*, Sc.D. Thesis, Massachusetts Institute of Technology.
- Janeiro, R.P. and Einstein, H. H. (2010) Experimental study of the cracking behavior of specimens containing inclusions (under uniaxial compression), *International Journal of Fracture*. 164:83–102
- Kemeny, J.M. and Cook, N.G.W. (1987) Crack models for the failure of rocks in compression. *In Proc. 2nd Int. Conf. on Constitutive Laws for Engineering Materials*, Tucson, Arizona.
- Lajtai, E.Z. 1970. A theoretical and experimental evaluation of the Griffith theory of brittle fracture, *Tectonophysics*, 11, pp. 129-156.
- Li, Y.P., Chen, L.Z. and Wang, Y.H. (2005) Experimental research on pre-cracked marble under compression, *International Journal of Solids and Structures*, 42, pp. 2505-2516.
- Lo, T.Y. and Cui, H.Z. (2004) Effect of porous lightweight aggregate on strength of concrete, *Materials Letters*, 58, pp. 916-919.
- Maji, A.K. and Shah, S.P. (1989) Application of acoustic emission and laser holography to study microfracture in concrete, *Nondestructive Testing, ACI SP-112*, edited by Lew, H.S., American Concrete Institute, Detroit, MI, pp. 83-109.
- Maji, A.K. and Shah, S.P. (1990) Mixed mode fracture in compression, *Analysis of Concrete Structures by Fracture Mechanics*, edited by Elfgren, L. and Shah, S.P., Chapman and Hall, New York, NY, pp. 55-68.
- Maji, A.K., Tasdemir, M.A., and Shah, S.P. (1991) Mixed mode crack propagation in quasi brittle material, *Engineering Fracture Mechanics*, 38(2/3), pp. 1058-1076.
- Maji, A.K. and Wang, J. (1992) Fracture mechanics of a tension-shear macrocrack in rocks. *Experimental Mechanics*, 32(2), pp. 190-196.
- Martinez, A.R. (1999) *Fracture coalescence in natural rock*, MSc Thesis, Massachusetts

Institute of Technology, 341 p.

Melville, P.H. (1977) Fracture mechanics of brittle materials in compression, *Int. J. Frac.*, 13, pp. 532-534.

Miller, J.T. (2008) *Crack coalescence in granite*, MSc Thesis, Massachusetts Institute of Technology, 474 p.

Moss, W.C. and Gupta, Y.M. (1982) A constitutive model describing dilatancy and cracking in brittle rocks. *Journal of Geophysical Research*, 87 (B4), pp. 2985-2998.

Mughieda, O. and Alzo'ubi, A.K. (2004) Fracture mechanics of offset rock joints – a laboratory investigation, *Geotechnical and Geological Engineering*, 22, pp. 545-562.

Nelson, R.A. (1968) *Modeling a jointed rock mass*, MSc Thesis, Massachusetts Institute of Technology, 218 p.

Nemat-Nasser and Horii. (1982) Compression-induced non-planar crack extension with application to splitting, exfoliation, and rockburst, *J. Geophys. Res.*, 87(8), pp 6805-6821.

Nesetova and Lajtai. (1973) Fracture from compressive stress concentrations around elastic flaws, *Int J. Rock Mech. Min. Sci. & Geomech. Abstr.*, 10, pp. 265-284.

Petit, J. and Barquins, M. (1988) Can natural faults propagate under Mode II conditions?, *Tectonics*, 7(6), pp. 1246-1265.

Reyes, O. (1991) *Experimental study and analytic modeling of compressive fracture in brittle materials*, Ph.D. Thesis, Massachusetts Institute of Technology, Cambridge, MA.

Reyes, O. and Einstein, H.H. (1991) Failure mechanism of fractured rock – a fracture coalescence model, *Proceedings of the 7th International Congress of Rock Mechanics, Aachen, Germany*, 1, pp. 333-340.

Reches, Z., 1998, Tensile fracturing of stiff rock layers under triaxial compressive stress states, 3rd NARMS, Mexcio, June, 1998, *Int. J. of Rock Mech. & Min. Sci.* 35: 4-5, Paper No. 70

Sagong, M. (2001) *The study of the fracture of multiple flaw specimens*, Ph.D. Thesis, Purdue University, Indiana.

Sagong, M. and Bobet, A. (2002) Coalescence of multiple flaws in a rock-model material in uniaxial compression, *Int. J. Rock. Mech. Min. Sci.*, 39, pp. 229-241.

- Segall, P. and Pollard, D.D. (1983) Nucleation and growth of strike slip faults in granite, *J. Geophys Res*, 88, pp. 555-568.
- Shen, B., Stephansson, O., Einstein, H.H. and Ghahreman, B. (1995) Coalescence of fractures under shear stress experiments, *J. Geophys Res*, 100(6), pp. 5975-90.
- Tasdemir, M.A., Maji, A.K. and Shah, S.P. (1990) Crack propagation in concrete under compression, *Journal of Engineering Mechanics*, 116(5), pp. 1058-1076.
- Wang, E.Z. and Shrive, N.G. (1995) Brittle fracture in compression: mechanics, models and criteria, *Engineering Fracture Mechanics*, 52(6), pp. 1107 – 1126.
- Wong, L.N.Y. (2008) *Crack coalescence in molded gypsum and Carrara Marble*, PhD Thesis, Massachusetts Institute of Technology, Cambridge, MA 2008. 876 p.
- Wong, L.N.Y. and Einstein, H.H. (2009) Using high speed video imaging in the study of cracking processes in rock, *Geotechnical Testing Journal*, 32(2).
- Wong, R.H.C. and Chau, K.T. (1998) Crack coalescence in a rock-like material containing two cracks. *Int. J. Rock. Mech. Min. Sci.*, 35(2), pp. 147-164.
- Zaitsev YB, Wittmann FH (1981) Simulation of crack propagation and failure of concrete. *Mat Struc* 14(83):357–365
- Zhang, M.H. and GjØrv O.E. (1990) Microstructure of the interfacial zone between lightweight aggregate and cement paste, *Cement and Concrete Research*, 20(4), pp. 610-618.

APPENDIX A – Poisson’s Ratio of Inclusion Material

A.1 Background:

The following experiment was conducted to determine the Poisson’s ratio of two different gypsum materials in the MIT rock mechanics laboratory; Ultracal and Molding Plaster. The Poisson’s ratio is the ratio of horizontal strain to vertical strain in a specimen loaded in the vertical axis.

A.1.1 Classical Definition

Poisson’s effect is a material constant representing the transverse strain when a material is stressed axially. The ratio of this transverse strain to axial strain is dependent on a material property, and is referred to as the Poisson’s ratio. The Poisson’s ratio is related to the material bulk and shear modulus, and vice-versa.

A.1.2 Engineering Definition

The Poisson’s ratio expresses the transverse strain to axial strain. In the case of this experiment the specimen is being compressed axially (considered negative). This means the transverse dimensions of the specimen will increase as the axial dimensions decrease in compression (Figure A.1). In this situation the Poisson’s ratio can vary between -1 and 0.5. Negative Poisson’s ratio is a rare material property and would for example refer to something that expands when stressed in tension.

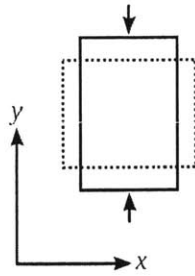


Figure A.1 – Poisson's Effect in Compression

A.1.3 Testing methods

A.1.3.1 Static Method

This test involves uniaxial compression along with the measurement of the vertical and horizontal displacements. This is the type of test used for this experiment and will be described in more detail in the following sections.

A.1.3.1.1 Lateral Extensometer

Used to measure transverse or radial displacements on a cylindrical specimen, this is a tool used in the static method of determining Poisson's Ratio (Figure A.2). This is an accepted method of determining radial strains and could potentially be a more accurate alternative to the axially determined test setups (explained later in Section A.2.1).

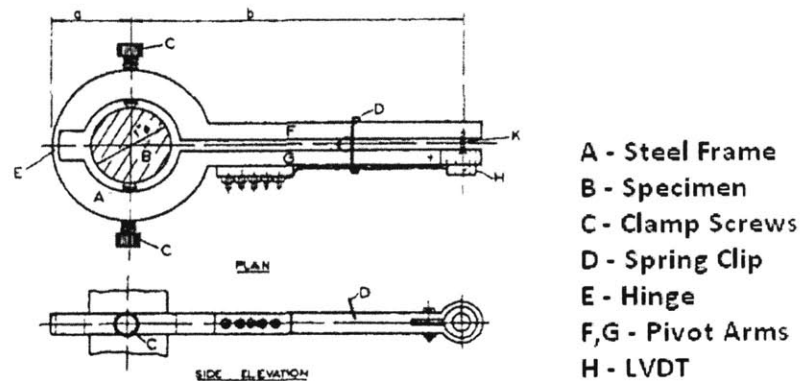


Figure A.2 – Early Version of a Lateral Extensometer (Leeman, 1957)

A.1.3.2 Dynamic Method (Burshtein, 1968):

By sending pulses through the rock specimen, the Poisson's ratio can be determined from the velocities of the longitudinal and transverse wave propagation. The Poisson's ratio is expressed in the following equation:

$$\mu = \frac{\frac{1}{2} \left(\frac{v_L}{v_T} \right)^2 - 1}{\left(\frac{v_L}{v_T} \right)^2 - 1}$$

Where: μ – Poisson's Ratio
 v_L – Longitudinal Wave Velocity
 v_T – Transverse Wave Velocity

A.1.4 Known Values

Mineral	Poisson's ratio
α -Cristobalite (SiO ₂)	-0.164
Diamond (C)	0.069
α -Quartz (SiO ₂)	0.079
Periclase (MgO)	0.182
Topaz (Al ₂ (F, OH) ₂ SiO ₄)	0.221
Graphite (C)	0.223
Sapphire (Al ₂ O ₃)	0.234
Magnesite (MgCO ₃)	0.251
Halite (NaCl)	0.253
Magnetite (Fe ₃ O ₄)	0.262
Galena (PbS)	0.270
Anhydrite (CaSO ₄)	0.273
Rutile (TiO ₂)	0.278
Chromite (FeO · Cr ₂ O ₃)	0.280
Albite (NaAlSi ₃ O ₈)	0.285
Fluorite (CaF ₂)	0.289
Dolomite (CaMg(CO ₃) ₂)	0.292
Calcite (CaCO ₃)	0.309
Sphalerite (ZnS)	0.320
Uraninite (UO ₂)	0.325
Gypsum (CaSO ₄ · 2H ₂ O)	0.336 ★
Zincite (ZnO)	0.353
Bunsenite (NiO)	0.369
Celestite (SrSO ₄)	0.379

Table A.1 – Typical Mineral Poisson's Ratio Values (Gereck, 2007). The Poisson's Ratio for gypsum is starred.

A.1.4.1 Hydrocal

In a study done at MIT by Nelson (1963) on the modeling of a jointed rock mass several different types of gypsum material were assessed as possible materials to use. After considering the compressive and tensile strength of these gypsum compositions Hydrocal-B11 gypsum was used. Using gages pasted to a cylindrical specimen several material properties of Hydrocal-B11 gypsum were determined; the elastic modulus and Poisson's ratio (Figure A.3). From this test Nelson (1963) calculated the Hydrocal-B11 gypsum to have a modulus of approximately 10,760 MPa and a Poisson's ratio of 0.24 (Refer to Figure A.3).

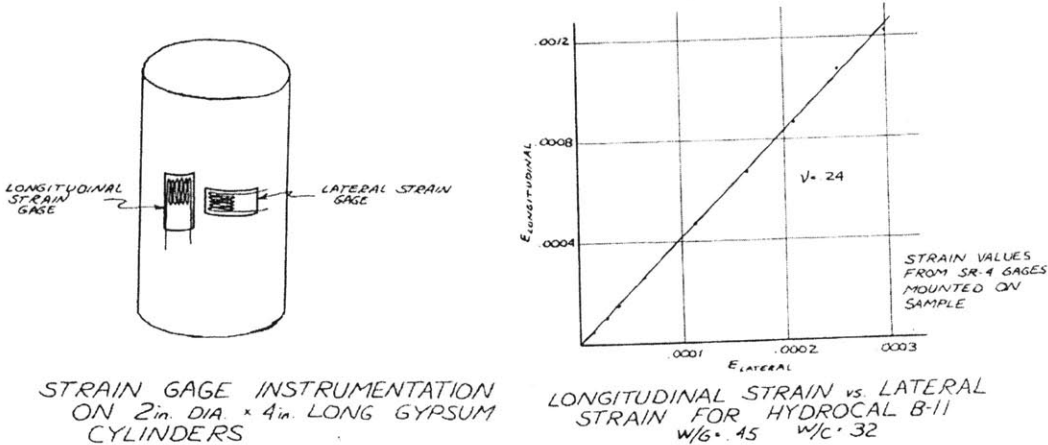


Figure A.3 – Nelson Test Setup and Hydrocal-B11 Results (Nelson, 1960)

A.1.4.2 Ultracal

In an article by Alejandro Mota (2006) discussed the fragmentation and fracturing of artificial kidney stones these artificial stones are made from Ultracal gypsum. This research used a finite element model, in which the properties of Ultracal-30 gypsum were determined as input parameters in the computational model. For this model a Poisson's ratio of 0.3461 was used. Since there can be different versions of Ultracal, depending on the basic Ultracal composition and water-cement ratio, this value may not be the same for the Ultracal used in the MIT rock mechanics laboratory but a general value may be assumed from this

A.1.4.3 Molding Plaster

In a study by A.J. Majumdar and R.W. Nurse (1974) on glass fiber reinforced cement, plaster gypsum is described as having a Poisson's ratio of "...0.20-0.30 depending on the water/solid ratio."(1974). However, this study does not give an exact Poisson's ratio for the plaster gypsum but it does give a general range, which could potentially be related to the molding plaster gypsum used in the current study.

From these articles the general ranges of these two materials can be predicted with the Ultracal gypsum having a higher Poisson's ratio of almost 0.35 and the Plaster gypsum having a lower Poisson's ratio around 0.25.

A.2 Experimental Preparation

The two different types of gypsum materials required for the following Poisson's ratio tests were Ultracal and Molding Plaster. Both were molded in standard 2 inch diameter, 4 inch tall cylinders used for concrete testing. The smallest available cylinder (2"x4") was used due to the fact that with gypsum there is no aggregate size restriction on the specimens' mold size (as opposed to concrete). Two specimens were cast of each type of material thus resulting in four different specimen cylinders (2 Ultracal, 2 Plaster). Along with the four gypsum specimens an additional Aluminum cylinder of similar diameter and height was manufactured in order to compare the systems' accuracy by comparing this cylinder's results to the known Poisson's ratio values of Aluminum. The final specimen dimensions of the four cylinders can be seen in Table A.2 below. It can be seen that there is a difference in the diameter of the cylinders with respect to material type. Looking at the final diameters of the specimens, there is slightly more shrinking in the Ultracal than the Plaster specimens. This could be an important factor in considering the integrity of inclusions of Ultracal versus Plaster

	Final Dimension (in)	
	Height*	Diameter
Aluminum	4.000	2.000
Plaster #1	4.125	2.008
Plaster #2	4.093	2.023
Ultracal #1	3.932	2.005
Ultracal #2	3.931	2.006

*With Plaster End Caps

Table A.2 – Specimen Dimensions

Due to the uneven ends of the cylinders the standard technique used in concrete cylinder preparation was used to have flat and leveled the ends. This technique uses plaster caps applied to both ends of the specimens. The plaster used for the end caps did not have the water to powder ratio as the plaster used in the molding plaster specimens, very likely resulting in different material properties. Since the lateral displacements were determined from 1.5 inch extensometers placed in the middle of the specimens, the different material properties of the end caps do not have an effect on the Poisson's ratio results. One problem that arose when applying the plaster caps was that the dried specimens caused the plaster to harden almost instantaneously. The solution to this was to not apply the plaster on the end with a spatula but to push the specimen down onto a circular heap of the plaster and then trim the excess plaster around the edges (See Figures A.4 and A.5).

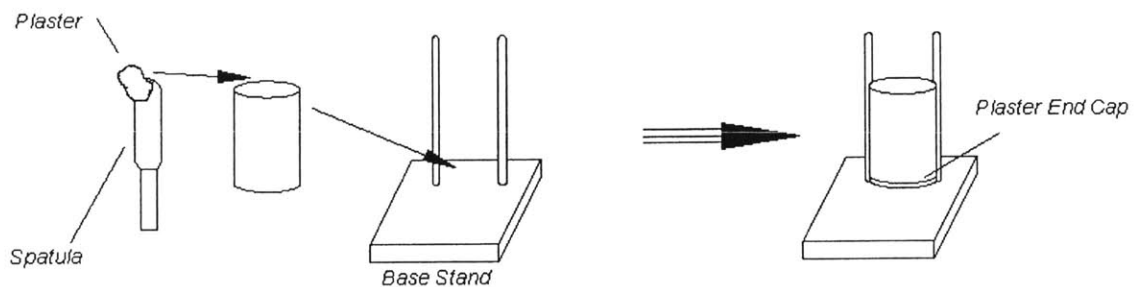


Figure A.4 – Traditional Method for *Concrete* End Capping

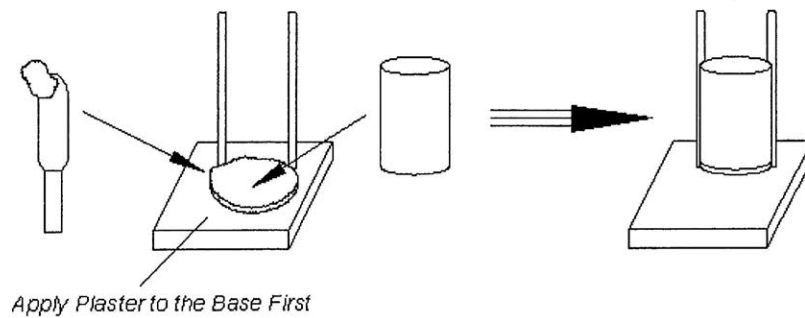


Figure A.5 – Modified Method for *Gypsum* End Capping

A.2.1 Setup

The experimental setup consisted of two 1.5 inch extensometers, two small LVDTs, a magnetic stand, and a Baldwin 60 kip loading machine (See Figures A.6 to A.10). From the magnetic stand a cross bar was placed horizontally and the two LVDT's were attached, creating an axis perpendicularly aligned between the LVDT's. The bar and LVDT's were aligned parallel to the base of the loading frame and their height was set at approximately at the mid-height of the specimen. The LVDT's were separated by a distance at which their initial values were approximately 0 volts. Spacing the LVDTs to as close to zero initially gave them better accuracy. This setup also allowed the tester to remove the specimen without moving the stand. The only parts that needed to be reset were the extensometers on the side. To determine the effect of the setup, two separate sets of tests were run with everything reset and realigned.

The Baldwin loading frame was controlled by a computer running the program MTEST. Due to large amount of channels necessary another computer was used to acquire the data.

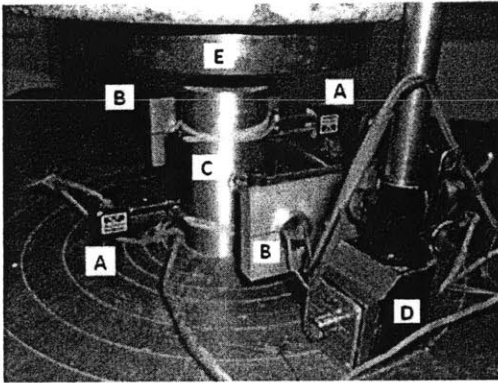


Figure A.6 – Test Setup

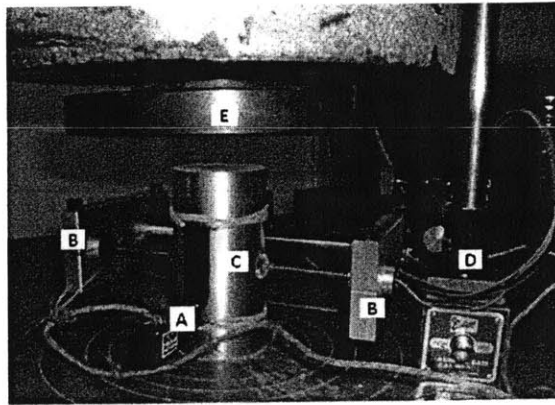


Figure A.7 – Test Setup

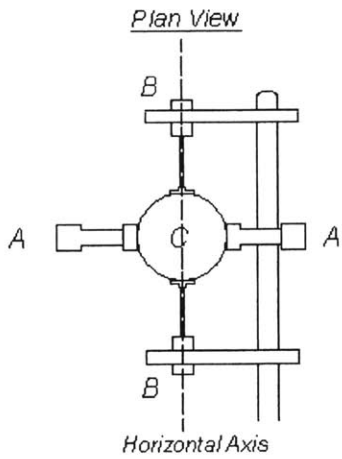


Figure A.8 –Plan View Sketch

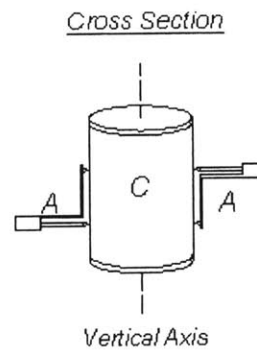


Figure A.9– Cross Section Sketch

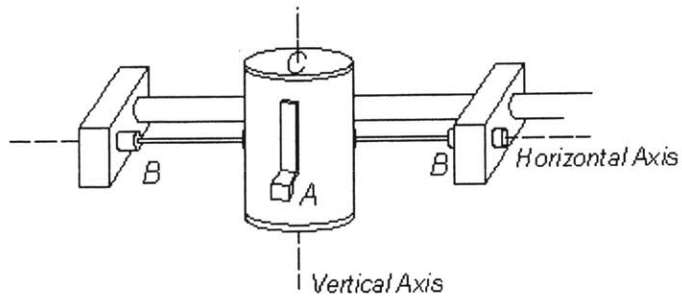


Figure A.10 – Perspective Sketch

- KEY:**
- A - Extensometer**
 - B - LDVT**
 - C - Specimen**
 - D - Magnetic Stand**
 - E - Baldwin Loading Frame**

A.2.2 Testing

With the setup described above vertical displacements on the specimen were recorded on both sides using two extensometers on opposite vertical sides of the specimen. The horizontal displacements on each side of the specimen, at the mid-height, were determined with the LDVTs. From the load cell in the Baldwin machine the load on the specimen was also recorded. All of these values, as well as input voltages, were recorded with a data acquisition computer separate from the computer controlling the machine.

A.3 Analysis Procedure

Using the data collected from the test several engineering values could be determined. These values consist of the average vertical displacement and strain, the cumulative horizontal displacement and strain, and the Poisson's ratio. To determine all of these values an acceptable range of data was selected to remove any seating effects or potential failure effects.

To determine the average vertical displacement the displacements from the two extensometers were averaged. This displacement was then divided by the extensometer length of 1.5 inches to determine the vertical strain. The horizontal displacement was calculated by adding the relative displacements of the LVDTs. It should be noted that there are one of two scenarios that occurred: either both LVDTs move out away from the specimen, or the specimen shifts in one direction with one LVDT moving out and one LVDT moving in (See Figures A.8 and A.9). Since both LVDTs have the same sign when moving away from the specimen the relative displacement values of each LVDT should be added. If the specimen shifts then one LVDT's relative movement will be negative and the two readings will be subtracted from each other. The horizontal strain was calculated by dividing the horizontal displacement by the specimen diameter. The Poisson's ratio was determined by dividing the horizontal strain by the vertical strain.

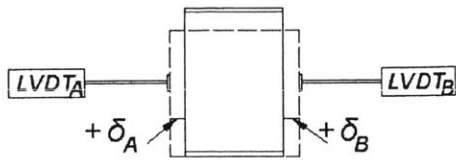


Figure A.8 – Case 1 (No Shifting)

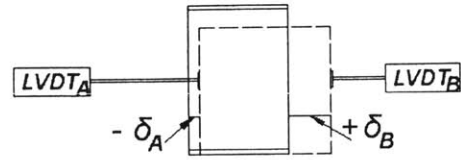


Figure A.9 – Case 2 (Shifting)

A.4 Results

A.4.1 Modulus of Elasticity

From the stress-strain curves (Figure A.10) the Modulus of Elasticity for each test was calculated (Table A.3). Due to the fact that the properties of the Ultracal and Plaster were unknown these tests were load controlled around approximately 7 kips and 5 kips respectively. Since Plaster has a much lower modulus than Ultracal a much higher strain was experienced in the Plaster specimens when loading to approximately 5 kips. During the second set of tests runs on the plaster these specimens' failed at a lower maximum load than the load applied originally to them in the first test run these results. This high strain could have caused the Plaster specimens to fail during the first set of tests. Therefore the second sets of tests were removed due to pre-failure or fatigue effects on the material. It should also be noted that one of the Ultracal specimens in the second set had unusual numbers and it was removed due to an error in the data collection.

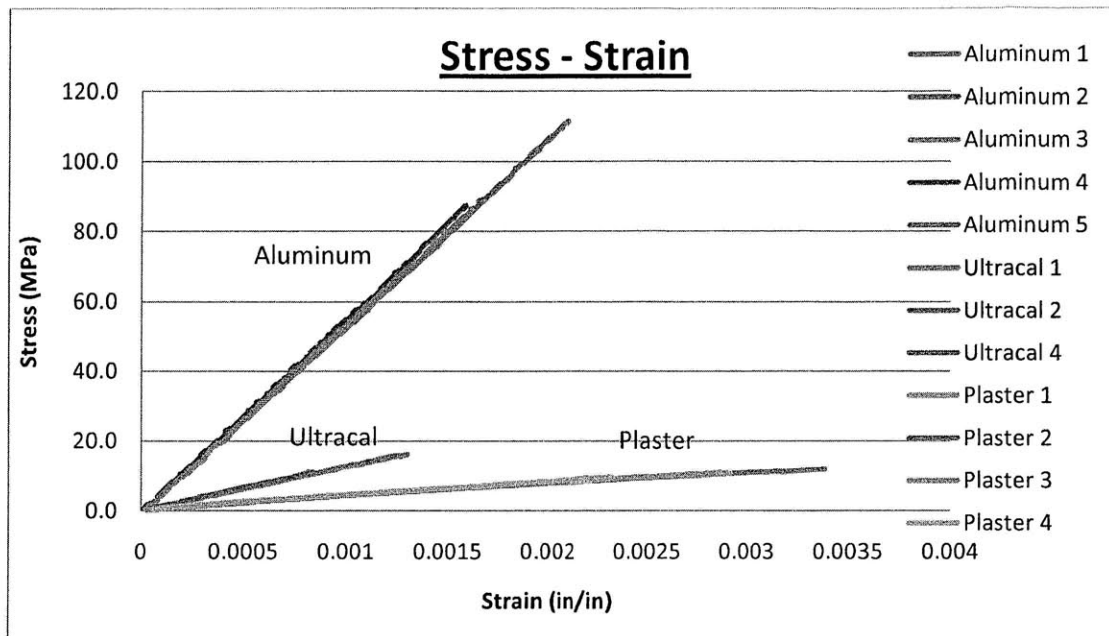


Figure A.10 – Stress-Strain Curves

	Modulus of Elasticity (MPa)					Average
	Test #					
	1	2	3	4	5	
Aluminum	53,115	53,523	53,240	53,240	55,955	53,815
Ultracal	13,149	12,744	-	13,173		13,022
Plaster	3,342	3,315	3,757	3,698		3,328

*Failed Lower than Set 1 Peak Load – Possible Fatigue Effects

Table A.3 – Modulus of Elasticity

From the work done in the MIT Rock mechanics laboratory by Nelson, the modulus of elasticity for Hydrocal B-11 was determined to be approximately 10,760 MPa. From this it can be concluded that the moduli of Ultracal and Plaster gypsum are higher and lower respectively to that of Hydrocal gypsum.

A.4.1 Poisson's Ratio

This Poisson's ratio analysis was done for each specimen and each test (See Table 1.4 Below).

	Test # (Set 1)		Test # (Set 2)			Average, ν
	1	2	1	2	3	
Aluminum	0.435	0.313	0.263	0.252	0.369229	0.316
Plaster	0.216	0.186	0.369*	0.390*		0.201
Ultracal	0.412	0.313	-	0.423		0.383

*Failed Lower than Set 1 Peak Load – Possible Fatigue Effects

Table A.4 – Final Poisson Values

A.5 Discussion and Conclusion

Aluminum was used as the baseline material to determine if the described test setup was consistent with the accepted values of Poisson's ratio for Aluminum. Known Poisson's ratios for Aluminum are between 0.33 and 0.35, depending on the alloy. For this experiment it will be assumed that the acceptable Poisson's ratio of the Aluminum used is 0.33. From this the difference from the acceptable value is determined for each test on the Aluminum specimen (See Table A.5). Also, the standard deviation for both Aluminum (5 Tests) and Ultracal (3 Tests) were determined; The standard deviation for plaster was not determined due to the fact that only two viable test results were determined (See Table 1.6).

	Test # (Set 1)		Test # (Set 2)		
	1	2	1	2	3
Aluminum					
Test Determined	0.435	0.313	0.263	0.252	0.369229
Difference from 0.33	0.105	-0.017	-0.067	-0.078	0.039

Table A.5 – Aluminum Differences from Acceptable Value

Standard

	Deviation
Aluminum	0.0764
Plaster	N/A
Ultracal	0.0608

Table 1.6 – Standard Deviations

From these two tables, it can be seen that relatively large standard deviations exist for both the Ultracal and Aluminum test data. Essentially all tests for Aluminum lie between 0.25 and 0.44, as well as 0.31 and 0.42 for the Ultracal. This is a wide range since many materials lie between these values. It is unknown whether the plaster values are in fact as consistent in value as they appear since there are only two tests for this material type.

For the purpose of this experimental setup it is recommended that only the ranges of each material Poisson's ratio are used. For more accurate values of Poisson's ratio a more precise test setup specifically designed for determining horizontal and vertical strains in compression is recommended.

A.6 Recommendations

More sensitive equipment, especially equipment determining the transverse displacement, is suggested for a more precise approximation of Poisson's ratio. Since there are many techniques to determine the axial strain the controlling factor appears to be determining the radial strain. Some suggestions include possibly using a clamping device for determining the radial displacement of the specimen, or using a higher precision tool such as a laser displacement device to determine the changes in radius. High resolution image processing could also be used to determine the transverse strain using the changes in images between loads.

A.7 References

Burshtein, L.S. "Determination of Poisson's Ratio for Rocks by Static and Dynamic Methods" *Journal of Mining Science* vol.4-3 (1968):235-238

Gercek, H. "Poisson's Ratio Values for Rocks" *International Journal of Rock Mechanics and Mining Sciences*. Vol 44-1 (2007): 1-13

Leeman, E. R., C. Grobbelaar "A Lateral Extensometer for the Determination of Poisson's Ratio of Rock" *Journal of Scientific Instruments*. Vol. 34, December 1957

Majumdar, A.J., R.W. Nurse "Glass Fibre Reinforced Cement" *Materials Science and Engineering*. Vol 15-2,3 (1974):107-127

Mota, Alejandro, Jaroslaw Knap, and Michael Ortiz "Three-Dimensional fracture and fragmentation of artificial kidney stones" *Journal of Physics: Conference Series*. Vol 46 (2006):299-303

Nelson, R.A. (1960) "Modeling a Jointed Rock Mass,". M.S. Thesis, M.I.T., Cambridge Mass.

APPENDIX B – Gypsum Preparation Caveats

(Julie Harrow - MIT UROP Student)

Materials Needed:

Specimen

560g Hydrocal B-11 powder

6.4g celite powder

224mL water

Materials

heat resistive tape with a smooth texture

double sided tape

grease

geometric templates (base and top)

nylon bars (inclusions)

(2) large weighted blocks

(3) cloth hand towels

Tools

graduated cylinder

hammer

steel mold (cast)

screws

chisel

flathead screwdriver

mass scales

kitchen mixer (with bowl and mixing insert)

B.1 Before Getting Started

Be sure that the cast is properly taped—the tape should cover the entire base with as few seams as possible and allow for the “inclusion insert gap” to be as smooth a transition as possible. The sides must be taped such that all the surfaces to come in contact with the specimen are covered smoothly, and again, with as few seams as possible. I suggest strips of tape going lengthwise; the final layer taped along the lower half of the cast so that the entire specimen rests in a region without seams (Figure B.1).

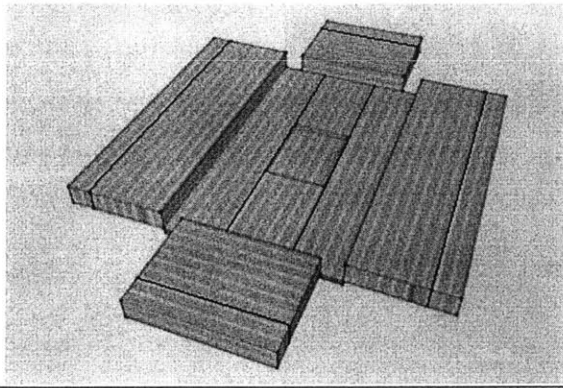


Figure B.1- Open cast taped

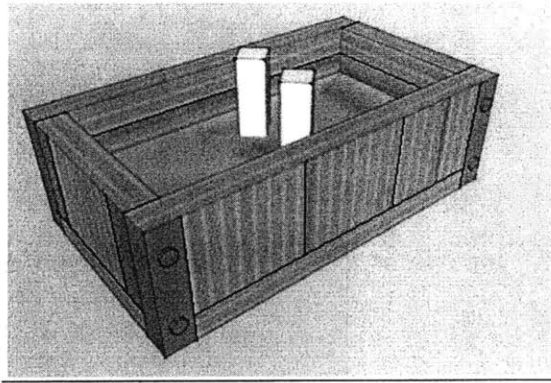


Figure B.2- Closed cast taped to base

Finally, the base must be taped to the walls of the cast such that each side remains attached after the cast is unscrewed. One/two long strips of tape should reach up both [out]sides of the cast on the shorter ends. The longer ends require the same procedure with three/four pieces of tape. The last pieces of tape should be placed along the edges to ensure little leakage (Figure B.2).

B.2 Mixing Gypsum

1. Measure out 560g Hydrocal, 6.4g celite, 224mL water

***Be sure to tare scales before each measurement*

2. Assemble mixer and add water and then celite to the bowl. Mix on lowest speed (1) for 20 seconds and turn off mixer. (See mixer below)

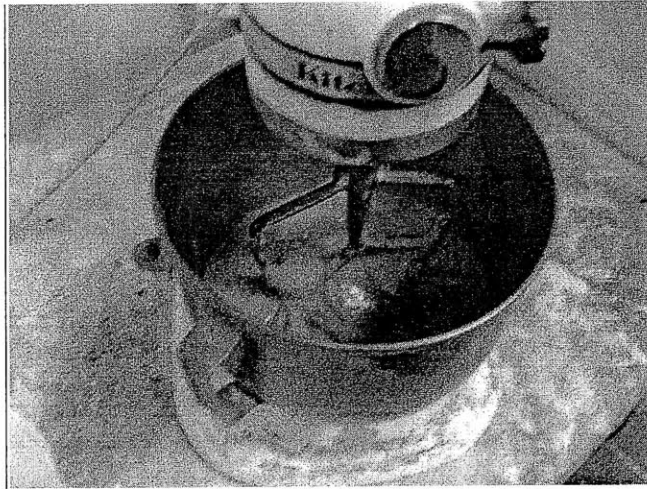


Figure B.3-Mixer and mixing instrument used for gypsum fabrication

3. Disassemble mixer and add Hydrocal to the water and celite solution (you may tip the bowl slightly when pouring in the Hydrocal to get as little on the sides as possible). Reassemble the mixer. Mix on lowest speed for 4 minutes and use a spatula to push unmixed Hydrocal into the mixture.

4. While the mixer is working for four minutes, prepare the mold:

- a. Tape the base geometric template to the base of the cast edge-to-edge using double-sided tape (See Figure B.4)

**If the templates ever become soggy or crinkled, then flatten them with flat heavy blocks while they dry.

***Also, the template may begin to sag or crease in between the inclusion holes. This may be rectified by using a spacer of sorts throughout casting: 2-3 strips of stacked poster board, wrapped in duct tape at dimensions that complement the “inclusion insert gap” dimensions and the shape/orientation of the inclusions. Attached to base template with double sided tape. (See figure B.5)

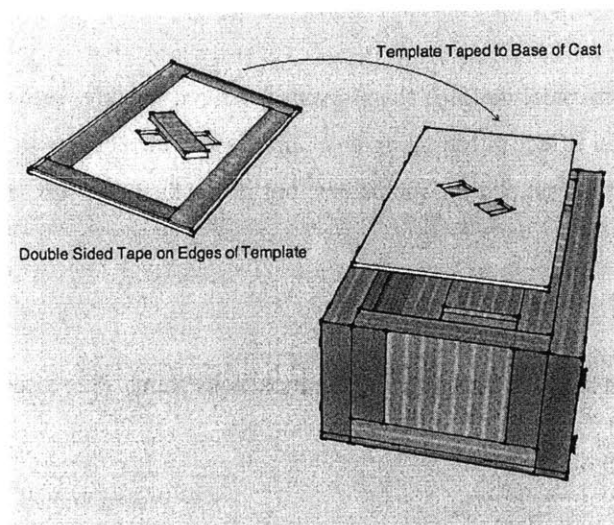


Figure B.4 - Preparing cast with template

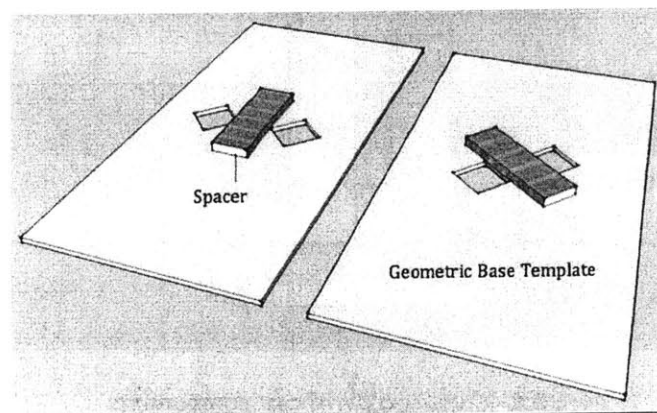


Figure B.5- Template “spacers” in two orientations

b. Using your finger, grease the lower three-quarters of the inclusion (nylon bars) just enough to make it slippery (you should only see a very thin and somewhat transparent coating of grease)

- c. Place template into the closed cast and insert inclusions appropriately

(See Gypsum Preparation Considerations for use with shims)

***Step #4 may be completed before mixing, for the mixture should be poured as soon as the 4 minutes have passed in order to avoid premature setting.*

5. Pour gypsum quickly into steel mold. If the gypsum is poured quickly, before it begins to set, the vibration will have a greater effect in removing any bubbles and air pockets in the specimen. Avoid dripping onto the sides of the cast and the inclusions, but if that happens, just wipe it away. (See step #7)

6. Place the top template in the cast, thus aligning the inclusions/shims. See assembly below.

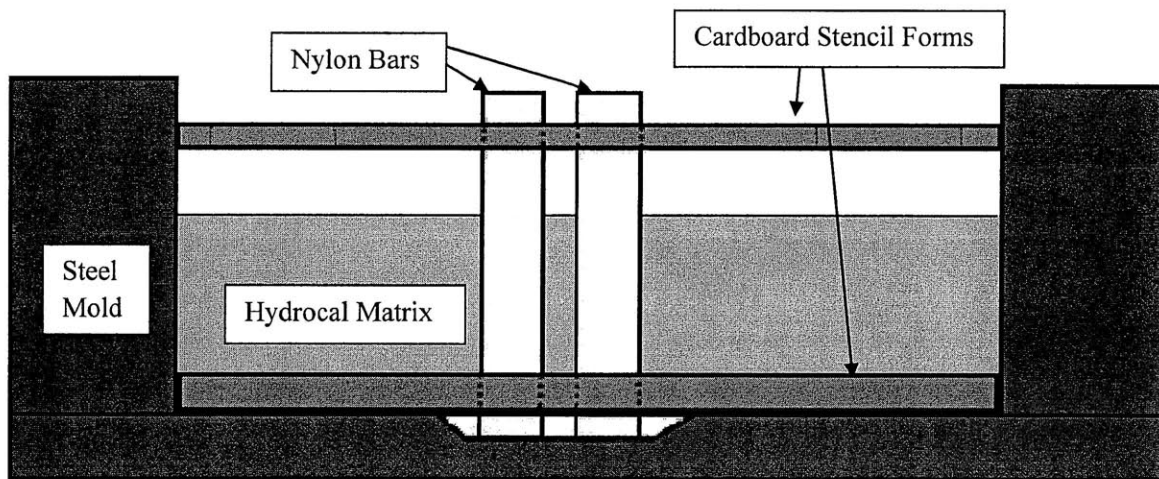


Figure B.6 - Cross section of cast components

7. Put the cast on the vibrating table and vibrate it for at least two minutes. You must hold the cast down firmly on the table and you may shift it from time to time in order to settle out the mixture once bubbles rise to the surface. *Make sure all bubbles are thoroughly removed, especially around inclusion/shim contacts with the gypsum.* Bubbles can form near the inclusions/shims and edges of the mold. If these bubbles are very large they can cause fracturing of the gypsum during inclusion/shim removal and handling. Also these voids (bubbles) will need to be sanded down, effectively reducing the thickness of the gypsum specimen.

8. Place the cast someplace that is very level. It will need at least 50 minutes to air dry and should sit for no longer than 24 hours. . If the inclusions/shims are removed before the first 24 hours while air-drying, the effort required is greatly reduced. This also prevents the possibility of creating cracks on the edges of the flaws.

***Make sure the actual mold is level in all direction, not just the surface that it is placed on.* Many times the two gypsum blocks the mold is on may be level in one direction but not the other. Be sure to check that the actual gypsum mold is level in both directions and not just that the gypsum blocks are level. (See Figure B.7) It may be suggested that more precise metal blocks be used instead of gypsum ones.

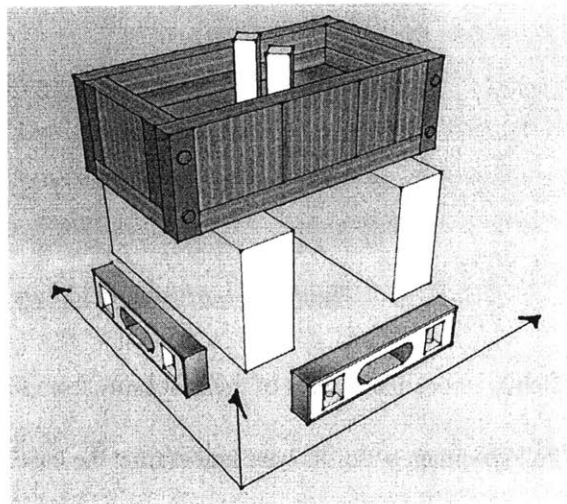


Figure B.7 – Leveling the Mold

9. Record the time that the cast begins to set.

10. Clean the mixer tools immediately. You do not want to wait to clean them even one step later, because the mix will harden and be very difficult to remove.

***Be sure to clean the mixing bowl, mixing instrument, and spatula in a bucket of water and not the sink because the gypsum will clog the pipes.*

B.3 Removing Specimen from its Cast

1. Unscrew cast and remove screws. I suggest placing the screws in a similar configuration on the table to how they were in the cast; the screws do not fit each hole. (See Figure B.8)

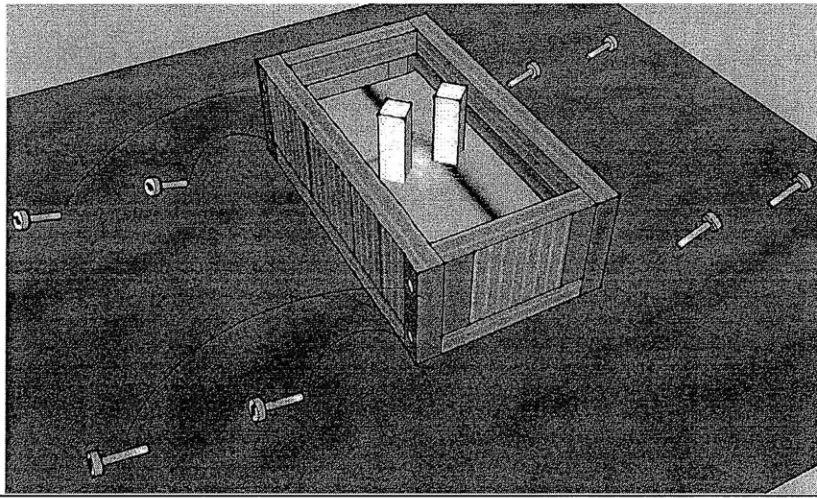


Figure B.8 - Arranging screws during disassembly

2. Gently knock the insides of the cast away from the gypsum block so that the sides fall away.
3. Pull specimen off of its base and extract the base template from the mold.
4. Elevate the specimen. Place two sturdy metal blocks covered with cloth towels on the table approximately 2 inches apart. The gypsum block's long edges rest on the edges of the "towel blocks" so that the inclusions can be pushed through the gypsum and onto the table. First tap the long ends of the inclusions lightly with a hammer. Then turn the block over to hit the inclusions all the way through. Do this by using an instrument of smaller diameter than each inclusion and the hammer. (See figure B.9)

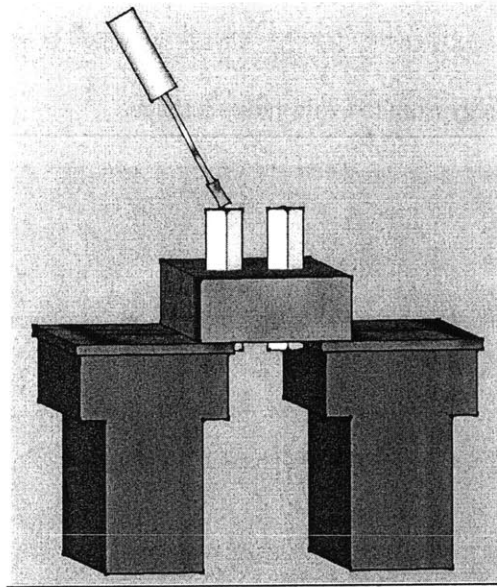


Figure B.9 - Elevated gypsum block

5. Clean excess grease from the specimen. Removing any excess grease while the specimen is drying prevents adverse effects around flaw openings.
6. Finally, sand the edges and sides of the gypsum block. Be careful not to chip the material at the corners. (See **Suggested Sanding Procedure**)
7. Label and date the prepared block in pencil. Place it into the 40°C oven. (Record the time upon placing it in the oven)

Clean the cast

1. Gently chisel large pieces of gypsum off of the insides of the cast. Try to use a blunter object when in direct contact with the surfaces so as not to nick the tape.
2. Smaller bits may be dissolved with a slightly dampened towel rubbed in the direction of the tape.

3. Be sure that the entire cast is smooth and wiped dry before you screw it back together securely.

***Keep in mind that a thin layer of gypsum may seep beneath each side of the cast. (See Figure B.10)*

3.3) Always removing the excess gypsum to avoid future leakage.

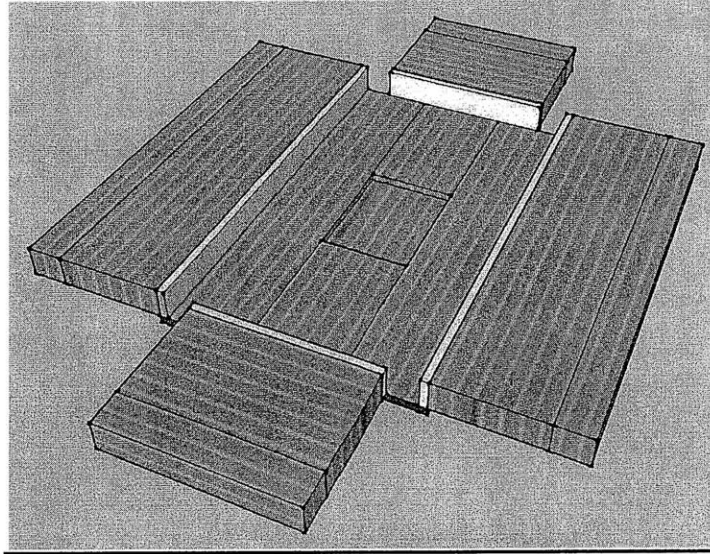


Figure B.10 - Cast with excess gypsum

B.4 Gypsum Preparation Considerations Using Shims

Often, specimen preparation involving shims is parallel to that of nylon inclusions. With regard to these specific considerations, however, additional measures must be taken to ensure efficient casting.

Uniform Thickness

Check before each mold that no material has gotten between the shim halves causing one end to be thicker than the other. Gypsum and other material can potentially build up between the two pieces of metal that make up the shim causing it to be thicker on one-side (See Figure B.11). This will cause the flaw aperture to be different for the front and back surfaces, as well as a different aperture for each of the two flaws.

Cleaning

Make sure to clean off each shim before greasing and placing in the mold. Many times the shims can have foreign particles stuck to them such as hardened gypsum. It is important to clean off the shims before greasing them for the next gypsum mold.

Greasing

Apply the correct amount of grease to the shims. Make sure not to add too much grease because it can cause pockets of gypsum not to form near the flaw surface, especially where it collects at the bottom surface of the specimen. Also, enough grease needs to be added so that the shims will not stick to the gypsum. Also, a quicker removal time will help prevent the shims from sticking to the gypsum (above). Add more grease if the shims in the hardening gypsum in order to remove them easier.

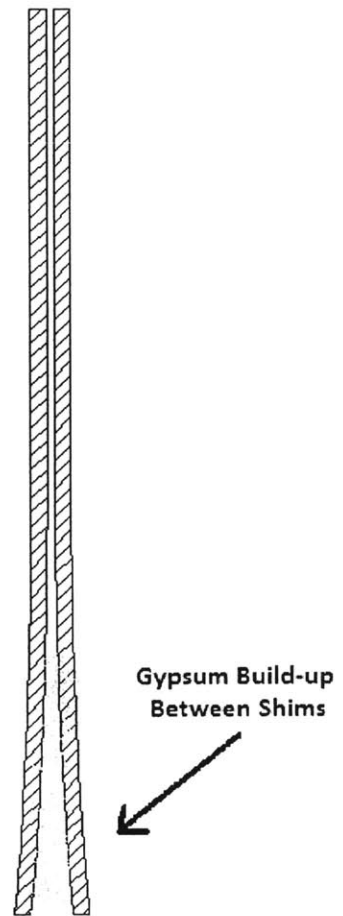


Figure B.11 – Shim Build-up

B.5 Suggested Sanding Procedure

***Prior to sanding any specimen, one must take precautions to ensure their health. Eye protection and masks covering the mouth and nose must be worn while sanding the specimens.*

Step 1: Pre - Hand sanding

Hand sand before machine sanding to remove any sharp edges that can be broken off by the orbit sander. Some specimens may have sharp pieces on the edges and flaws that cause larger pieces to be broken off if they are directly sanded with the orbital sander. (See Figure B.12)

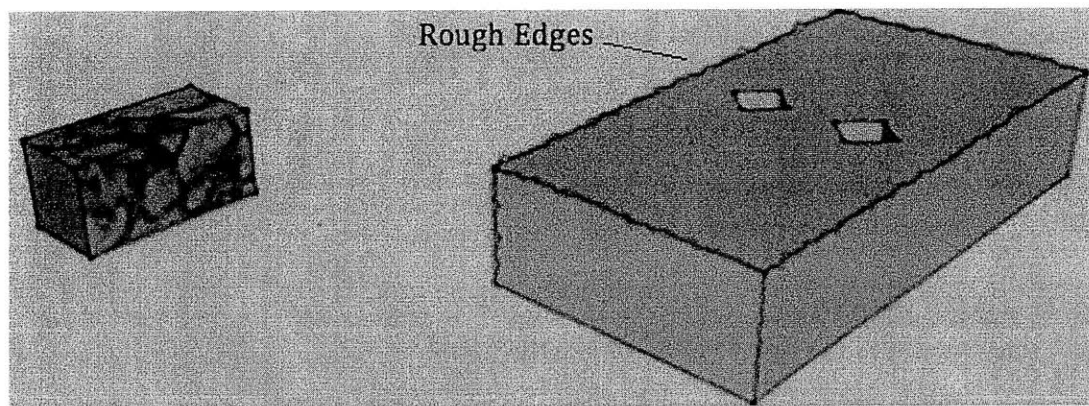


Figure B.12 – Pre Hand Sanding

Step 2: Machine Sanding (Orbital Sander)

Use the machine sander and guides to flatten all surfaces to create a prismatic specimen. (See Figure B.13)

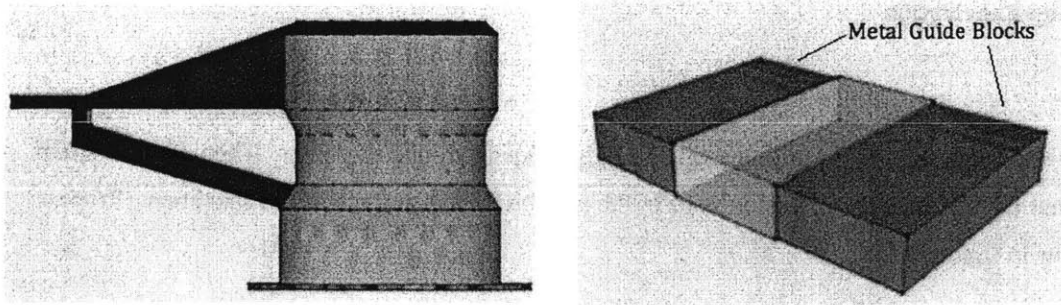


Figure B.13 – Machine (Orbital) Sander and Guide Blocks

Step 3: Post - Hand sanding

Hand sanding should be done after using the orbital sander to get a smooth surface. In order to get a level surface on the edges of the specimen since using the orbital sander can be very imprecise and sometimes lead to over-sanding small areas; hand sanding should be used to get very flat surfaces on the prismatic samples. (See Figure B.14)

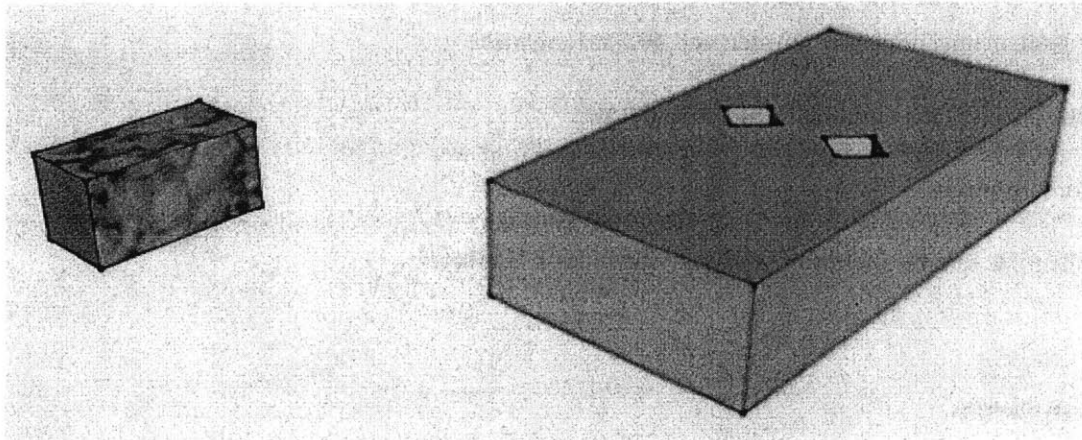


Figure B.14 – Post Hand Sanding

B.6 Inclusion Fabrication

Prepare the specimen for the inclusion casting by tightly taping around its center. Then, using a sharp blade, cut out the shape of the inclusion void in the tape on the top surface of the specimen. Process shown below in figure B.15

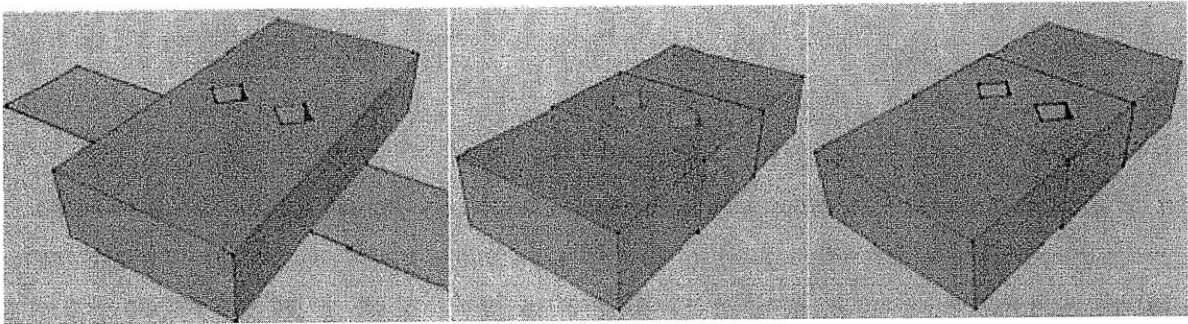


Figure B.15 - Preparing specimens for inclusion casting

Plaster Inclusions

1. Measure **60 grams** of plaster powder, and **40.5 mL** of water.
2. Pour the powder into a mixing bowl and add water.
3. Mix for **2 minutes**.
4. Pour the paste into the inclusion void and vibrate for **1 ½ minutes**.

Ultracal Inclusions

1. Measure **56 grams** of Ultracal[®] 30 powder and **19.0 mL** of water.
2. Pour the powder into a mixing bowl and add water.
3. Mix for **2 minutes**.

4. Pour the paste into the inclusion void and vibrate for **1 ½ minutes**.

The plaster paste will be a thicker consistency than that of the Ultracal[®] 30, however both pastes may need prodding to eliminate air bubbles. Use a thin rod (like a pencil) to pop potential air bubbles within the paste while vibrating.

It is also possible that after vibration, the paste will settle in the void beneath the surface of the specimen and it will be necessary to add paste before it dries.

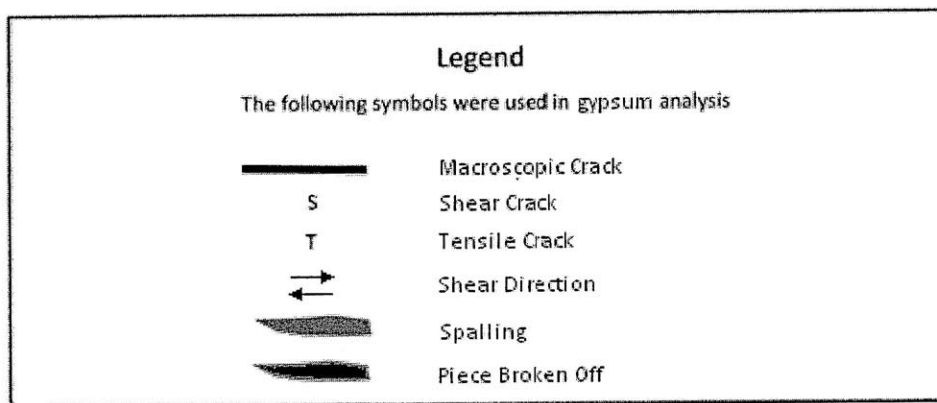
Once the inclusions solidify, remove the tape and gently chisel the extra material smooth at the surface of the specimen. Any remaining inclusion paste should be rubbed off of the specimen using a cloth towel.

****If any inclusion paste should be left behind to dry on the surface of the specimen, sanding will be much more difficult in the future. Be sure to keep the specimen surface as clean as possible before setting it inside the oven.**

APPENDIX C – Half-Inch Single Ellipse Inclusion Analysis

The following appendix section presents the most representative test repetitions for the single ellipse test series.

Legend Used:

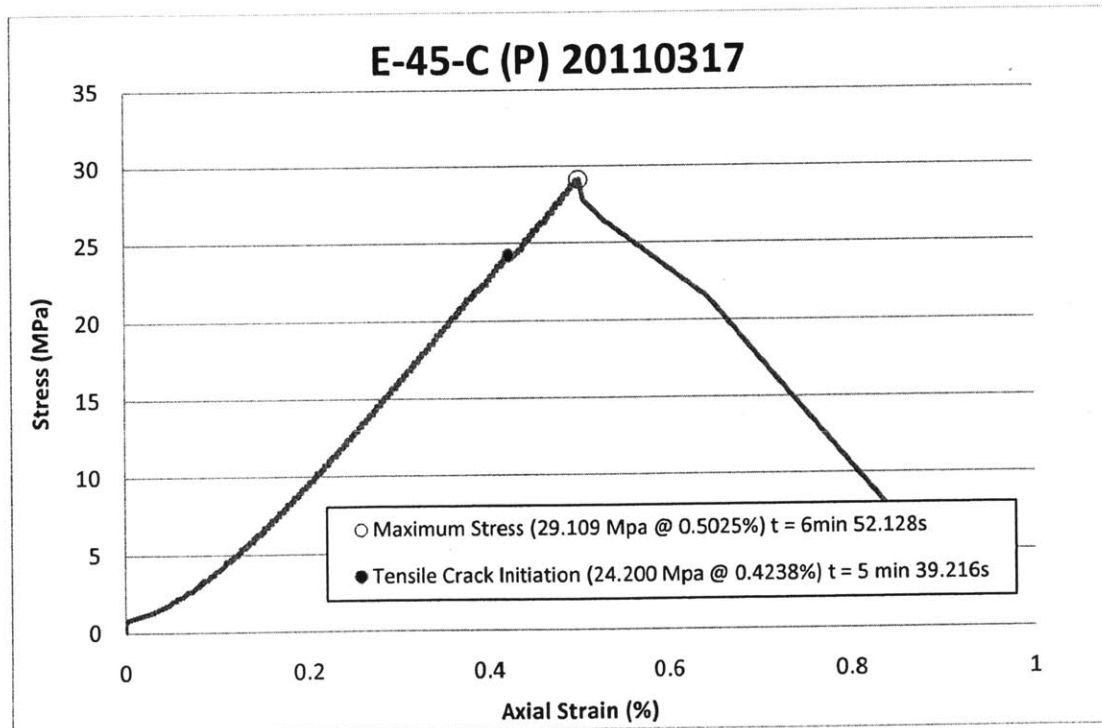
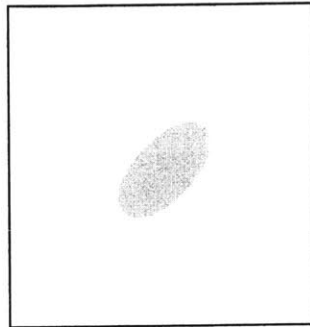




Notes:

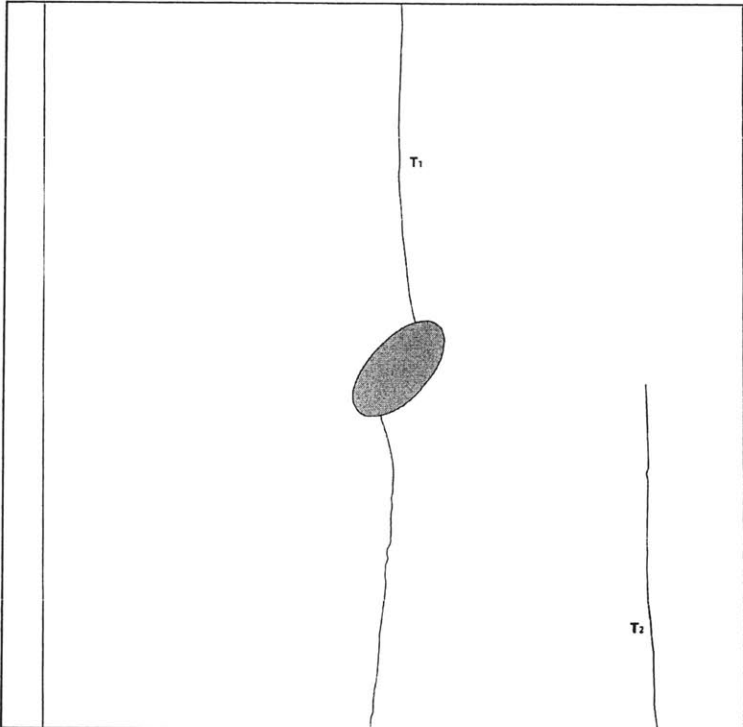
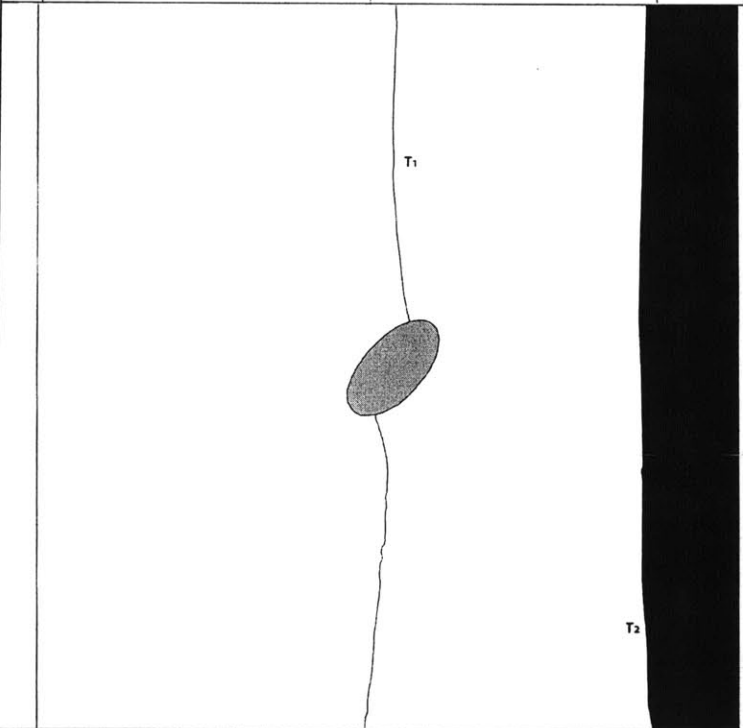
- Subscripts which do not indicate sequence are noted in the description.
- Times and stresses correlate to when the picture was taken, not when the events happened.
- Shear cracks with an arrow indicate the direction of shear crack development. Shear cracks without an arrow denote cracks in which the direction could not be determined.

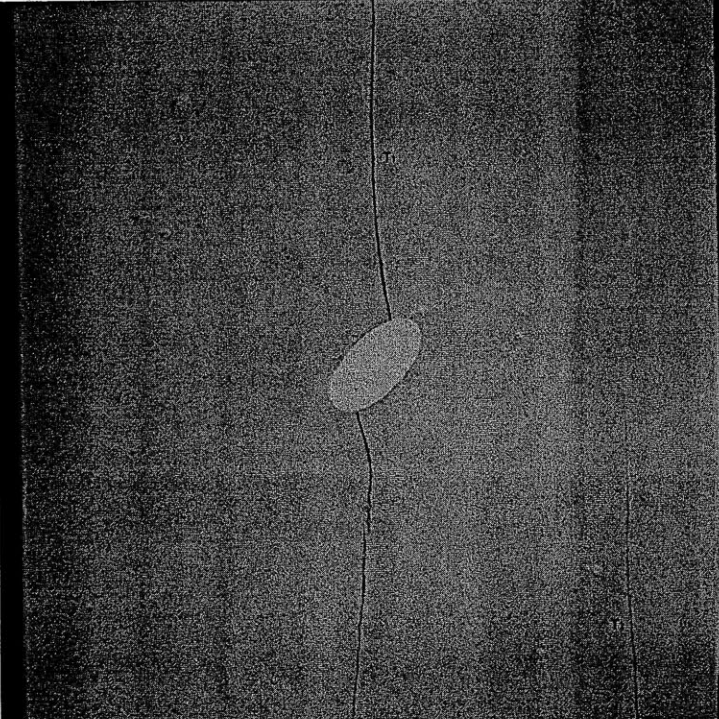
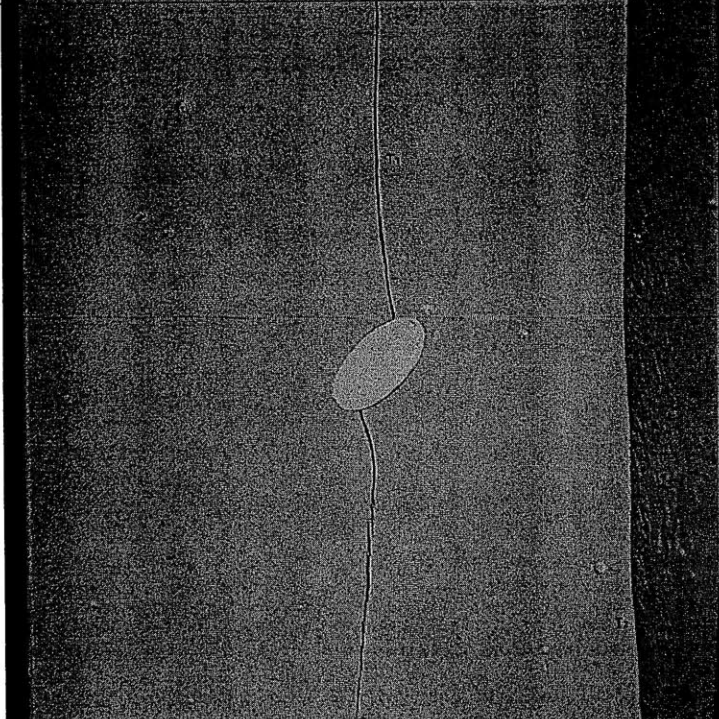
E-45-Cp

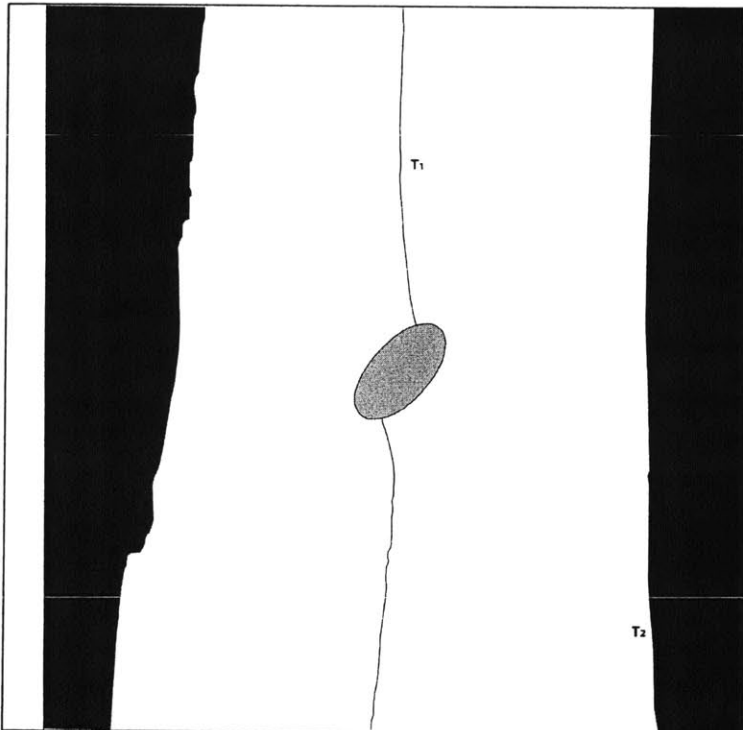
Shape = Ellipse
Inclination = 45°
Test Repetition = C
Material = Plaster
Size = 1/2" (major axis) – 1/4" (minor axis)



	<p>Time: 0m 0s σ: ~0 MPa</p> <p>Picture taken prior to testing.</p> <p>0</p>
	<p>Time: 0m 0s σ: ~0 MPa</p> <p>Picture taken prior to testing.</p> <p>0</p>

	<p>Time: 5m 39.216s σ: 24.200 MPa</p> <p>Tensile Crack Initiation</p> <p>Still image captured with High Speed Camera before High Speed Recording.</p> <p>Tension crack T_1 forms above, below, and along the inclusion interface (complete debonding). T_2 forms on the bottom right side of the specimen.</p> <p style="text-align: right;">1</p>
	<p>Time: 6m 51.344s σ: ~29.052 MPa</p> <p>Frame 4323 of the High Speed Camera footage.</p> <p>T_2 extends up to the top of the specimen and a piece breaks off of the right side of the specimen.</p> <p style="text-align: right;">2</p>

	<p>Time: 5m 39.216s σ: 24.200 MPa</p> <p>Tensile Crack Initiation</p> <p>Still image captured with High Speed Camera before High Speed Recording.</p> <p>1</p>
	<p>Time: 6m 51.344s σ: ~29.052 MPa</p> <p>Frame 4323 of the High Speed Camera footage.</p> <p>2</p>

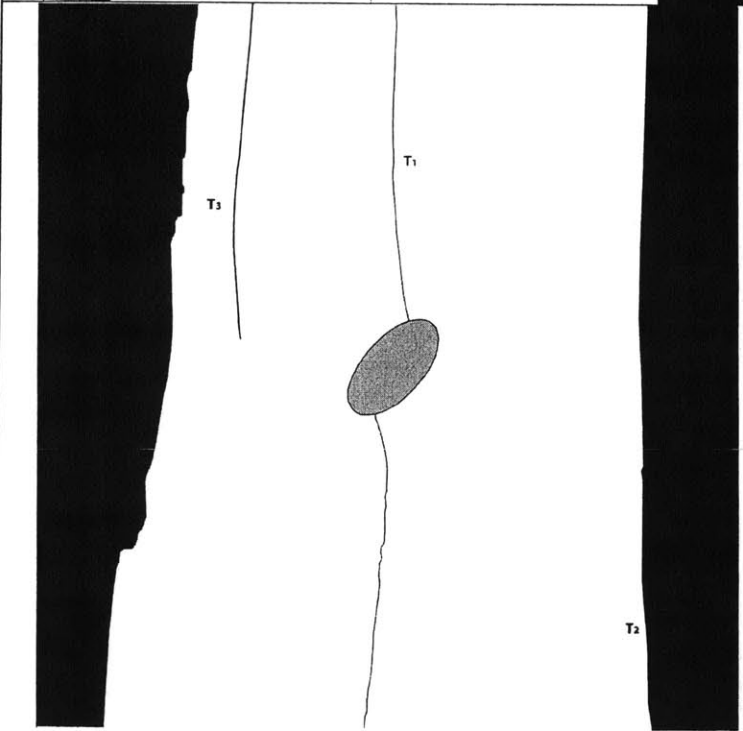


Time: 6m 52.026s
 σ : ~29.102 MPa

Frame 915 of the High Speed Camera footage.

A large piece breaks off of the left side of the specimen. T₁ widens.

3

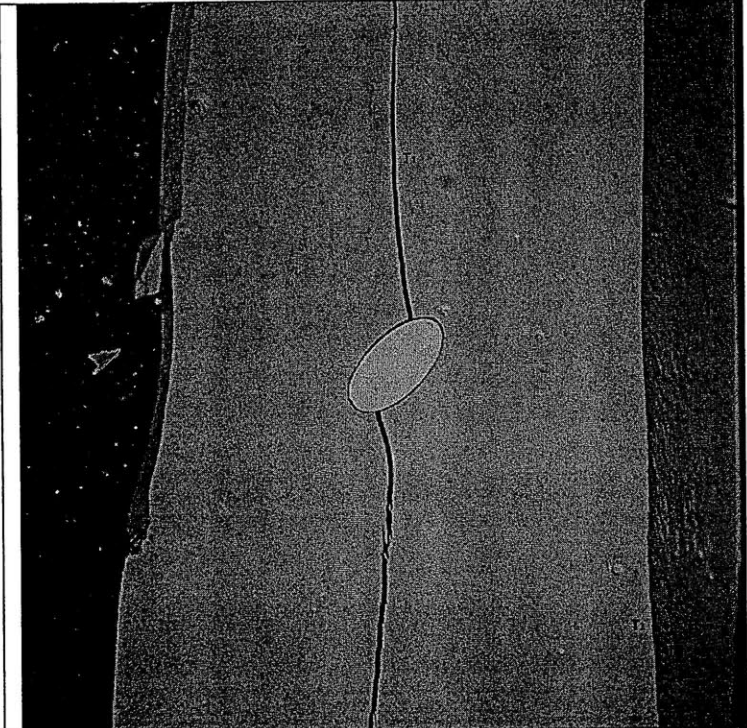
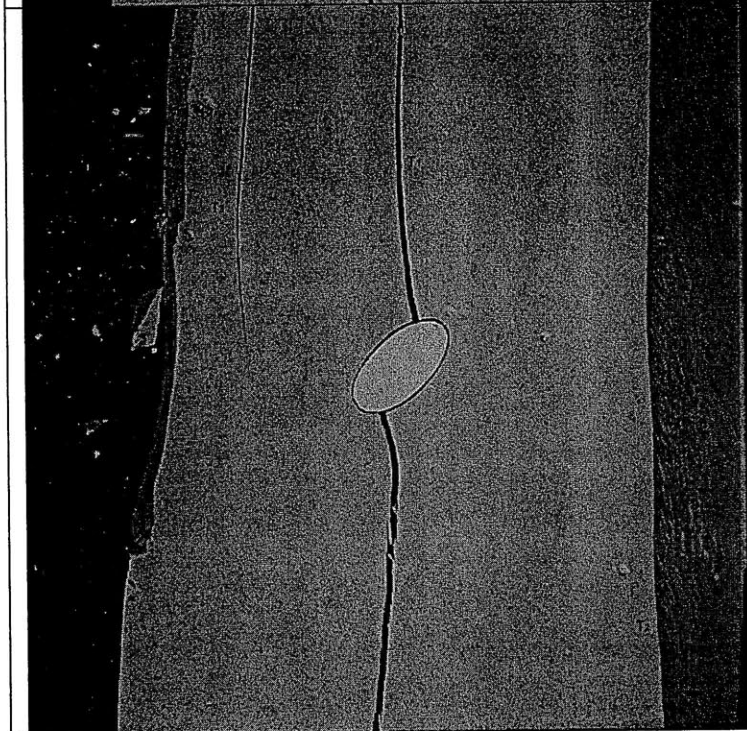


Time: 6m 52.038s
 σ : ~29.102 MPa

Frame 854 of the High Speed Camera footage.

T3 forms at the top left side of the specimen and extends downward. T₁ widens slightly.

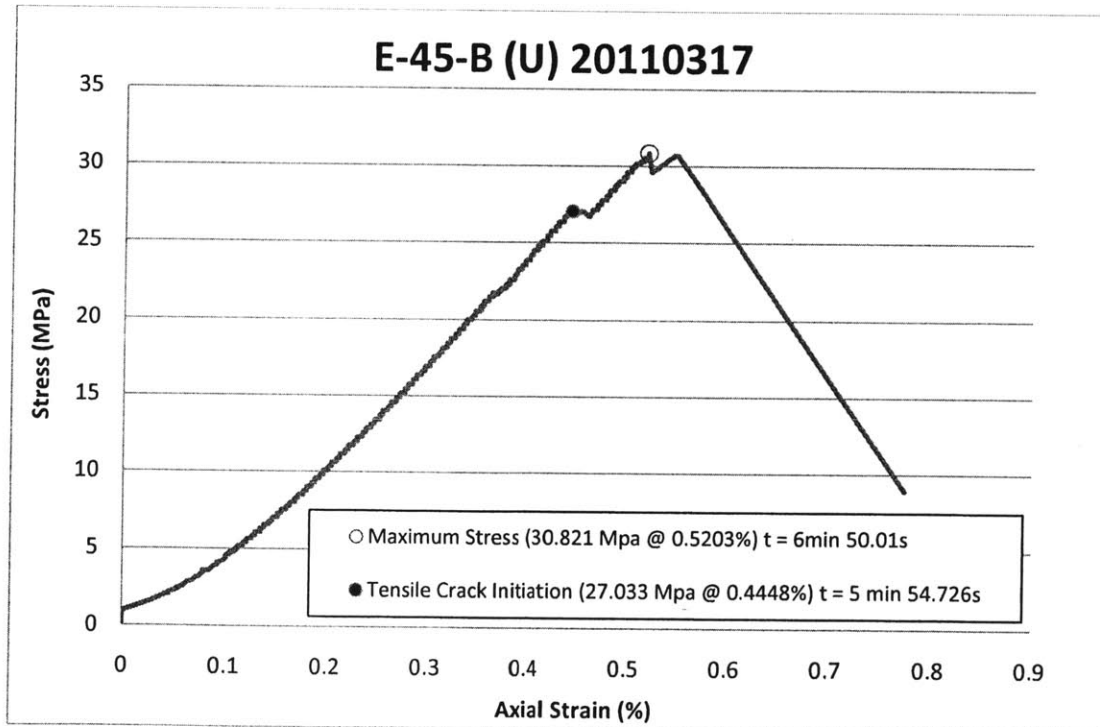
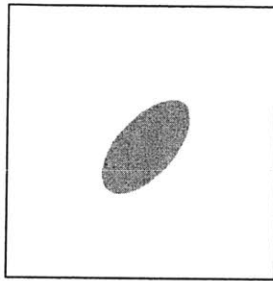
4

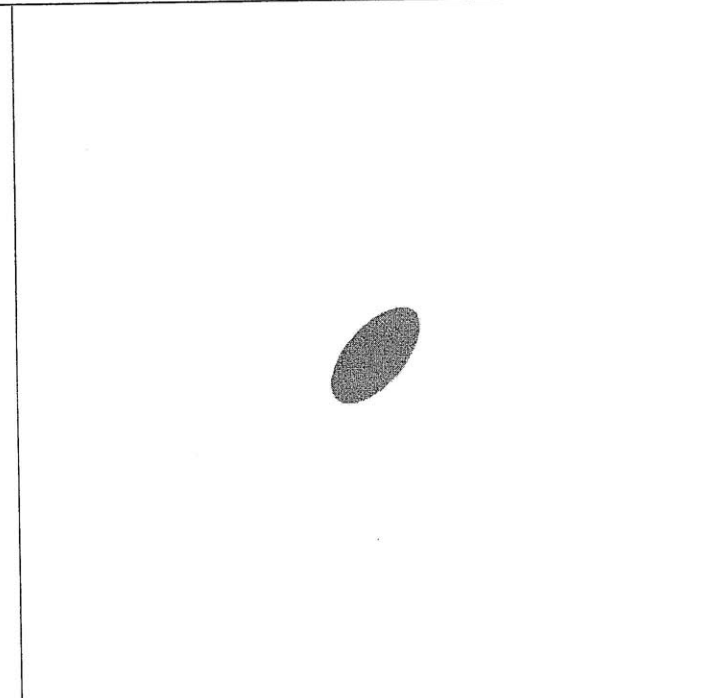
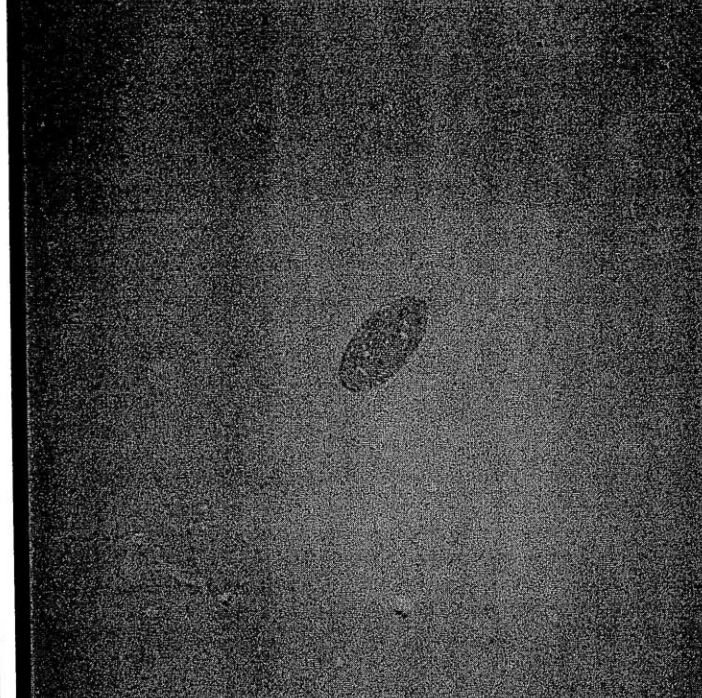
	<p>Time: 6m 52.026s σ: ~29.102 MPa</p> <p>Frame 915 of the High Speed Camera footage.</p> <p>3</p>
	<p>Time: 6m 52.038s σ: ~29.102 MPa</p> <p>Frame 854 of the High Speed Camera footage.</p> <p>4</p>

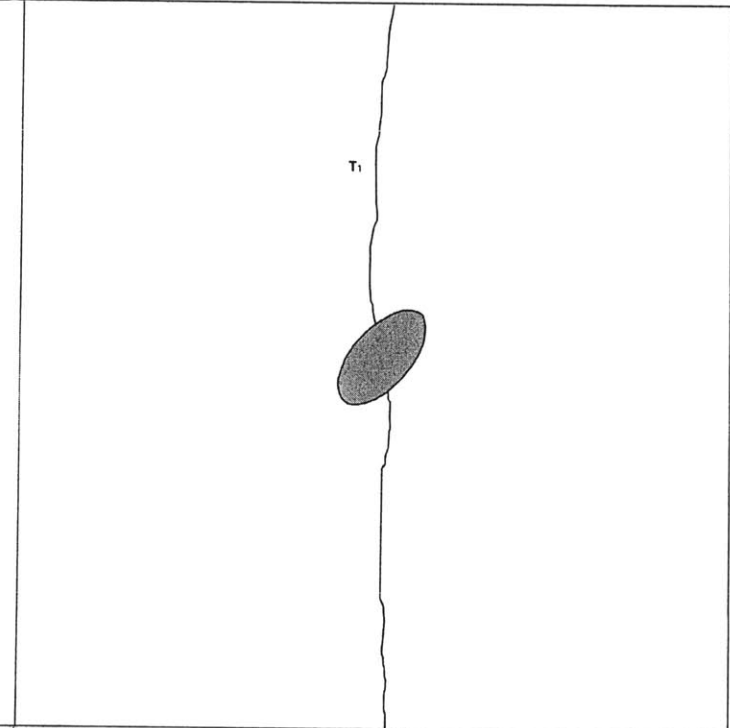
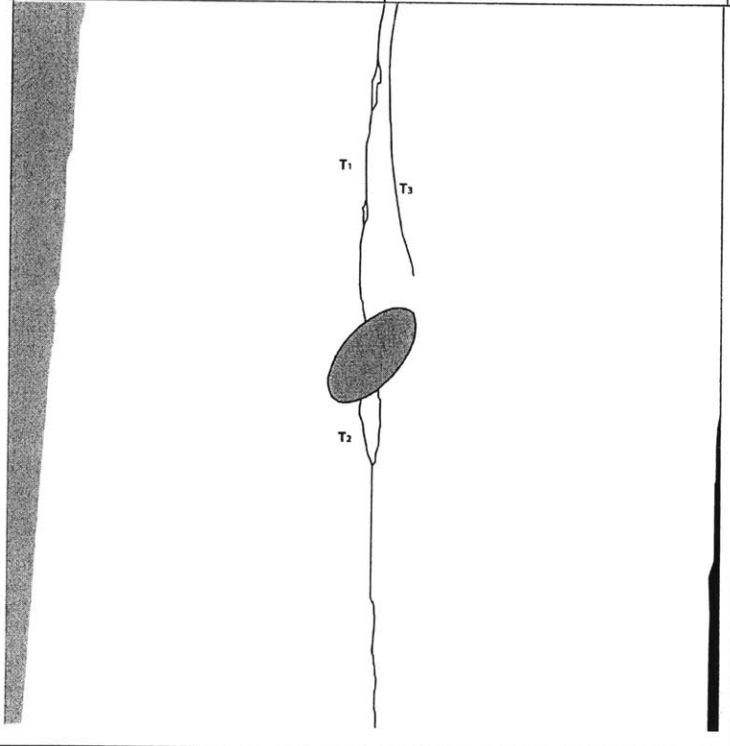
Ultracal

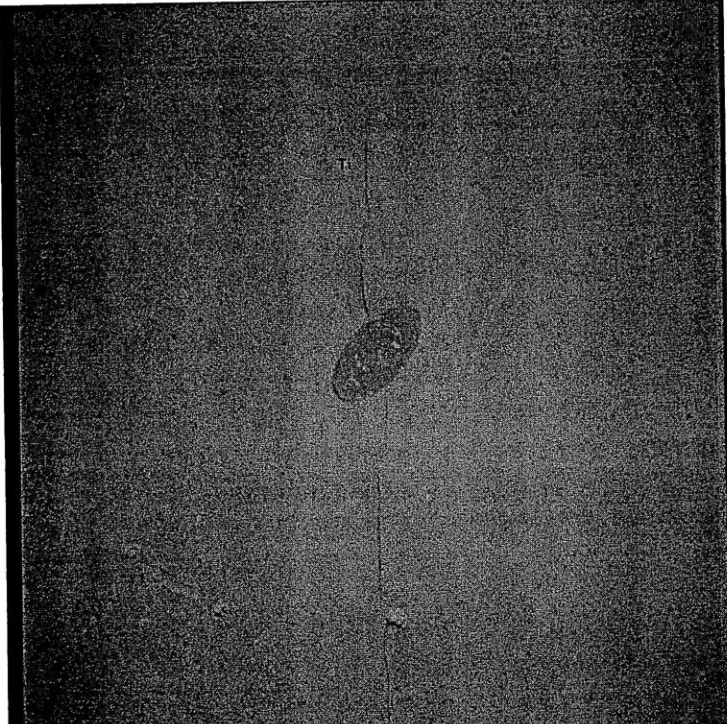
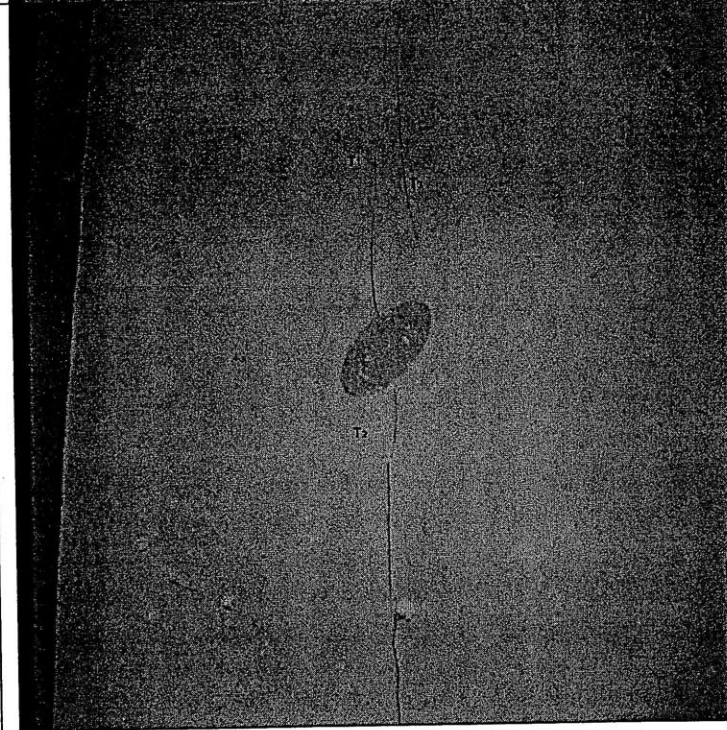
E-45-Bu

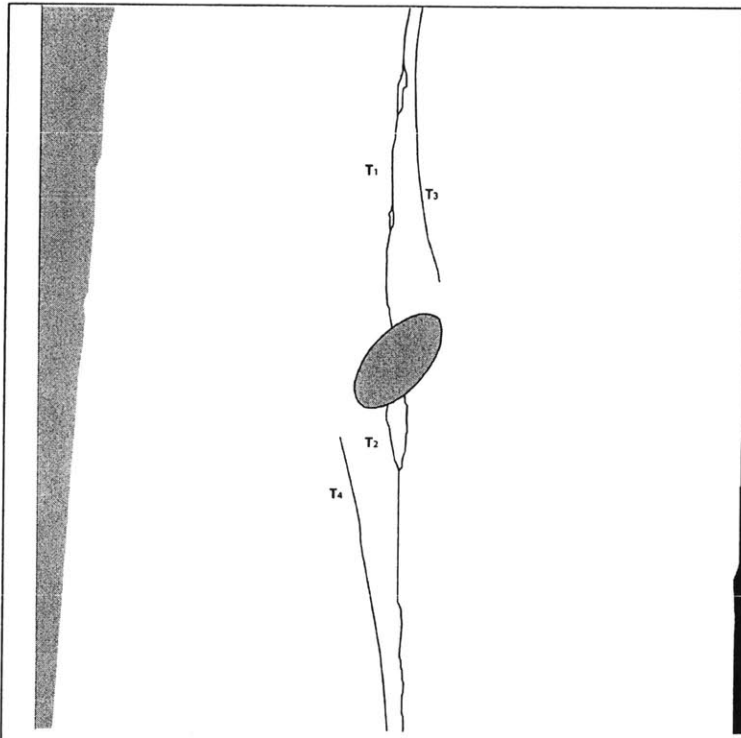
Shape = Ellipse
Inclination = 45°
Test Repetition = B
Material = Ultracal
Size = 1/2" (major axis) – 1/4" (minor axis)



	<p>Time: 0m 0s σ: ~0 MPa</p> <p>Picture taken prior to testing.</p> <p>0</p>
	<p>Time: 0m 0s σ: ~0 MPa</p> <p>Picture taken prior to testing.</p> <p>0</p>

	<p>Time: 5m 54.726s σ: ~27.033 MPa</p> <p>Tensile Crack Initiation</p> <p>Still image captured with High Speed Camera before High Speed Recording.</p> <p>T1 form above, below, and along the inclusion interface (complete tensile debonding).</p> <p style="text-align: right;">1</p>
	<p>Time: 5m 55.920s σ: ~27.096 MPa</p> <p>Still image captured with High Speed Camera before High Speed Recording.</p> <p>(Before high speed images. New cracks not number in a chronological order)</p> <p>T₂ forms below the inclusion, between the bottom inclusion interface and T₁. T₃ forms to the right of T₁. A piece breaks off the left edge of the specimen.</p> <p style="text-align: right;">2</p>

 A grayscale still image showing a vertical crack in a material specimen. The crack is slightly wider at the top and tapers towards the bottom. The surrounding material has a grainy texture.	<p>Time: 5m 54.726s σ: ~27.033 MPa</p> <p>Tensile Crack Initiation</p> <p>Still image captured with High Speed Camera before High Speed Recording.</p> <p>1</p>
 A grayscale still image showing a vertical crack in a material specimen, similar to the one above. The crack is slightly wider at the top and tapers towards the bottom. The surrounding material has a grainy texture.	<p>Time: 5m 55.920s σ: ~27.096 MPa</p> <p>Still image captured with High Speed Camera before High Speed Recording.</p> <p>2</p>

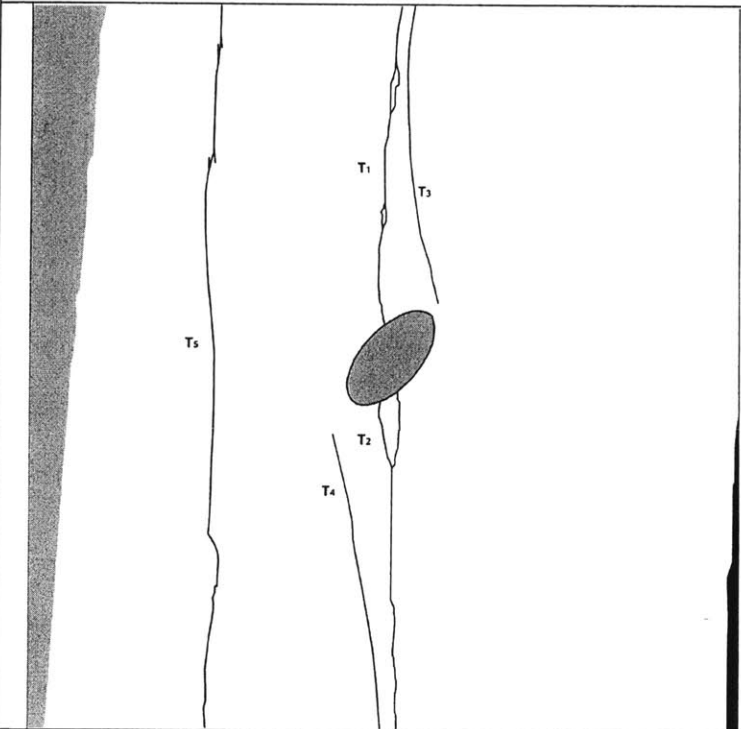


Time: 6m 43.236s
 σ : ~30.358 MPa

Still image captured with High Speed Camera before High Speed Recording

T₄ forms below the inclusion to the left of T₁ and T₂.

3

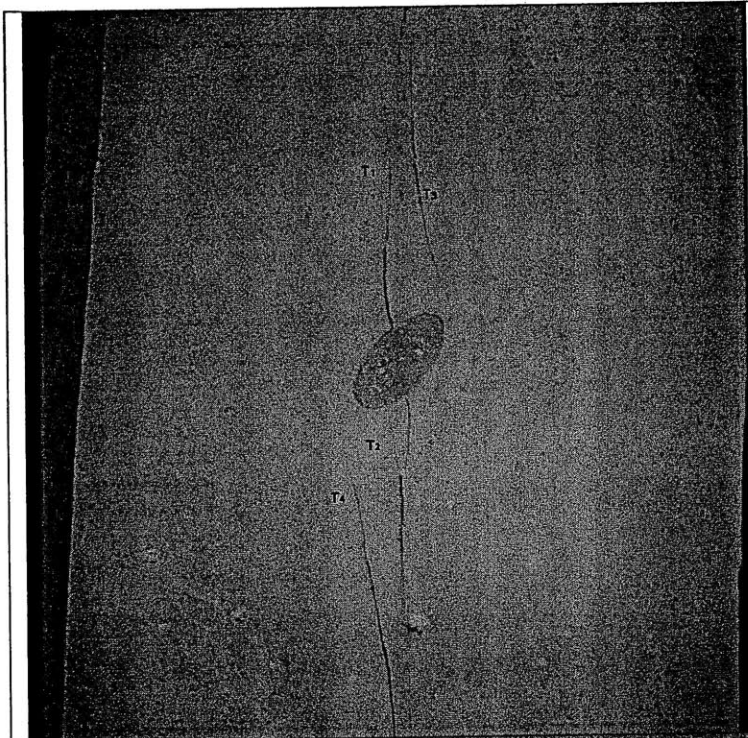


Time: 6m 49.561s
 σ : ~30.791 MPa

Frame 2700 of the High Speed Camera footage.

Tension crack T₅ forms at the top of the specimen and extends down to the bottom.

4



Time: 6m 43.236s
 σ : ~30.358 MPa

Still image captured with High Speed Camera before High Speed Recording

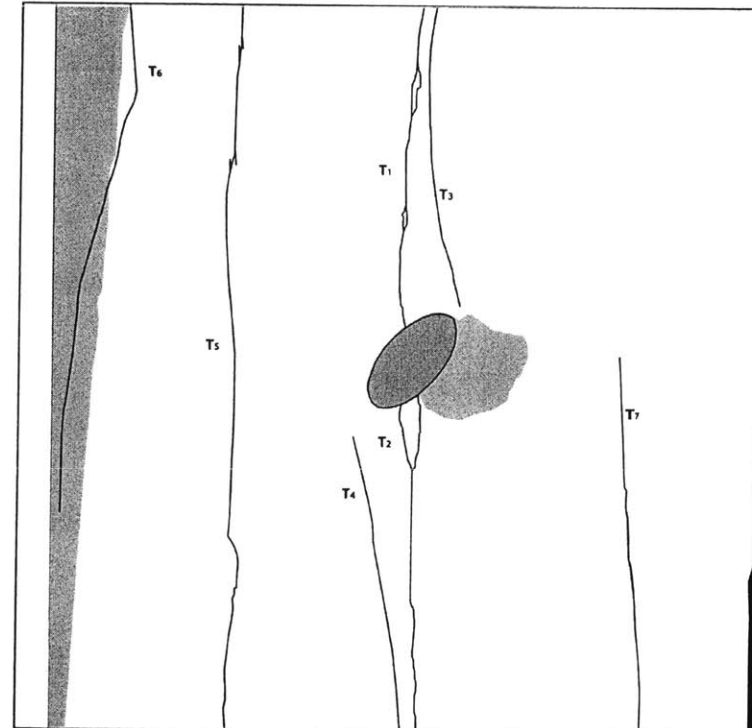
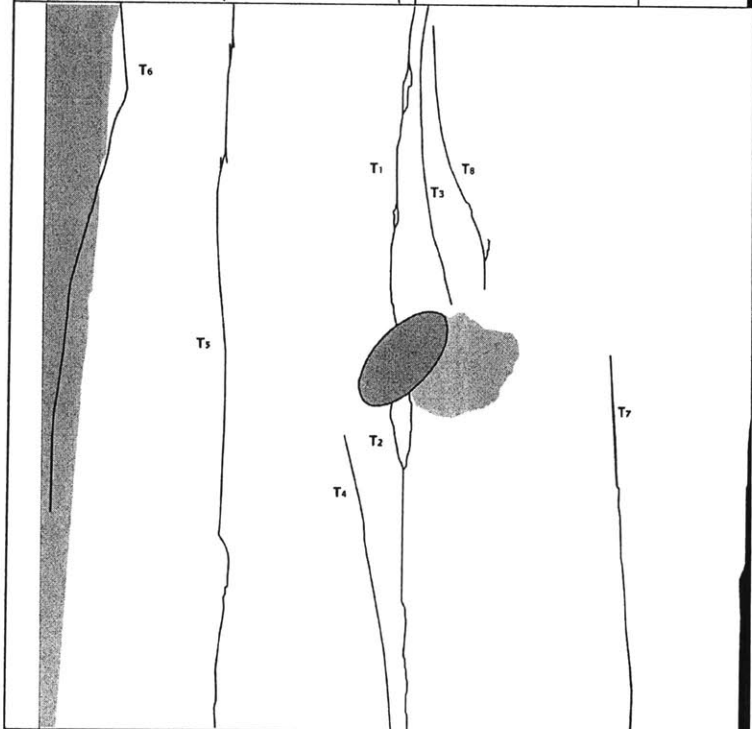
3

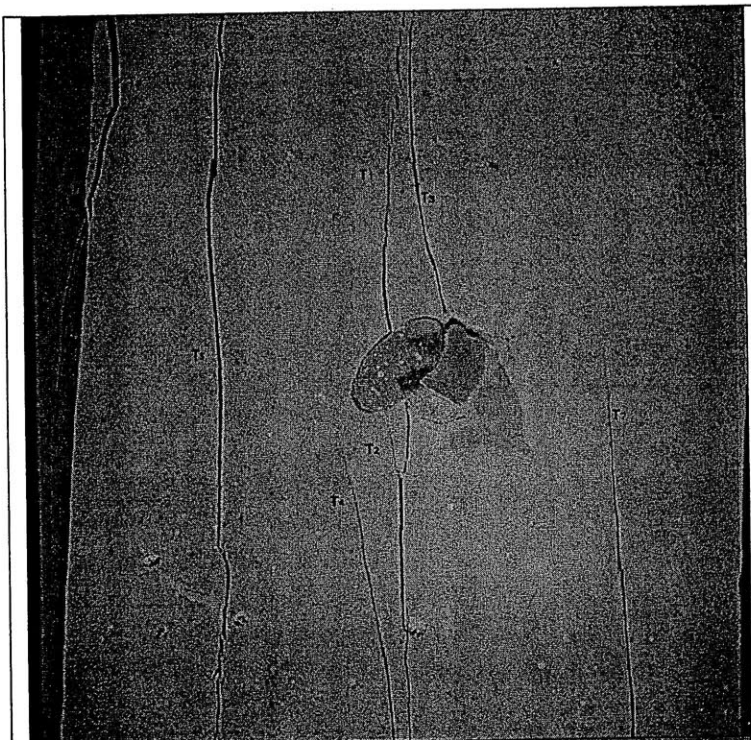


Time: 6m 49.561s
 σ : ~30.791 MPa

Frame 2700 of the High Speed Camera footage.

4

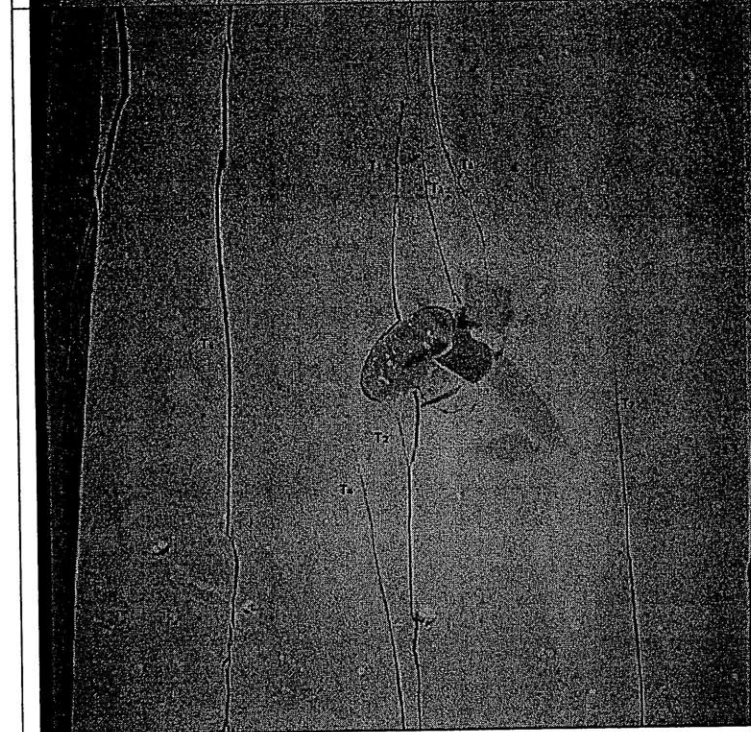
	<p>Time: 6m 49.948s σ: ~30.812 MPa</p> <p>Frame 767 of the High Speed Camera footage.</p> <p>T₆ forms at the top of the specimen and extends downward along the left side of the specimen. T₇ forms at the bottom right side of the specimen and extends upward along the right side. Spalling occurs on the surface to the right of the inclusion. T₁ widens.</p> <p style="text-align: right;">5</p>
	<p>Time: 6m 49.951s σ: ~30.812 MPa</p> <p>Frame 752 of the High Speed Camera footage.</p> <p>T₈ forms to the right of T₃.</p> <p style="text-align: right;">6</p>



Time: 6m 49.948s
 σ : ~30.812 MPa

Frame 767 of the High Speed Camera footage.

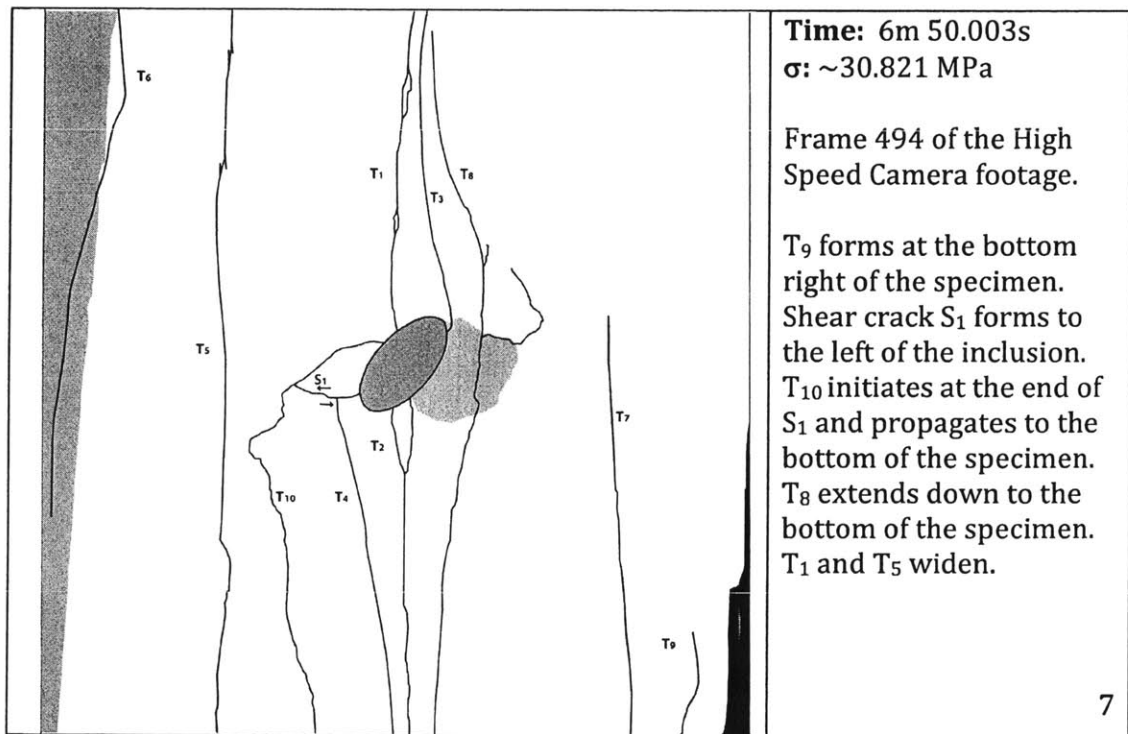
5



Time: 6m 49.951s
 σ : ~30.812 MPa

Frame 752 of the High Speed Camera footage.

6

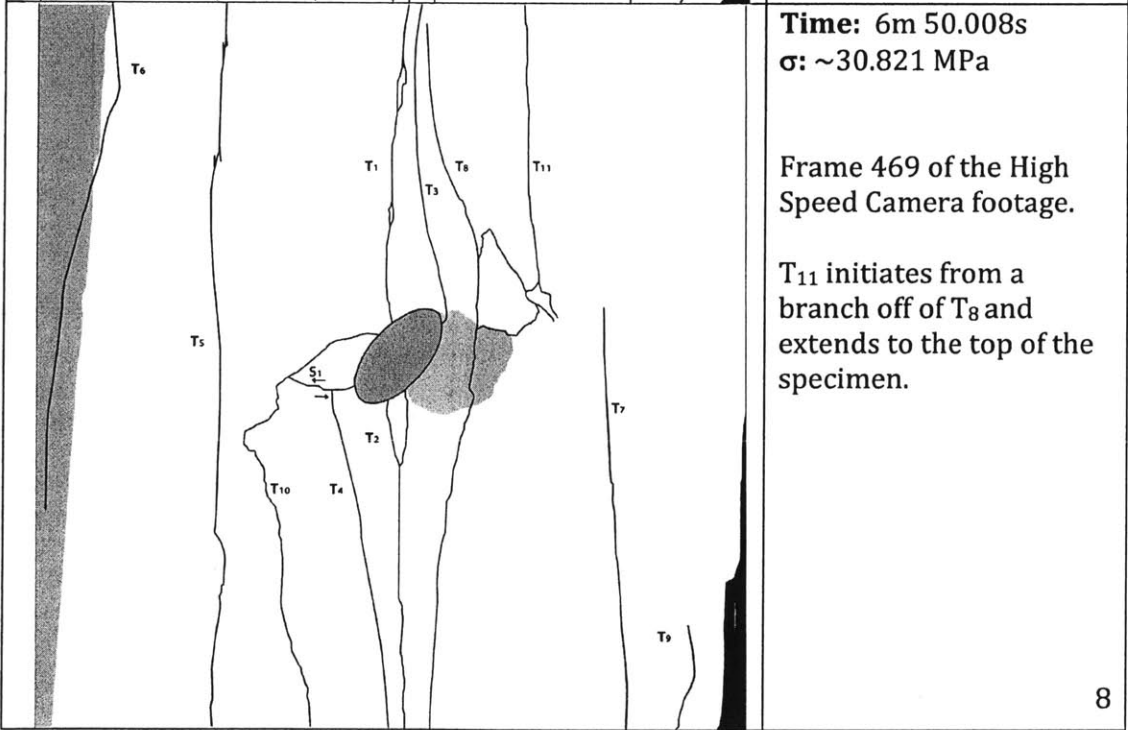


Time: 6m 50.003s
 σ : ~30.821 MPa

Frame 494 of the High Speed Camera footage.

T₉ forms at the bottom right of the specimen. Shear crack S₁ forms to the left of the inclusion. T₁₀ initiates at the end of S₁ and propagates to the bottom of the specimen. T₈ extends down to the bottom of the specimen. T₁ and T₅ widen.

7

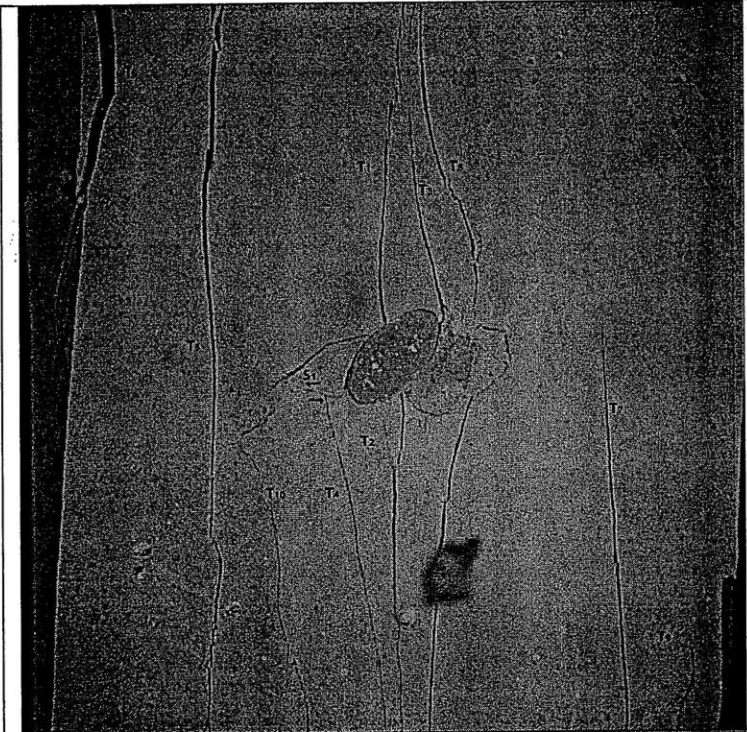


Time: 6m 50.008s
 σ : ~30.821 MPa

Frame 469 of the High Speed Camera footage.

T₁₁ initiates from a branch off of T₈ and extends to the top of the specimen.

8



Time: 6m 50.003s
 σ : ~30.821 MPa

Frame 494 of the High Speed Camera footage.

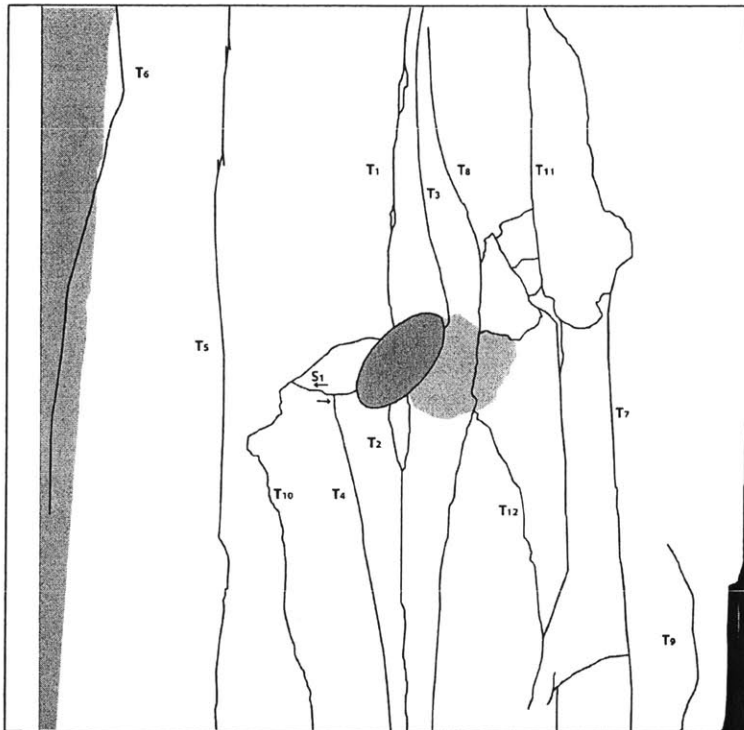
7



Time: 6m 50.008s
 σ : ~30.821 MPa

Frame 469 of the High Speed Camera footage.

8



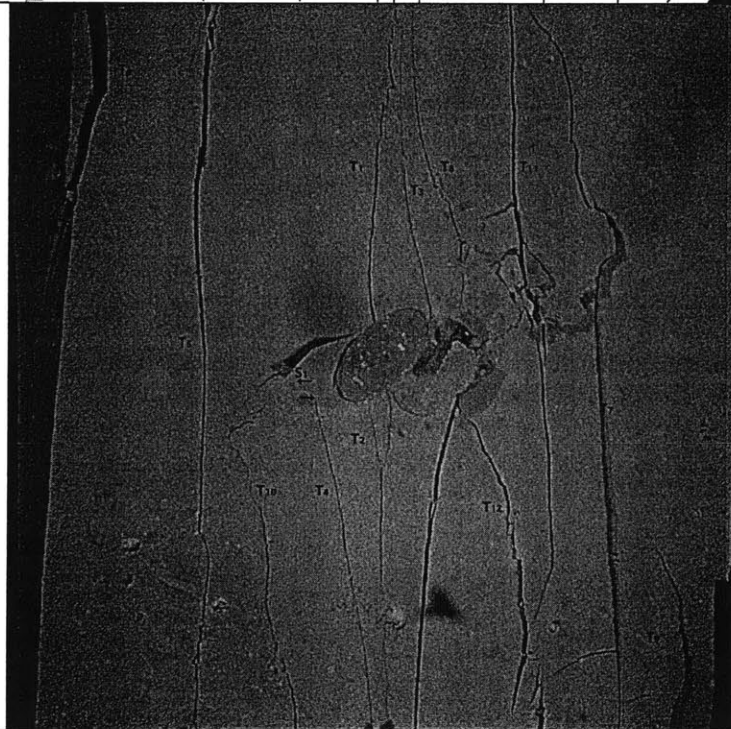
Time: 6m 50.010s
 σ : ~30.821 MPa

FAILURE

Frame 459 of the High Speed Camera footage.

T₇ extends to the top of the specimen. T₁₁ extends down toward the bottom of the specimen. T₁₁ connects with T₁₂, which initiates off of T₈ and extends downward.

9



Time: 6m 50.010s
 σ : ~30.821 MPa

FAILURE


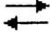


Frame 459 of the High Speed Camera footage.

9

APPENDIX D – Half-Inch Hexagon Inclusion Pair Analysis

The following appendix section presents the most representative test repetitions for the hexagon pair test series.

Legend Used:

Legend	
The following symbols were used in gypsum analysis	
	Macroscopic Crack
S	Shear Crack
T	Tensile Crack
	Shear Direction
	Spalling
	Piece Broken Off

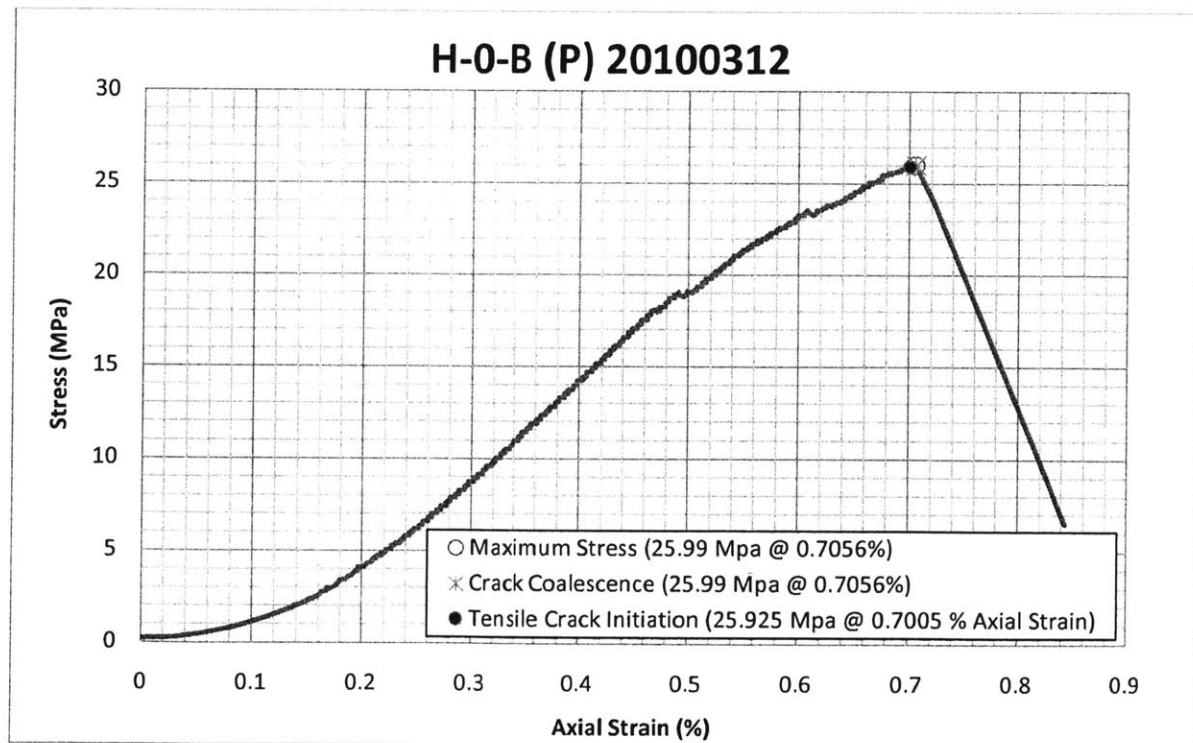
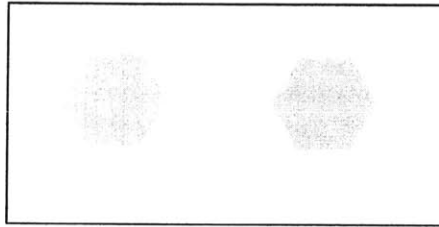
Notes:


- Subscripts which do not indicate sequence are noted in the description.
- Times and stresses correlate to when the picture was taken, not when the events happened.
- Shear cracks with an arrow indicate the direction of shear crack development. Shear cracks without an arrow denote cracks in which the direction could not be determined.

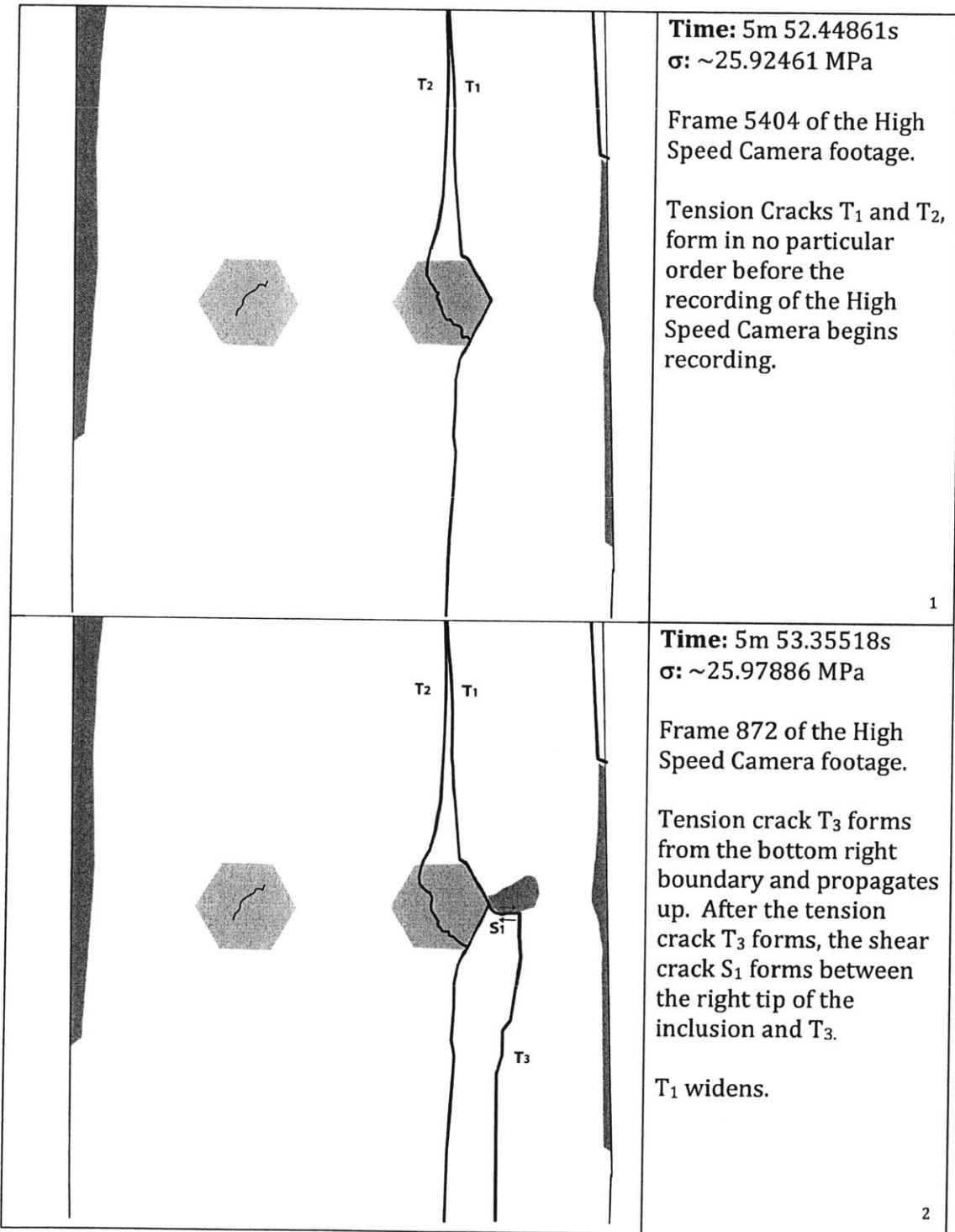
PLASTER

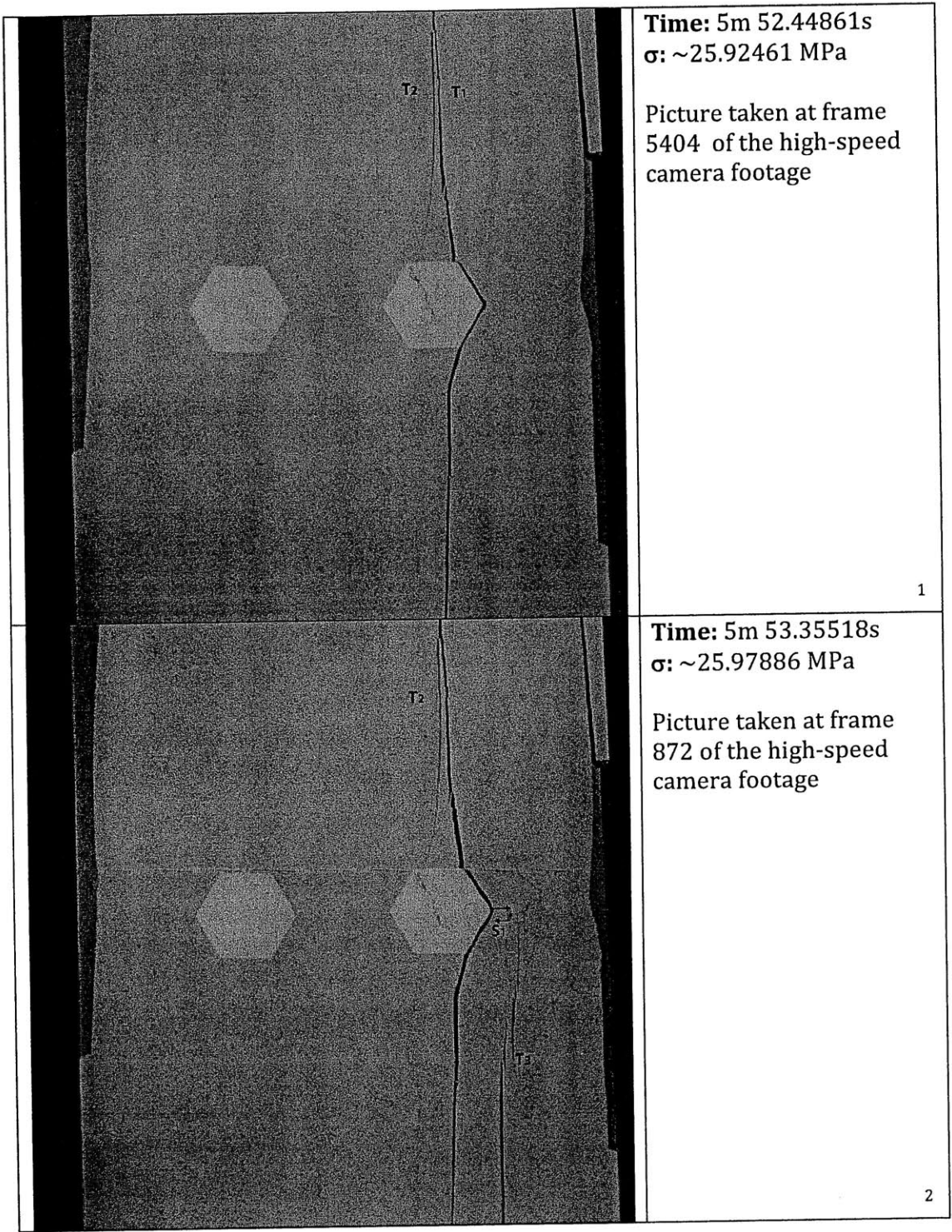
H-0-Bp

Shape = Hexagon
(Inclination = 0°)
Bridging Angle = 0°
Test Repetition = B
Material = Plaster
Size = 1/2"



		<p>Time: 0m 0s σ: ~0 MPa</p> <p>Picture taken prior to testing.</p> <p>Surface Cracks can be seen on both inclusions.</p>
--	---	---





Time: 5m 52.44861s
 σ : ~25.92461 MPa

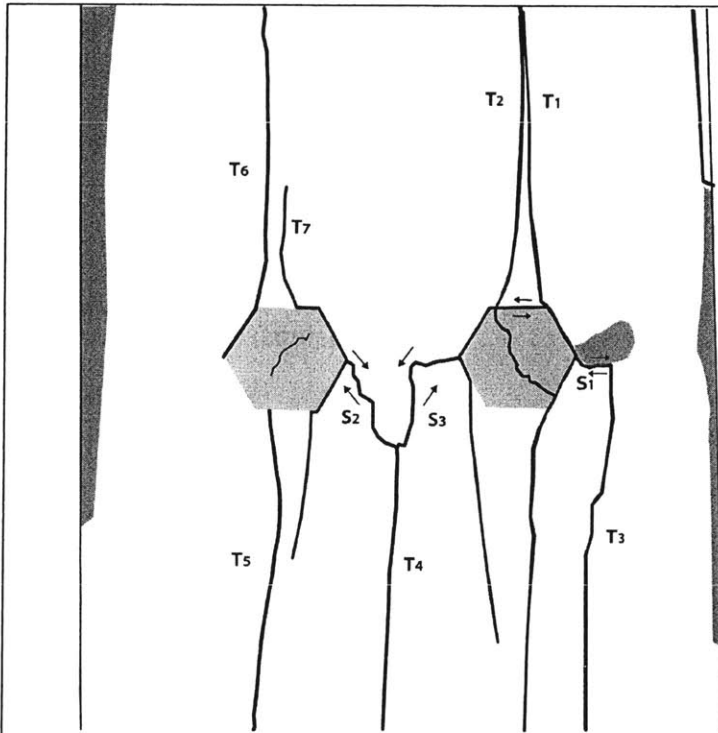
Picture taken at frame 5404 of the high-speed camera footage

1

Time: 5m 53.35518s
 σ : ~25.97886 MPa

Picture taken at frame 872 of the high-speed camera footage

2



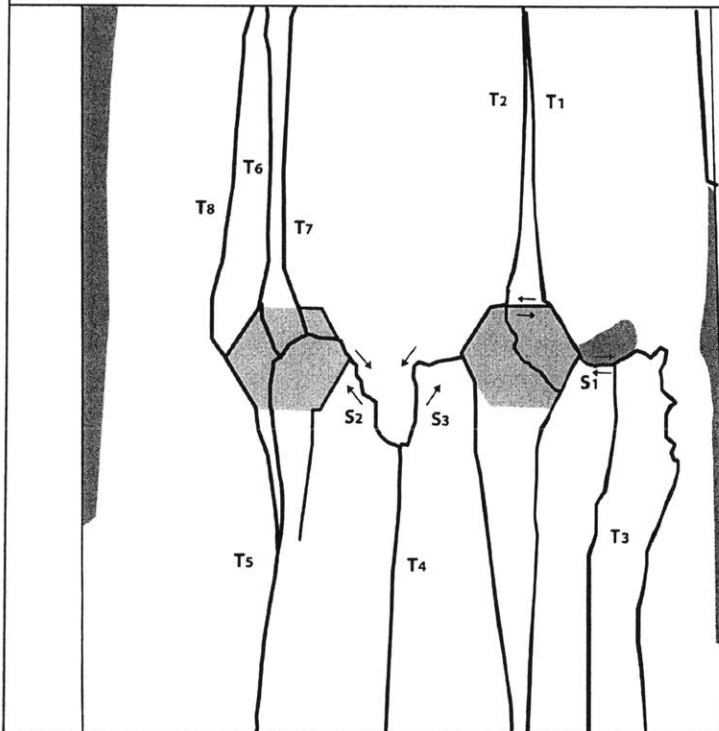
Time: 5m 53.4614s
 σ : ~25.98971 MPa

Frame 341 of the High Speed Camera footage.

COALESCENCE

Tension cracks T₄, T₅ and T₆ form simultaneously from the specimen boundaries and move inward. After these tension cracks form shear cracks S₂ and S₃ propagate from the tip of T₄ and move toward the inclusion edges. As S₂ and S₃ form, T₂ extends down past the left side of the right inclusion.

3



Time: 5m 53.478s
 σ : ~25.98971 MPa

Frame 258 of the High Speed Camera footage.

FAILURE

T₂ and T₇ extend to the ends of the specimen. Tension Cracks T₅ and T₆ extend and connect together. T₈ forms from the specimen boundary and moves down to the left tip of the left inclusion.

T₅ and T₁ widen.

4



Time: 5m 53.4614s
 σ : ~25.98971 MPa

Picture taken at frame 341 of the high-speed camera footage.

Falling pieces can be seen between T₆ and T₂ above the inclusions.



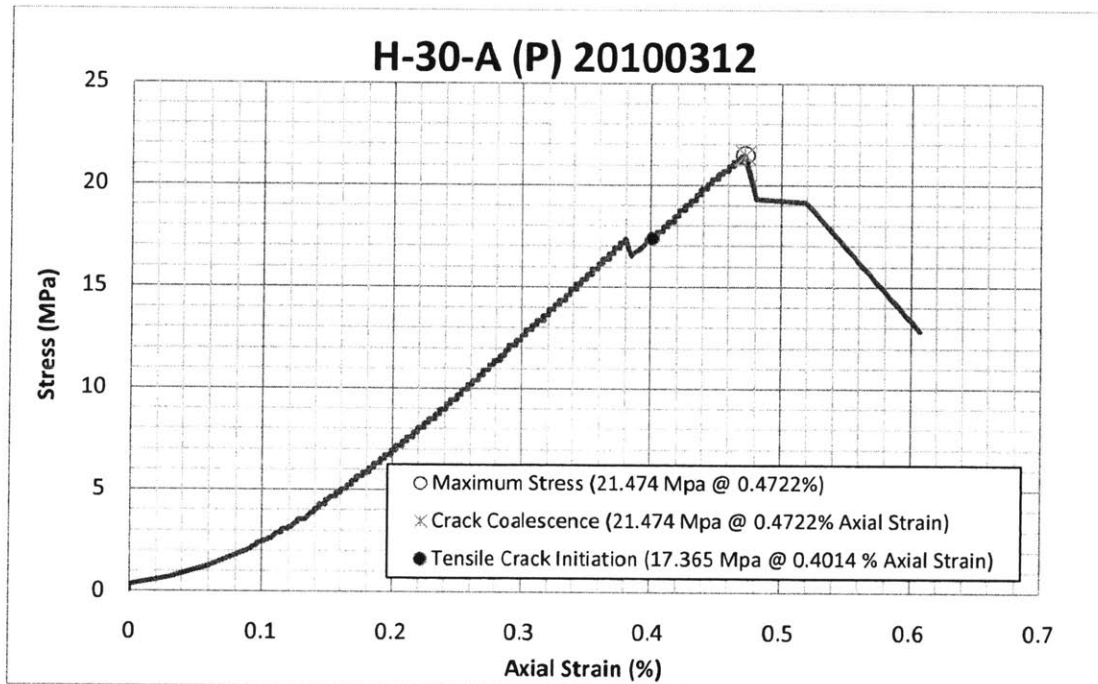
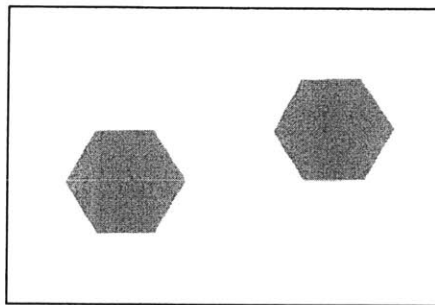
Time: 5m 53.478s
 σ : ~25.98971 MPa

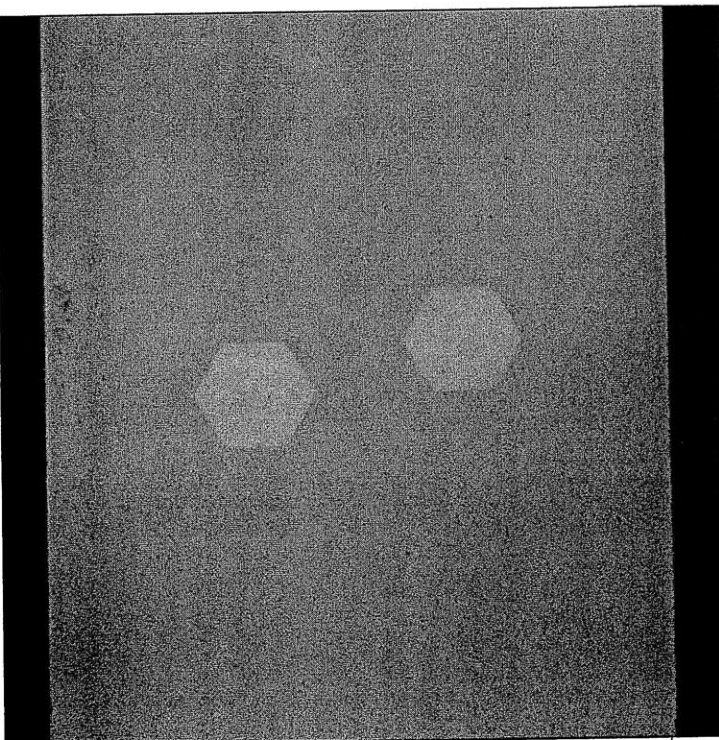
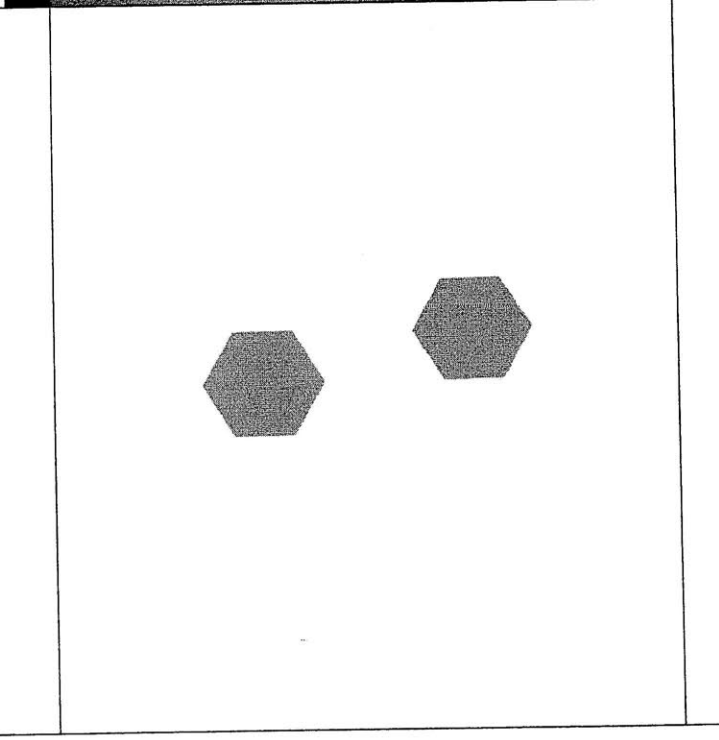
Picture taken at frame 258 of the high-speed camera footage.

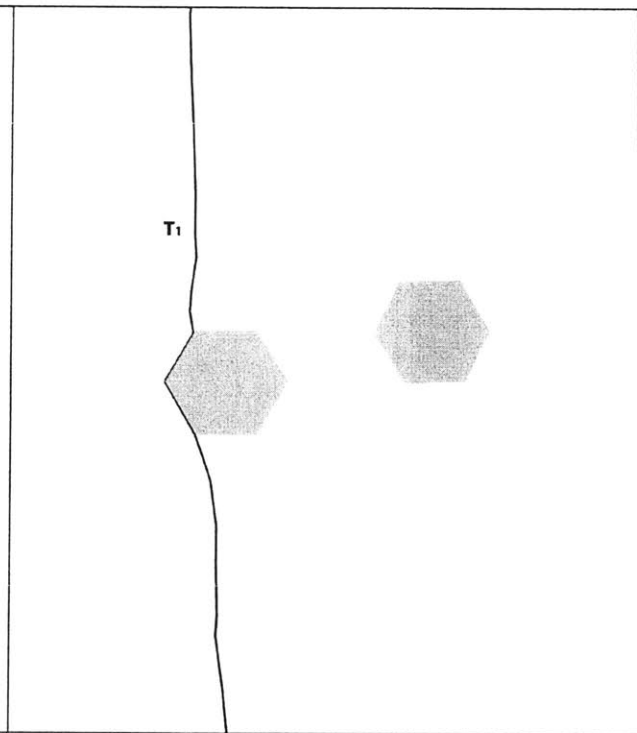
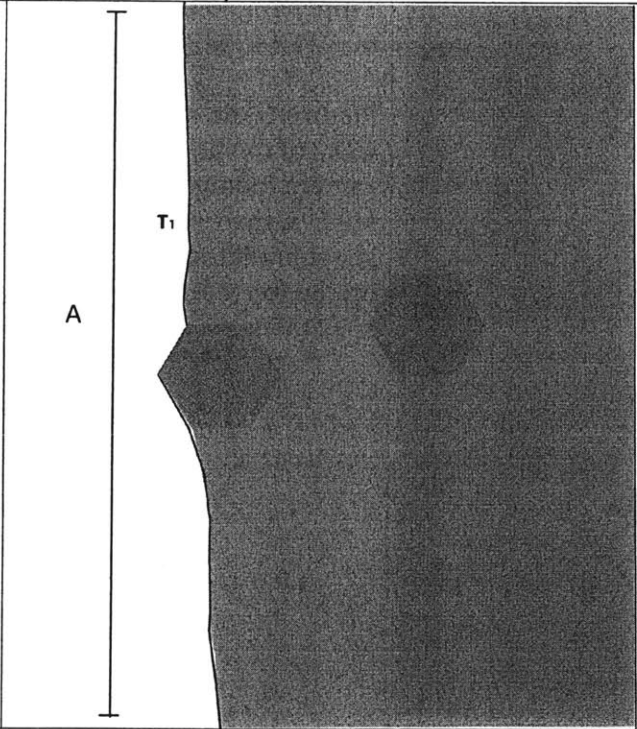
Falling pieces can be seen between the inclusions.

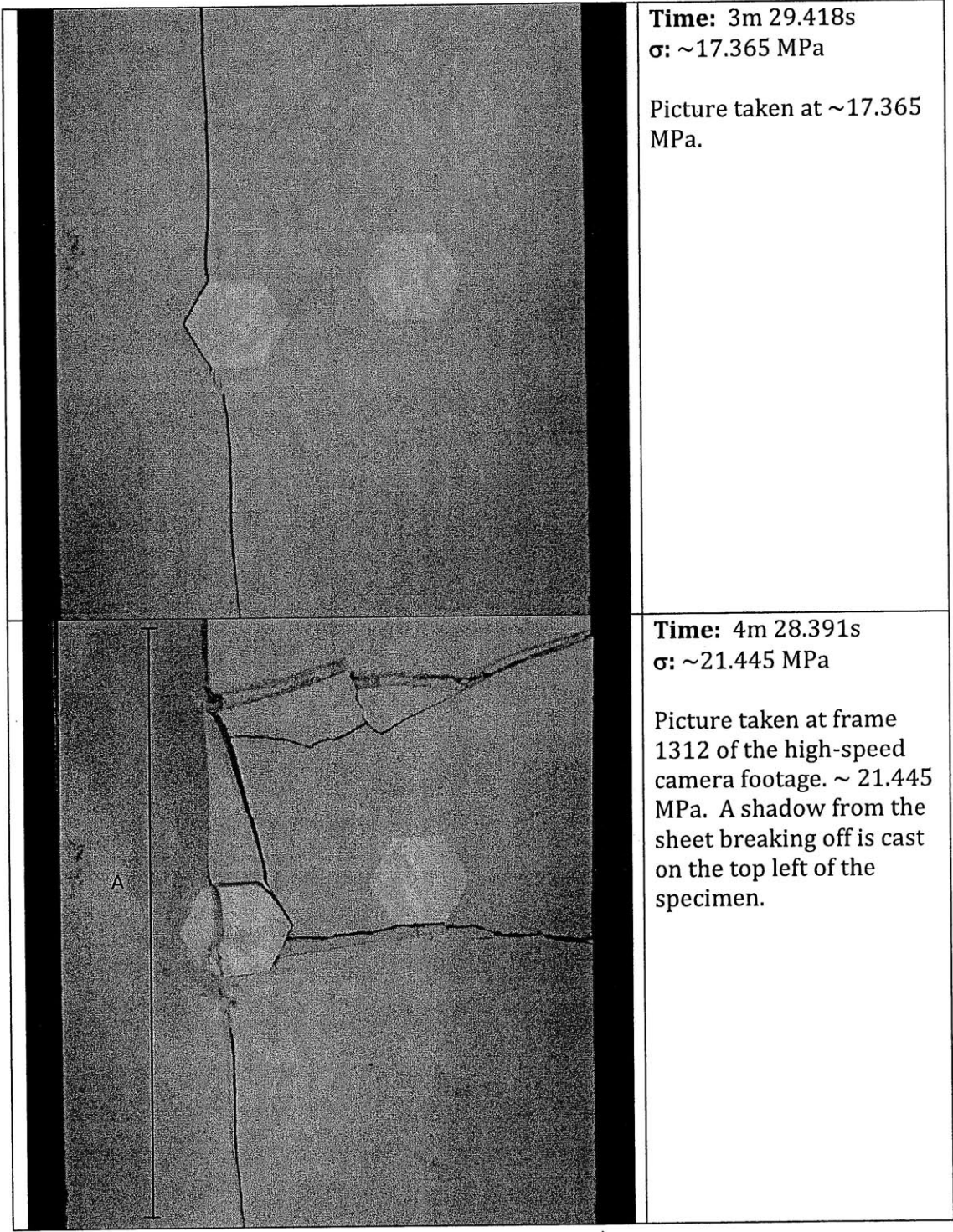
H-30-Ap

Shape = Hexagon
(Inclination = 0°)
Bridging Angle = 30°
Test Repetition = A
Material = Plaster
Size = 1/2"

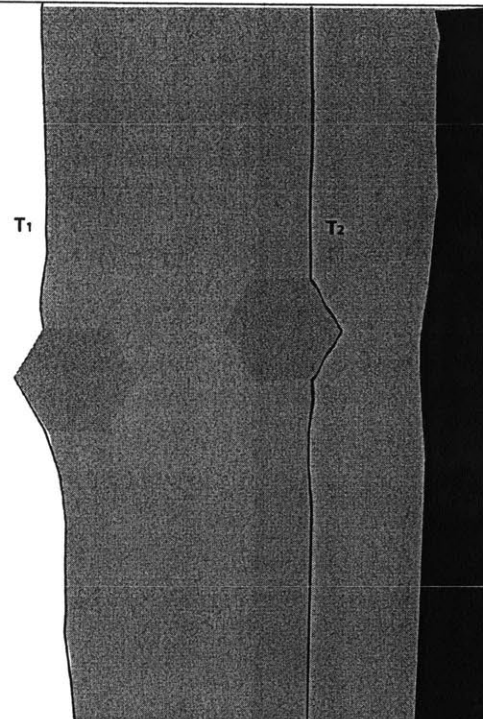
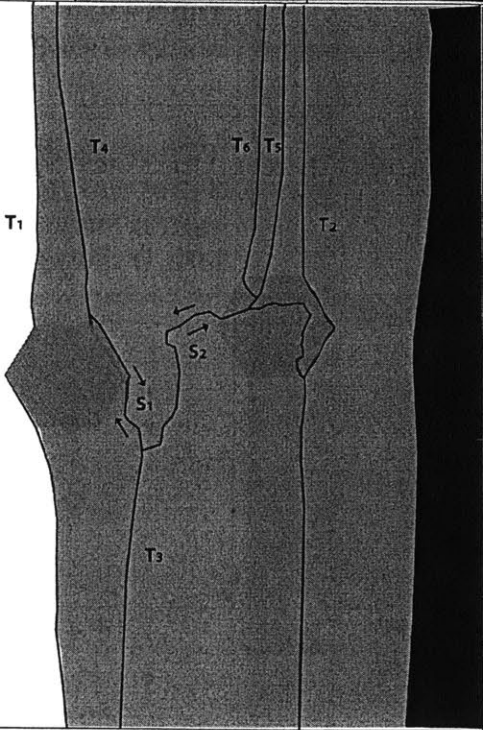


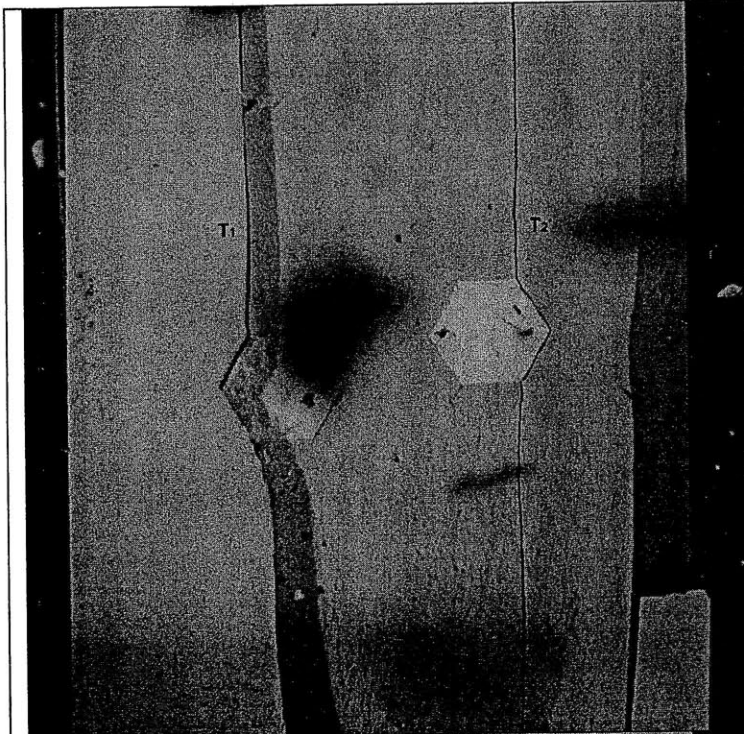
	<p>Time: 0m 0s σ: ~0 MPa</p> <p>Picture taken prior to testing.</p>
	<p>Time: 0m 0s σ: ~0 MPa</p> <p>Picture taken prior to testing.</p>

	 <p>A still image showing a specimen with two hexagonal inclusions. A crack labeled T_1 is visible on the left inclusion, extending from the top edge downwards. The right inclusion is intact.</p>	<p>Time: 3m 29.418s σ: ~17.365 MPa</p> <p>Still image captured with High Speed Camera before High Speed Recording.</p> <p>Tension crack T_1 forms on the left inclusion before the high speed frame initialize. The crack forms along a debonded surface at the edge of the left plaster inclusion.</p>
	 <p>A high-speed camera frame showing a large, dark, textured area on the right side of the specimen. A crack labeled T_1 is visible on the left side. A vertical dimension line labeled A is shown on the left, and a horizontal dimension line labeled A' is shown at the bottom.</p>	<p>Time: 4m 28.391s σ: ~21.445 MPa</p> <p>Frame 1312 of the High Speed Camera footage.</p> <p>A sheet approximately 1 cm thick breaks off from the right side of the specimen surface. This area includes the entire surface to the right of tension crack T_1 denoted by A'-A.</p>



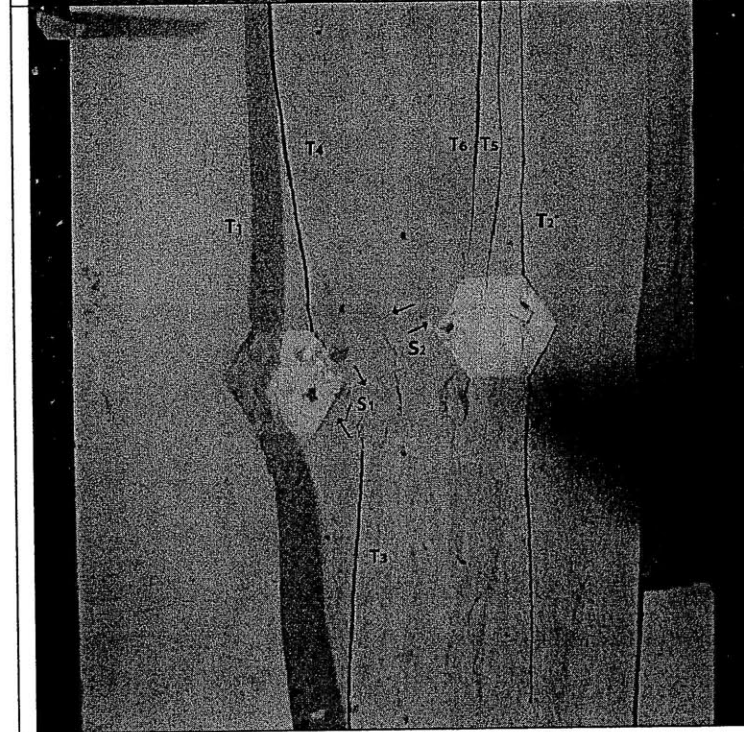
A'

		<p>Time: 4m 28.498s σ: ~21.458 MPa</p> <p>Frame 779 of the High Speed Camera footage.</p> <p>Tension crack T_2 forms from both boundary ends and moves inward toward the right side of the right inclusion. The crack moves along a debonded surface to the right of the inclusion.</p>
		<p>Time: 4m 28.584 s σ: ~24.474 MPa</p> <p>Frame 347 of the High Speed Camera footage.</p> <p>Tension cracks T_3 and T_4 form at the specimen boundaries and move toward the center of the specimen. Shear crack S_1 develops between tension cracks T_3 and T_4. Tension crack T_5 and shear crack S_2 initiate simultaneous and coalesce with T_3. Finally tension crack T_6 forms from the top specimen boundary.</p>



Time: 4m 28.498s
 σ : ~21.458 MPa

Picture taken at frame 779 of the high-speed camera footage. ~ 21.458 MPa.

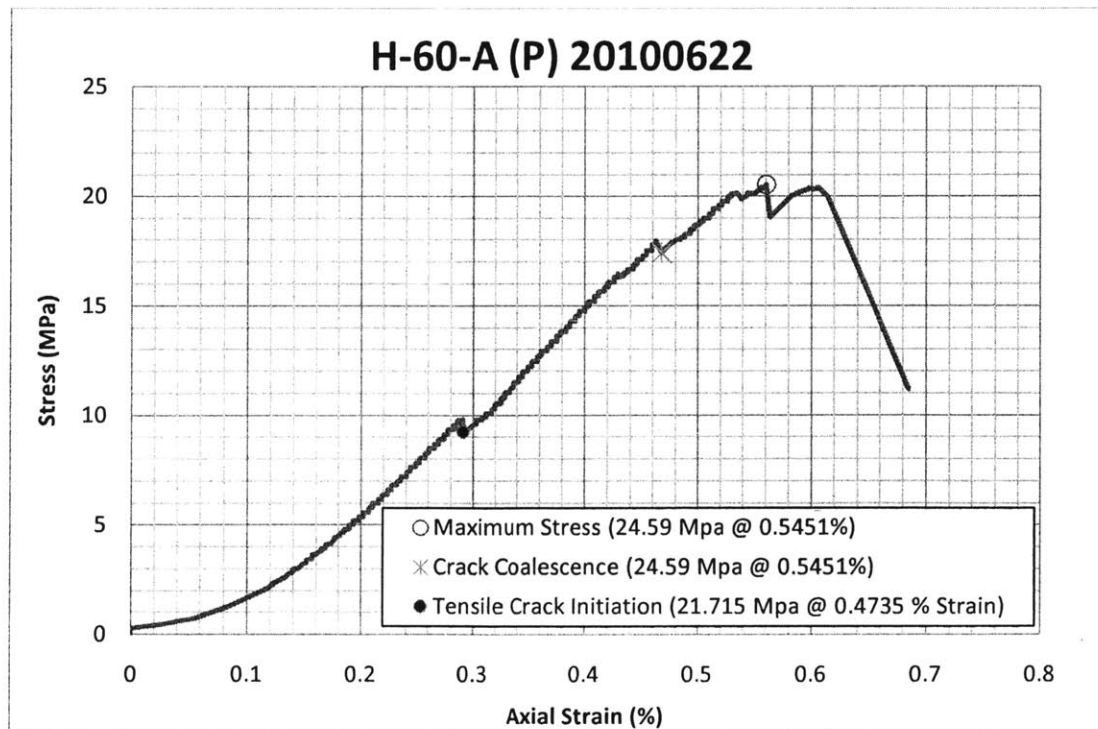
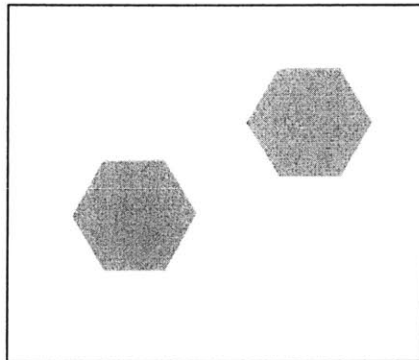


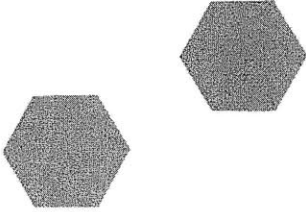
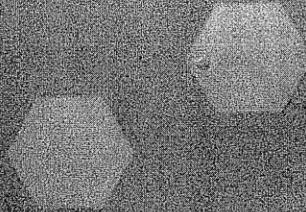
Time: 4m 28.584 s
 σ : ~24.474 MPa

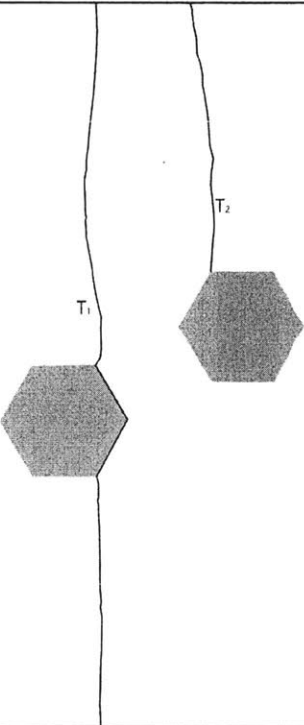
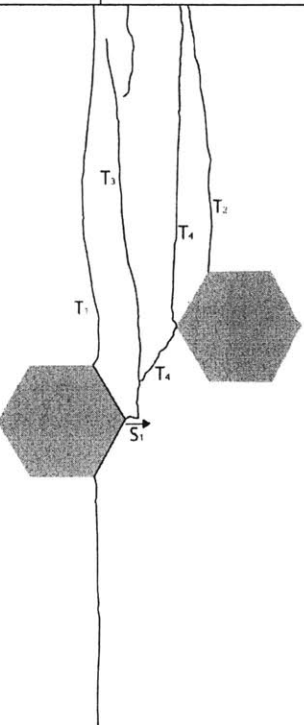
Picture taken at frame 347 of the high-speed camera footage. ~ 21.474 MPa. (Failure)

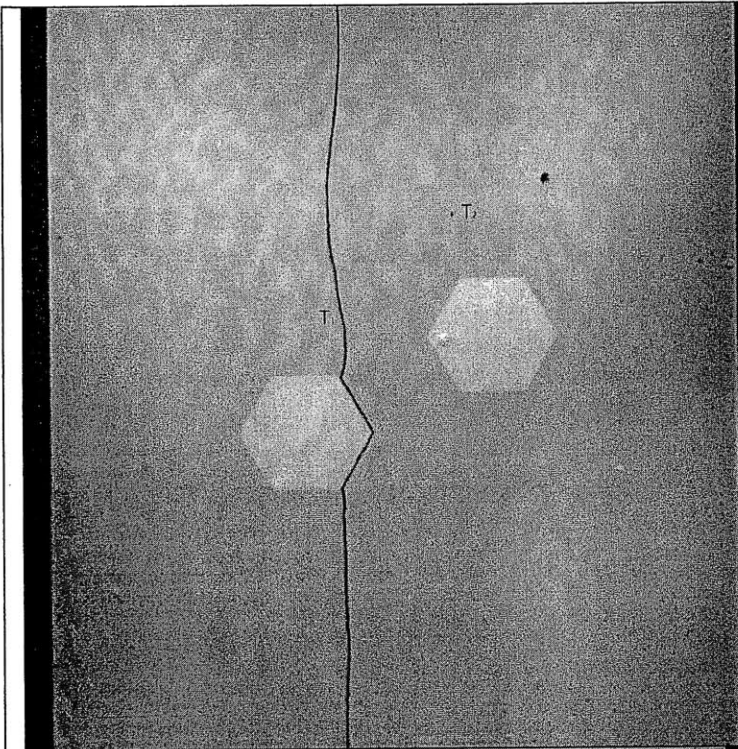
H-60-Ap

Shape = Hexagon
(Inclination = 0°)
Bridging Angle = 60°
Test Repetition = A
Material = Plaster
Size = 1/2"



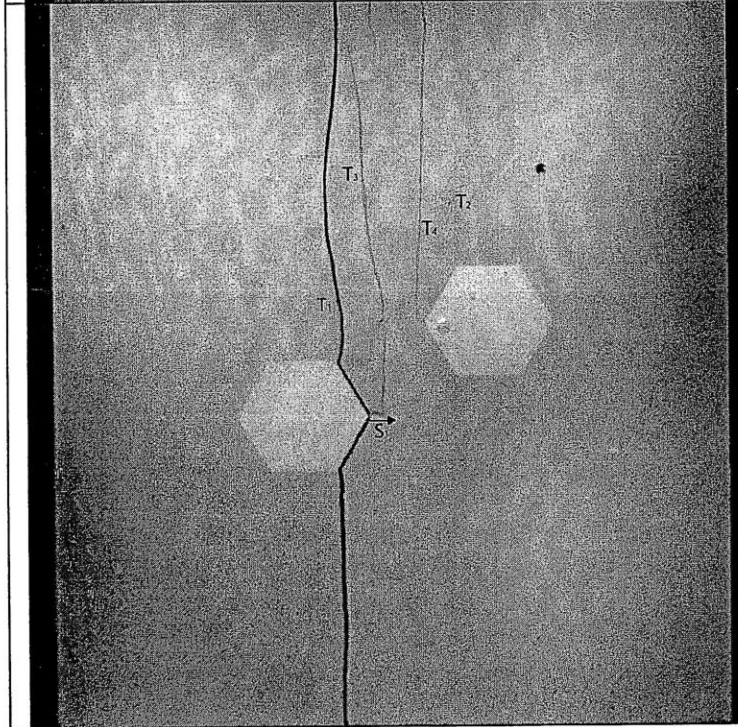
	<p>Time: 0m 0s</p> <p>σ: 0 MPa</p> <p>Picture taken prior to testing.</p> <p>1</p>
	<p>Time: 0m 0s</p> <p>σ: 0 MPa</p> <p>Picture taken prior to testing.</p> <p>Pre-test specimen.</p> <p>1</p>

		<p>Time: 1m 49.61s</p> <p>σ: ~9.235 MPa</p> <p>Still image captured with High Speed Camera before High Speed Recording.</p> <p>Tensile crack T_1 and T_2 form at the upper specimen boundary and propagate downward along the inner inclusion boundaries, thus causing debonding between the specimen and inclusion.</p> <p style="text-align: right;">2</p>
		<p>Time: 3m 49.644s</p> <p>σ: ~17.422 MPa</p> <p>Still image captured with High Speed Camera before High Speed Recording.</p> <p>COALESCENCE</p> <p>Shear crack, S_1, forms at the inner corner of the left inclusion and then coalescence occurs between the inclusions via tension cracks T_3 and T_4.</p> <p style="text-align: right;">3</p>



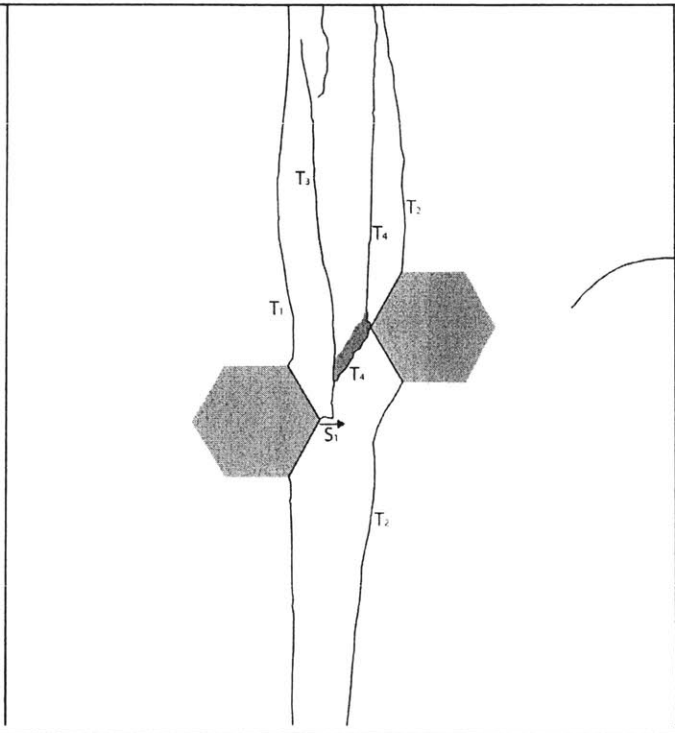
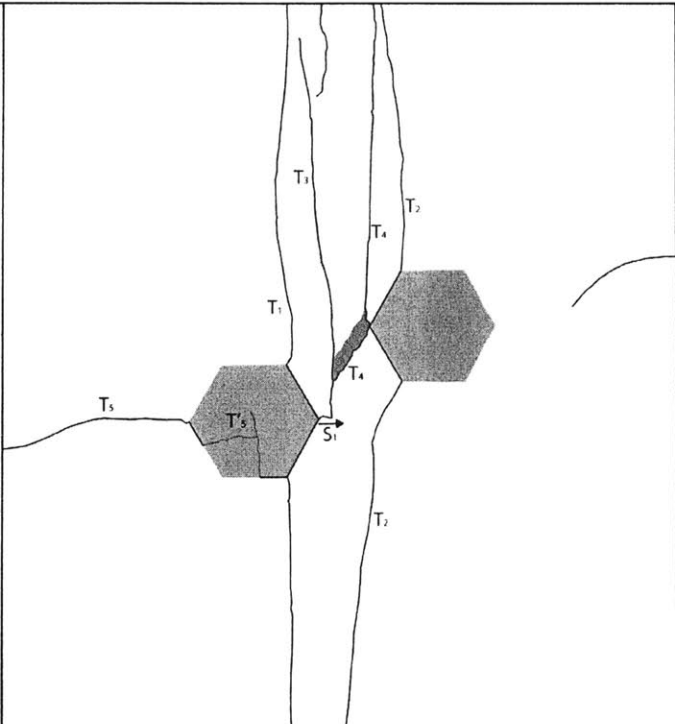
Time: 1m 49.61s
 σ : ~9.235 MPa
Still photo of specimen at
~9.235 MPa.

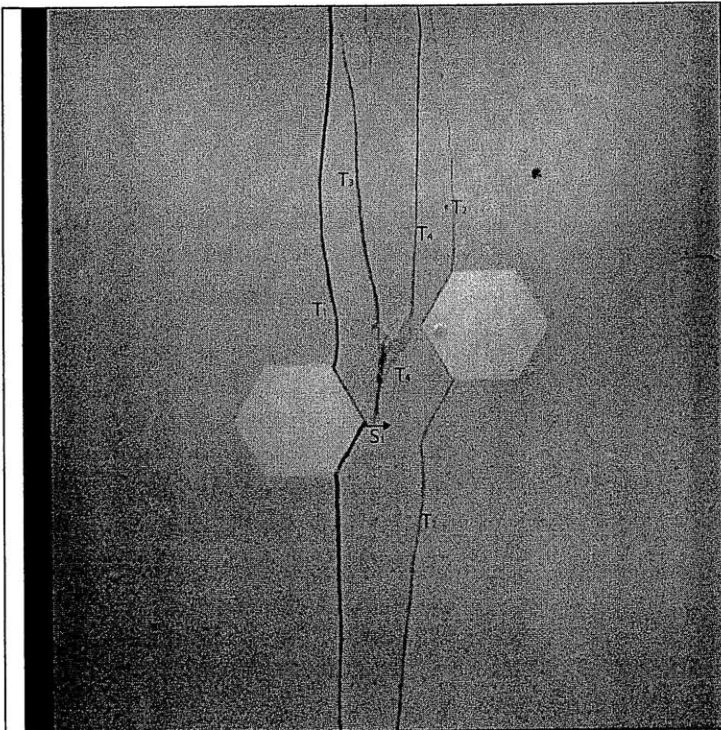
2



Time: 3m 49.644s
 σ : ~17.422 MPa
Still photo of specimen
taken at ~17.422 MPa

3

	<p>Time: 4m 22.818s</p> <p>σ: ~20.2123 MPa</p> <p>Still image captured with High Speed Camera before High Speed Recording.</p> <p>Tension crack, T_2, extends downward along the left boundary of, and thus initiating debonding along, the right inclusion. Spalling occurs between the inclusions, along T_4. Cracks T_1, T_2, T_3, and T_4 widen, or open slightly.</p> <p style="text-align: right;">4</p>
	<p>Time: 4m 26.362s</p> <p>σ: ~20.4646 MPa</p> <p>Frame 4223 of the High Speed Camera footage.</p> <p>T_5 propagates inward from the specimen boundary toward the left inclusion corner. Crack T_5 propagates within the inclusion and along the lower boundary of the inclusion.</p> <p style="text-align: right;">5</p>

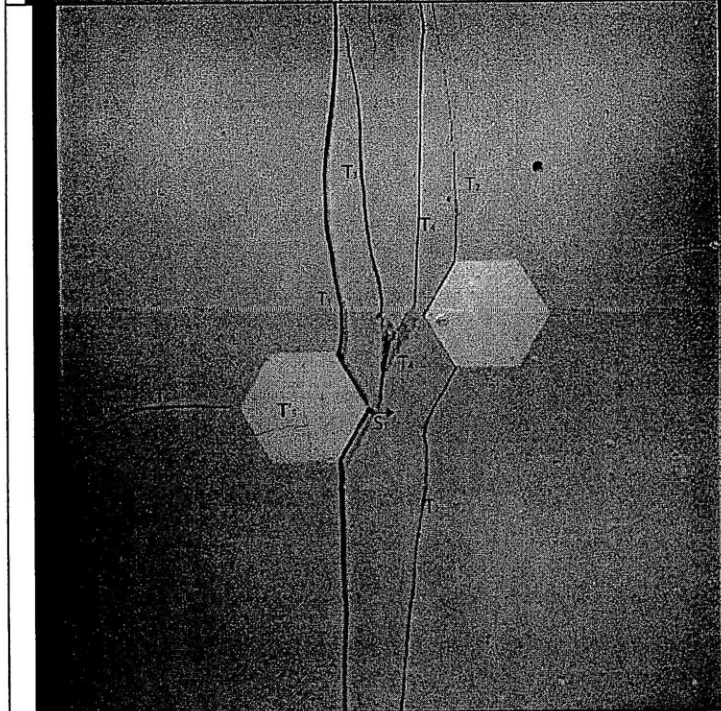


Time: 4m 22.818s

σ : ~20.2123 MPa

Still photo of specimen
taken at ~ 20.212 MPa

4



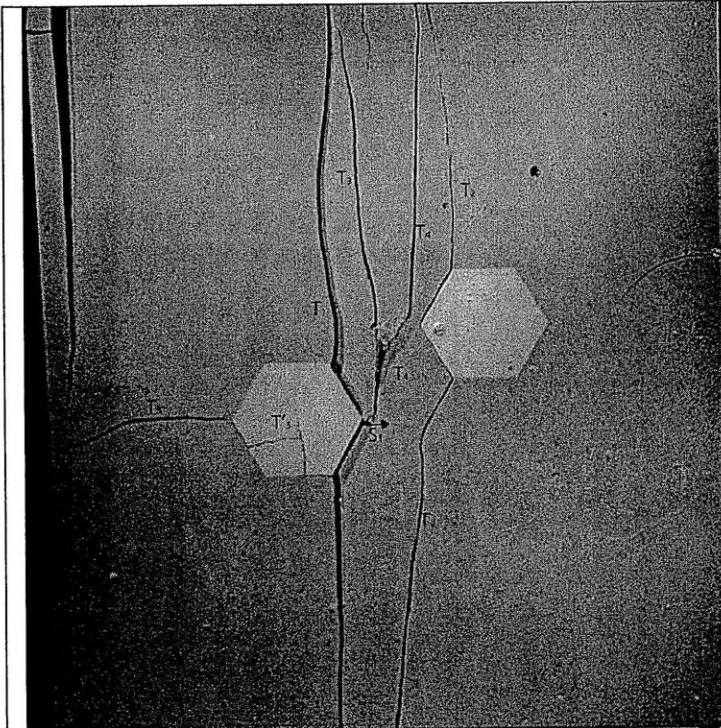
Time: 4m 26.362s

σ : ~20.4646 MPa

High speed photo of
specimen at frame 4223
(~20.465 MPa).

5

	<p>Time: 4m 26.816s</p> <p>σ: ~20.4916 MPa</p> <p>Frame 1952 of the High Speed Camera footage.</p> <p>The upper left edge of the specimen breaks away. T_1 opens further.</p> <p style="text-align: right;">6</p>
	<p>Time: 4m 27.162s</p> <p>σ: ~20.5187 MPa</p> <p>Frame 220 of the High Speed Camera footage.</p> <p>Tension crack T_6 forms from the specimen boundary and propagates upward.</p> <p style="text-align: right;">7</p>

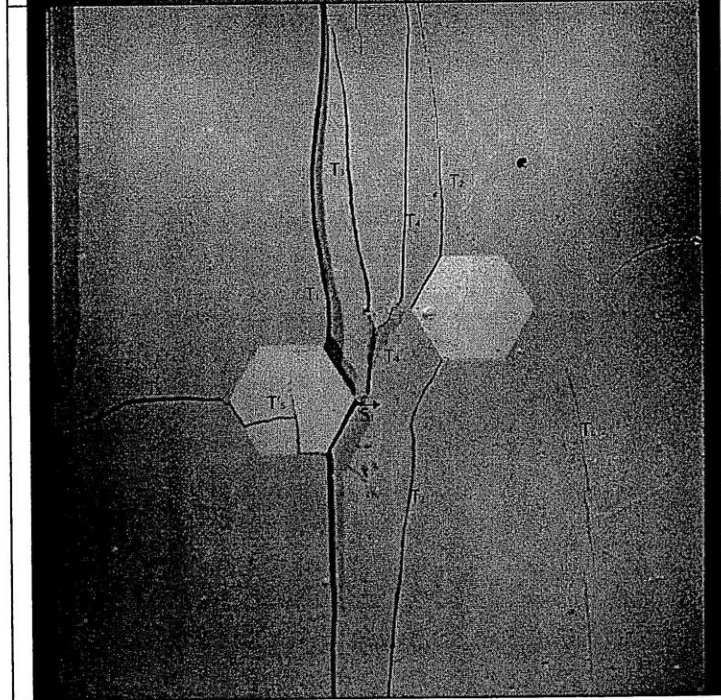


Time: 4m 26.816s

σ: ~20.4916 MPa

High speed photo of specimen at frame 1952 (~20.492 MPa).

6



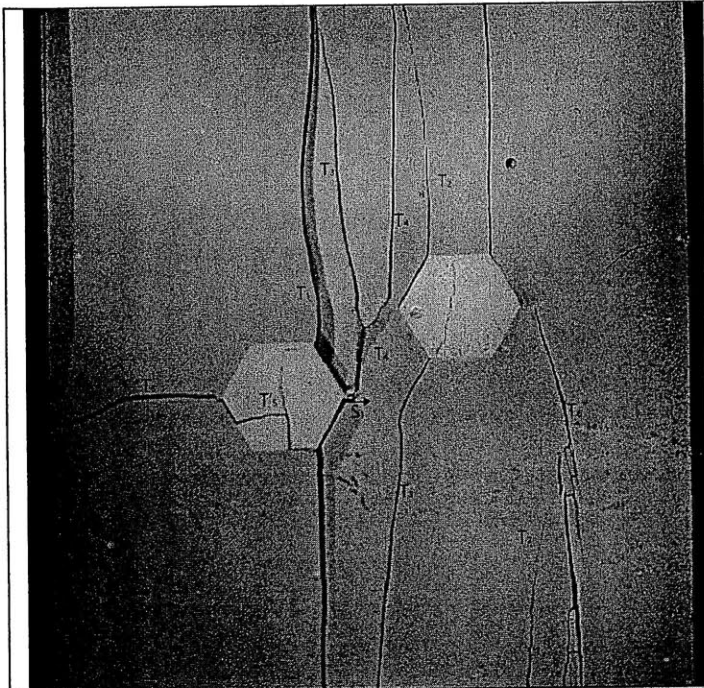
Time: 4m 27.162s

σ: ~20.5187 MPa

High speed photo of specimen at frame 220 (~20.519 MPa).

7

	<p>Time: 4m 27.165s</p> <p>σ: ~20.5187 MPa</p> <p>Frame 205 of the High Speed Camera footage.</p> <p>Tension crack T₇ and a series of cracks associated with T₆ propagate upward from the specimen boundary.</p> <p style="text-align: right;">8</p>
	<p>Time: 4m 27.198s</p> <p>σ: ~20.5187 MPa</p> <p>Frame 42 of the High Speed Camera footage.</p> <p>T₆ debonds the inclusion boundary and propagates upward to the specimen boundary. T₇ connects with T₆ at the right corner of the right inclusion. T₆ inclusion cracks propagate between T₂ and T₆.</p> <p style="text-align: right;">8</p>

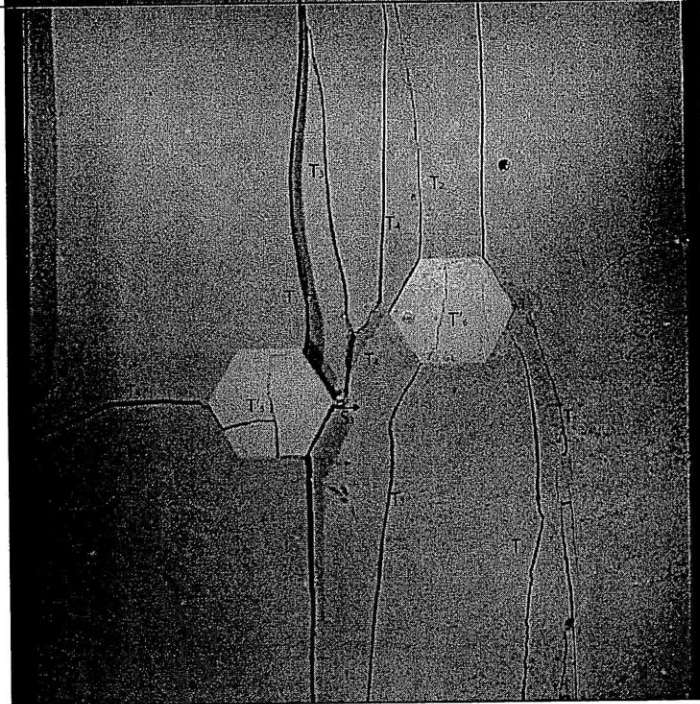


Time: 4m 27.165s

σ : ~20.5187 MPa

High speed photo of specimen at frame 205 (~20.519 MPa).

8



Time: 4m 27.198s

σ : ~20.5187 MPa

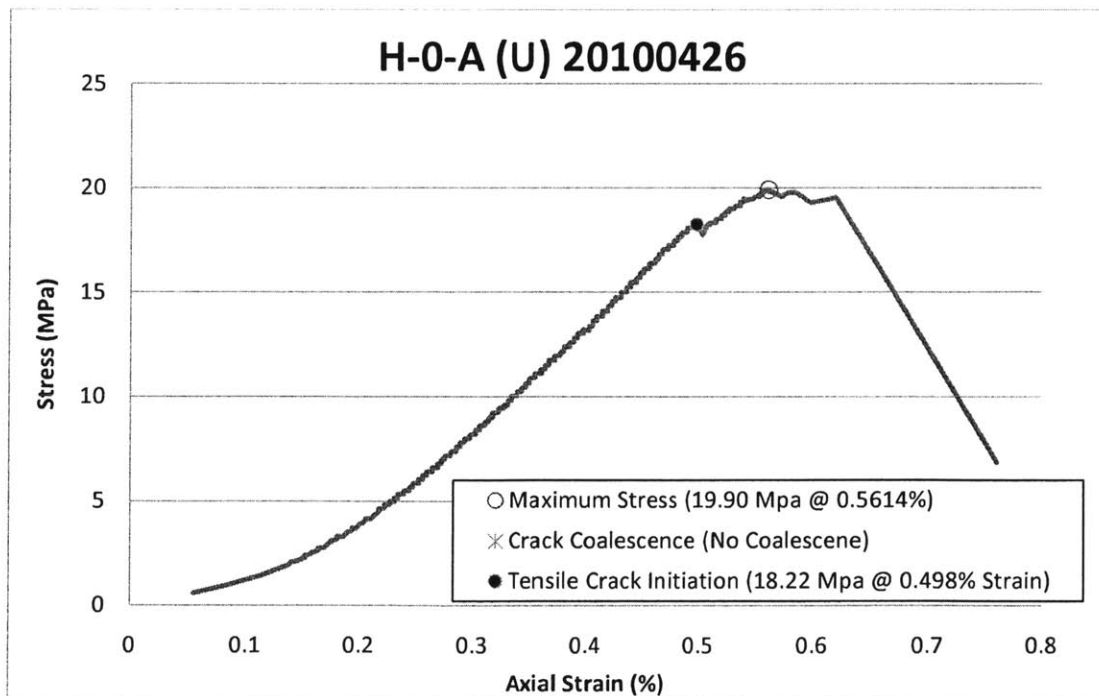
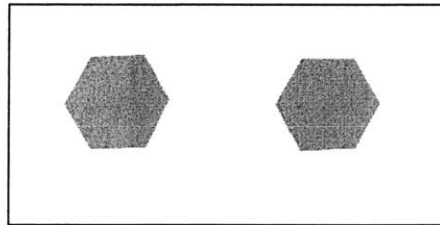
High speed photo of specimen at frame 204 (~20.159 MPa).

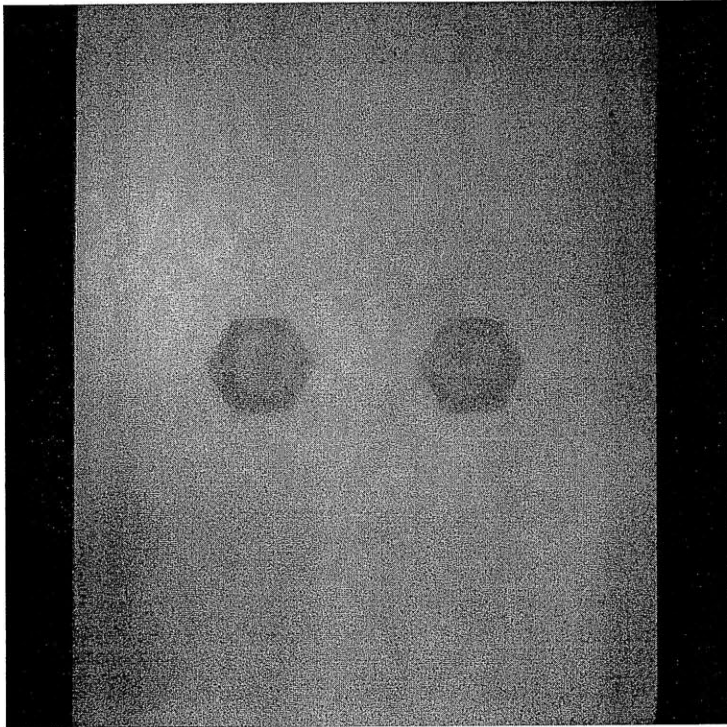
9

ULTRACAL



H-0-Au

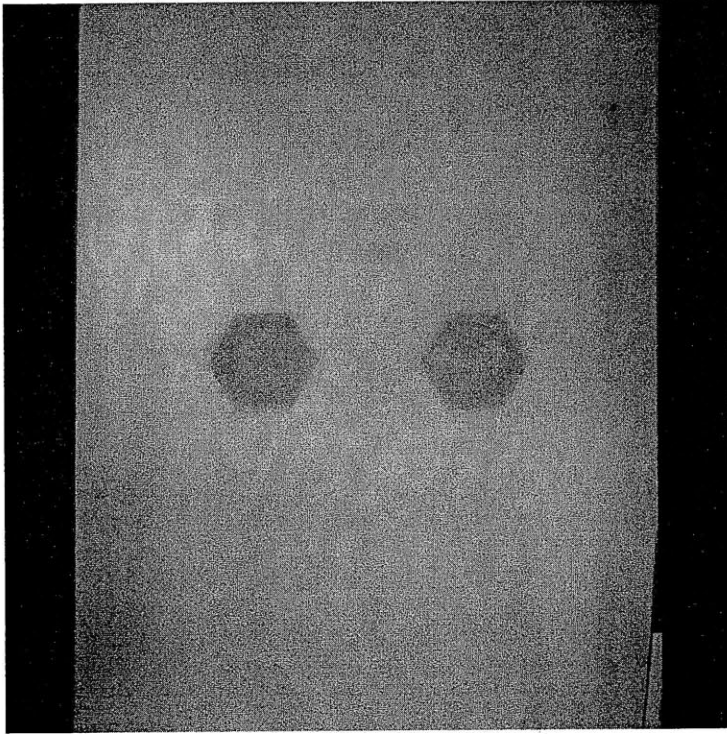
Shape = Hexagon
(Inclination = 0°)
Bridging Angle = 0°
Test Repetition = A
Material = Ultracal
Size = 1/2"



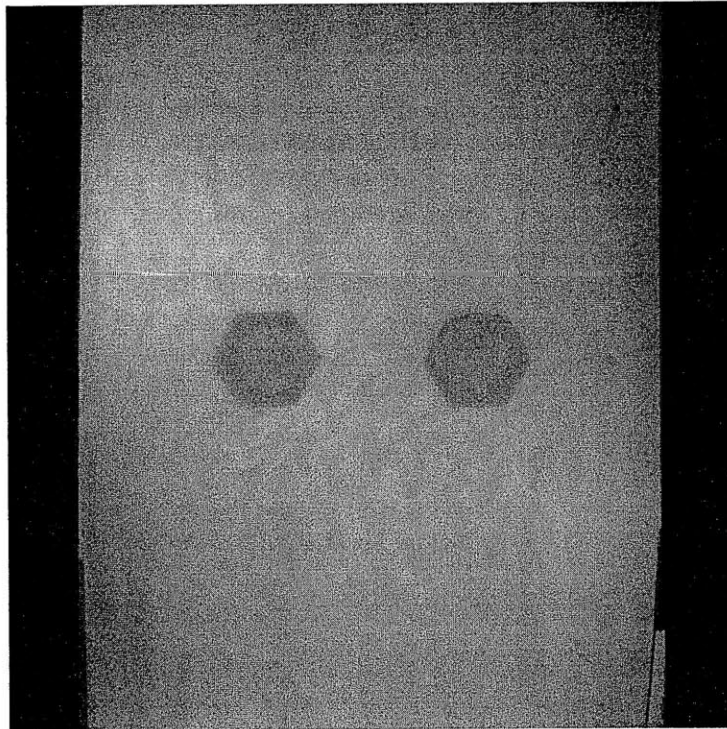


Picture taken prior to testing.

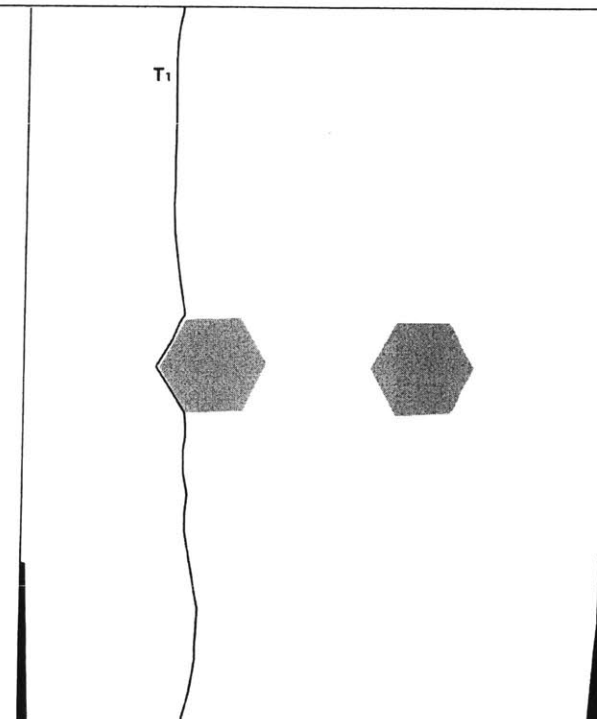
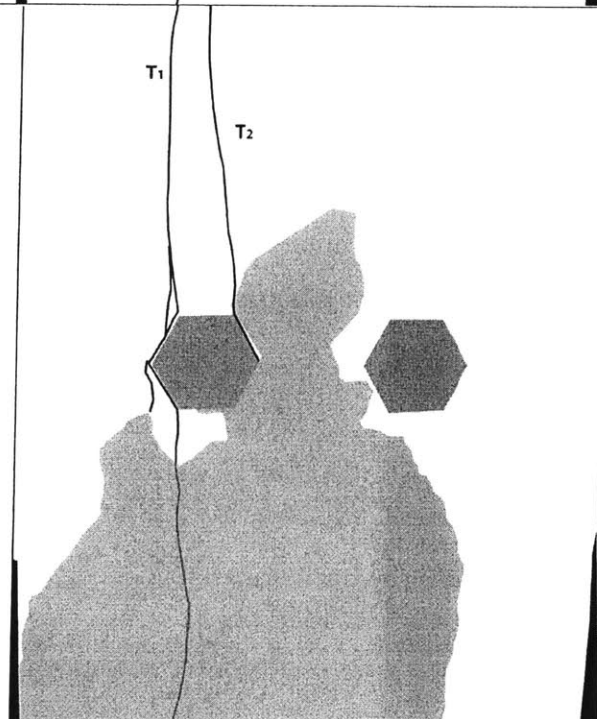
		<p>Time: 3m 57.288s σ: ~10.915 MPa</p> <p>Still image captured with High Speed Camera before High Speed Recording.</p> <p>A small piece breaks off of the bottom right of the specimen.</p>
		<p>Time: 3m 41.148s σ: ~17.157 MPa</p> <p>Still image captured with High Speed Camera before High Speed Recording.</p> <p>A small piece at the bottom left boundary of the specimen surface breaks off.</p>

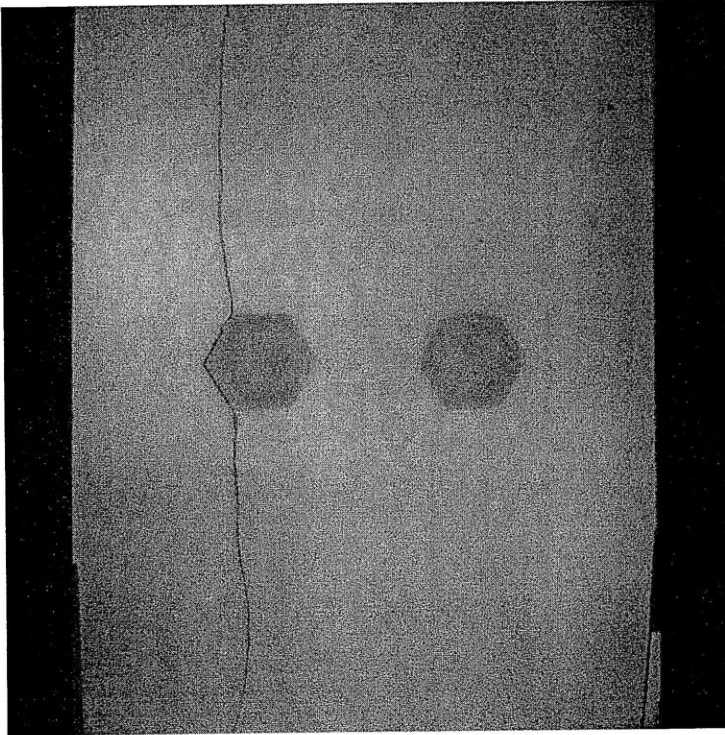


Picture taken at ~10.915 MPa.

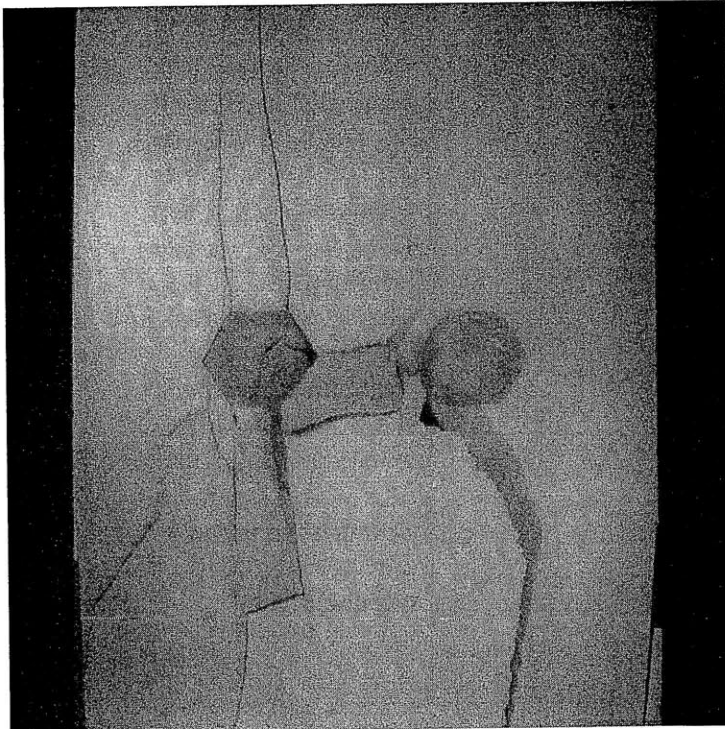


Picture taken at ~17.157 MPa.

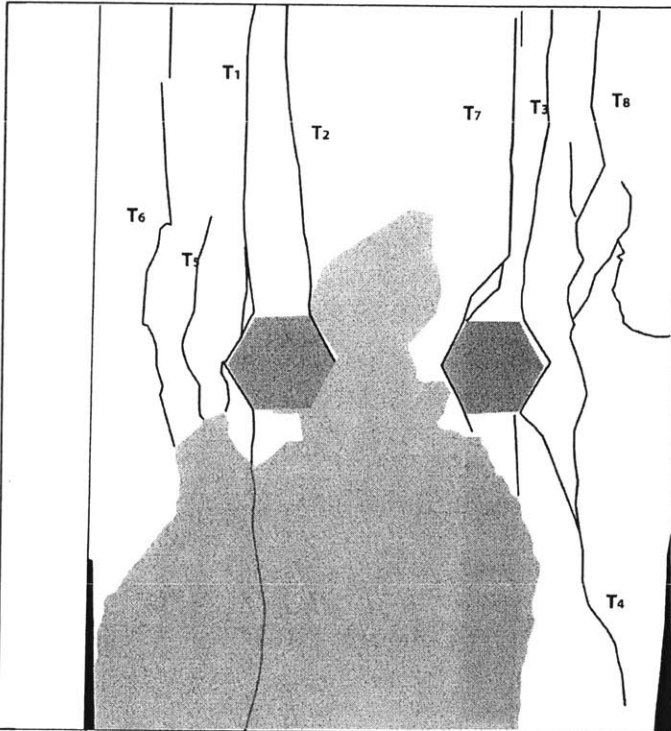
 <p>A grayscale image of a specimen under tension. A vertical crack, labeled T₁, is visible on the left side of the specimen. Two dark, hexagonal inclusions are present: one on the left side of the crack and one on the right side.</p>	<p>Time: 3m 57.288s σ: ~18.229 MPa</p> <p>Still image captured with High Speed Camera before High Speed Recording.</p> <p>Tension crack T₁ forms along the left side of the left inclusion. (debonding)</p>
 <p>A grayscale image of a specimen under tension, showing significant damage. A vertical crack, labeled T₁, is on the left side. A diagonal crack, labeled T₂, is on the right side of the left inclusion. There is a large, irregularly shaped area of spalling at the bottom and middle of the specimen.</p>	<p>Time: 4m 21.443s σ: ~19.885 MPa</p> <p>Frame 2080 of the High Speed Camera footage.</p> <p>Tension crack T₂ forms along the right side of the left inclusion. (debonding) Significant spalling occurs as multiple pieces break of the bottom and middle sections of the specimen. As it will be seen later in a post-failure image the cracks under this spalling were analyzed.</p>



Picture taken at ~ 18.229 MPa.



Picture taken at frame 2080 of the high-speed camera footage. (21.443 Mpa)

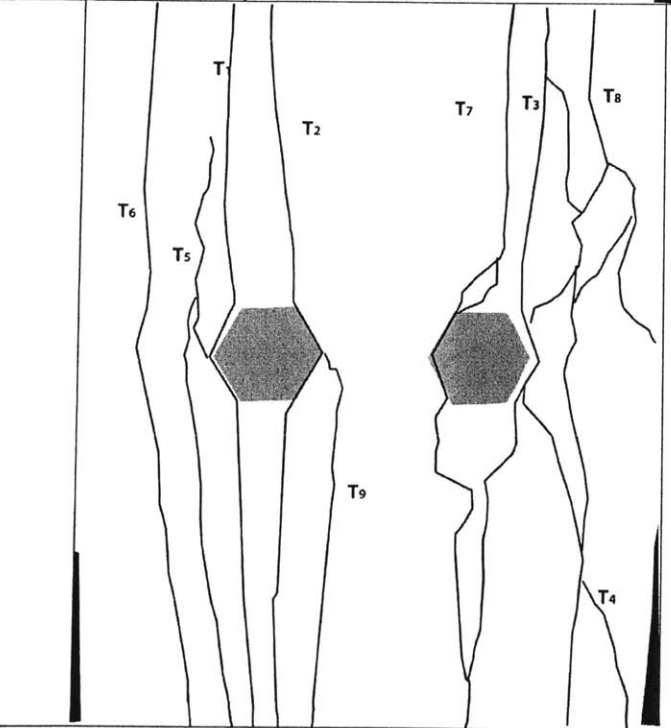


Time: 4m 21.792s

σ : ~19.899 MPa

Frame 335 of the High Speed Camera footage.

Tension Crack T₃ formed along the right side of the right inclusion. From the bottom of the specimen tension crack T₄ formed up to connect with T₃ and moves up to the right of the right inclusion. Tension crack T₅ forms to the left of the left inclusion but moves under the spalling zone. To the left of T₅, T₆ forms and moves from the middle up to the top of the specimen. From the left side of the right inclusion T₇ forms and moves upward to the top of the specimen (debonding). After this, T₄ moves up beyond the right inclusion and connects to T₈, which moves up toward the top of the specimen.

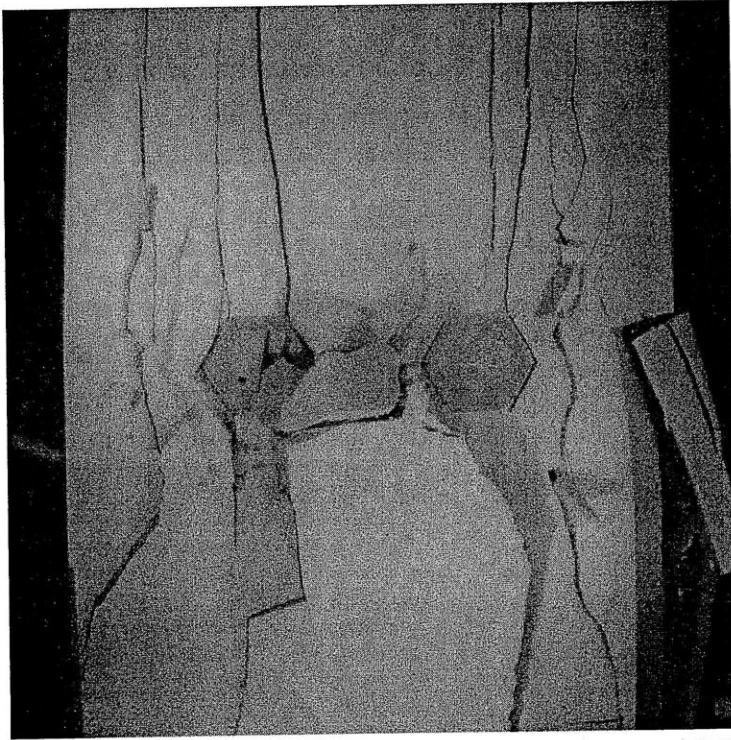


Time: 4m 23.286s

σ : ~ N/A

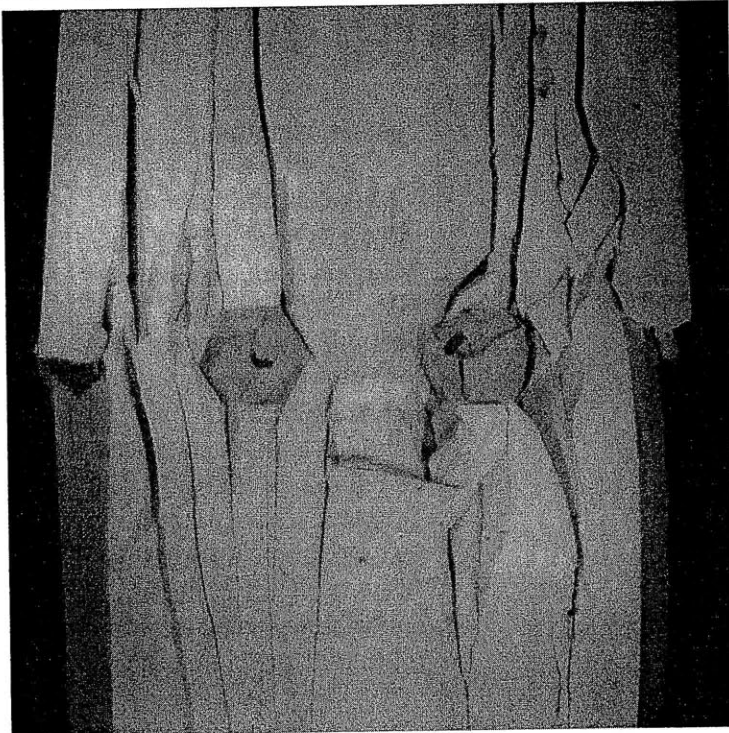
Post-Failure Image.

After the spalling pieces fell off the bottom half of the cracks were revealed. Although their propagation at certain time points was not determined their behavior can be seen. An additional tension crack T₉ was discovered to have formed from the right side of the left inclusion and extend to the bottom-middle of the specimen.



Picture taken at frame 335 of the high-speed camera footage. (19.899 Mpa)

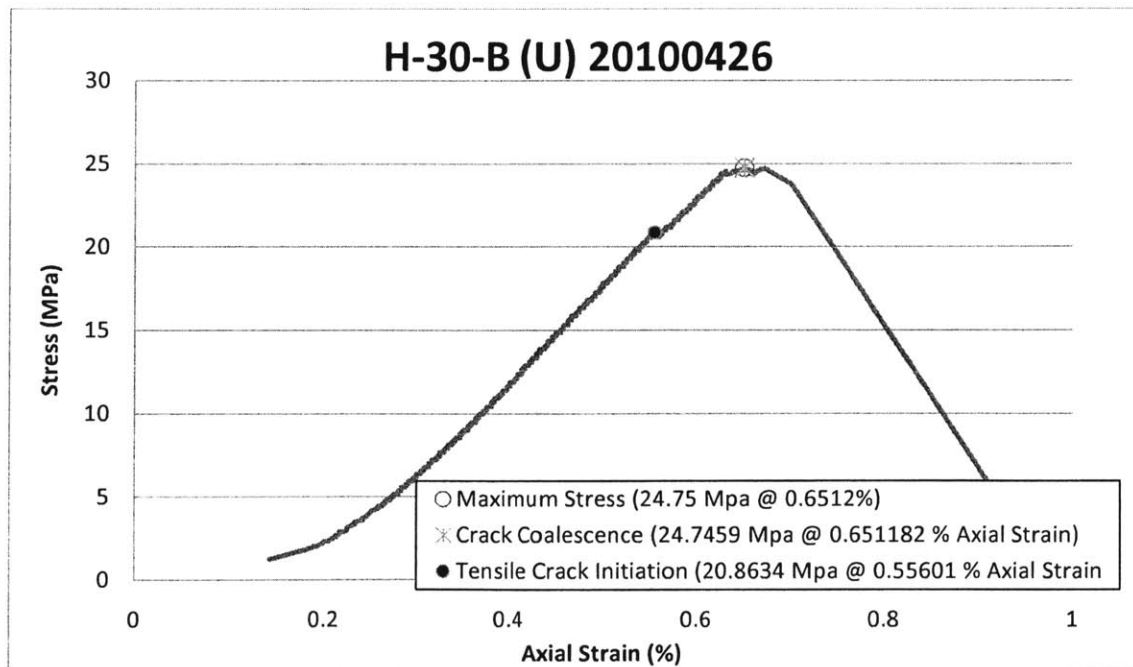
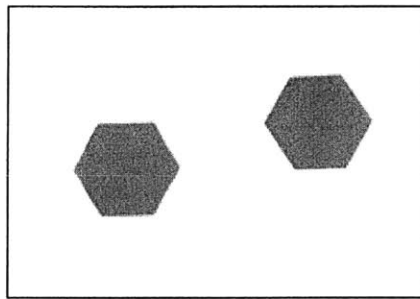
(Failure)

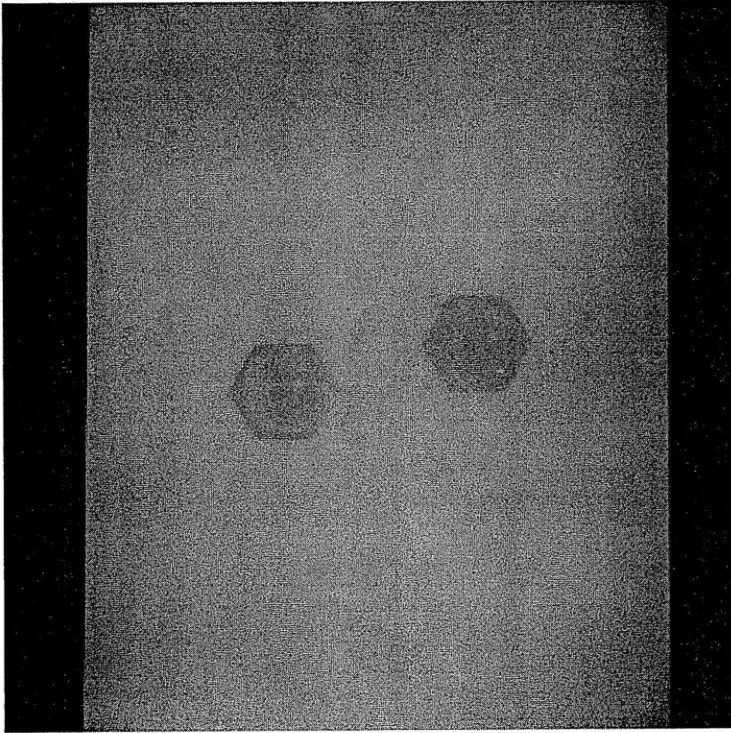


Picture taken after Failure

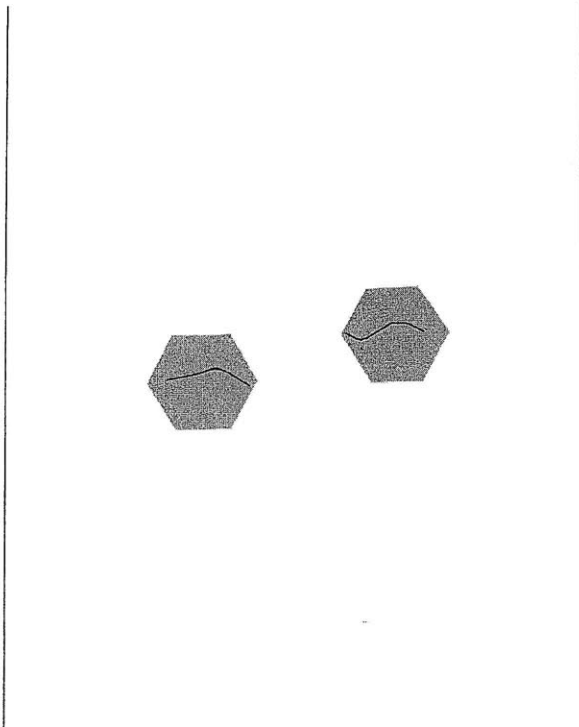
H-30-Bu

Shape = Hexagon
(Inclination = 0°)
Bridging Angle = 30°
Test Repetition = B
Material = Ultracal
Size = 1/2"

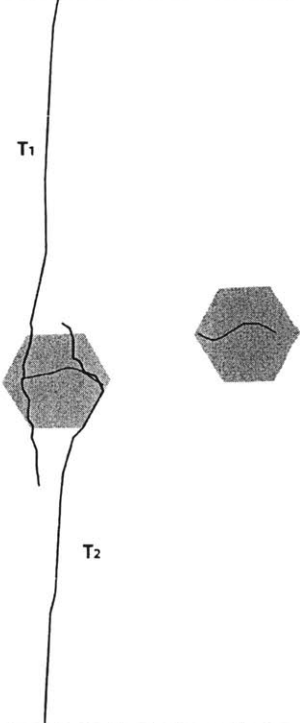
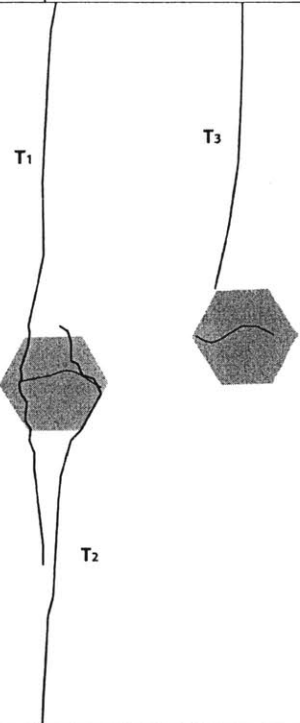


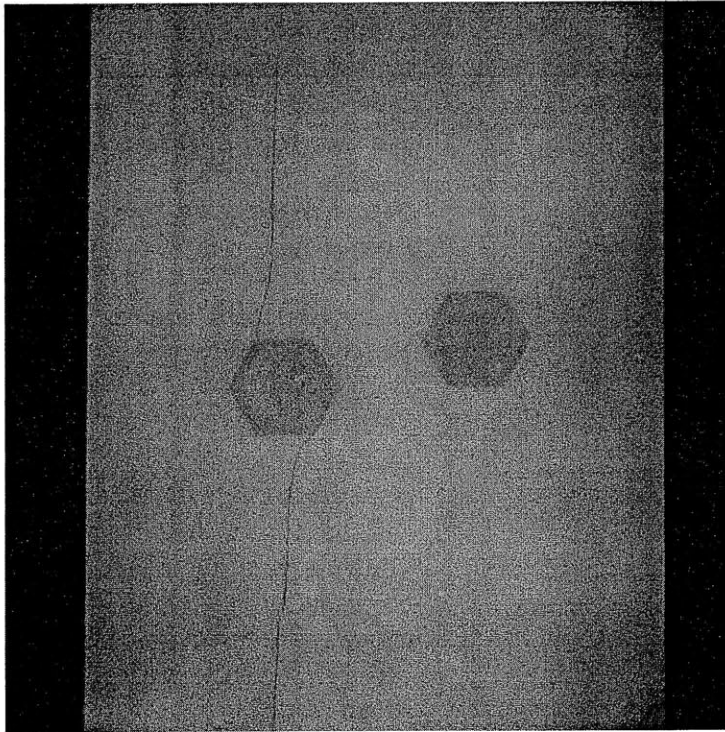


Picture taken prior to testing.

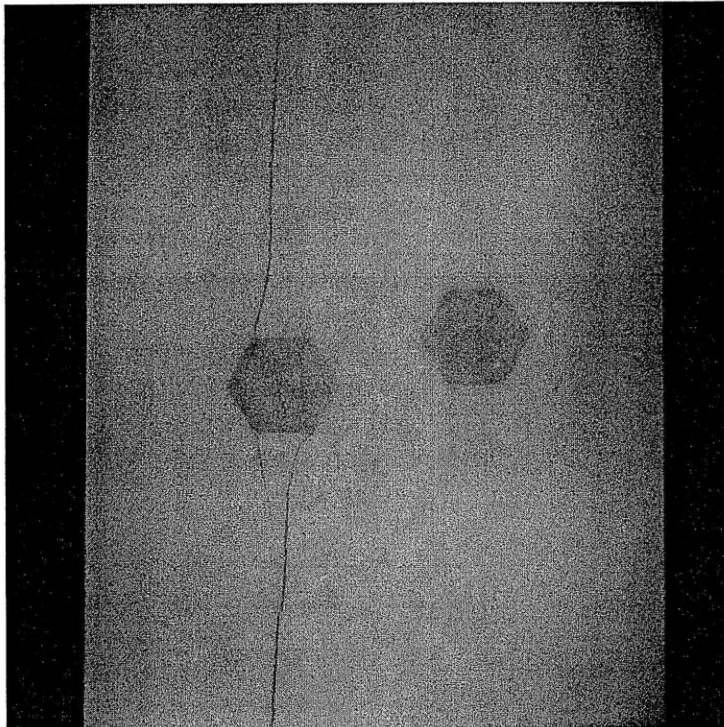


Surface cracking in the inclusion prior to testing.

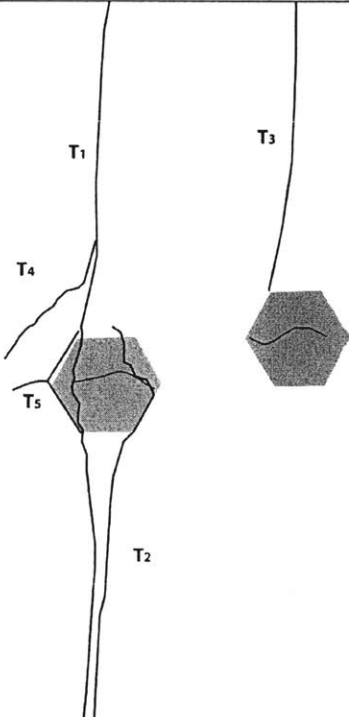
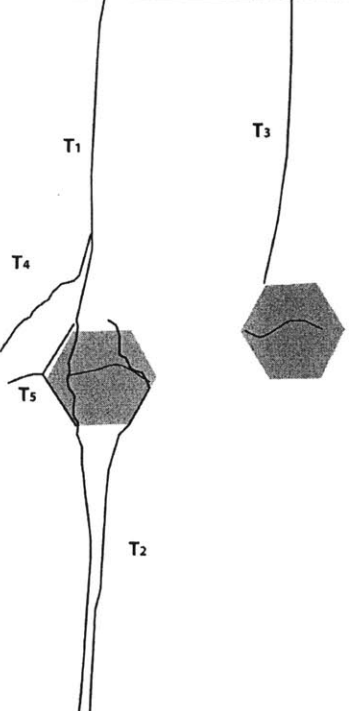
		<p>Time: 4m 52.452s σ: ~20.8634 MPa</p> <p>Still image captured with High Speed Camera before High Speed Recording.</p> <p>(In no particular order, Numbers Arbitrarily Assigned) Tension crack T₁ forms on the on the top left side of the specimen and goes through the left inclusion. Tension crack T₂ forms on the bottom left side of the specimen and moves through the left inclusion (debonding).</p>
		<p>Time: 5m 36.378s σ: ~23.7257 MPa</p> <p>Still image captured with High Speed Camera before High Speed Recording.</p> <p>Tension crack T₁ moves downward toward T₂. Tension crack T₃ forms above the right inclusion and moves down toward the top of the right inclusion.</p>

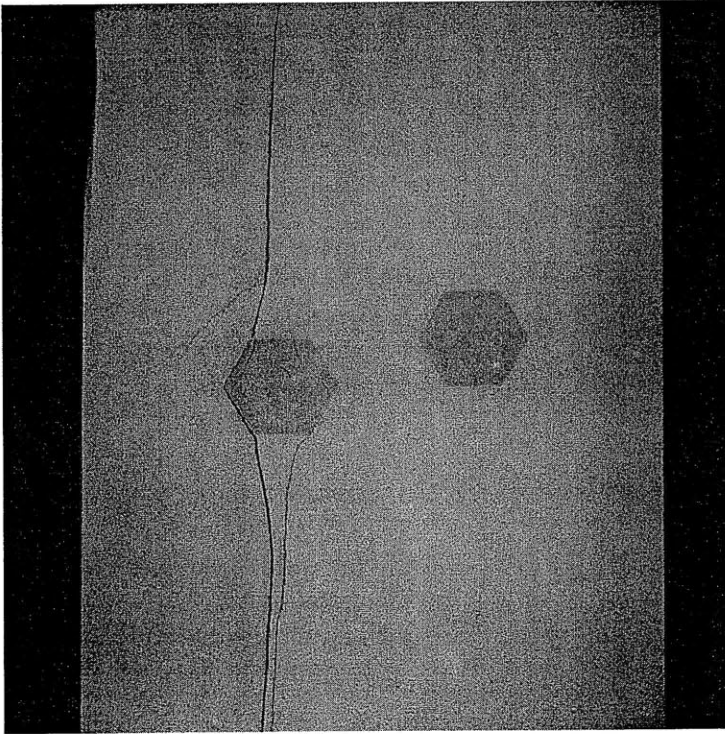


Picture taken at ~ 20.8634
Mpa

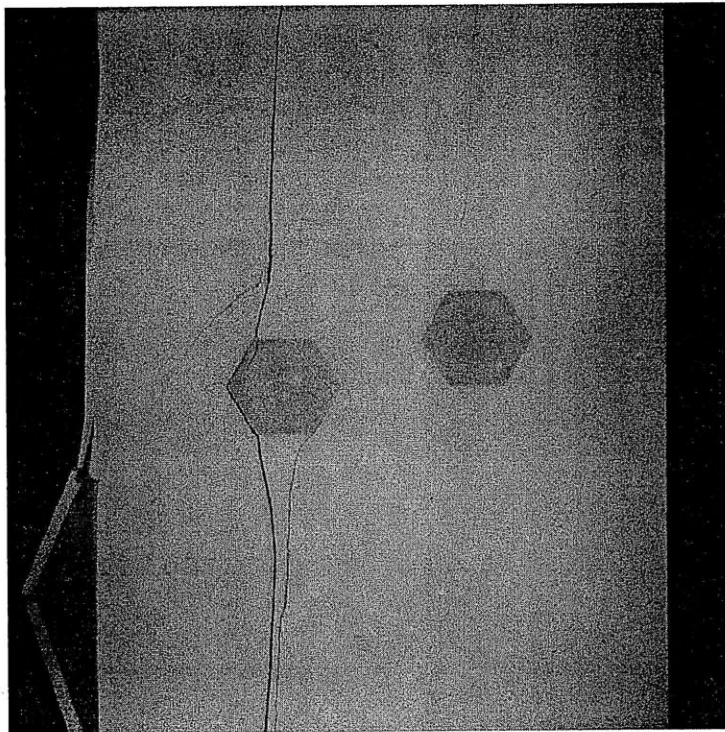


Picture taken at ~ 23.7257
Mpa

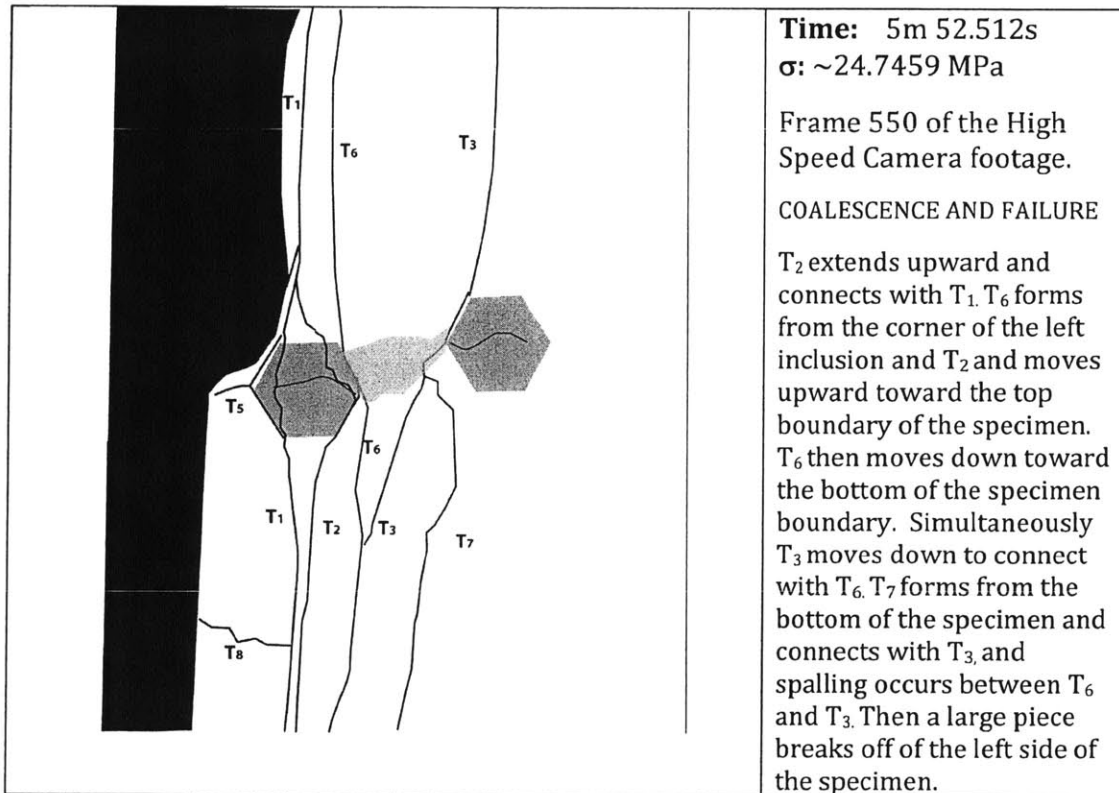
		<p>Time: 5m 51.5410s σ: ~24.6747 MPa</p> <p>Frame 5404 of the High Speed Camera footage.</p> <p>(In no particular order, Numbers Arbitrarily Assigned) Tension crack T₄ forms from the left side of T₁ and moves leftward toward the left boundary of the specimen. T₅ forms from the debonding of the left side of the left inclusion and T₁. T₅ moves left toward the left specimen boundary.</p>
		<p>Time: 5m 51.8933s σ: ~24.69846MPa</p> <p>Frame 3643 of the High Speed Camera footage.</p> <p>A small piece of the specimen breaks off of the bottom left side of the specimen.</p>



Picture taken at frame 5404
of the high-speed camera
footage. (24.6747 Mpa)

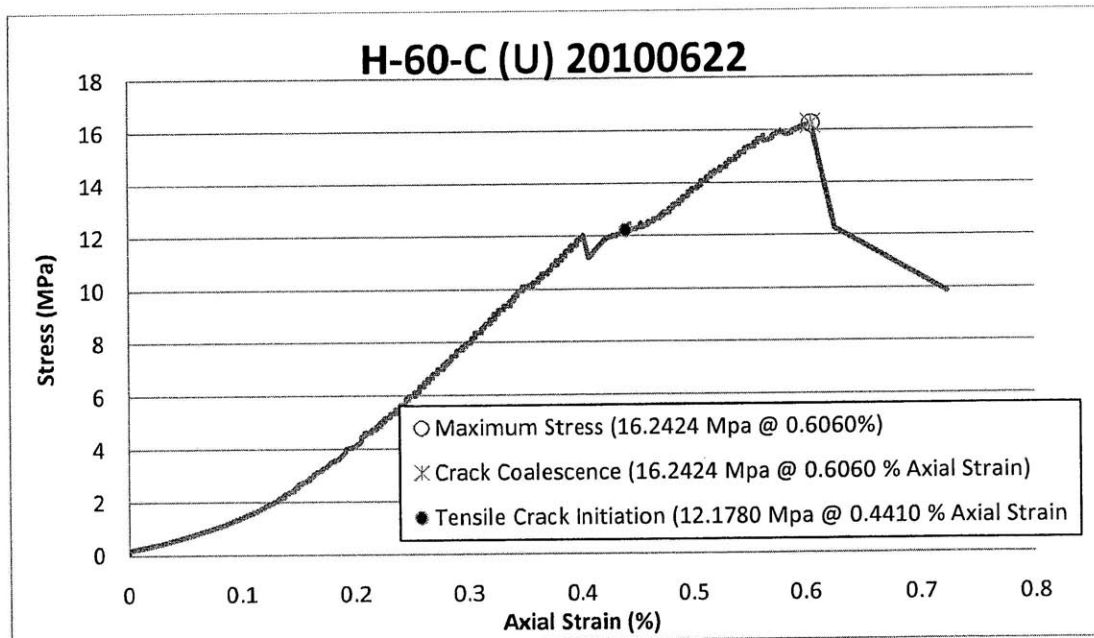
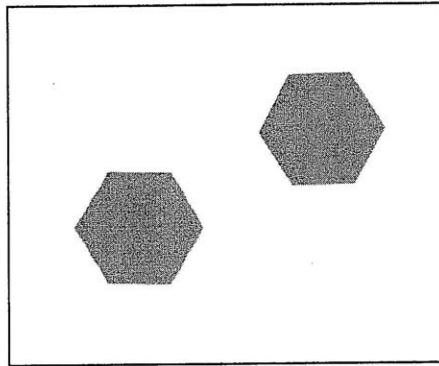


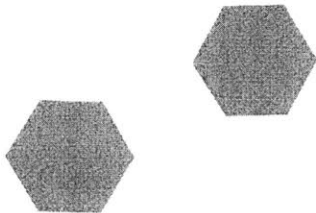
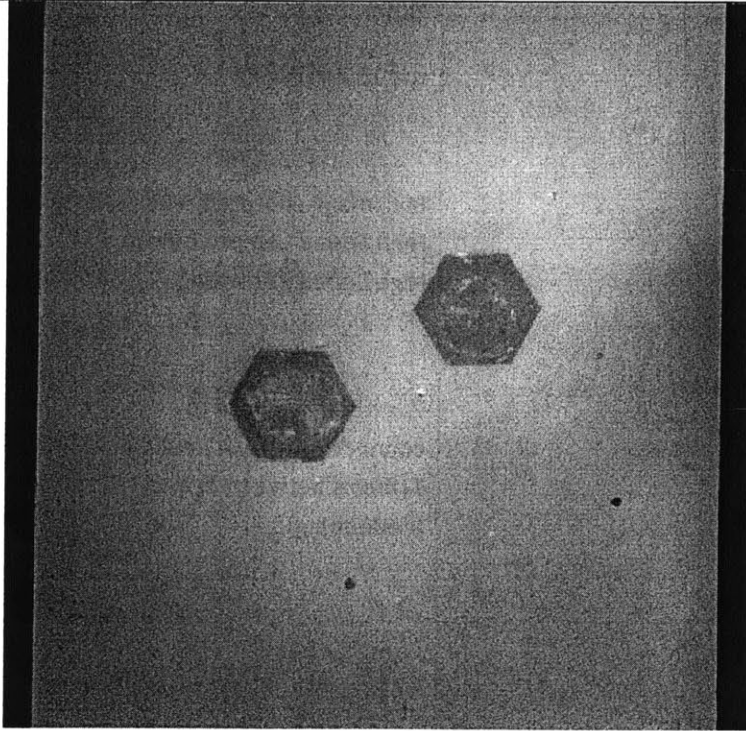
Picture taken at frame 3643
of the high-speed camera
footage. (24.6985 Mpa)



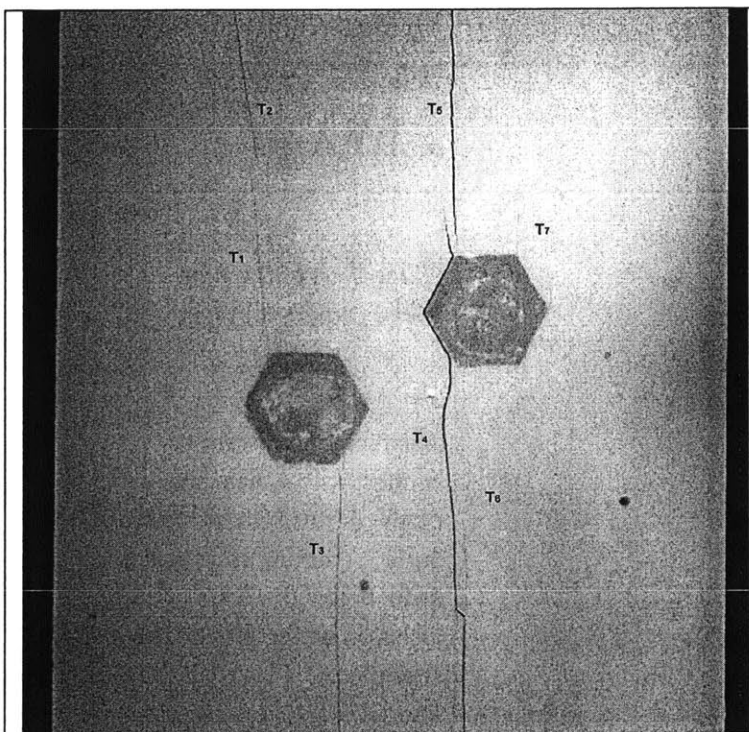
H-60-Cu

Shape = Hexagon
(Inclination = 0°)
Bridging Angle = 60°
Test Repetition = C
Material = Ultracal
Size = 1/2"

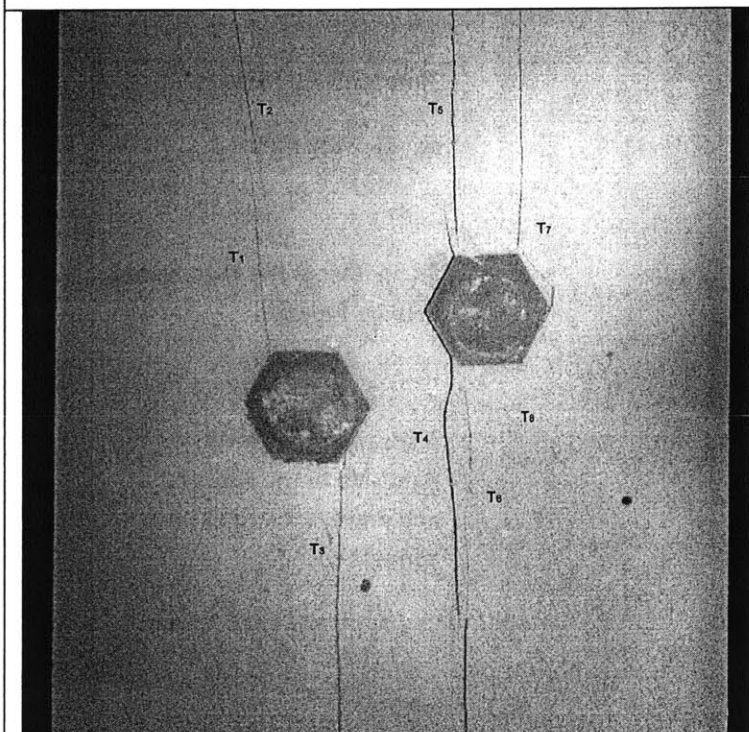


	<p>Time: 0</p> <p>σ: ~0 MPa</p> <p>Picture taken prior to testing.</p>
	<p>Time: 0</p> <p>σ: ~0 MPa</p> <p>Picture taken prior to testing.</p>

	<p>Time: 2m 20.34s</p> <p>σ: ~12.1880 MPa</p> <p>Still image captured with High Speed Camera before High Speed Recording.</p> <p>(Ordered from Left-Right not necessarily chronologically)</p> <p>Tension crack T_1, T_2, and T_3 form above and below the left inclusion. T_4, T_5, T_6, and T_7 form above and below the right inclusion. T_3, T_4, and T_7 exhibit some amount of debonding at the inclusion interface.</p>
	<p>Time: 2m 36.18s</p> <p>σ: ~13.2417 MPa</p> <p>Still image captured with High Speed Camera before High Speed Recording.</p> <p>T_6 extends upward to connect with T_4. A new crack T_8 forms between T_6 and T_7 (debonding).</p>

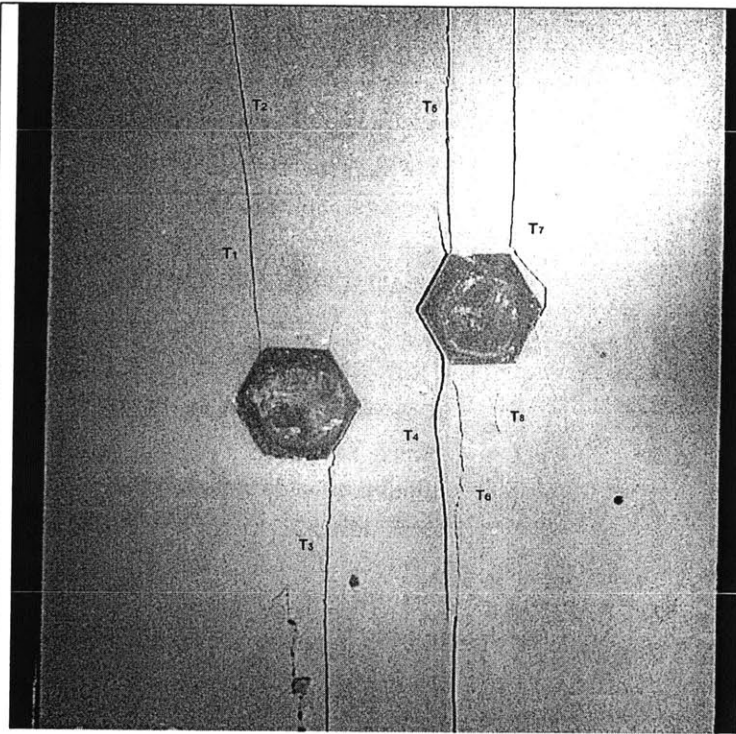


Picture taken at ~12.1880 MPa



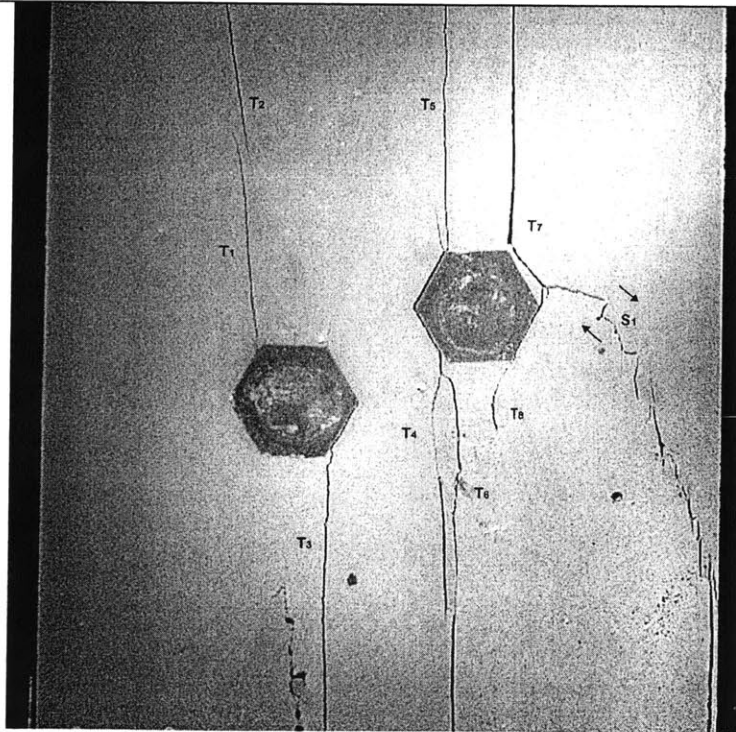
Picture taken ~13.2417 MPa

	<p>Time: 3m 20.450s</p> <p>σ: ~16.1171 MPa</p> <p>Frame 5404 of the High Speed Camera footage.</p> <p>T_5 extends downward to connect with T_4 near the corner of the right inclusion. Surface cracking and spalling occur below the left inclusion on the face of the specimen.</p>
	<p>Time: 3m 21.363s</p> <p>σ: ~16.2424 MPa</p> <p>Frame 840 of the High Speed Camera footage.</p> <p>A shear crack S_1 forms on the right side of the specimen and moves inward to connect with T_7.</p>

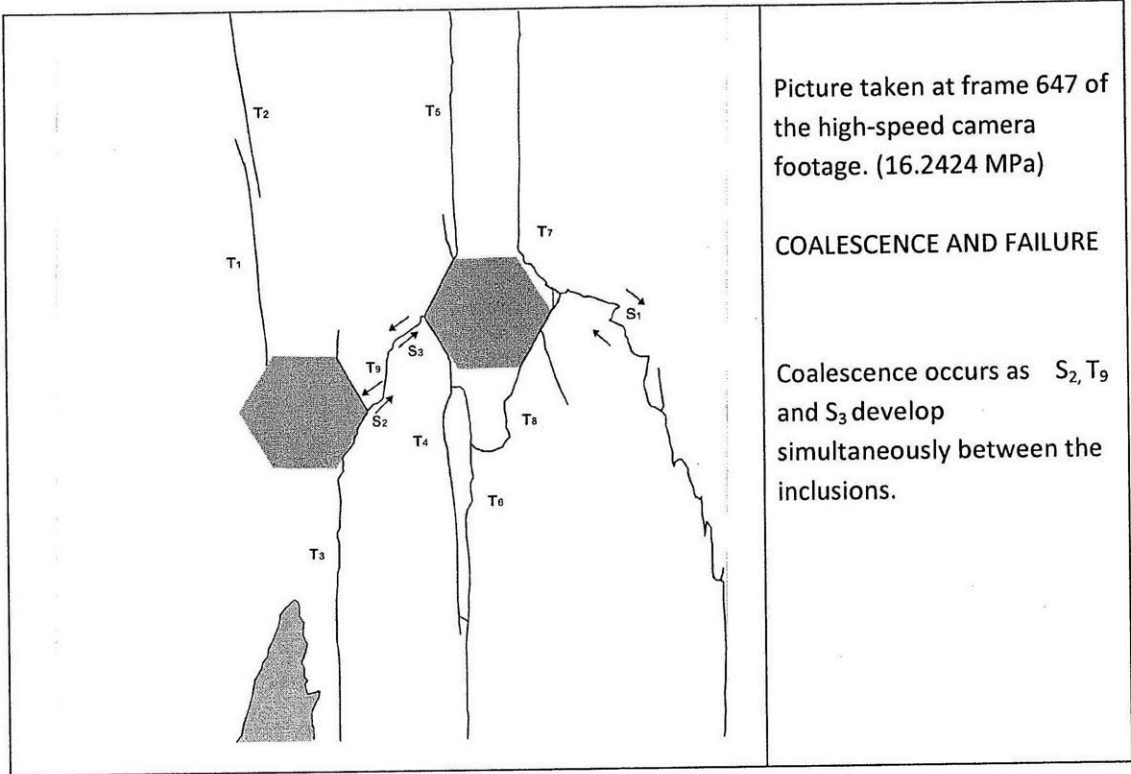


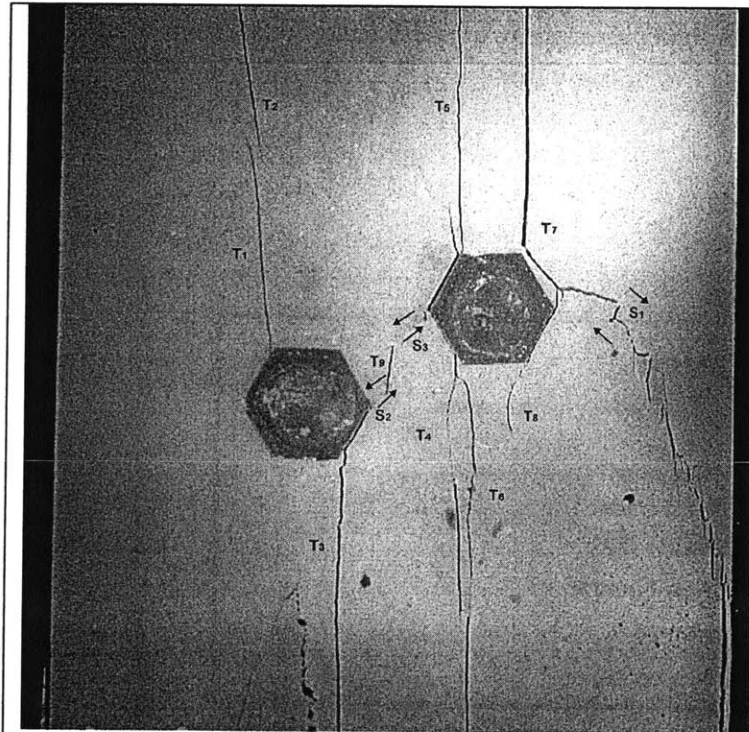
Picture taken at frame 5404 of the High Speed Camera footage.

(16.1171 MPa)



Picture taken at frame 840 of the high-speed camera footage. (16.2424 MPa)





Time: 3m 21.402s

σ : ~16.2424 MPa

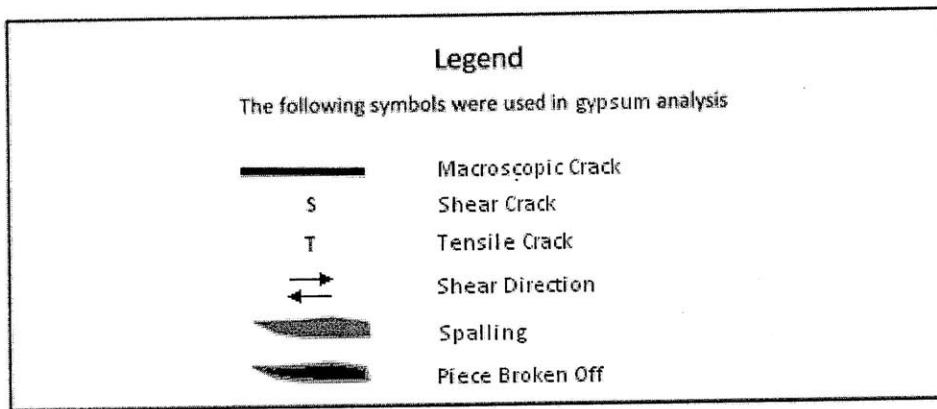
Frame 647 of the High Speed
Camera footage.

COALESCENCE AND FAILURE

APPENDIX E – Half-Inch Diamond Inclusion Pair Analysis

The following appendix section presents the most representative test repetitions for the diamond pair test series.

Legend Used:



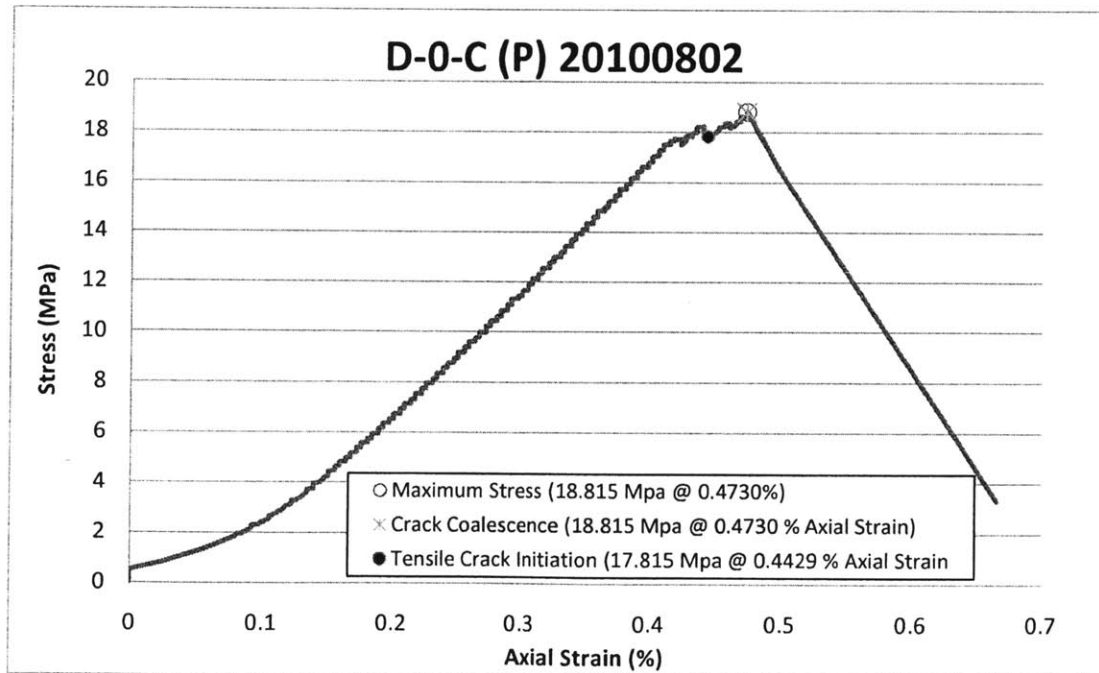
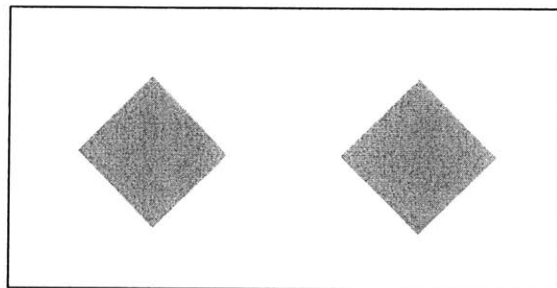
Notes:

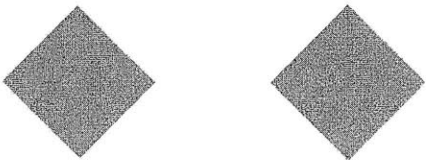
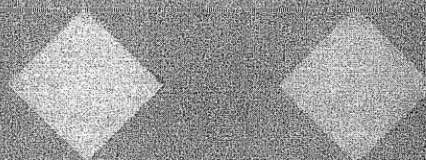
- Subscripts which do not indicate sequence are noted in the description.
- Times and stresses correlate to when the picture was taken, not when the events happened.
- Shear cracks with an arrow indicate the direction of shear crack development. Shear cracks without an arrow denote cracks in which the direction could not be determined.

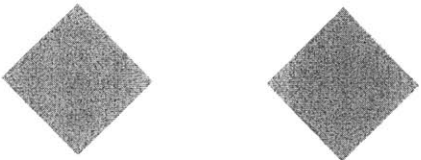
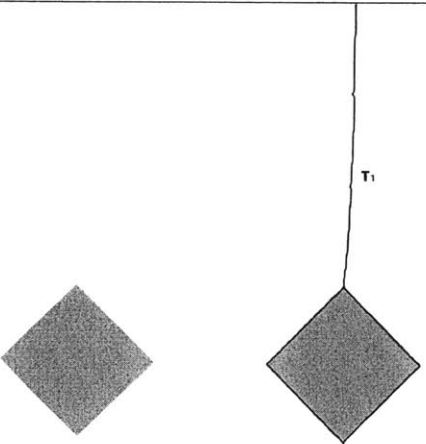
PLASTER

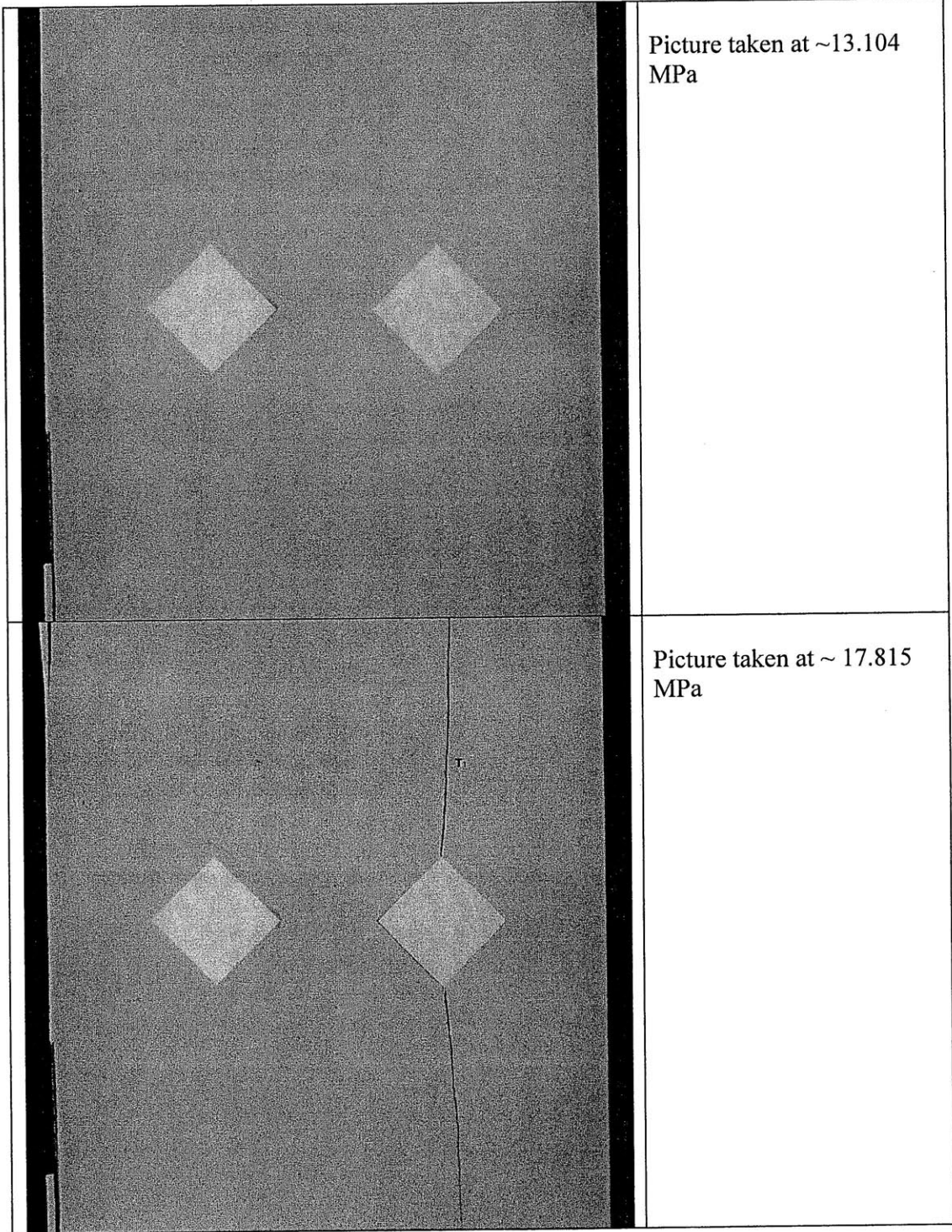
D-0-Cp

Shape = Diamond
(Inclination = 0°)
Bridging Angle = 0°
Test Repetition = C
Material = Plaster
Size = 1/2"



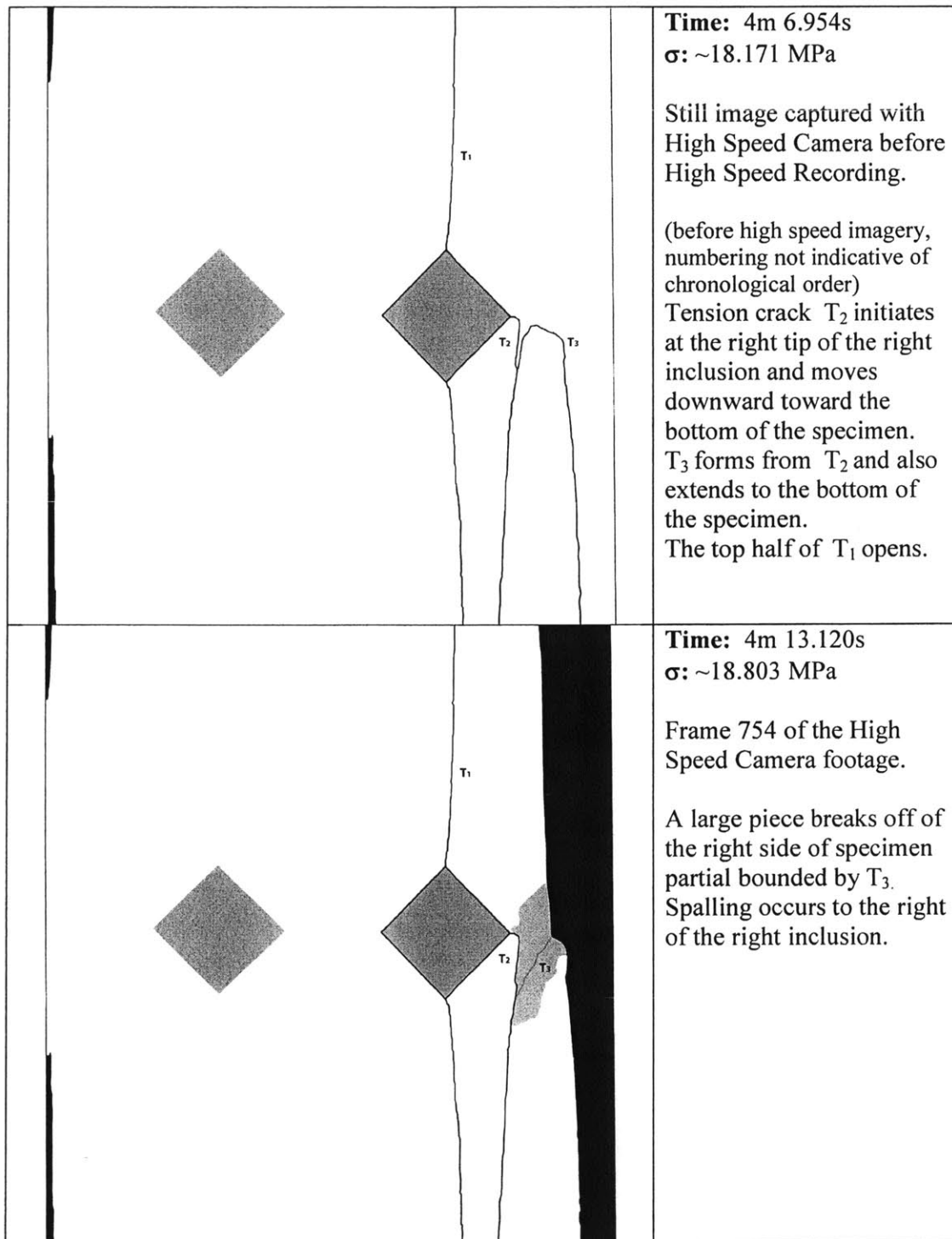
	<p>Time: 0m 0s σ: ~0 MPa</p> <p>Picture taken prior to testing.</p>
	<p>Time: 0m 0s σ: ~0 MPa</p> <p>Picture taken prior to testing.</p>

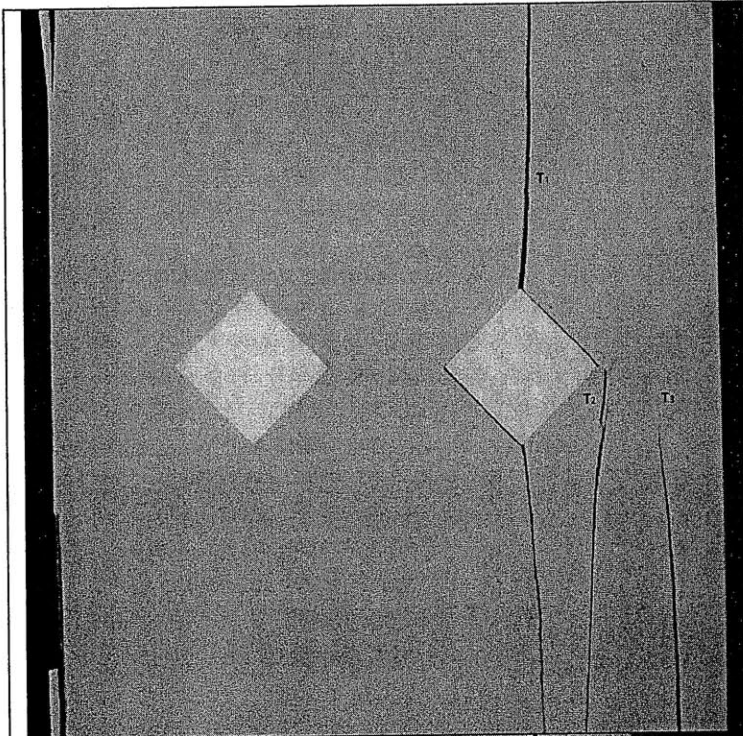
	<p>Time: 2m 49.254s σ: ~13.104 MPa</p> <p>Still image captured with High Speed Camera before High Speed Recording.</p> <p>A small piece breaks off of the bottom left hand side of the specimen.</p>
	<p>Time: 4m 5.058s σ: ~17.815 MPa</p> <p>Still image captured with High Speed Camera before High Speed Recording.</p> <p>T_1 forms along the right inclusion causing complete debonding of the entire inclusion (tensile debonding).</p>



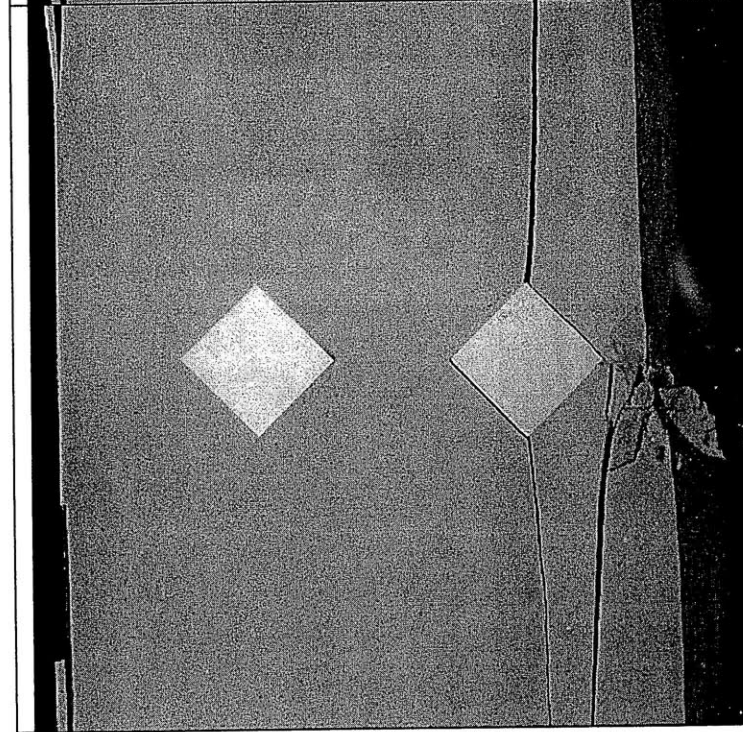
Picture taken at ~13.104 MPa

Picture taken at ~ 17.815 MPa

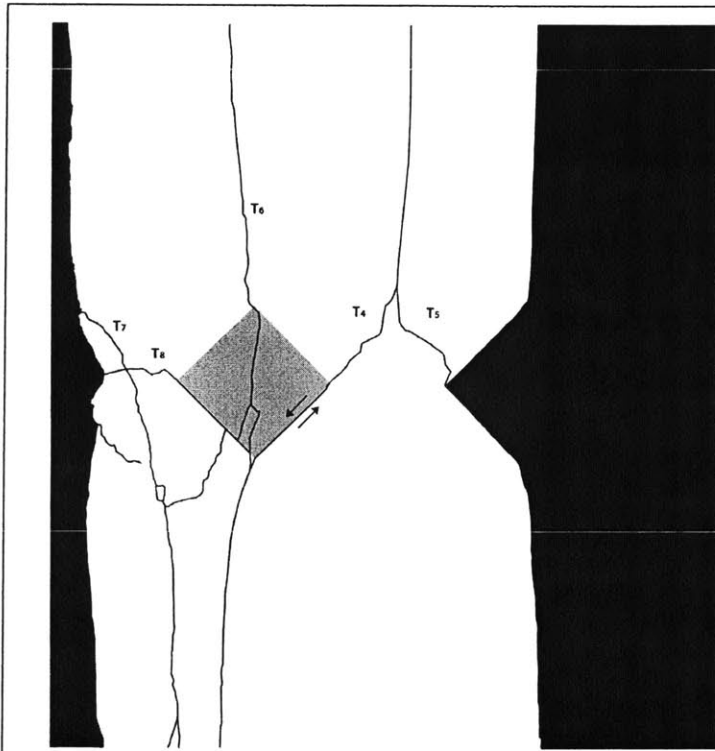




Picture taken at ~ 18.171 MPa



Picture taken at frame 754 of the high-speed camera footage. (18.803 Mpa)



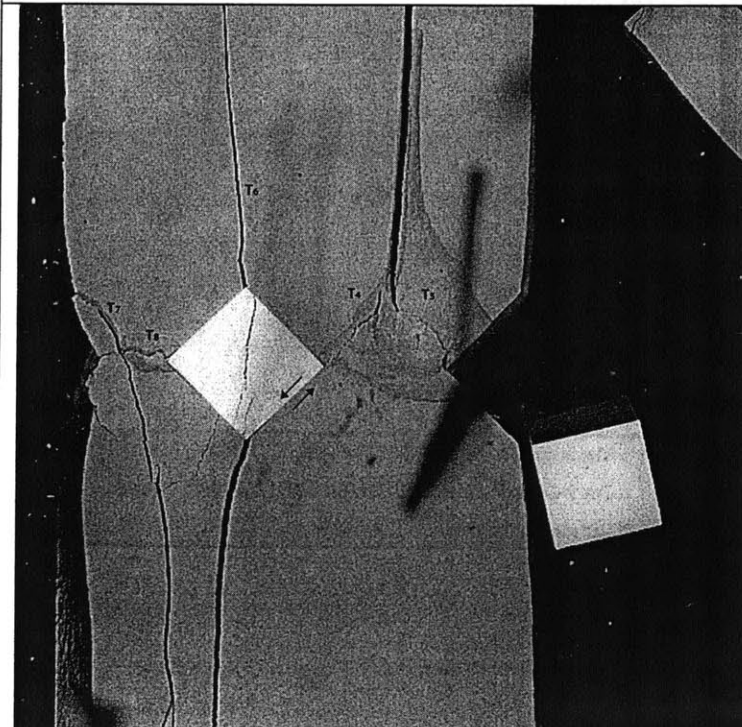
Time: 4m 13.23s

σ : ~18.815 MPa

Frame 206 of the High Speed Camera footage.

COALESCENCE + FAILURE

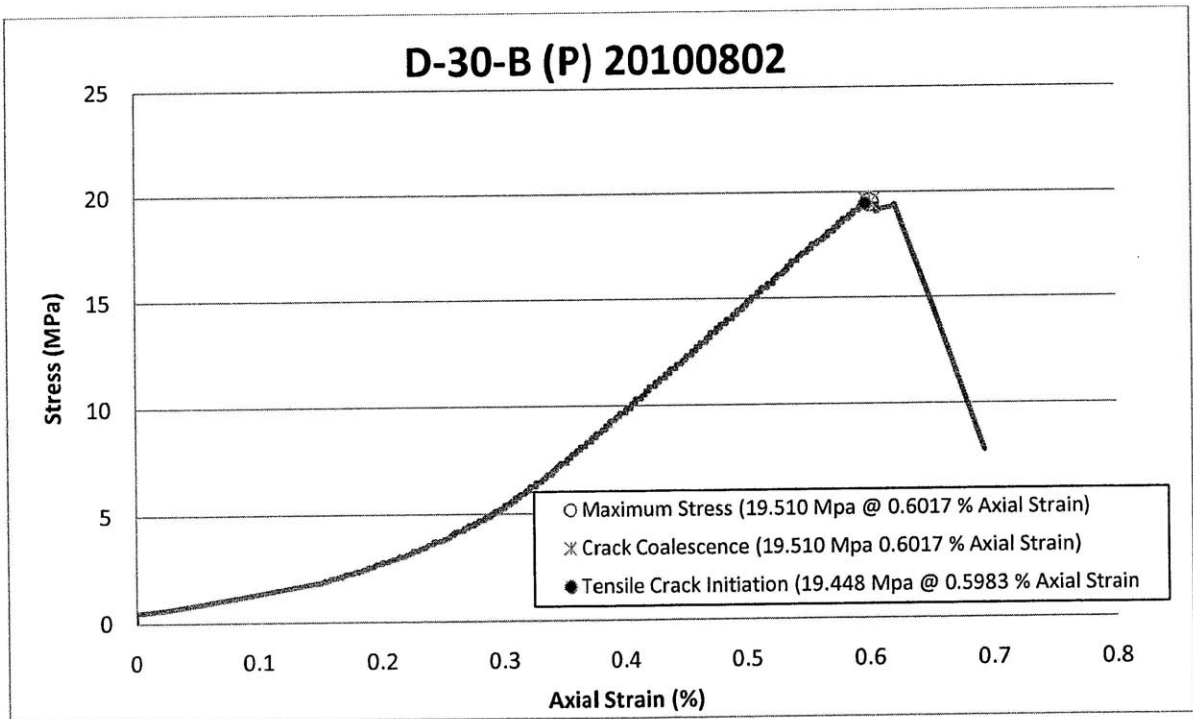
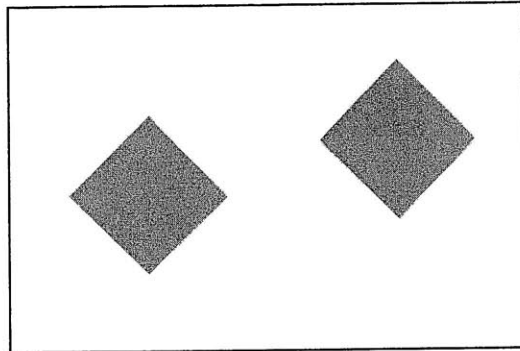
Tension crack T_4 forms along the middle of the specimen and extends down to the right side of the left inclusion. Shear debonding occurs along the right side of the left inclusion and T_4 extends to the bottom of the specimen (shear debonding). T_5 initiates from the left side of the right inclusion and connects with T_4 . T_6 forms above the left inclusion and moves directly through the inclusion matrix to T_4 (tensile debonding). T_7 and T_8 form to the left of the left inclusion. Large pieces break off of both sides of the specimen.

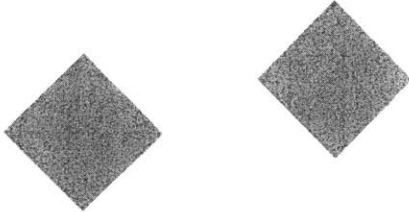
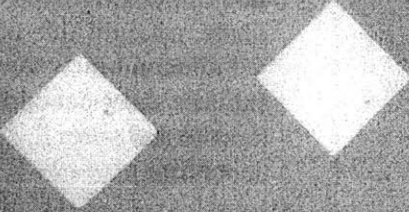


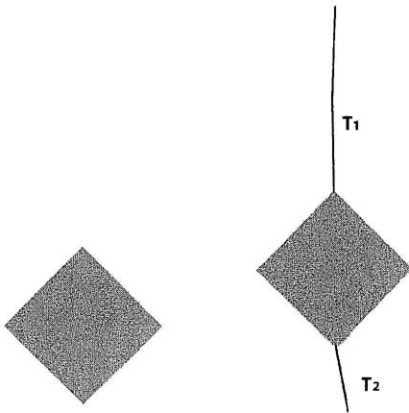
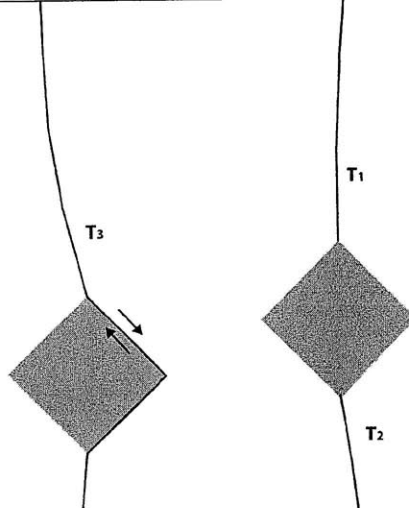
Picture taken at frame 206 of the high-speed camera footage. (18.815 Mpa)

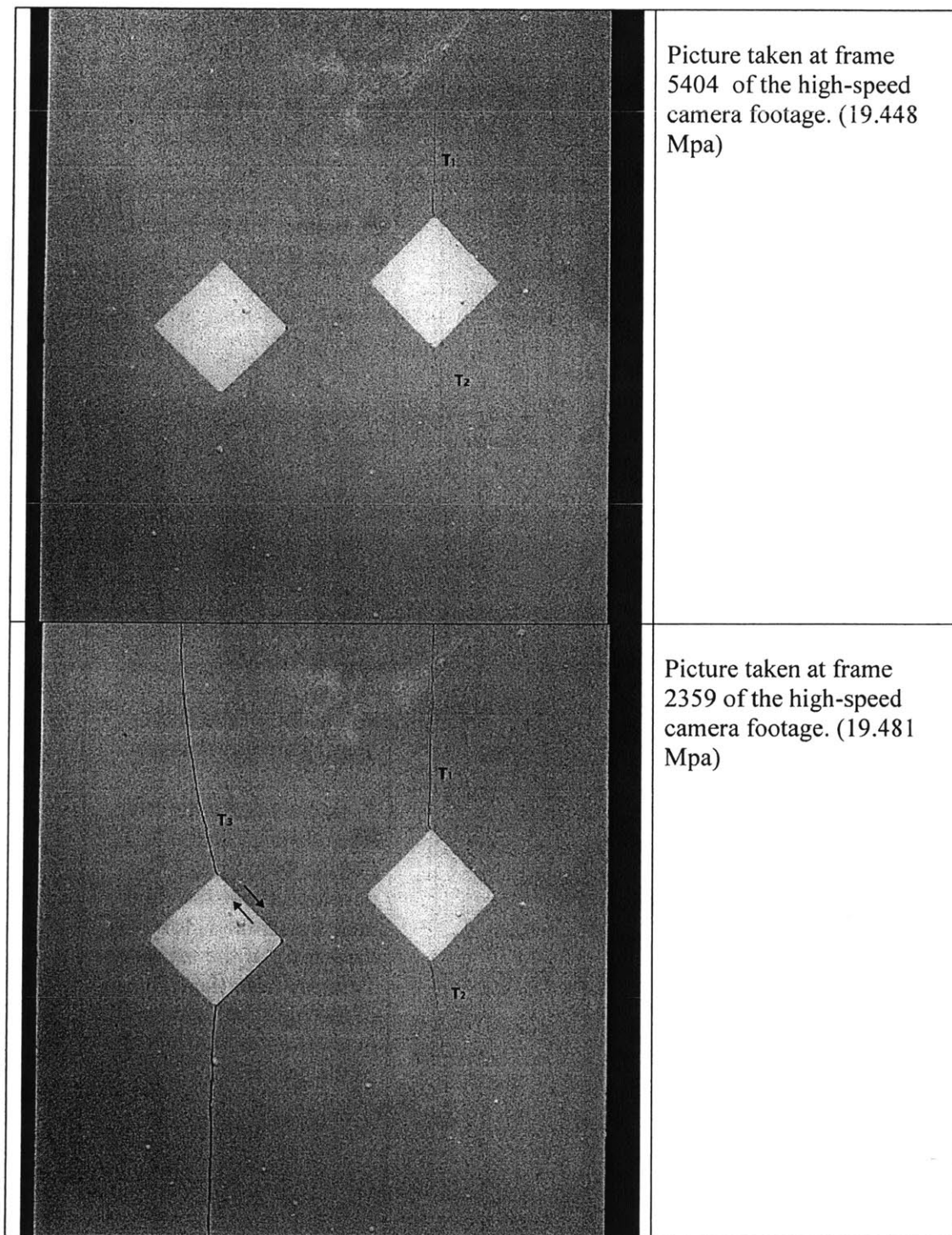
D-30-Bp

Shape = Diamond
(Inclination = 0°)
Bridging Angle = 30°
Test Repetition = B
Material = Plaster
Size = 1/2"

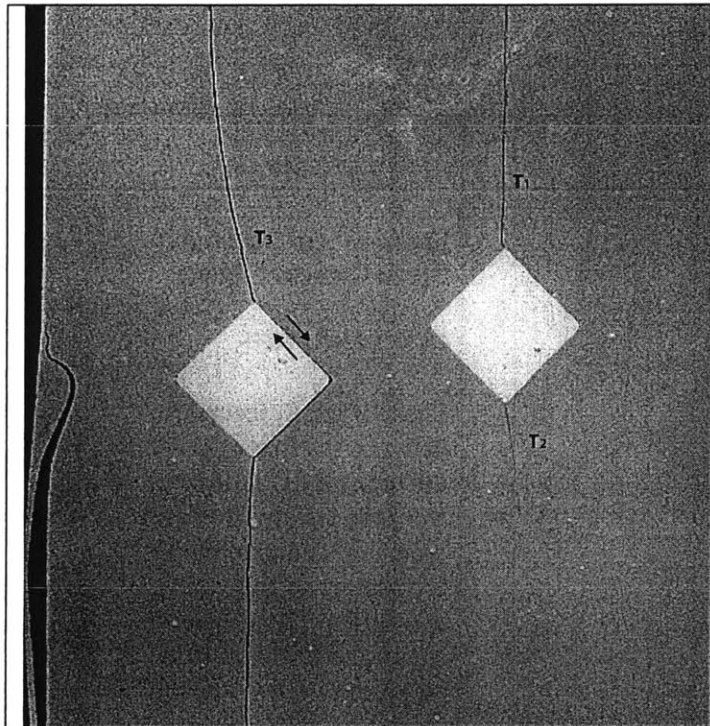


	<p>Time: 0m 0s σ: ~0 MPa</p> <p>Picture taken prior to testing.</p>
	<p>Time: 0m 0s σ: ~0 MPa</p> <p>Picture taken prior to testing.</p>

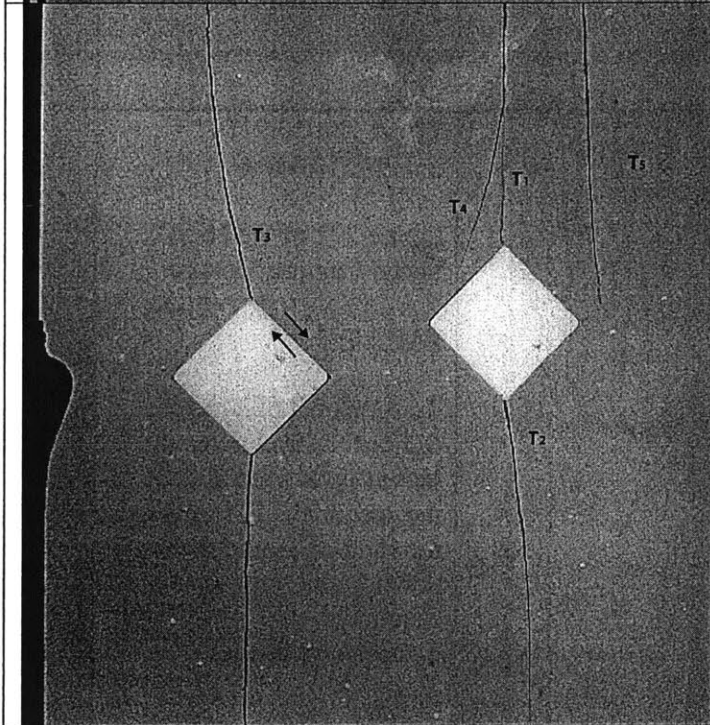
	<p>Time: 4m 35.895s σ: ~19.448 MPa</p> <p>Frame 5404 of the High Speed Camera footage</p> <p>TENSILE CRACK INITIATION</p> <p>Tension cracks T_1 and T_2 form on the top and bottom corner nodes of the right inclusion.</p>
	<p>Time: 4m 36.504s σ: ~19.481 MPa</p> <p>Frame 2359 of the High Speed Camera footage.</p> <p>T_3 forms along the right side of the left inclusion. There top right side of the left diamond inclusion exhibits shear debonding (tensile and shear debonding).</p>



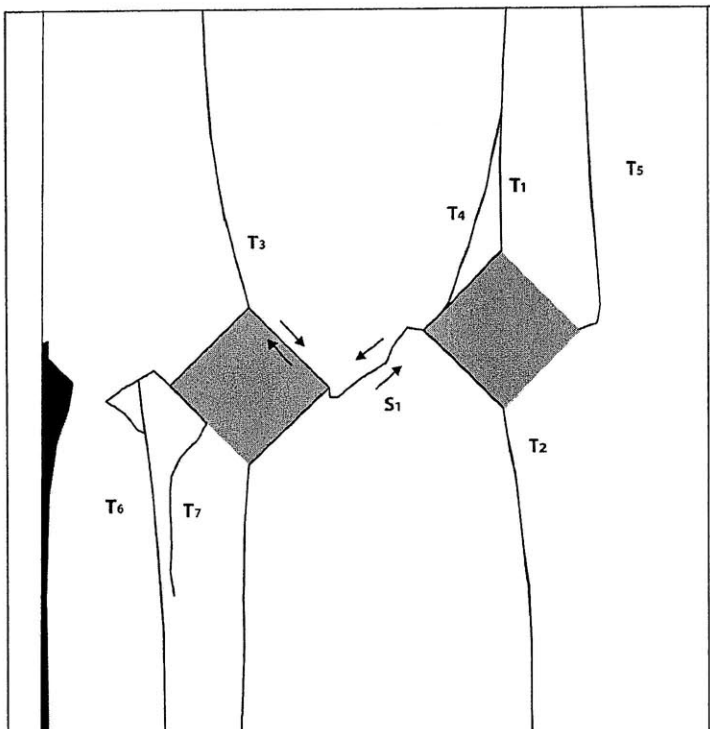
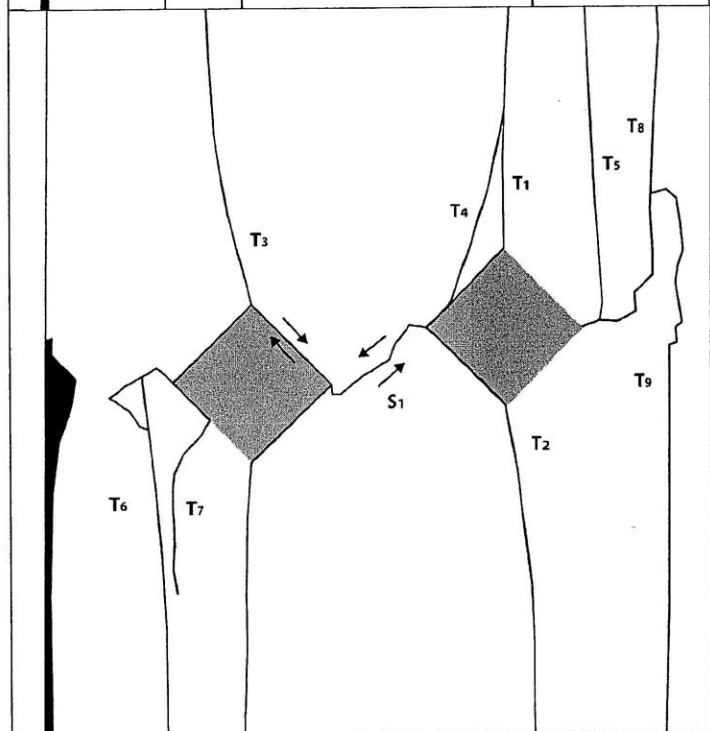
	<p>Time: 4m 36.646s σ: ~19.493 MPa</p> <p>Frame 1654 of the High Speed Camera footage.</p> <p>A small piece breaks off of the bottom left section of the specimen.</p>
	<p>Time: 4m 36.886s σ: ~19.510 MPa</p> <p>Frame 450 of the High Speed Camera footage.</p> <p>T₁ extends down the left side of the inclusion to T₂ (tensile debonding). T₄ develops above the right inclusion from T₁ toward the left tip of the inclusion. T₅ forms from the right tip of the right inclusion and extends up toward the top of the specimen.</p>

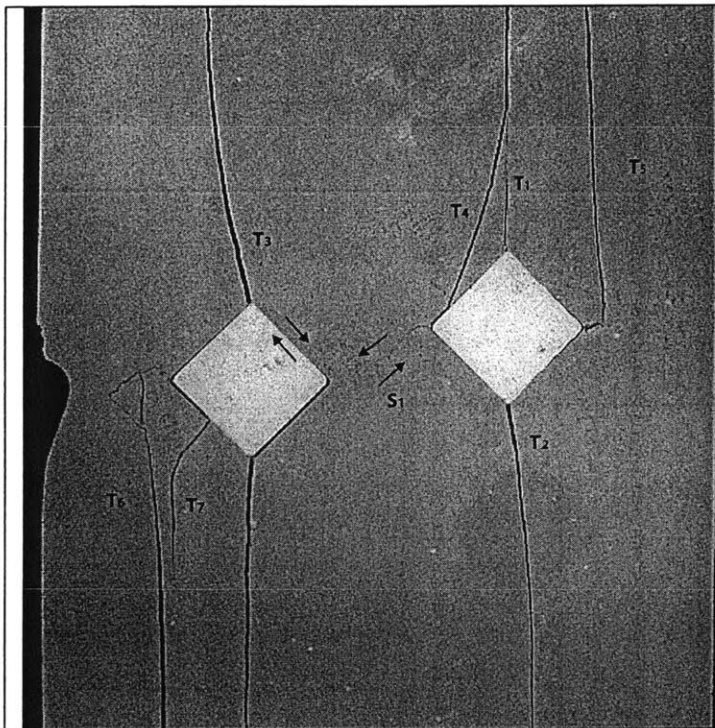


Picture taken at frame 1654 of the high-speed camera footage. (19.493Mpa)

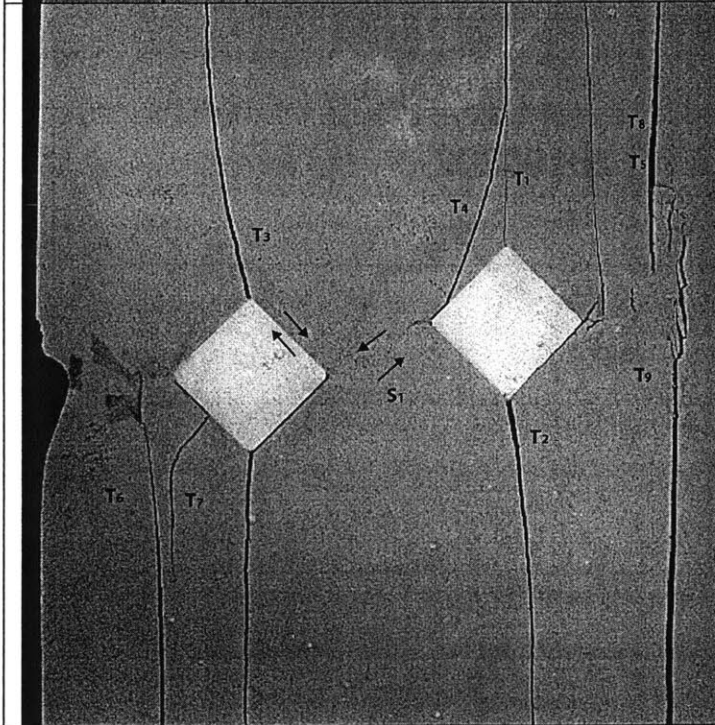


Picture taken at frame 450 of the high-speed camera footage. (19.510 Mpa)

 <p>The diagram shows a specimen with two diamond-shaped inclusions. A shear crack S₁ is located between the inner tips of the inclusions. Cracks T₁ through T₇ are shown. T₁ and T₂ are on the right inclusion, T₃ and T₄ are on the left inclusion, and T₆ and T₇ are on the left side of the specimen. Arrows indicate the direction of crack growth.</p>	<p>Time: 4m 36.915s σ: ~19.510 MPa</p> <p>Frame 309 of the High Speed Camera footage.</p> <p>COALESCENCE</p> <p>Shear crack S₁ forms between the inner tips of the inclusions. T₆ forms from the left tip of the left inclusion and extends to the bottom of the specimen. Then T₇ forms below the left inclusion and moves down as well. T₂ and T₃ open up.</p>
 <p>The diagram shows the specimen at a later stage. Cracks T₁ through T₉ are shown. T₁ through T₇ are on the left inclusion, T₈ and T₉ are on the right inclusion. S₁ is still present. Arrows indicate the direction of crack growth.</p>	<p>Time: 4m 36.918s σ: ~19.510 MPa</p> <p>Frame 292 of the High Speed Camera footage.</p> <p>FAILURE</p> <p>T₈ forms off of T₅ to the right of the inclusion and moves up toward the top of the specimen. T₉ forms to the right of T₈ and moves down to the bottom of the specimen. T₂ opens up further.</p>



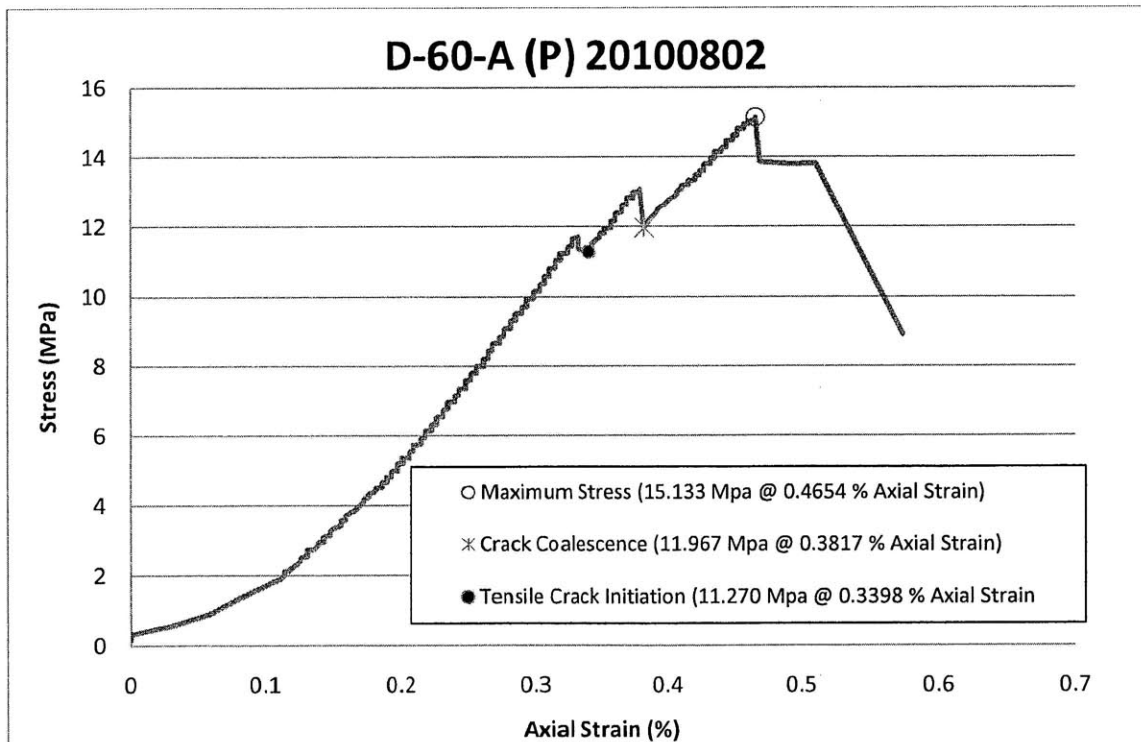
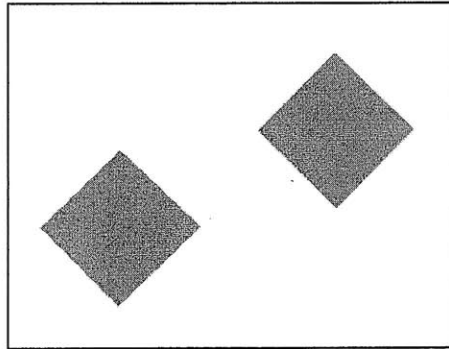
Picture taken at frame 309 of the high-speed camera footage. (19.510 Mpa)

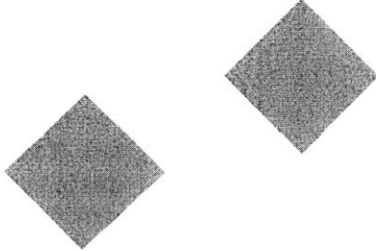
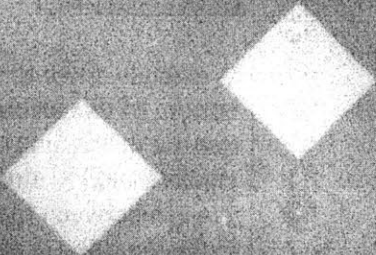


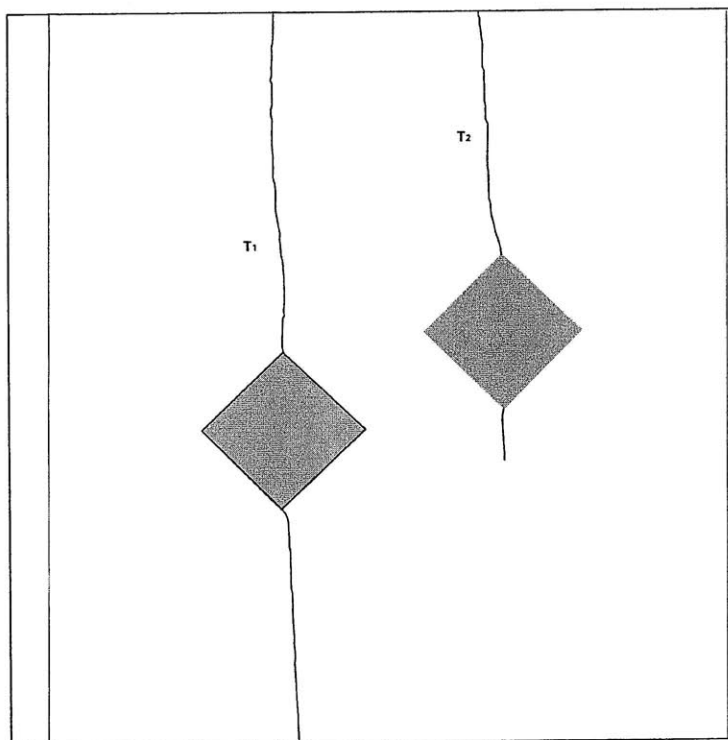
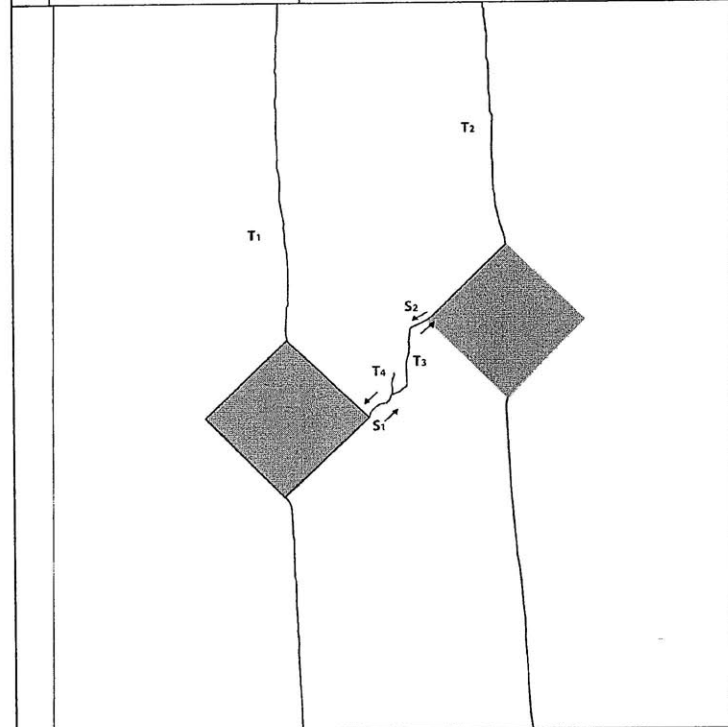
Picture taken at frame 292 of the high-speed camera footage. (19.510 Mpa)

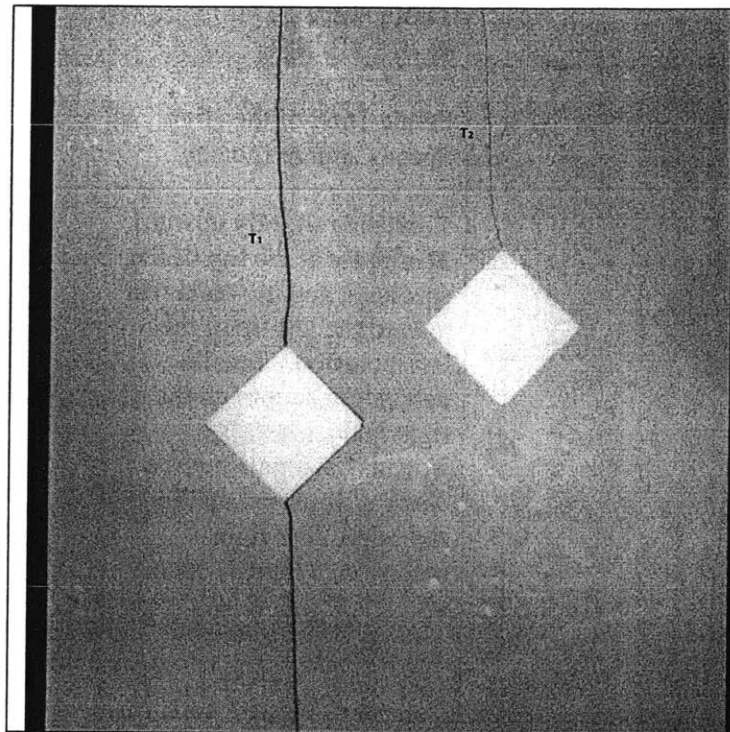
D-60-Ap

Shape = Diamond
(Inclination = 0°)
Bridging Angle = 60°
Test Repetition = A
Material = Plaster
Size = 1/2"

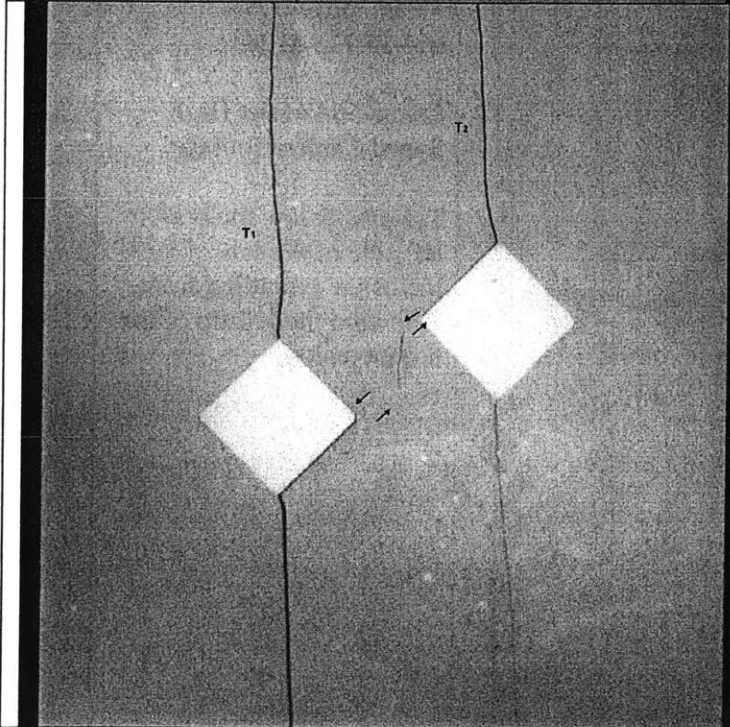


	<p>Time: 0m 0s σ: ~0 MPa</p> <p>Picture taken prior to testing.</p>
	<p>Time: 0m 0s σ: ~0 MPa</p> <p>Picture taken prior to testing.</p>

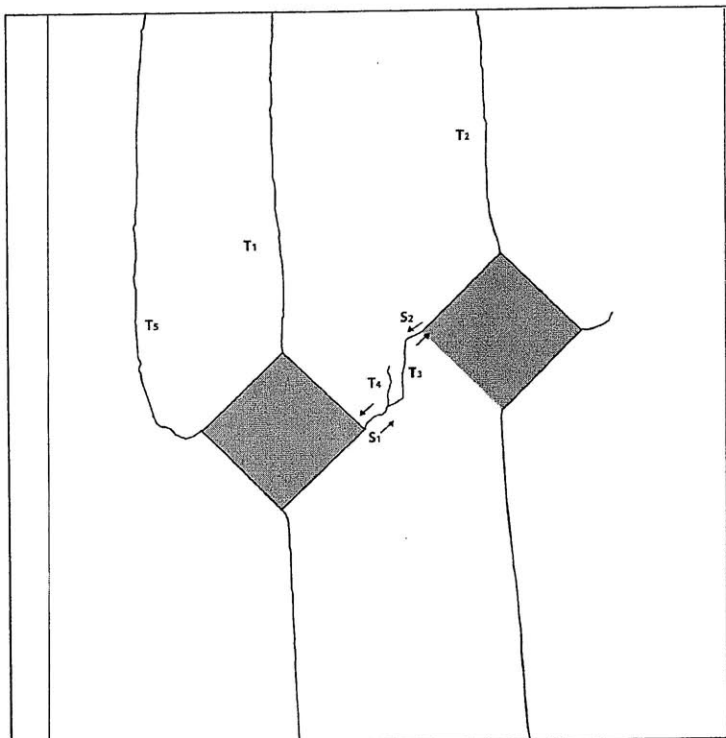
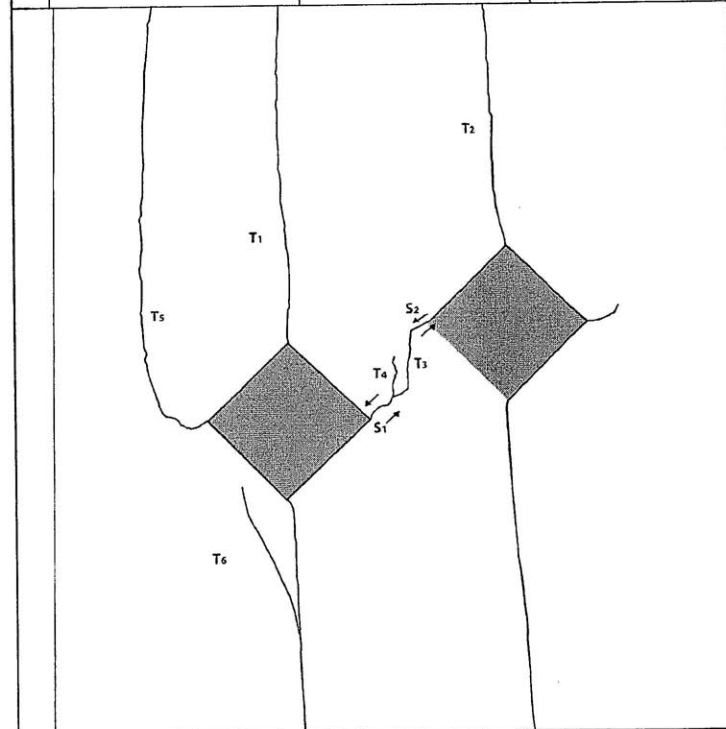
	<p>Time: 2m 13.062s σ: ~11.270 MPa</p> <p>Still image captured with High Speed Camera before High Speed Recording.</p> <p>TENSILE CRACK INITIATION</p> <p>(Before High Speed, Numbering not necessarily chronological). Tension crack T_1 forms along the left inclusion extending from the top to the bottom of the specimen and complete debonding on the left inclusion. (tensile debonding). T_2 forms above and below the right inclusion but no debonding is apparent.</p>
	<p>Time: 2m 33.282s σ: ~11.967 MPa</p> <p>Still image captured with High Speed Camera before High Speed Recording.</p> <p>COALESCENCE</p> <p>T_2 extends down to the bottom of the specimen (tensile debonding). Shear cracks S_1 and S_2 along with T_3 form between the inclusion tips. A small tension crack T_4 begins to form above S_1 parallel to T_3.</p>

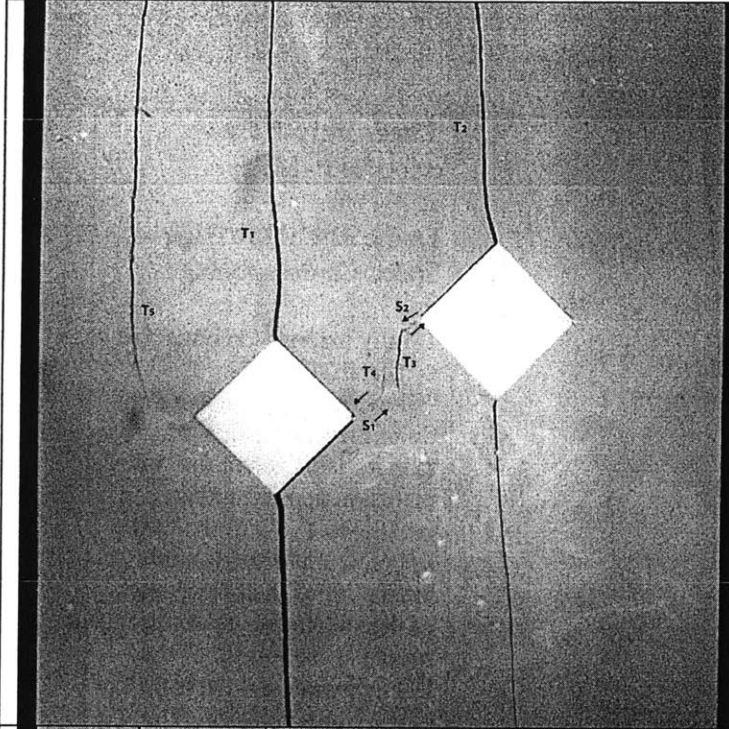


Picture taken at ~ 11.270 MPa

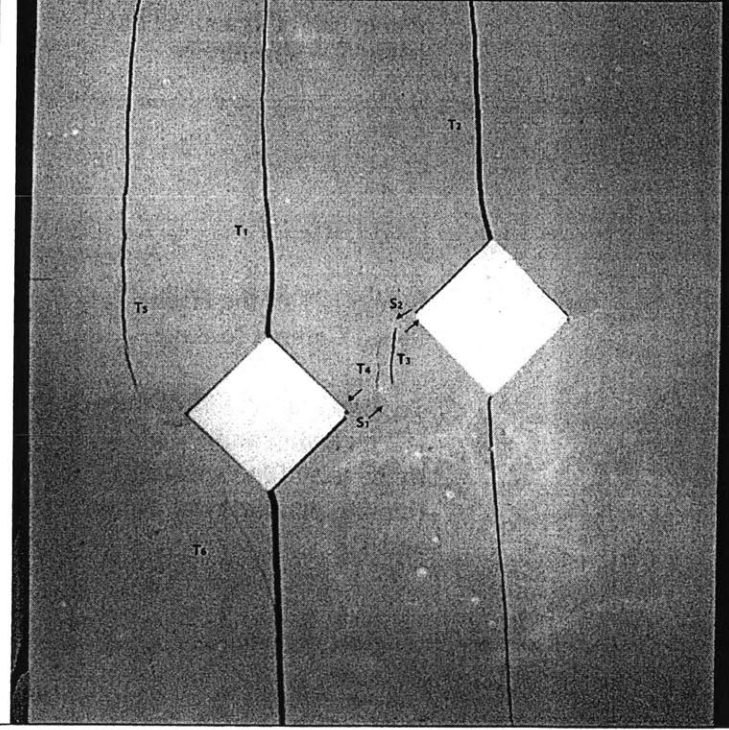


Picture taken at ~ 11.967 MPa

	<p>Time: 3m 3.357s σ: ~15.119 MPa</p> <p>Frame 1668 of the High Speed Camera footage.</p> <p>T₄ extends slightly upward. T₅ initiates at the top of the specimen and moves down toward the left tip of the left inclusion. Tensile debonding occurs on the right inclusion as T₂ extends. A small surface crack is observed on the right tip of the right inclusion. T₁ and T₂ open up.</p>
	<p>Time: 3m 3.577s σ: ~15.113 MPa</p> <p>Frame 564 of the High Speed Camera footage.</p> <p>T₆ forms below the bottom left side of the left inclusion extending from T₁ toward the left tip of the left inclusion.</p>

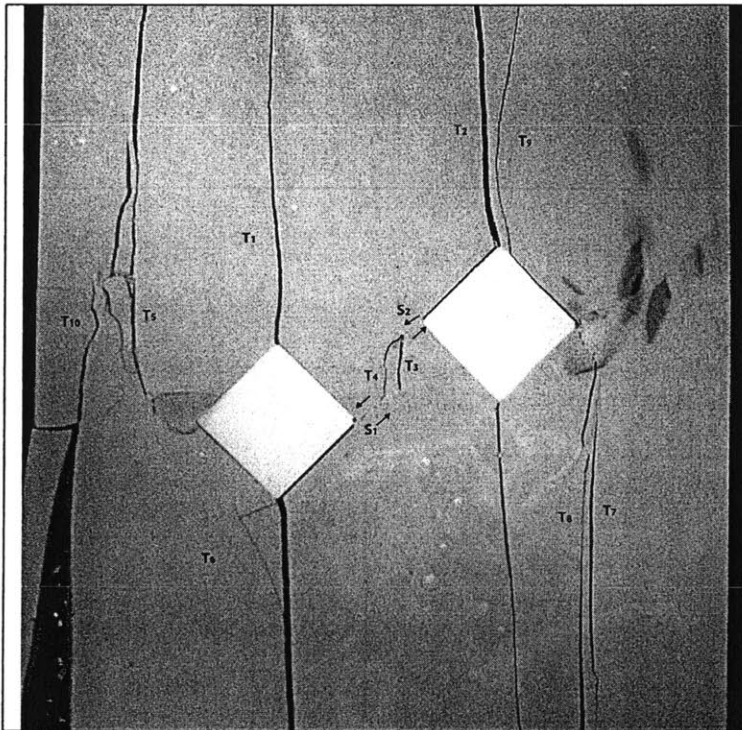


Picture taken at frame 1668 of the high-speed camera footage. (15.119Mpa)

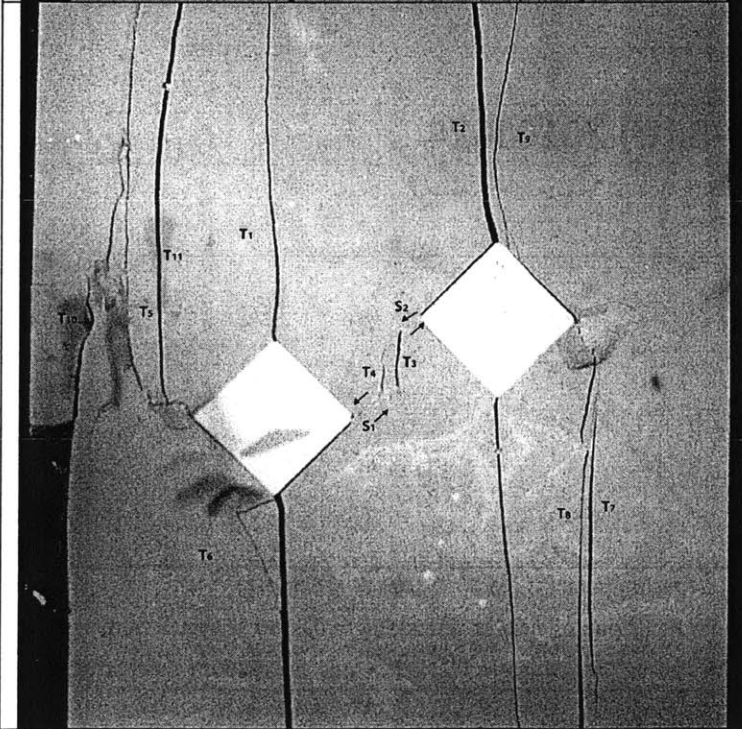


Picture taken at frame 564 of the high-speed camera footage. (15.113 Mpa)

	<p>Time: 3m 3.627s σ: ~15.133 MPa</p> <p>Frame 314 of the High Speed Camera footage.</p> <p>T₄ fully extends to connect to S₂. T₇ and T₈ initiate “simultaneously” at the right tip of the right inclusion. T₉ then initiates above the right inclusion approximately parallel to T₂. T₁₀ forms to the left of T₅ and a small piece breaks off of the bottom left of the specimen. Spalling occurs at the left tip of the left inclusion and the right tip of the right inclusion. The bottom half of T₁ and the top half of T₂ opens further.</p>
	<p>Time: 3m 3.666s σ: ~15.133 MPa</p> <p>FAILURE</p> <p>Frame 121 of the High Speed Camera footage.</p> <p>T₁₁ forms to the left of the left inclusion and extends to the top of the specimen running parallel with T₅ and T₁.</p>



Picture taken at frame 314 of the high-speed camera footage. (15.133Mpa)

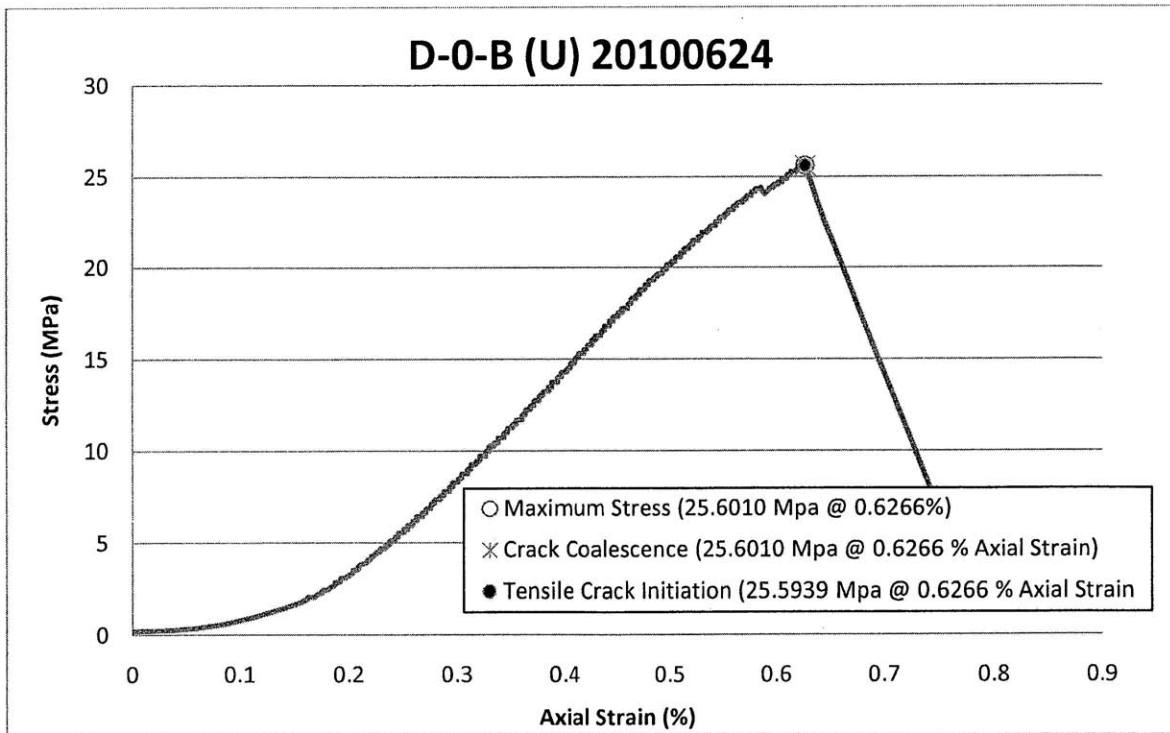
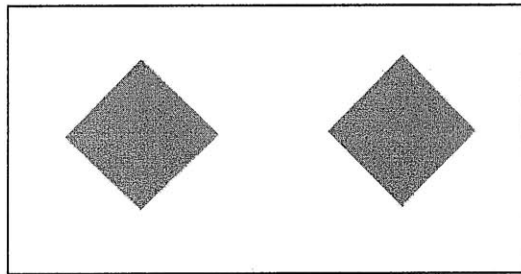


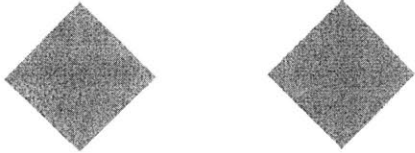
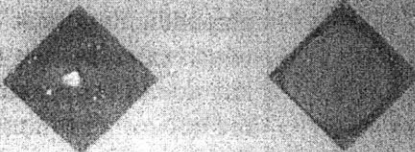
Picture taken at frame 121 of the high-speed camera footage. (15.133 Mpa)

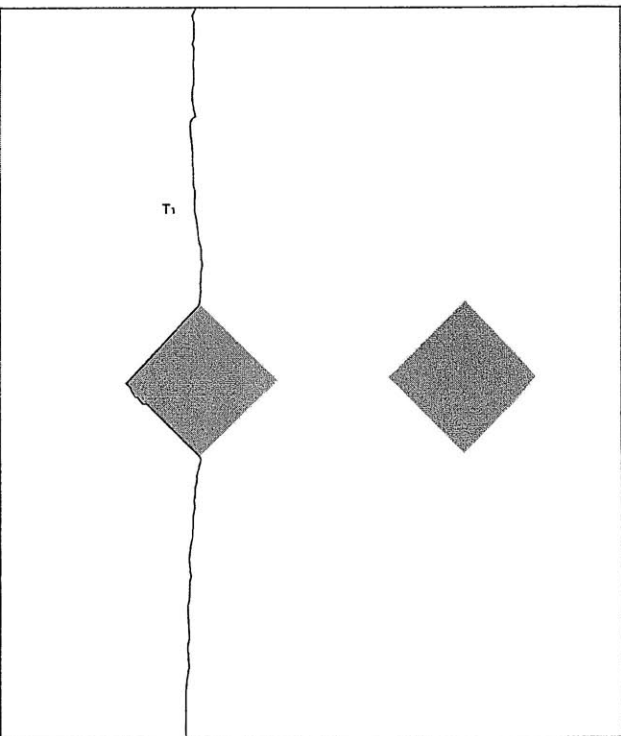
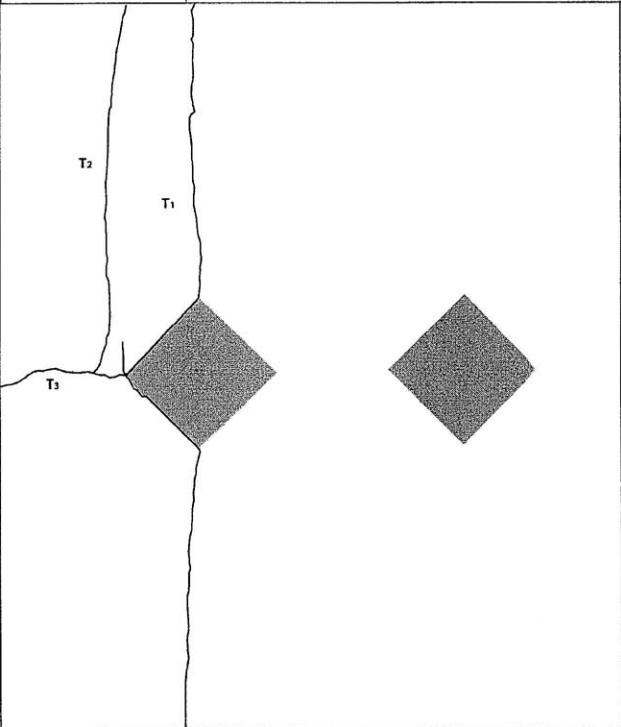
ULTRACAL

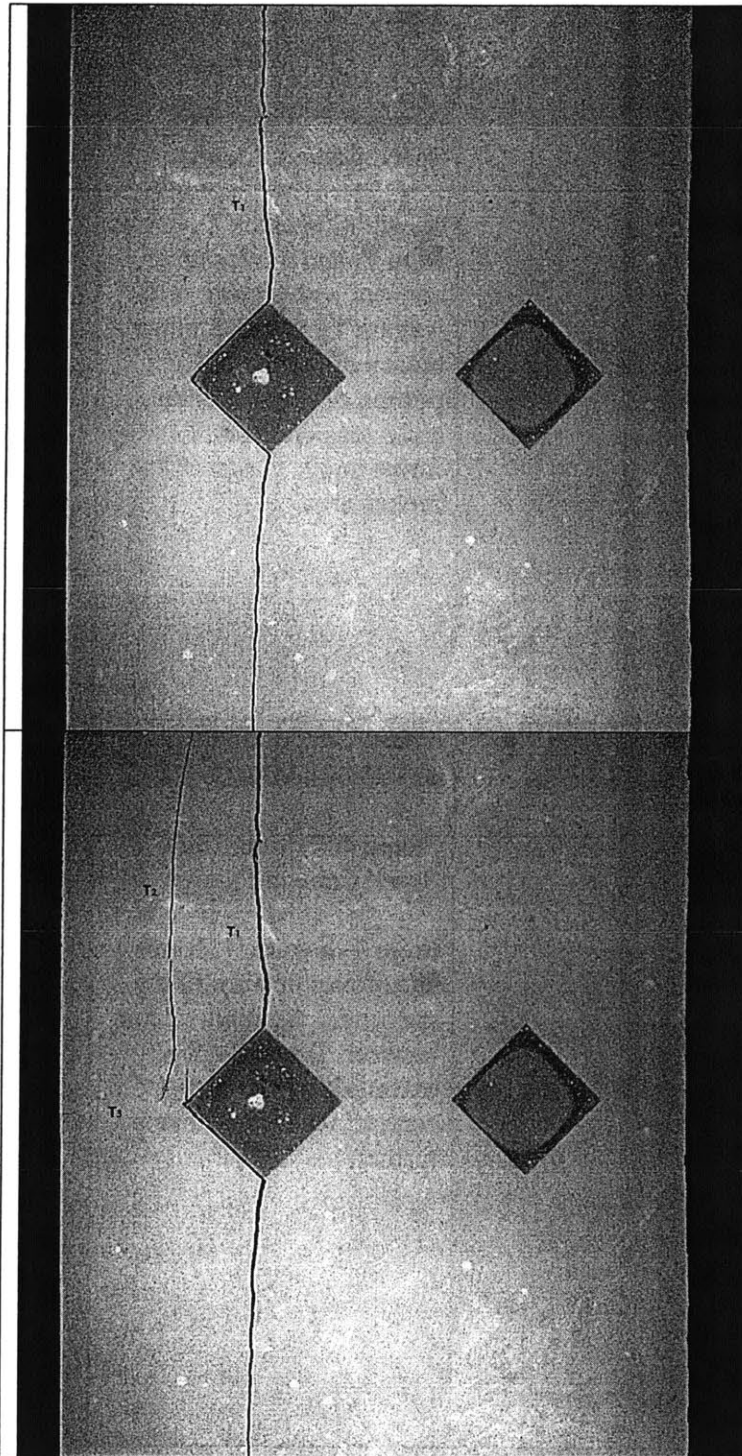
D-0-Bu

Shape = Diamond
(Inclination = 0°)
Bridging Angle = 0°
Test Repetition = B
Material = Ultracal
Size = 1/2"



	<p>Time: 0m 0s σ: ~0 MPa</p> <p>Picture taken prior to testing.</p>
	<p>Time: 0m 0s σ: ~0 MPa</p> <p>Picture taken prior to testing.</p>

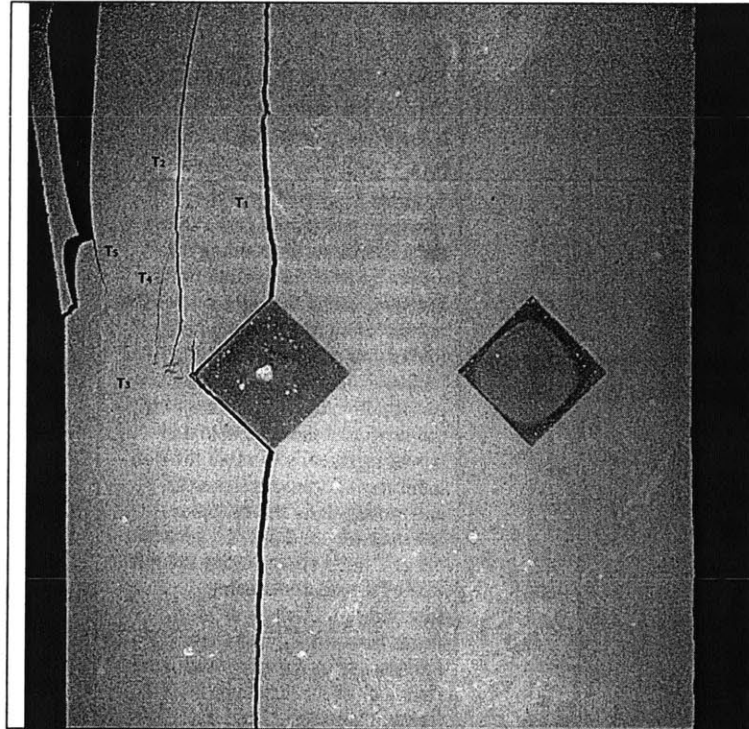
 <p>The diagram shows a vertical specimen with two diamond-shaped inclusions. A vertical crack labeled T_1 is shown on the left side of the left inclusion, extending from the top edge down to the top of the inclusion.</p>	<p>Time: 5m 53.7210s σ: ~25.5939 MPa</p> <p>Frame 847 of the High Speed Camera footage.</p> <p>Tension crack T_1 propagates down the left side of the specimen along the left side of the left inclusion (debonding).</p>
 <p>The diagram shows the same specimen as above. A vertical crack T_1 is shown on the left side of the left inclusion. A horizontal crack T_2 is shown to the left of the left inclusion, parallel to T_1. A vertical crack T_3 is shown on the left side of the specimen, extending from the left edge to the left corner of the left inclusion. T_2 connects to T_3 at the left corner of the left inclusion. T_1 is shown slightly open.</p>	<p>Time: 5m 53.7338s σ: ~25.5939 MPa</p> <p>Frame 783 of the High Speed Camera footage.</p> <p>Tension crack T_2 forms to the left (parallel) to T_1 and then connects to a perpendicular crack T_3 which extends from the left side of the specimen to the left corner of the left specimen. T_1 opens slightly.</p>



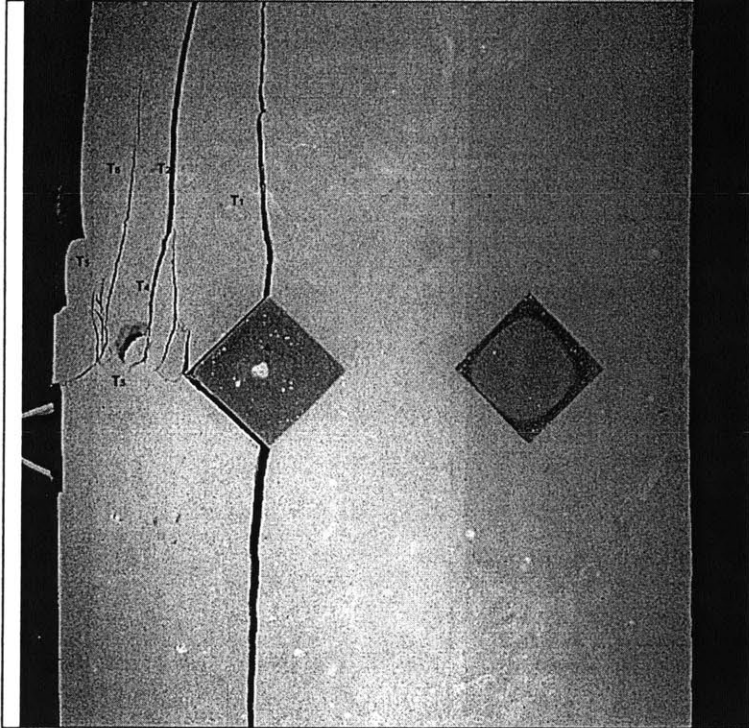
Picture taken at frame 847 of the high-speed camera footage. (25.5939 MPa)

Picture taken at frame 783 of the high-speed camera footage. (25.5939 MPa)

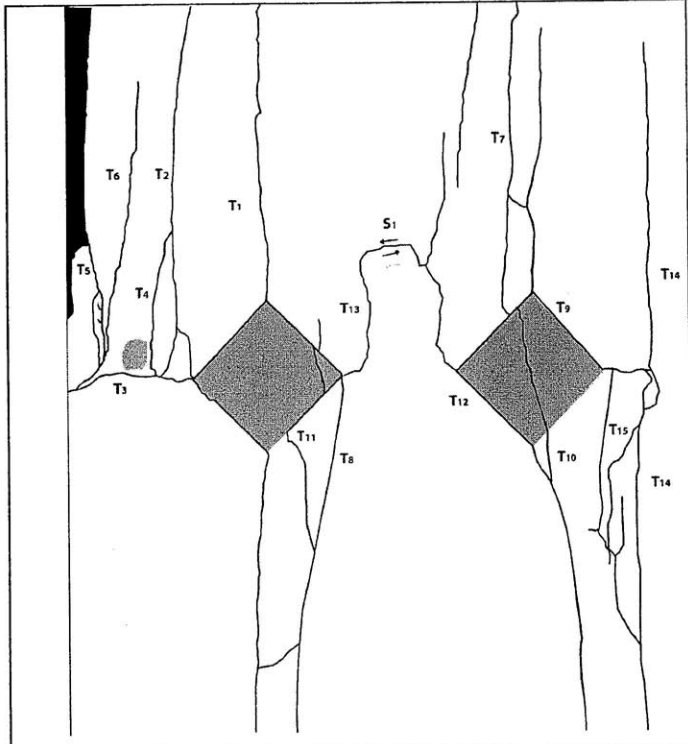
	<p>Time: 5m 53.7548s σ: ~25.5939 MPa</p> <p>Frame 678 of the High Speed Camera footage.</p> <p>An addition crack T_4 forms from T_3 and moves up to connect with a point midway up T_2. A small piece breaks of the top left portion of the specimen and a tension crack T_5 forms on the corner of the broken area.</p>
	<p>Time: 5m 53.8090s σ: ~25.601 MPa</p> <p>Frame 407 of the High Speed Camera footage.</p> <p>From T_3 a crack T_6 forms and moves upward in the specimen. Spalling occurs between T_6 and T_4. T_5 extends downward to connect with T_6. T_1 opens further.</p>



Picture taken at frame 678 of the high-speed camera footage. (25.5939 MPa)

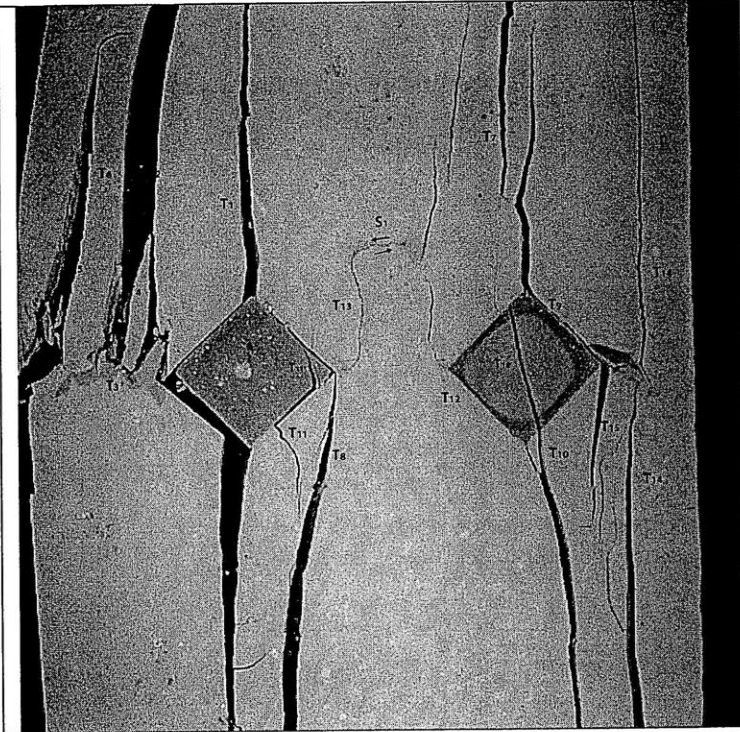


Picture taken at frame 407 of the high-speed camera footage. (25.601 MPa)



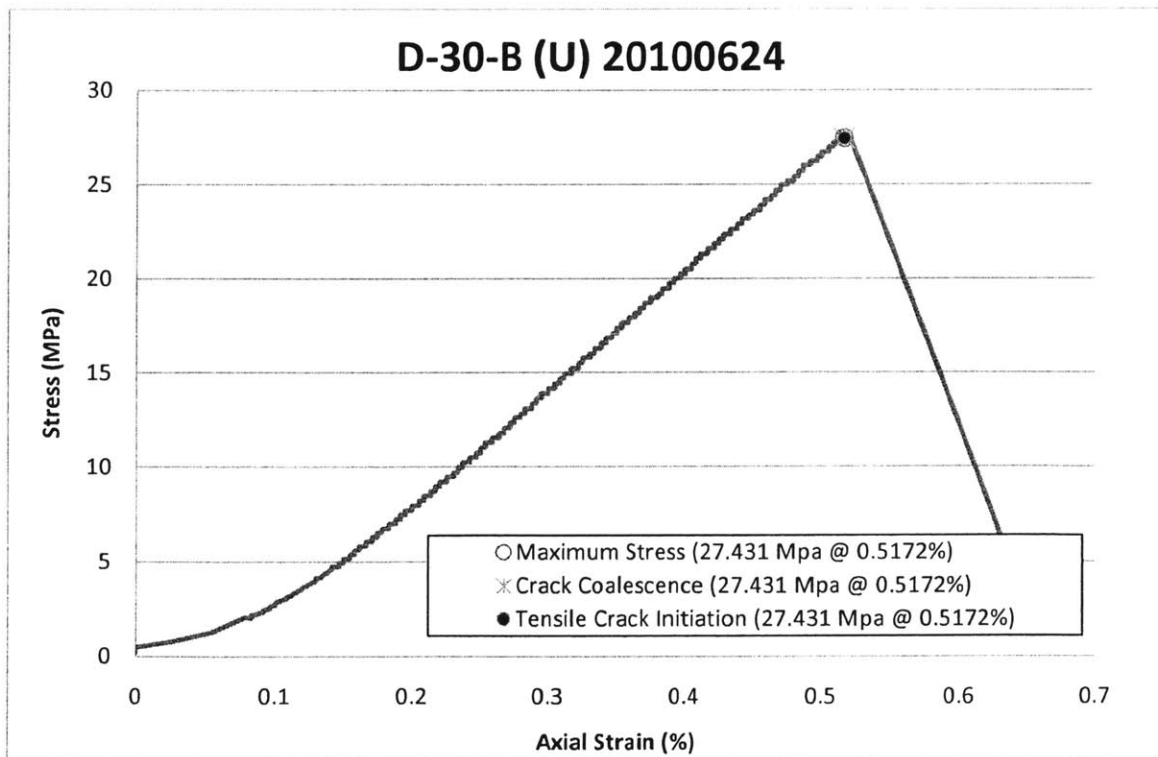
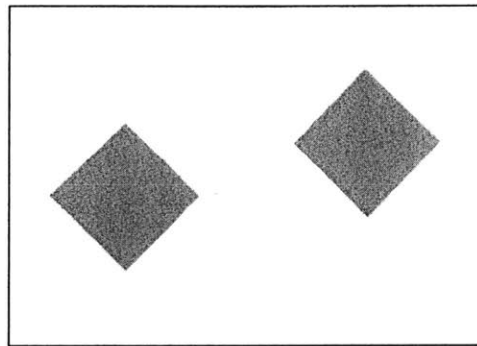
Time: 5m 53.838s
 σ : ~25.601 MPa
 Frame 262 of the High Speed Camera footage.
 (COALESCENCE AND FAILURE)

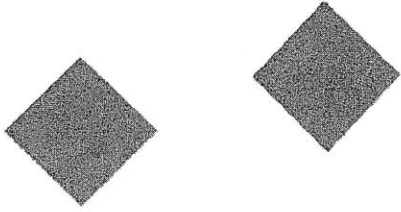
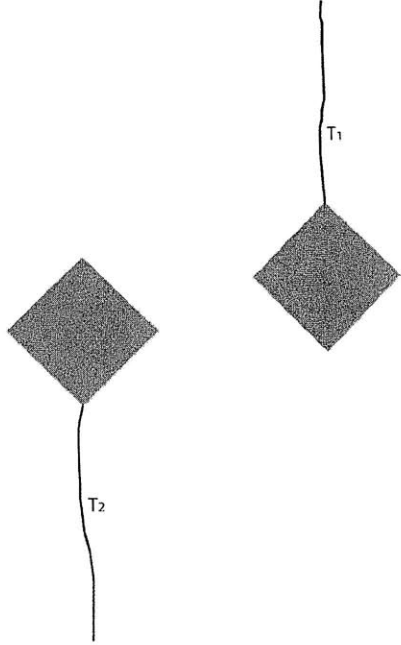
T₇ forms from the top of the specimen and moves down to the right inclusions (debonding). T₈ moves up from the bottom of the specimen along the right side of the left inclusion to connect with T₁ (debonding). T₉ forms at the inclusion interface and propagates in both directions. T₁₀ forms from the bottom of the specimen and moves up directly through the right inclusion. T₁₁ propagates from T₈ and moves along the inclusion interface (debonding). T₁₂ branches off of T₁₀ and moves along the left side of the right inclusion (debonding). A shear crack S₁ forms between T₁₂ and a crack T₁₃ (coalescence). T₁₄ forms along the right side of the specimen with T₁₅ forming between T₉ and T₁₄.

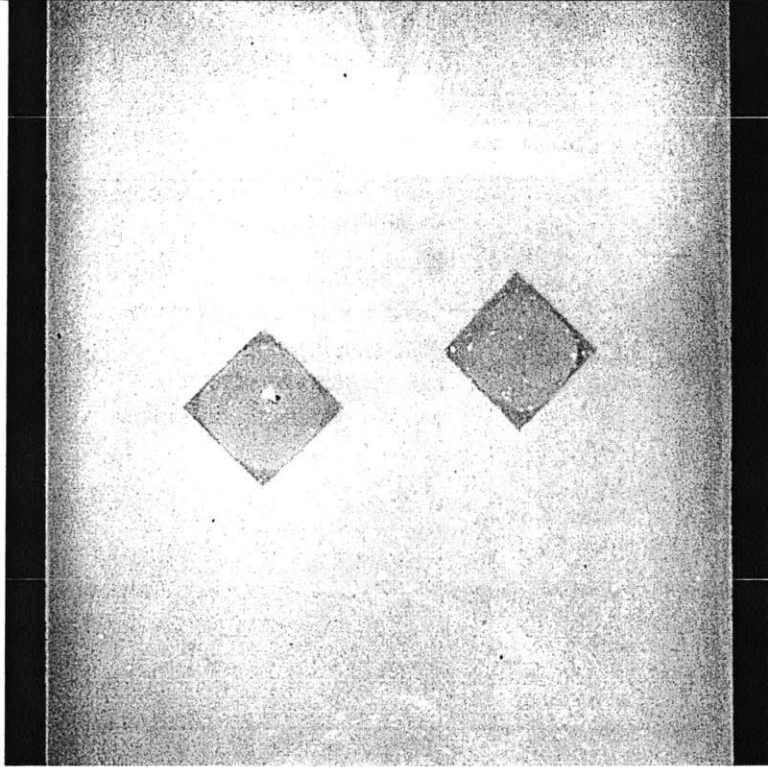


D-30-Bu

Shape = Diamond
(Inclination = 0°)
Bridging Angle = 30°
Test Repetition = B
Material = Ultracal
Size = 1/2"

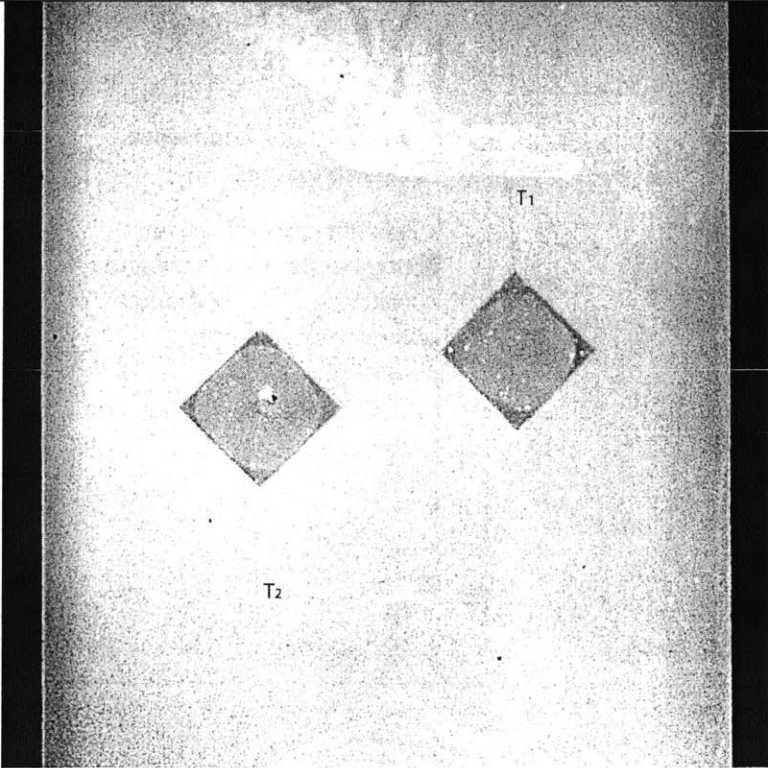


	<p>Time: 0m 0s</p> <p>σ: 0 MPa</p> <p>Still image captured with High Speed Camera before High Speed Recording.</p> <p>Pre-test specimen.</p> <p style="text-align: right;">1</p>
	<p>Time: 6m 12.806s</p> <p>σ: ~27.4312 MPa</p> <p>Frame 400 of High Speed Camera footage.</p> <p>Tension crack T_1 forms at the upper corner of the right inclusion and propagates upward. T_2 forms at the lower corner of the left inclusion and propagates downward.</p> <p style="text-align: right;">2</p>



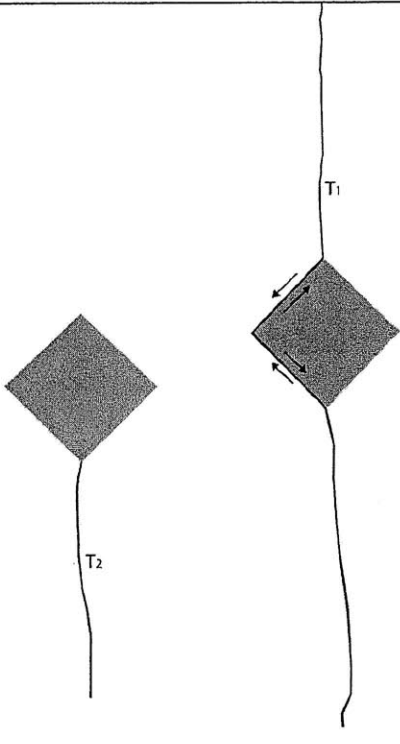
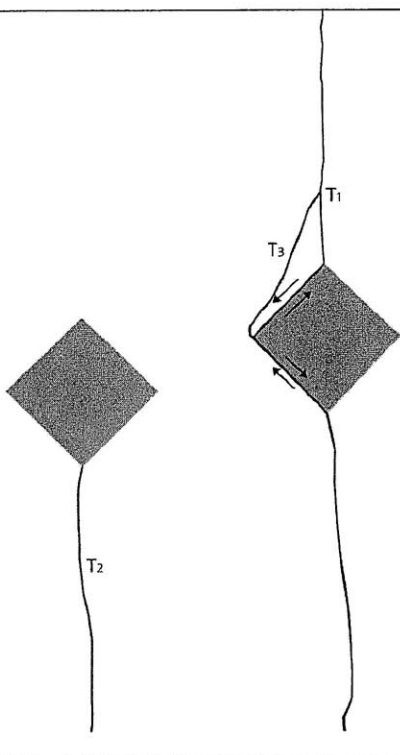
Still photo of specimen taken without load.

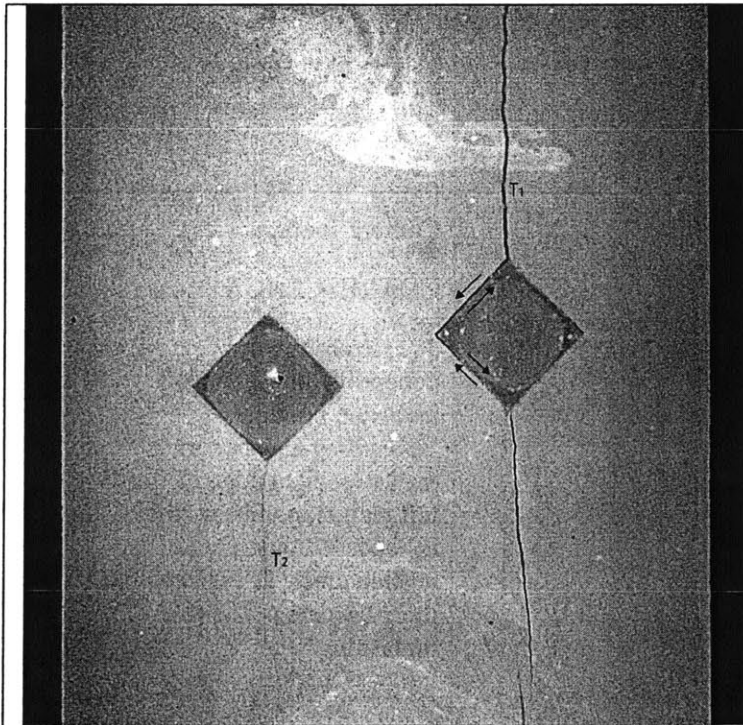
1



High speed photo of specimen at frame 400 (~27.4312 MPa).

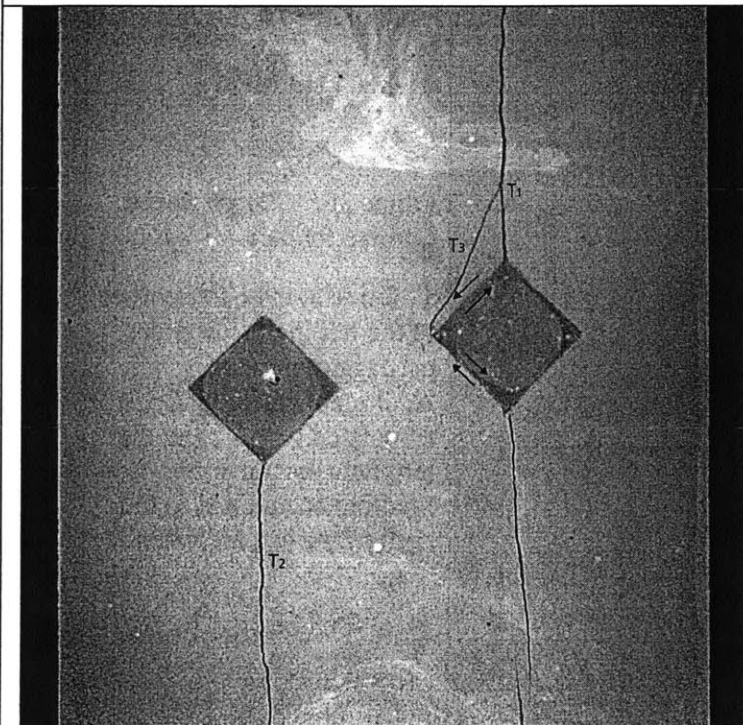
2

	<p>Time: 6m 12.824s</p> <p>σ: ~27.4312 MPa</p> <p>Frame 311 of High Speed Camera footage.</p> <p>T₁ debonds the inner edge of the right inclusion from the specimen and propagates toward the lower specimen boundary.</p> <p style="text-align: right;">3</p>
	<p>Time: 6m 12.823s</p> <p>σ: ~27.4312 MPa</p> <p>Frame 307 of High Speed Camera footage.</p> <p>Tension crack, T₃, forms between the inner inclusion corner and T₁. T₂ extends downward and opens slightly.</p> <p style="text-align: right;">4</p>



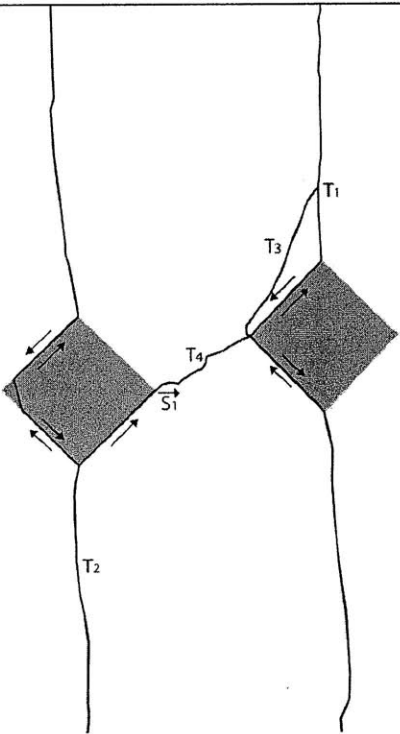
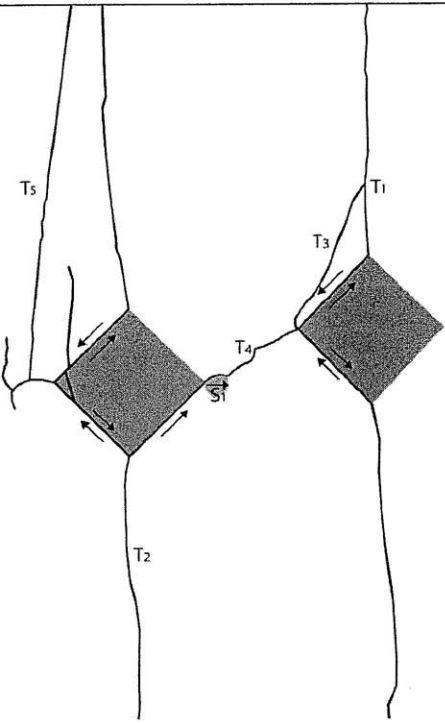
High speed photo of specimen at frame 311 (~27.4312 MPa).

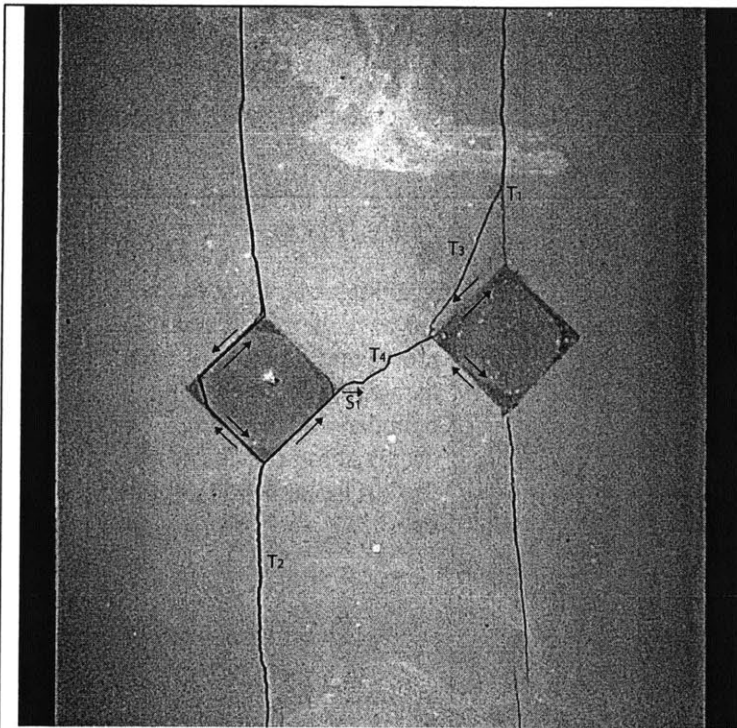
3



High speed photo of specimen at frame 307 (~27.4312 MPa).

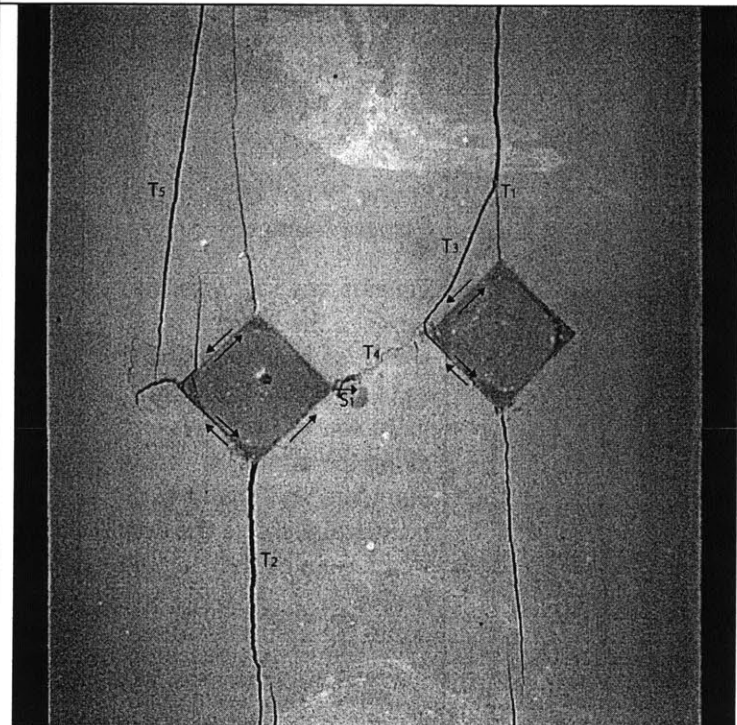
4

	<p>Time: 6m 12.825</p> <p>σ: ~27.4312 MPa</p> <p>Frame 306 of High Speed Camera footage.</p> <p>COALESCENCE</p> <p>T₂ extends upward, debonding along the left inclusion boundary. Debonding also occurs at the lower right edge of the left inclusion. Shear crack S₁ leads to coalescence via tension crack T₄ between the inner corners of the two inclusions.</p> <p style="text-align: right;">5</p>
	<p>Time: 6m 12.826s</p> <p>σ: ~27.4312 MPa</p> <p>Frame 301 of High Speed Camera footage.</p> <p>T₅ forms at the outer corner of the left inclusion and propagates upward. Additional cracking associated with T₅ and the left inclusion develop. Spalling occurs just to the right of the left inclusion.</p> <p style="text-align: right;">6</p>



High speed photo of specimen at frame 306 (~27.4312 MPa).

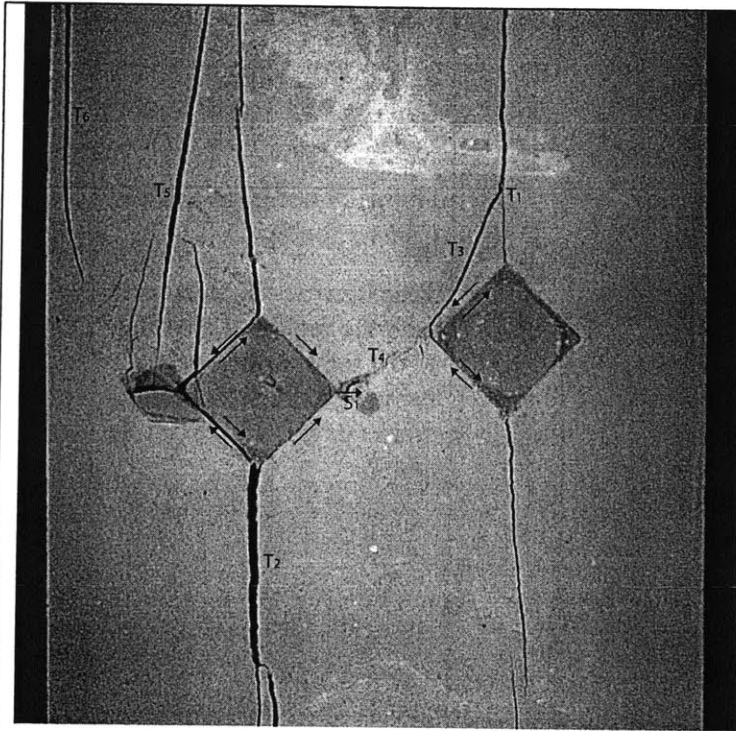
5



High speed photo of specimen at frame 301 (~27.4312 MPa).

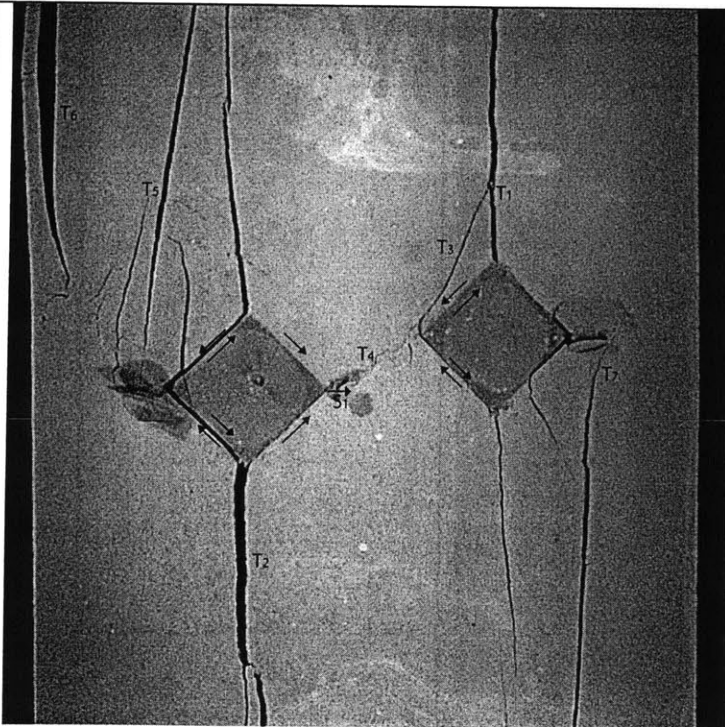
6

	<p>Time: 6m 12.826s</p> <p>σ: ~27.4312 MPa</p> <p>Frame 298 of High Speed Camera footage.</p> <p>Spalling occurs just to the left of the left inclusion. T_6 propagates downward from the upper specimen boundary. Debonding occurs at the final edge of the left inclusion. T_2 opens up.</p> <p style="text-align: right;">7</p>
	<p>Time: 6m 12.827s</p> <p>σ: ~27.4312 MPa</p> <p>Frame 296 of High Speed Camera footage.</p> <p>Tension crack, T_7, forms between the lower specimen boundary and the right corner of the right inclusion. T_7 extends along the inclusion boundary and spalling occurs just above the crack to the right of the inclusion.</p> <p style="text-align: right;">8</p>



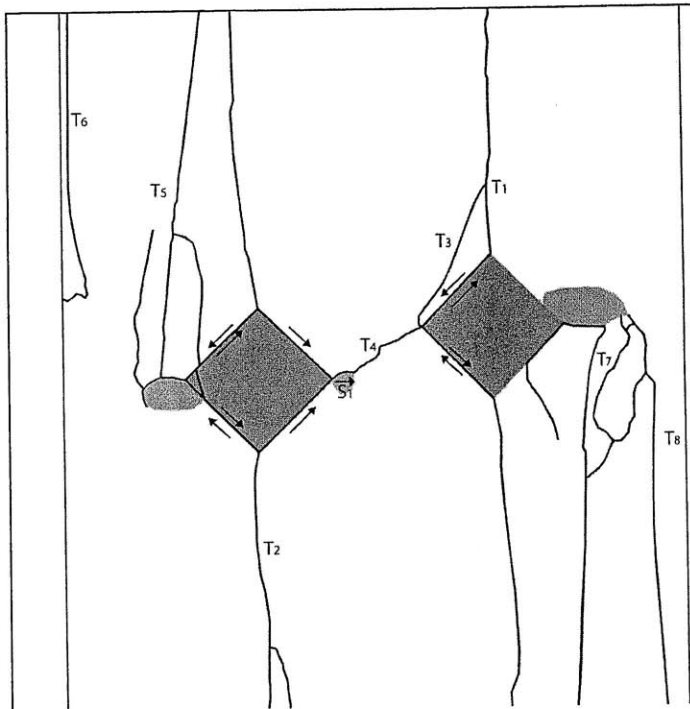
High speed photo of specimen at frame 298 (~27.4312 MPa).

7



High speed photo of specimen at frame 296 (~27.4312 MPa).

8



Time: 6m 12.827s

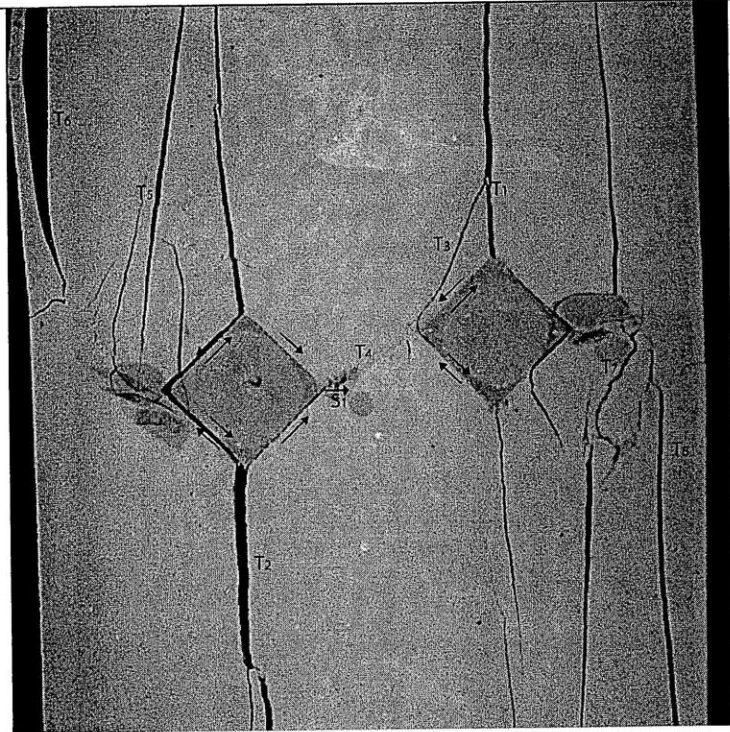
σ : ~27.4312 MPa

FAILURE

Frame 295 of High Speed Camera footage.

Tension crack T₈ intersects with the region of spalling to the right of the inclusions. A series of cracks develop between T₇ and T₈.

9

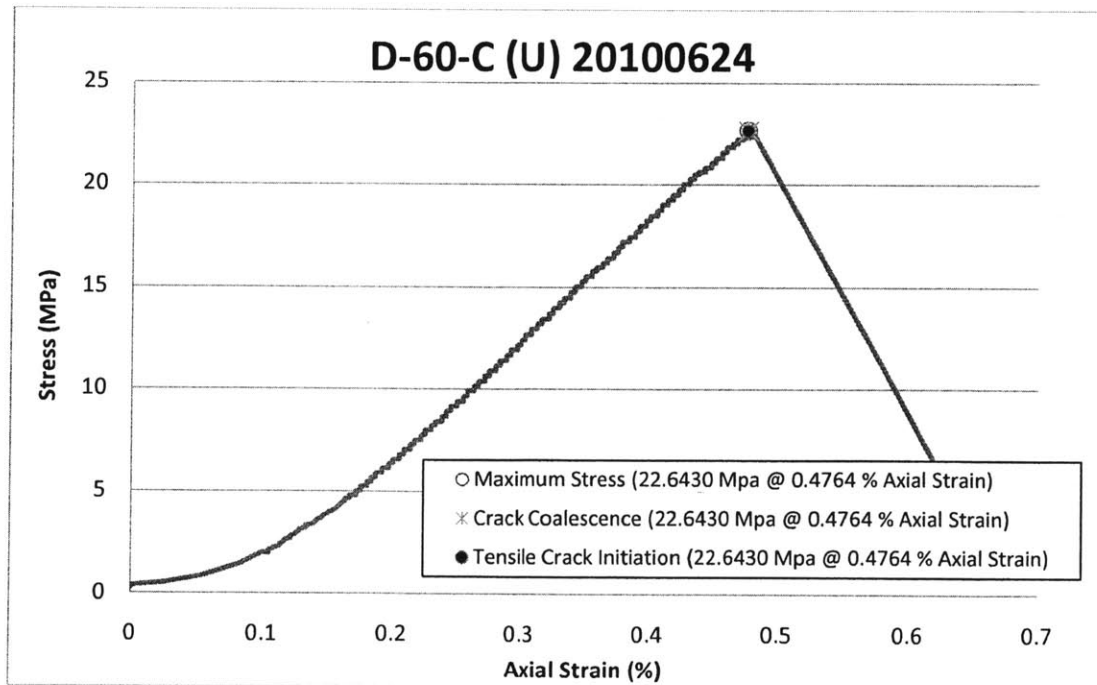
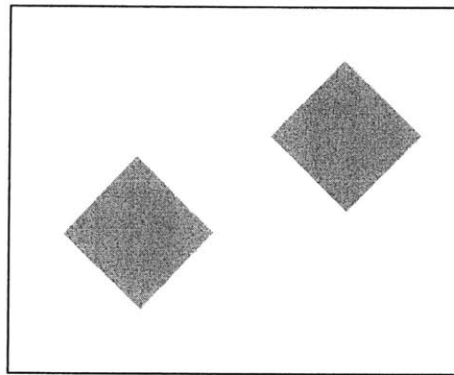


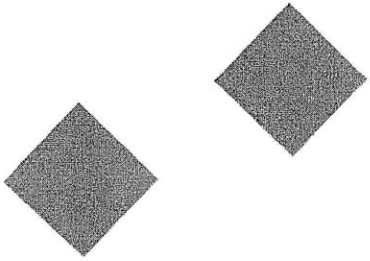
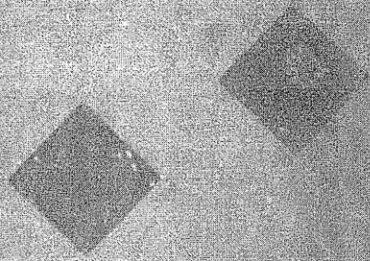
High speed photo of specimen at frame 295 (~27.4312 MPa).

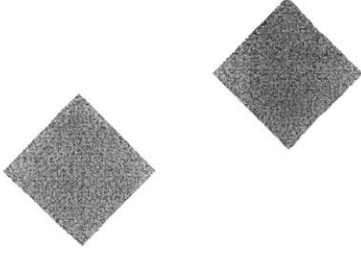
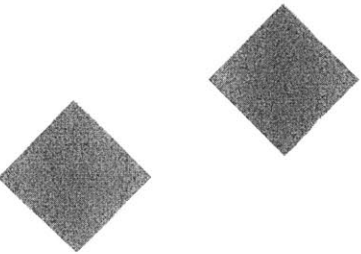
9

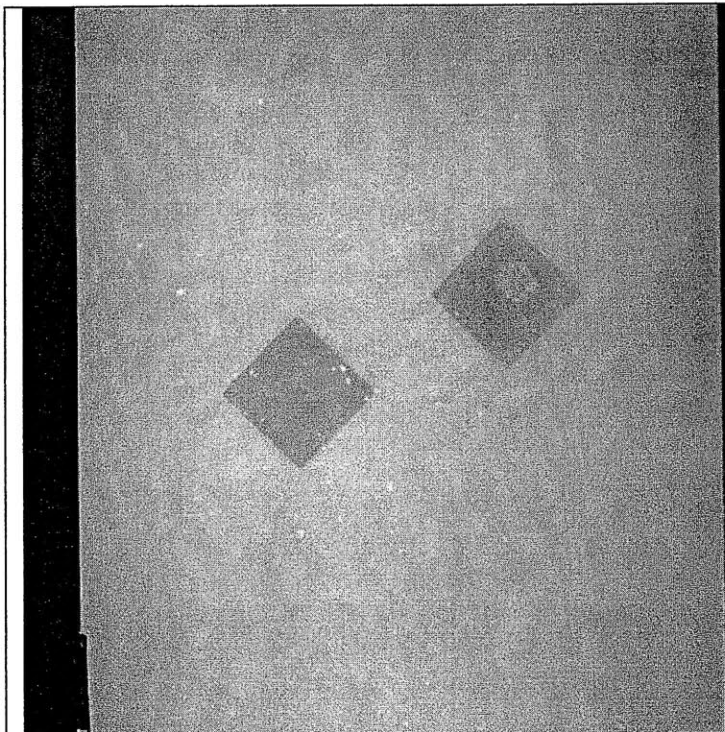
D-60-Cu

Shape = Diamond
(Inclination = 0°)
Bridging Angle = 60°
Test Repetition = C
Material = Ultracal
Size = 1/2"

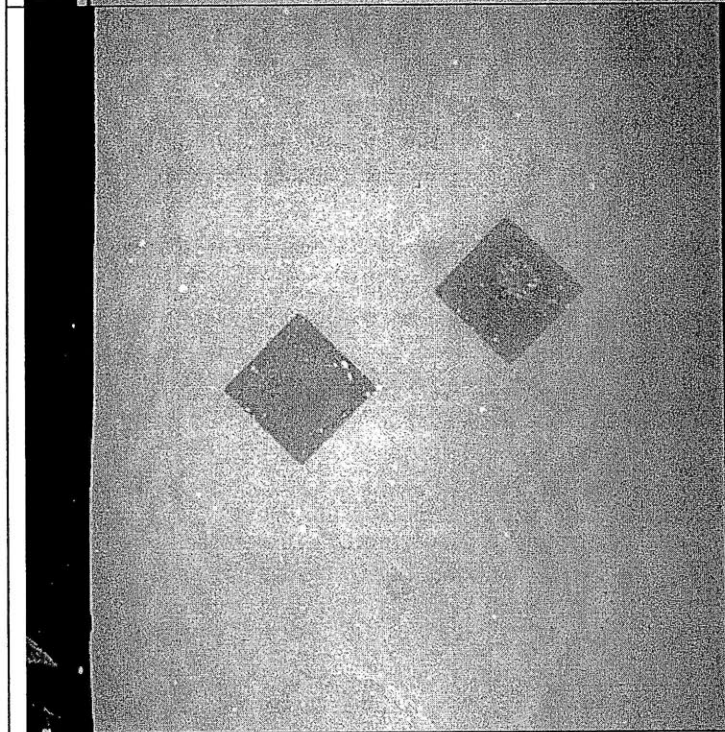


	<p>Time: 0m 0s σ: ~0 MPa</p> <p>Picture taken prior to testing.</p>
	<p>Time: 0m 0s σ: ~0 MPa</p> <p>Picture taken prior to testing.</p>

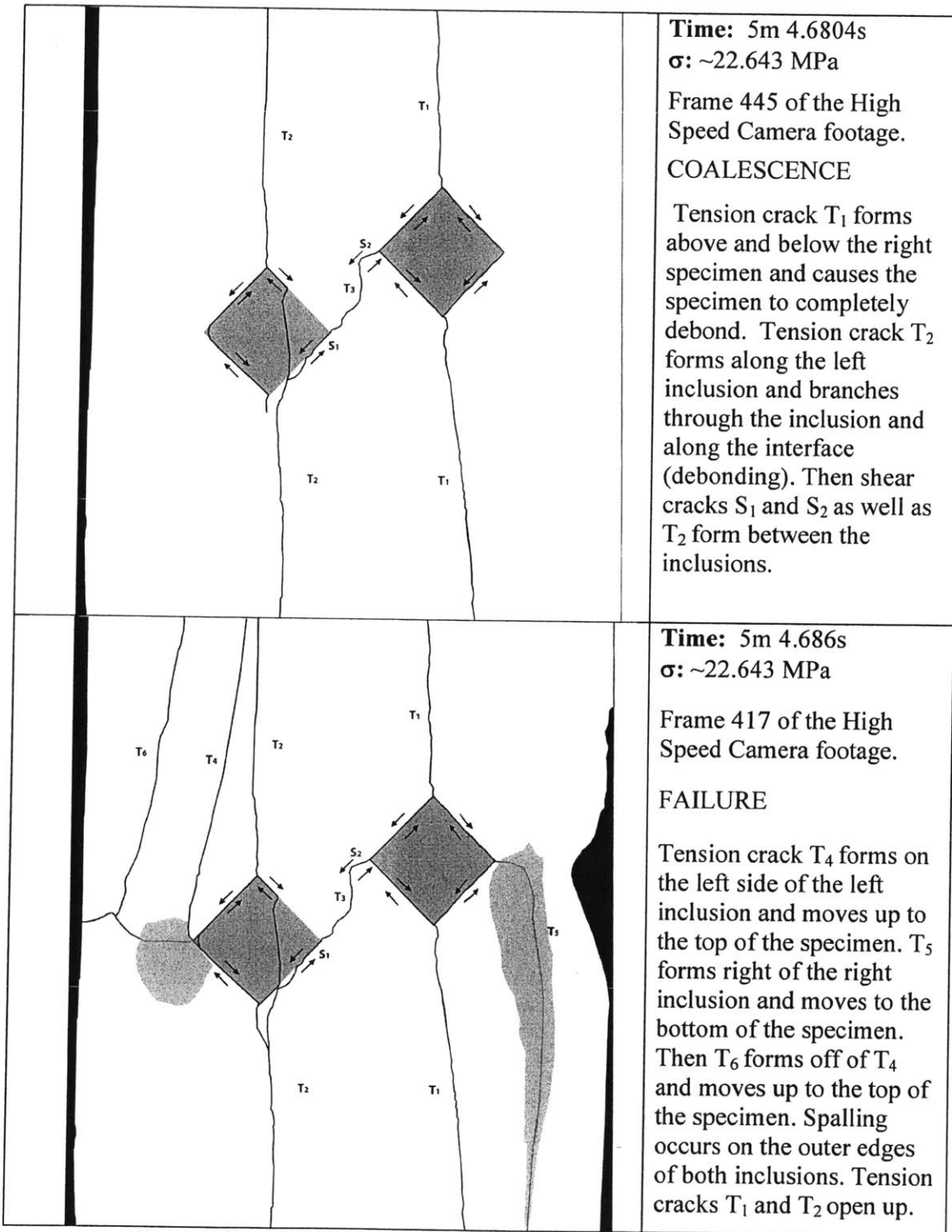
	<p>Time: 3m 24.582s σ: ~15.8398 MPa</p> <p>Still image captured with High Speed Camera before High Speed Recording.</p> <p>A small piece breaks off of the bottom left side of the specimen.</p>
	<p>Time: 5m 4.5276 s σ: ~22.6304 MPa</p> <p>Frame 1209 of the High Speed Camera footage.</p> <p>A large piece breaks off of the entire left side of the specimen.</p>

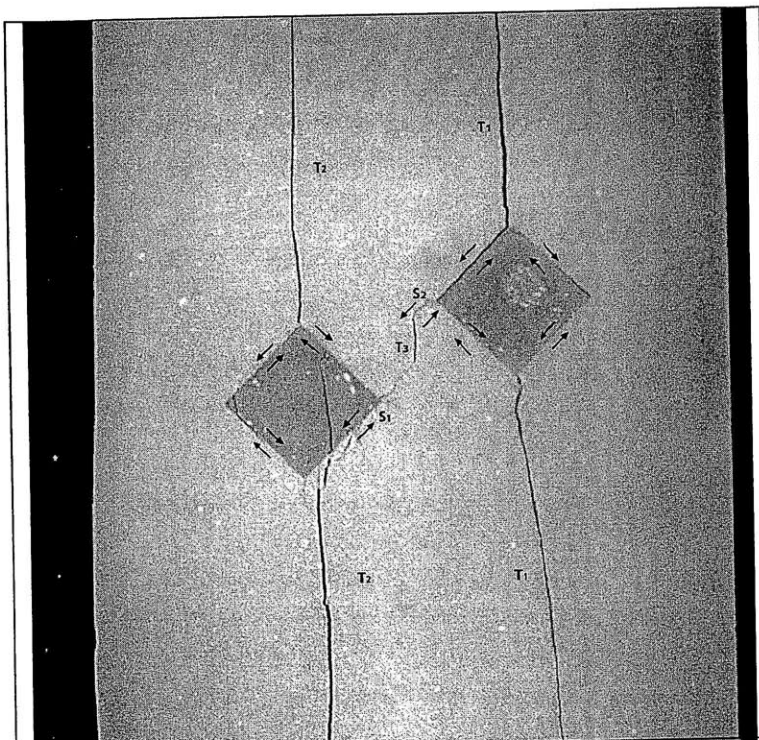


Picture taken at ~ 15.8398 MPa

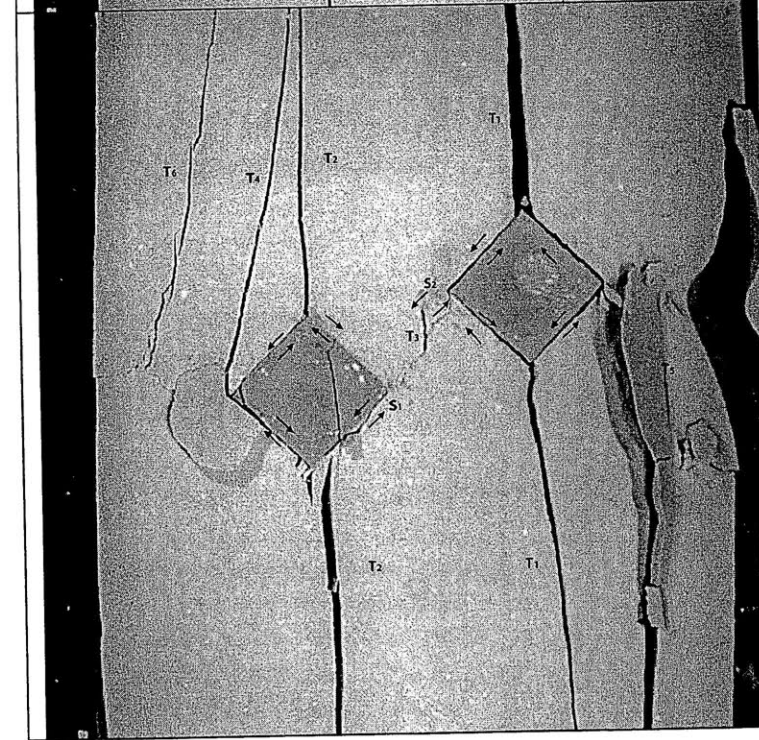


Picture taken at frame 1209 of the high-speed camera footage. (22.6304 MPa)





Picture taken at frame 445 of the high-speed camera footage. (22.643 MPa)

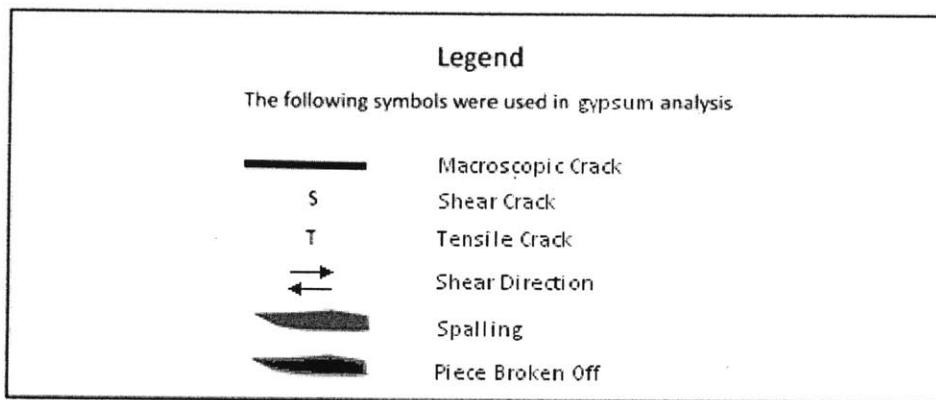


Picture taken at frame 417 of the high-speed camera footage. (22.643 MPa)

APPENDIX F – Half-Inch Ellipse Inclusion Pair Analysis

The following appendix section presents the most representative test repetitions for the ellipse pair test series.

Legend Used:



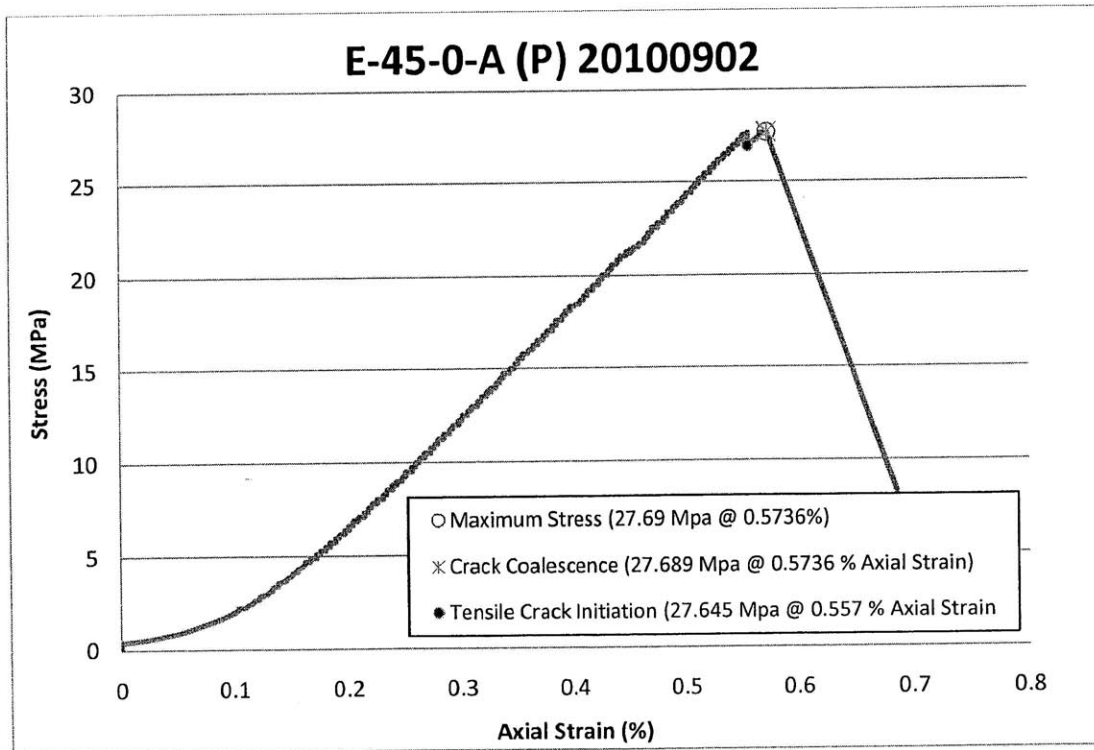
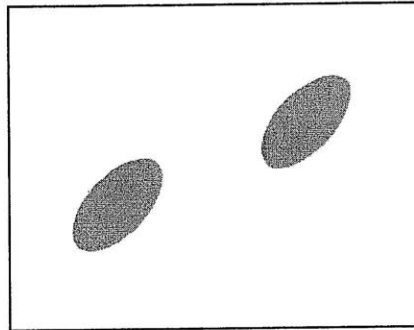
Notes:

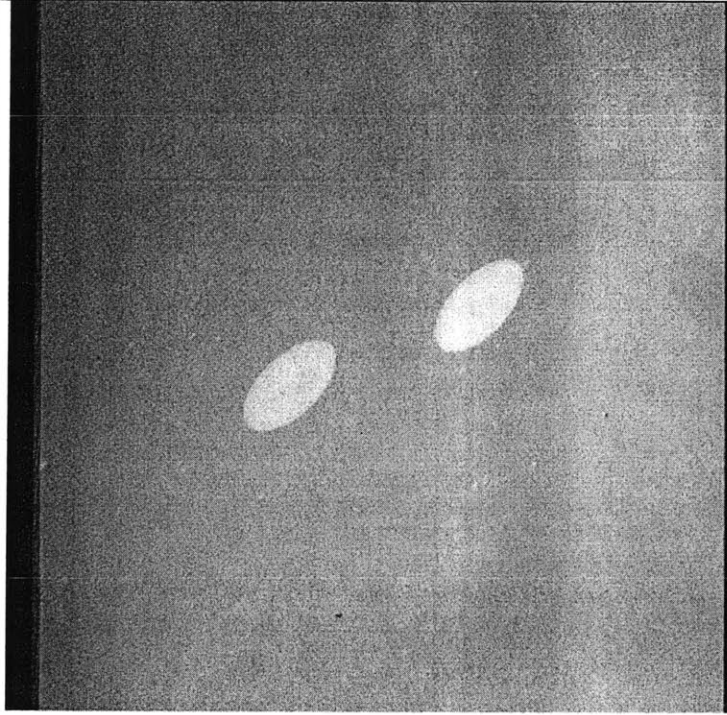
- Subscripts which do not indicate sequence are noted in the description.
- Times and stresses correlate to when the picture was taken, not when the events happened.
- Shear cracks with an arrow indicate the direction of shear crack development. Shear cracks without an arrow denote cracks in which the direction could not be determined.

PLASTER

E-45-0-Ap

Shape = Ellipse
(Inclination = 45°
Bridging Angle = 0°
Test Repetition = A
Material = Plaster
Size = 1/2"

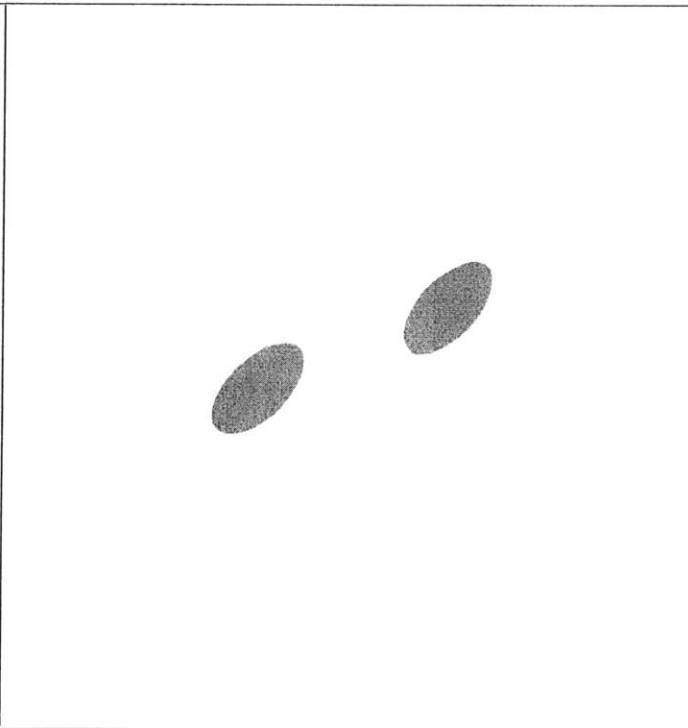




Time: 0m 0s

σ : ~0 MPa

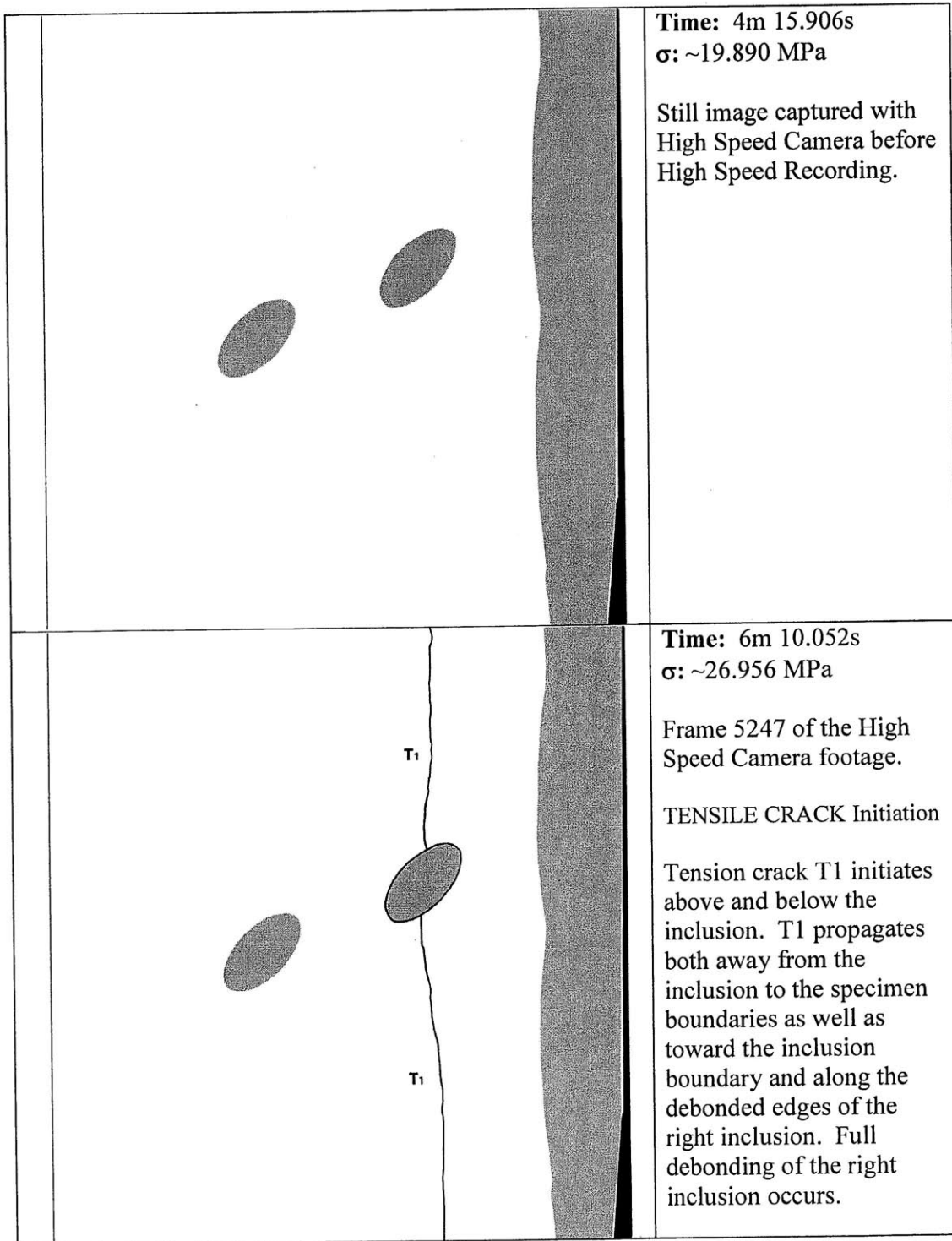
Picture taken prior to testing.

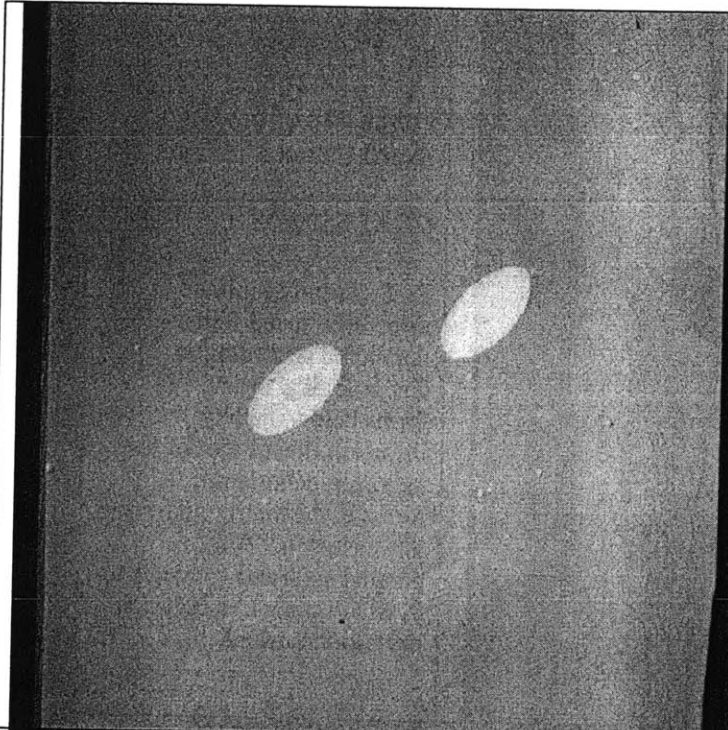


Time: 0m 0s

σ : ~0 MPa

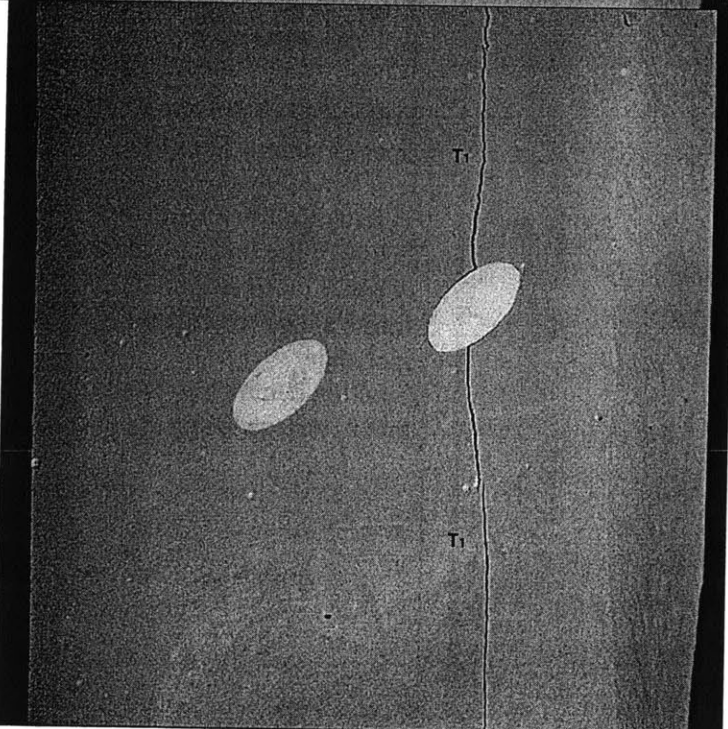
Picture taken prior to testing.





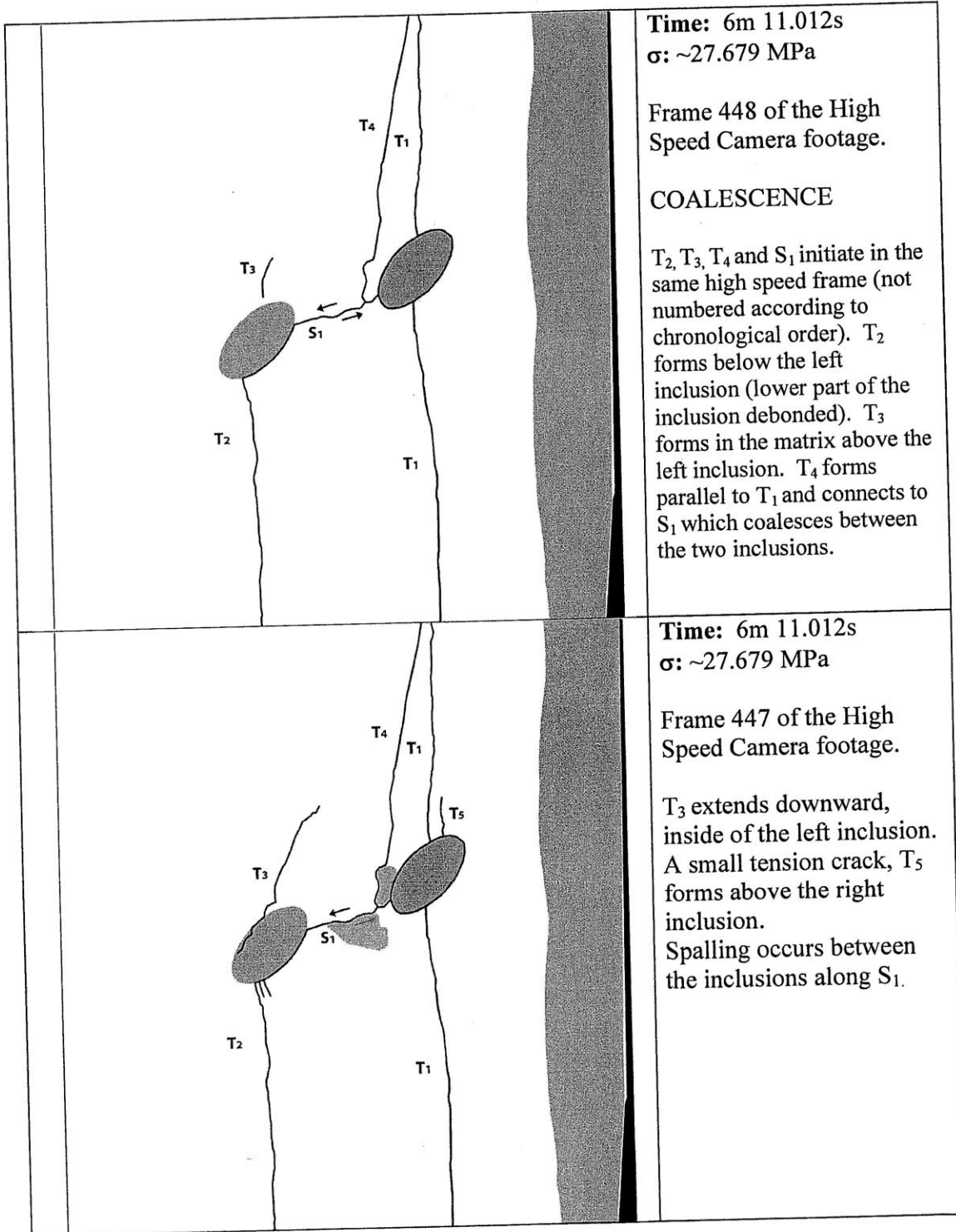
Time: 4m 15.906s
 σ : ~19.890 MPa

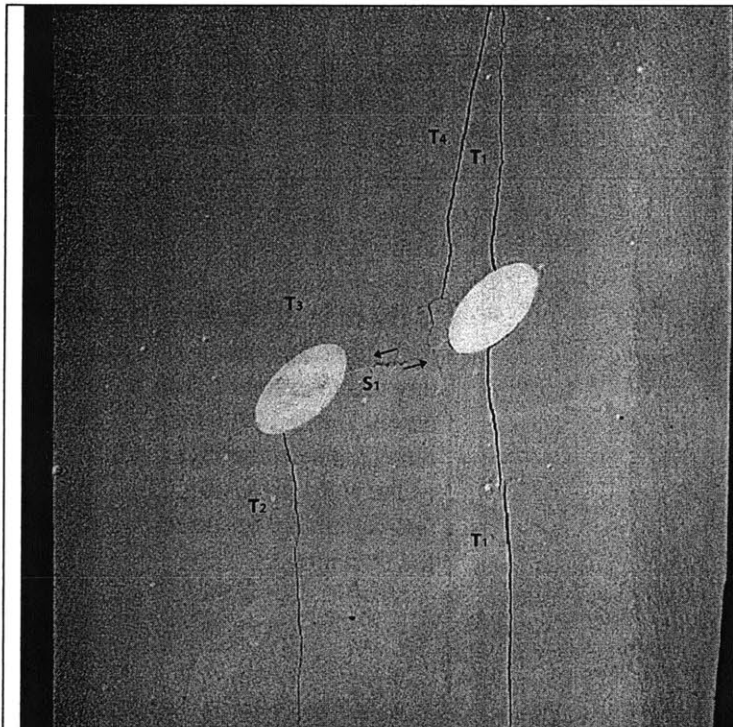
Still image captured with High Speed Camera before High Speed Recording.



Time: 6m 10.052s
 σ : ~26.956 MPa

Frame 5247 of the High Speed Camera footage.





Time: 6m 11.012s
 σ : ~27.679 MPa

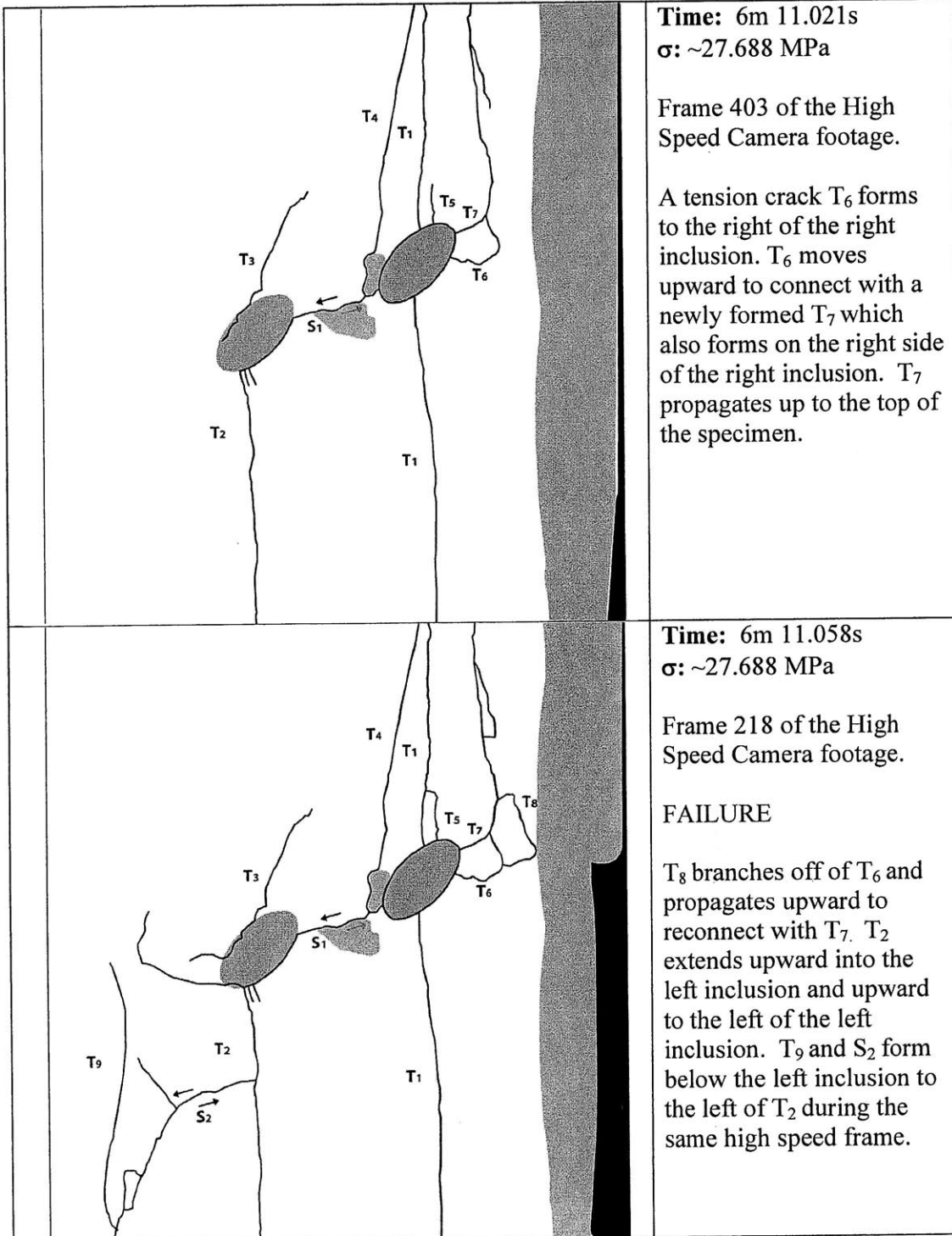
Frame 448 of the High Speed Camera footage.

COALESCENCE



Time: 6m 11.012s
 σ : ~27.679 MPa

Frame 447 of the High Speed Camera footage.



Time: 6m 11.021s
 σ : ~27.688 MPa

Frame 403 of the High Speed Camera footage.

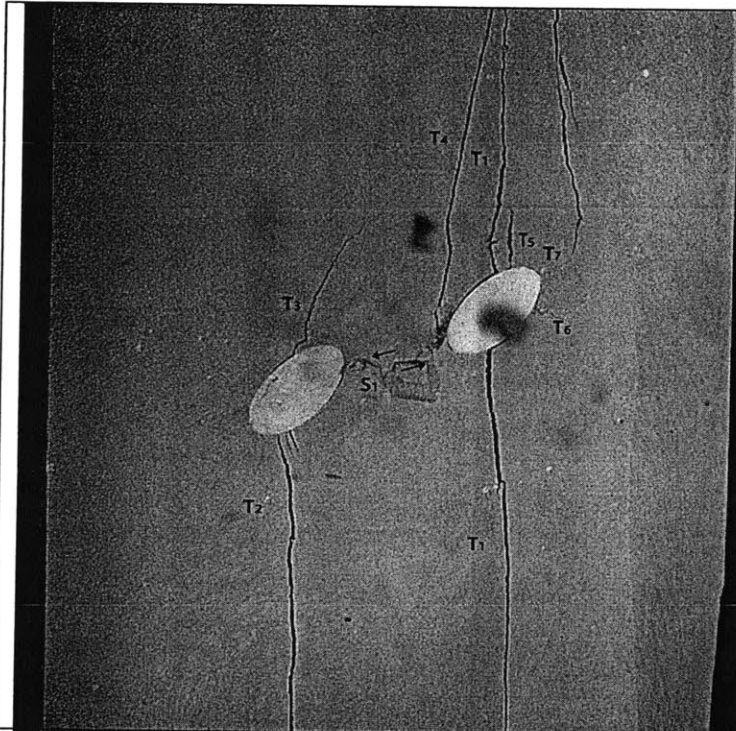
A tension crack T_6 forms to the right of the right inclusion. T_6 moves upward to connect with a newly formed T_7 which also forms on the right side of the right inclusion. T_7 propagates up to the top of the specimen.

Time: 6m 11.058s
 σ : ~27.688 MPa

Frame 218 of the High Speed Camera footage.

FAILURE

T_8 branches off of T_6 and propagates upward to reconnect with T_7 . T_2 extends upward into the left inclusion and upward to the left of the left inclusion. T_9 and S_2 form below the left inclusion to the left of T_2 during the same high speed frame.



Time: 6m 11.021s
 σ : ~27.688 MPa

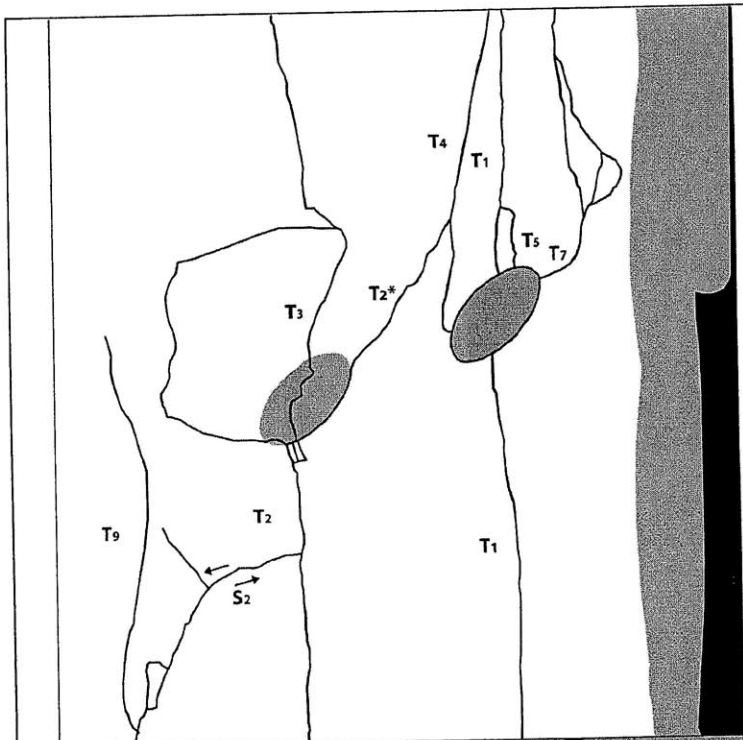
Frame 403 of the High Speed Camera footage.



Time: 6m 11.058s
 σ : ~27.688 MPa

Frame 218 of the High Speed Camera footage.

FAILURE



Time: POST-FAILURE
 $\sigma: \sim$

After the high speed recording ended a post-failure picture showed that significant surface spalling had revealed some cracks that had not been previously seen and that some previously noted cracks were only surface cracks.
 (continued below)

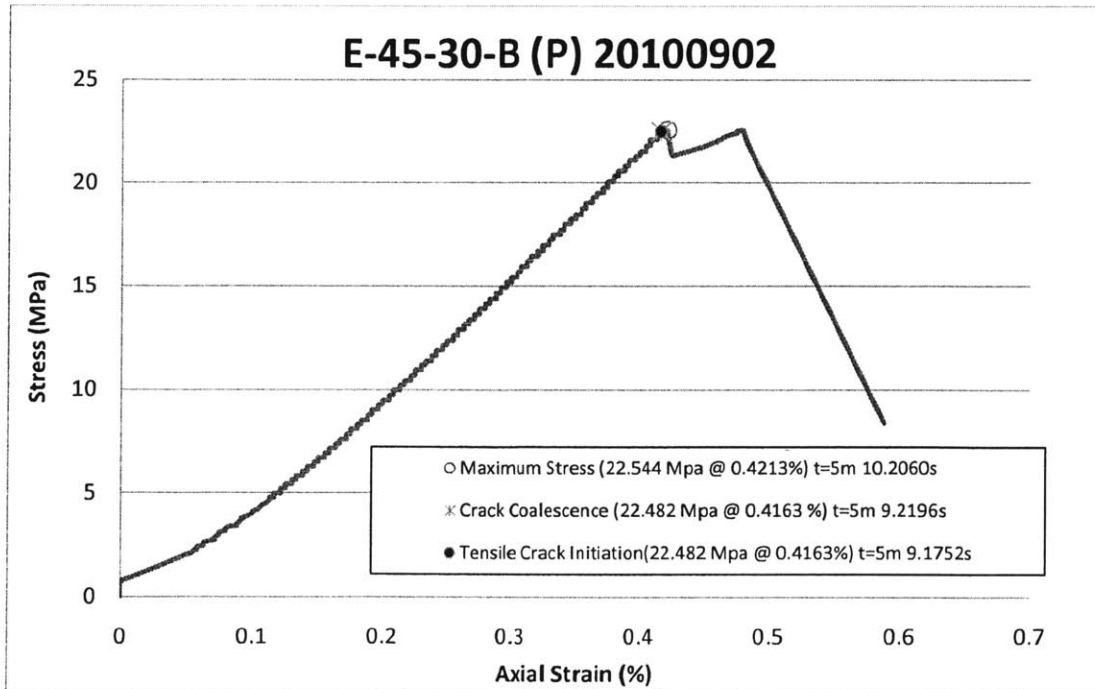
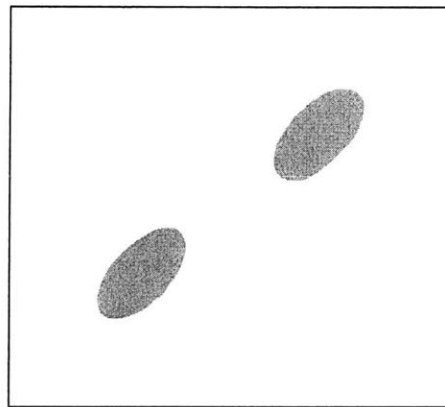


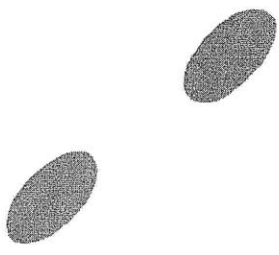
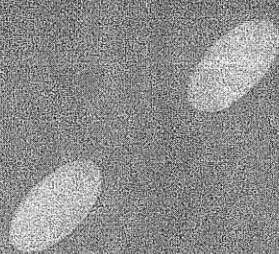
Time: POST-FAILURE
 $\sigma: \sim$

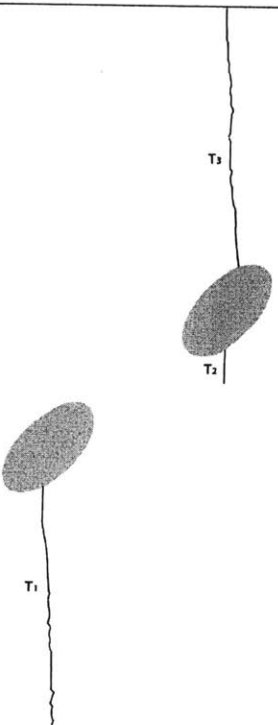
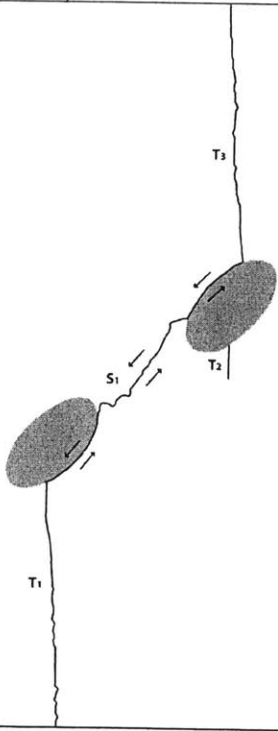
S_1 was not visible and now a new crack T_2^* can be seen to coalesce indirectly between the two inclusions. This T_2^* may be a shearing crack but since it was discovered post high-speed imagery, it cannot be determined. Also T_6 and T_8 were not visible. T_2 extended up and connected with T_3 which propagated to the top of the specimen and down through the inclusion to connect again with T_2 .

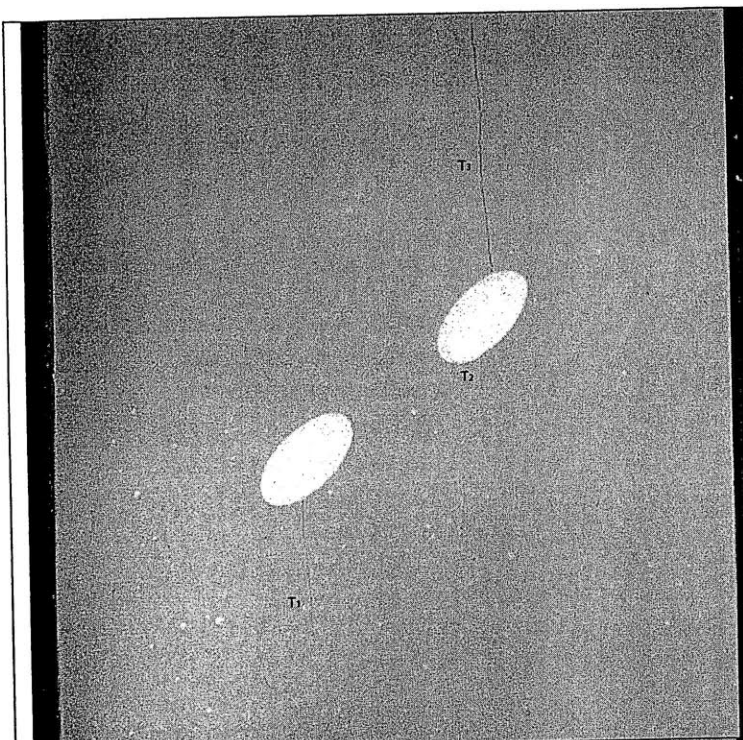
E-45-30-Bp

Shape = Ellipse
(Inclination = 45°
Bridging Angle = 30°
Test Repetition = B
Material = Plaster
Size = 1/2"



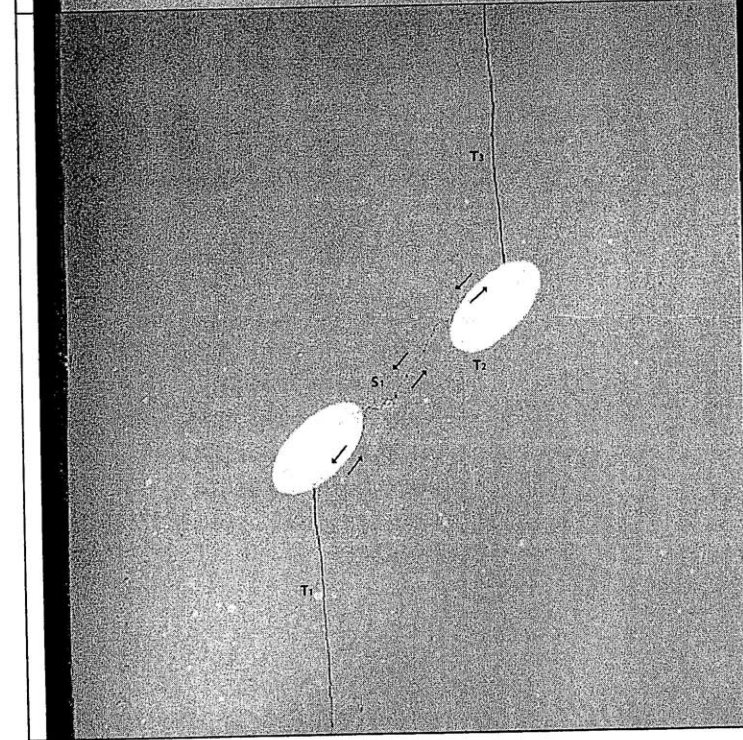
	<p>Time: 0m 0s σ: ~0 MPa</p> <p>Picture taken prior to testing.</p> <p>0</p>
	<p>Time: 0m 0s σ: ~0 MPa</p> <p>Picture taken prior to testing.</p> <p>0</p>

	<p>Time: 5m 9.172s σ: ~22.4821 MPa</p> <p>Frame 5404 of the High Speed Camera footage.</p> <p>Tensile Crack Initiation</p> <p>Before high speed imagery starts (Not numbered chronologically) Tension crack T_1 forms below the left inclusion, Tension crack T_2 forms below the right inclusion and T_3 forms above the right inclusion.</p> <p style="text-align: right;">1</p>
	<p>Time: 5m 9.220s σ: ~22.4821 MPa</p> <p>Frame 5182 of the High Speed Camera footage.</p> <p>COALESCENCE</p> <p>Shear crack S_1 forms between the two inclusions and shear debonding occurs at the bottom of the left inclusion and the top of the right inclusion. T_1 and T_2 open slightly.</p> <p style="text-align: right;">2</p>



Time: 5m 9.172s
 σ : ~22.4821 MPa
Frame 5404 of the High Speed Camera footage.

1



Time: 5m 9.220s
 σ : ~22.4821 MPa
Frame 5182 of the High Speed Camera footage.
COALESCENCE

2

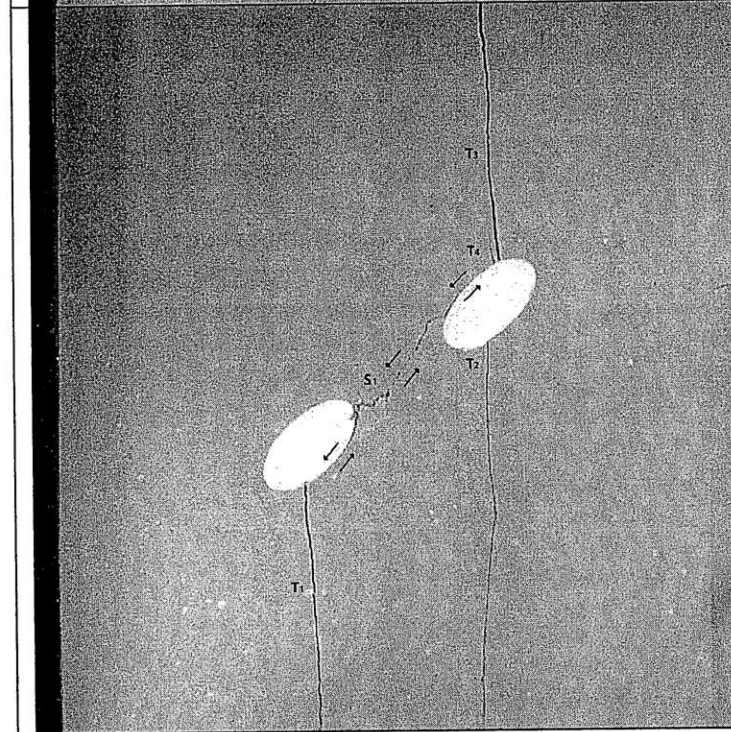
	<p>Time: 5m 9.342s σ: ~22.489 MPa</p> <p>Frame 4572 of the High Speed Camera footage.</p> <p>T2 extends downward and a medium sized piece spalls off of the bottom right side of the specimen.</p> <p style="text-align: right;">3</p>
	<p>Time: 5m 9.351s σ: ~22.489 MPa</p> <p>Frame 4524 of the High Speed Camera footage.</p> <p>T2 extends down to the bottom of the specimen. A small tension crack T4 moves up from the top of the right inclusion to the left of T3.</p> <p style="text-align: right;">4</p>



Time: 5m 9.342s
 σ : ~22.489 MPa

Frame 4572 of the High Speed Camera footage.

3



Time: 5m 9.351s
 σ : ~22.489 MPa

Frame 4524 of the High Speed Camera footage.

4

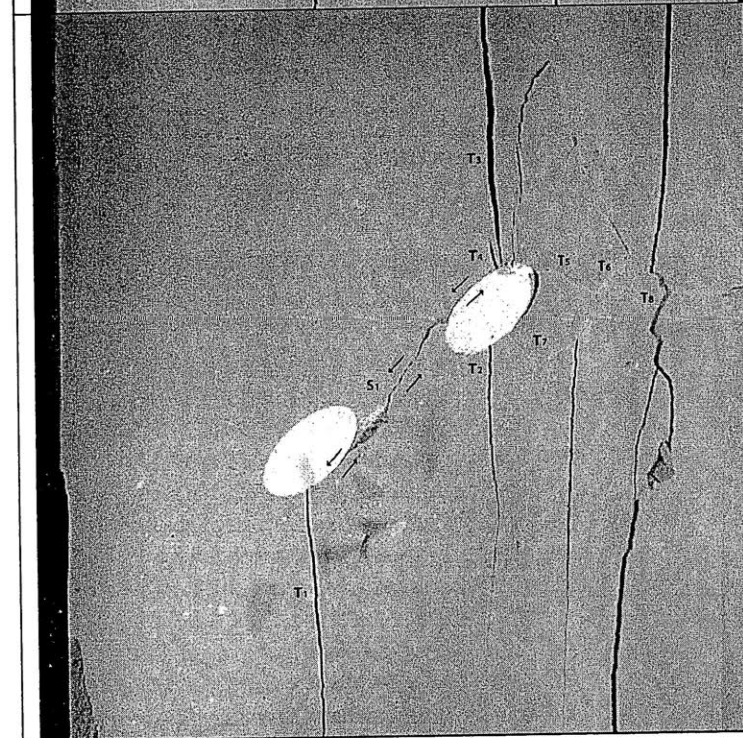
	<p>Time: 5m 10.134s σ: ~22.539 MPa</p> <p>Frame 609 of the High Speed Camera footage.</p> <p>T₅ initiates from the right end of the right inclusion and moves outward into the matrix. T₆ branches up off of T₅ and then T₇ forms between the right inclusion and T₅. Debonding occurs on the right side of the right inclusion and spalling occurs to the right of the left inclusion.</p> <p style="text-align: right;">5</p>
	<p>Time: 5m 10.184s σ: ~22.544 MPa</p> <p>Frame 363 of the High Speed Camera footage.</p> <p>T₆ extends upward looping back down around to the top of the right inclusions (possibly a surface crack). T₈ forms from inside the specimen and propagates up to the top of the specimen and down to the bottom of the specimen. A small piece breaks off of the bottom left of the specimen and there is a small area of spalling on the bottom left of the specimen as well.</p> <p style="text-align: right;">6</p>



Time: 5m 10.134s
 σ : ~22.539 MPa

Frame 609 of the High Speed Camera footage.

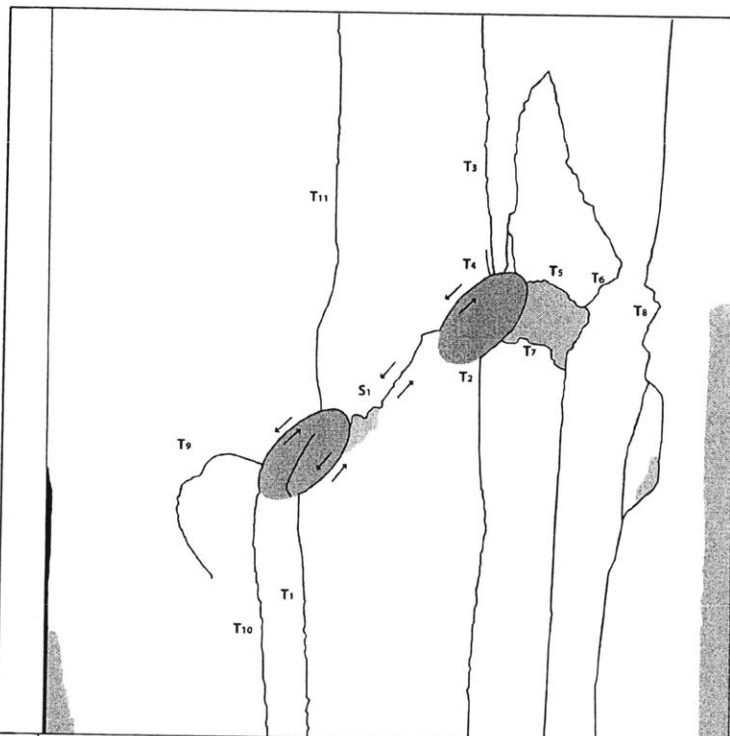
5



Time: 5m 10.184s
 σ : ~22.544 MPa

Frame 363 of the High Speed Camera footage.

6

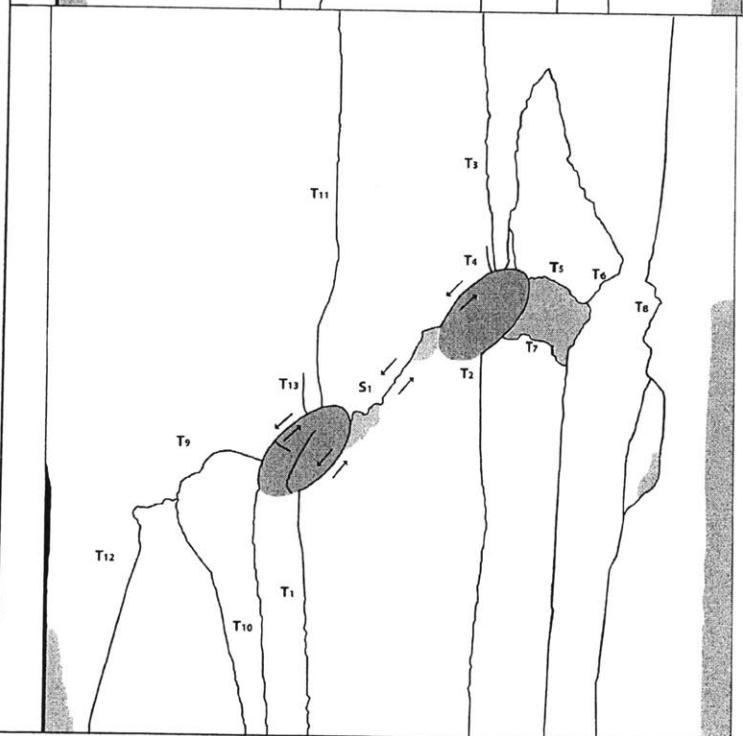


Time: 5m 10.205s
 σ : ~22.544 MPa

Frame 257 of the High Speed Camera footage.

T₉ forms on the left side of the left inclusion. T₁₀ and T₁₁ form at the same time and connect along a shearing debonding surface on the top-left side of the left inclusion. Also, spalling occurs between tension cracks T₅ and T₇. T₁ opens further.

7



Time: 5m 10.206s
 σ : ~22.544 MPa

FAILURE

Frame 251 of the High Speed Camera footage.

T₉ extends down to the bottom of the specimen, and T₁₂ branches off of T₉. T₁₃ forms on the top of the left inclusion. Spalling occurs to the left side of the right in inclusion. T₁ opens further.

8



Time: 5m 10.205s
 σ : ~22.544 MPa

Frame 257 of the High Speed Camera footage.

7



Time: 5m 10.206s
 σ : ~22.544 MPa

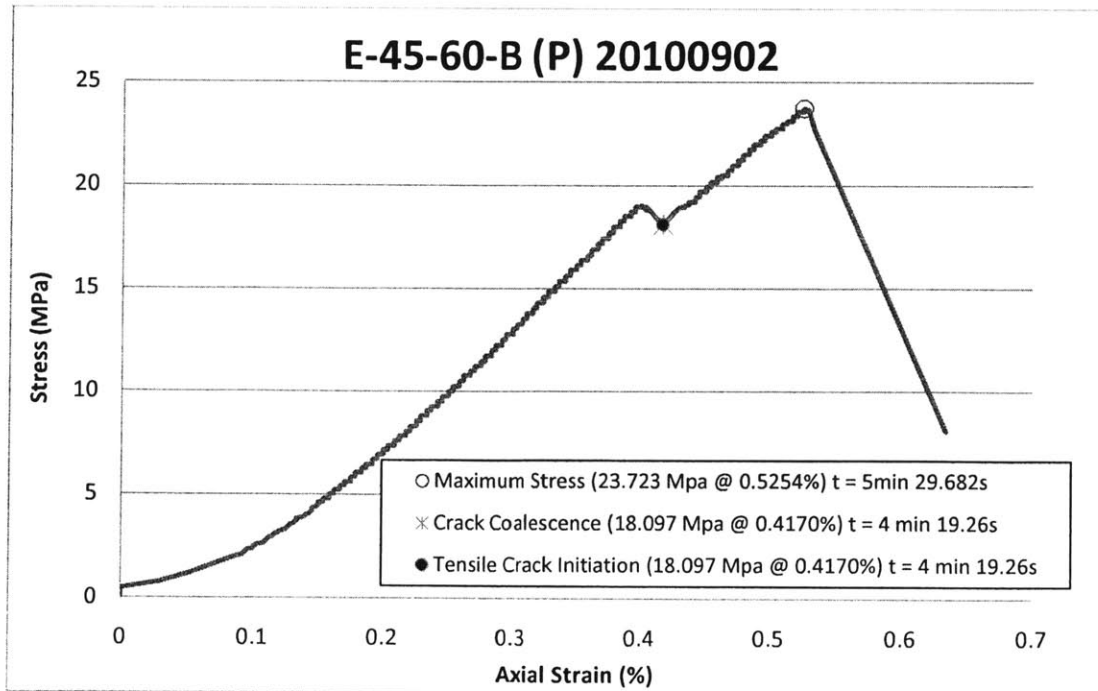
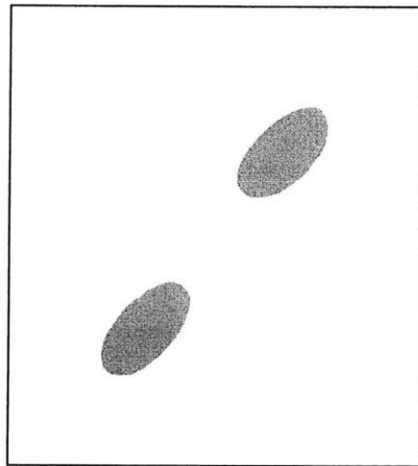
FAILURE

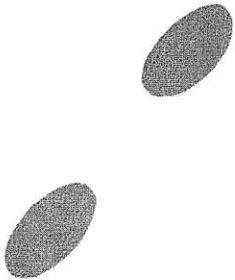
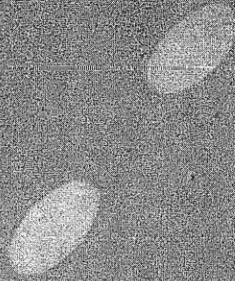
Frame 251 of the High Speed Camera footage.

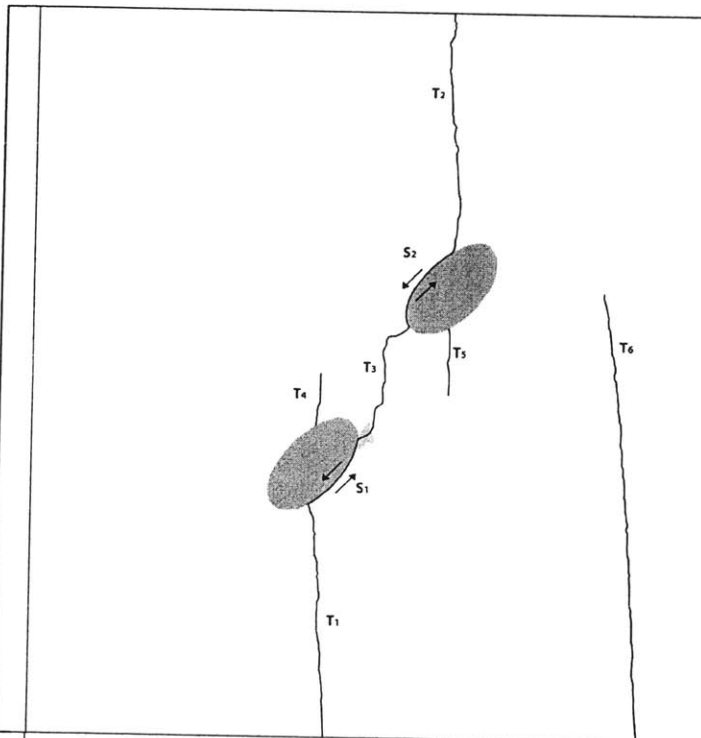
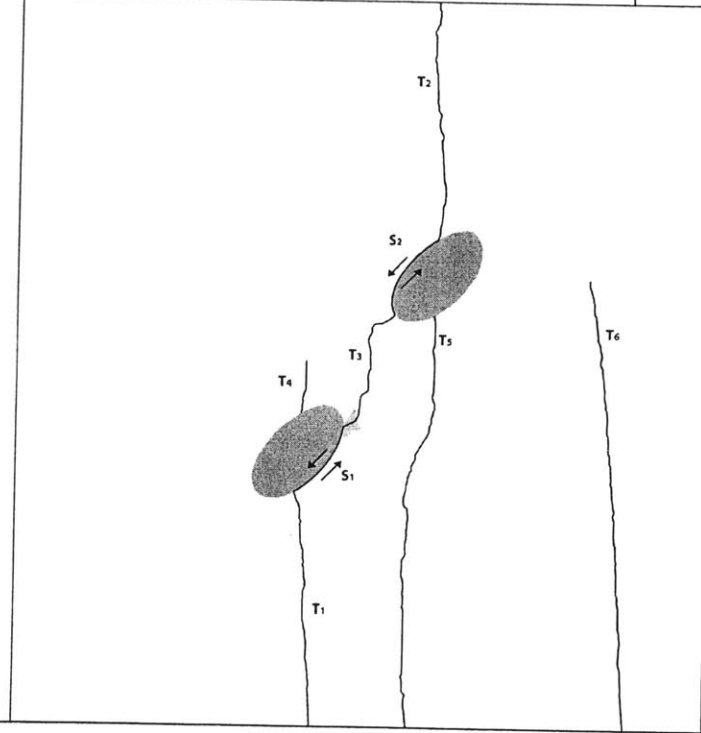
8

E-45-60-Bp

Shape = Ellipse
(Inclination = 45°
Bridging Angle = 60°
Test Repetition = B
Material = Plaster
Size = 1/2"



	<p>Time: 0m 0s σ: ~0 MPa</p> <p>Picture taken prior to testing.</p> <p>0</p>
	<p>Time: 0m 0s σ: ~0 MPa</p> <p>Picture taken prior to testing.</p> <p>0</p>

	<p>Time: 4m 19.260s σ: ~18.097 MPa</p> <p>COALESCENCE +Tensile Crack Initiation</p> <p>Still image captured with High Speed Camera before High Speed Recording.</p> <p>Before high speed imagery starts (Not numbered chronologically) Tension cracks T_1 and T_2 initiate below and above the left and right inclusions respectively. Shear cracks S_1 and S_2 initiate along the debonded surfaces of the inclusions. A tension crack T_3 forms between the inclusions, coalescing the two shear cracks. T_4 forms above the left inclusion. T_5 forms below the right inclusion. T_6 initiates at the bottom right side of the specimen.</p> <p style="text-align: right;">1</p>
	<p>Time: 4m 40.674s σ: ~20.449 MPa</p> <p>Still image captured with High Speed Camera before High Speed Recording.</p> <p>Before high speed imagery starts (Not numbered chronologically) Tension crack T_5 extends downward to the bottom of the specimen. T_1 and T_2 widen.</p> <p style="text-align: right;">2</p>

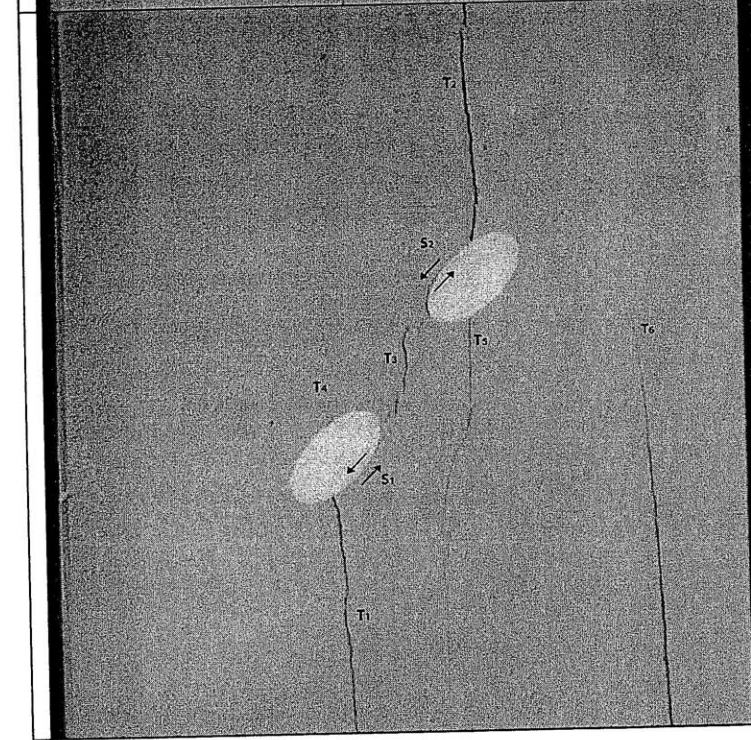


Time: 4m 19.260s
 σ : ~18.097 MPa

COALESCENCE
+Tensile Crack Initiation

Still image captured with High Speed Camera before High Speed Recording.

1



Time: 4m 40.674s
 σ : ~20.449 MPa

Still image captured with High Speed Camera before High Speed Recording.

2

	<p>Time: 5m 29.549s σ: ~23.723 MPa</p> <p>Frame 673 of the High Speed Camera footage.</p> <p>T₄ extends to the top of the specimen. T₇ forms at the bottom edge of the left inclusion. T₈ forms to the left of T₁. A small branch initiates off of T₂ and extends upward. Spalling occurs at the right edge of the left inclusion. T₁ and T₂ widen.</p> <p style="text-align: right;">3</p>
	<p>Time: 5m 29.577s σ: ~23.723 MPa</p> <p>Frame 535 of the High Speed Camera footage.</p> <p>T₉ forms below the left inclusion from T₁ and connect up to the left side of the left inclusion. T₁₀ forms below T₉ and extends from the bottom of the specimen to T₉. T₁ and T₂ widen.</p> <p style="text-align: right;">4</p>



Time: 5m 29.549s

σ : ~23.723 MPa

Frame 673 of the High Speed Camera footage.

3

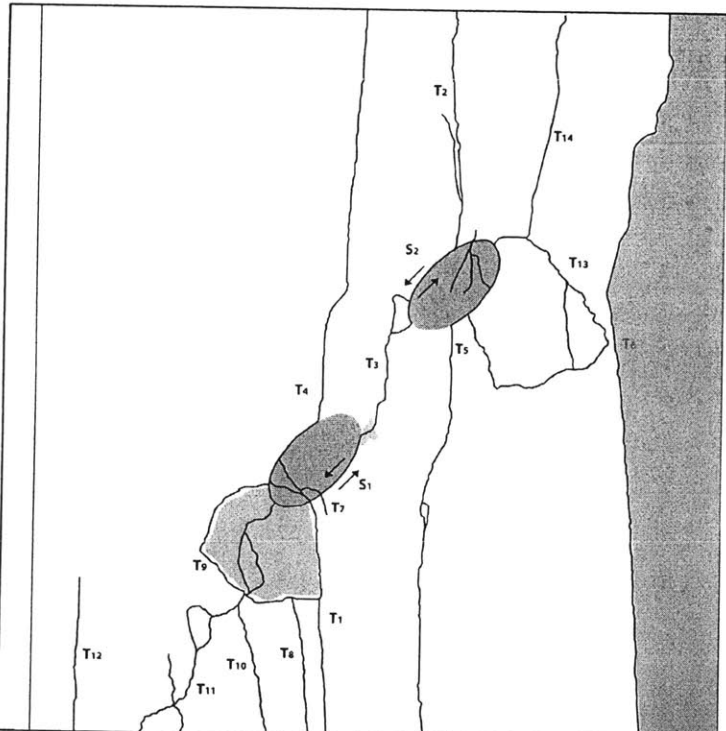


Time: 5m 29.577s

σ : ~23.723 MPa

Frame 535 of the High Speed Camera footage.

4

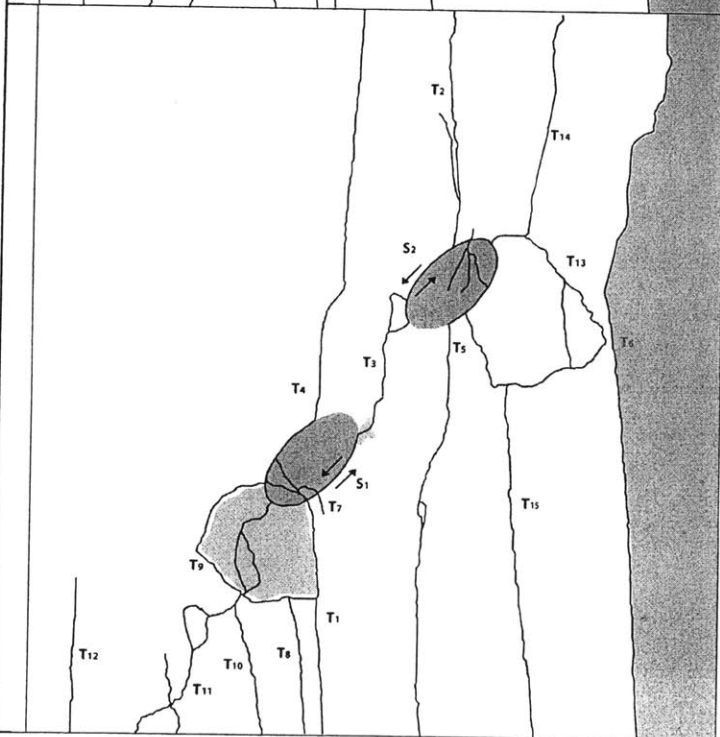


Time: 5m 29.642s
 σ : ~23.723 MPa

Frame 210 of the High Speed Camera footage.

T₁₁ forms to the left of T₁₀ and connects to T₉ (tensile debonding of left inclusion). T₁₂ initiates at the bottom left edge of the specimen and moves upward. T₁₃ forms at the right inclusion edge and propagates around to the bottom of the specimen (tensile debonding of right inclusion) (possible surface crack). T₁₄ extends from the top of the specimen to T₁₃. T₆ extends upward. A piece breaks off of the right side of the specimen. Spalling occurs below of the left inclusion (bounded by T₉). T₄ and T₅ widen.

5



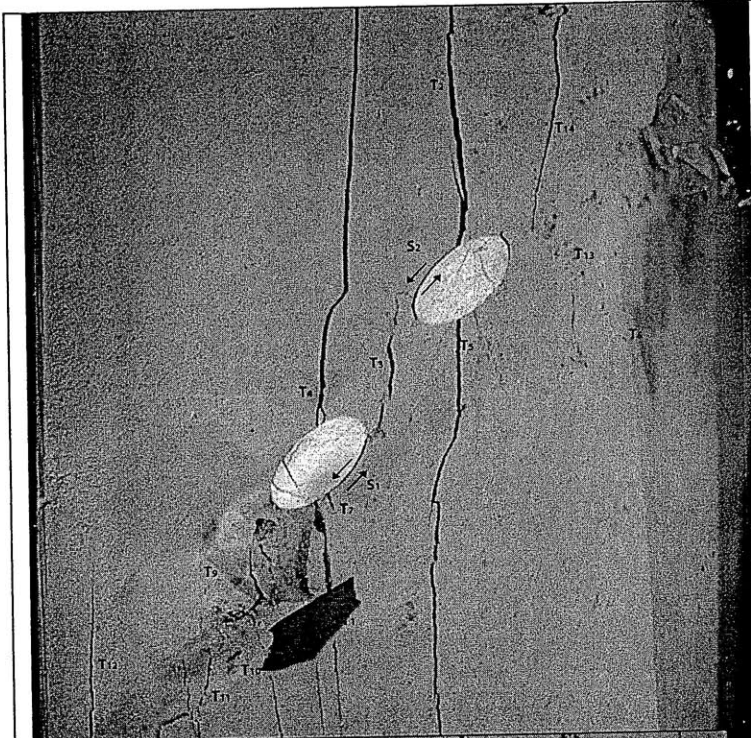
Time: 5m 29.682s
 σ : ~23.723 MPa

FAILURE

Frame 10 of the High Speed Camera footage.

T₁₅ extends from the bottom of the specimen to T₁₃. T₄ and T₅ widen.

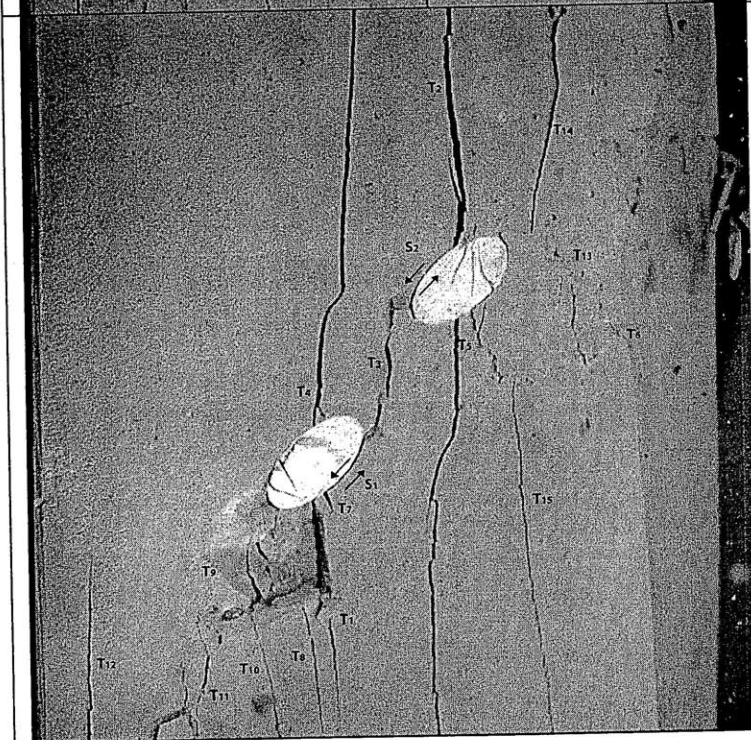
6



Time: 5m 29.642s
 σ : ~23.723 MPa

Frame 210 of the High Speed Camera footage.

5



Time: 5m 29.682s
 σ : ~23.723 MPa

FAILURE

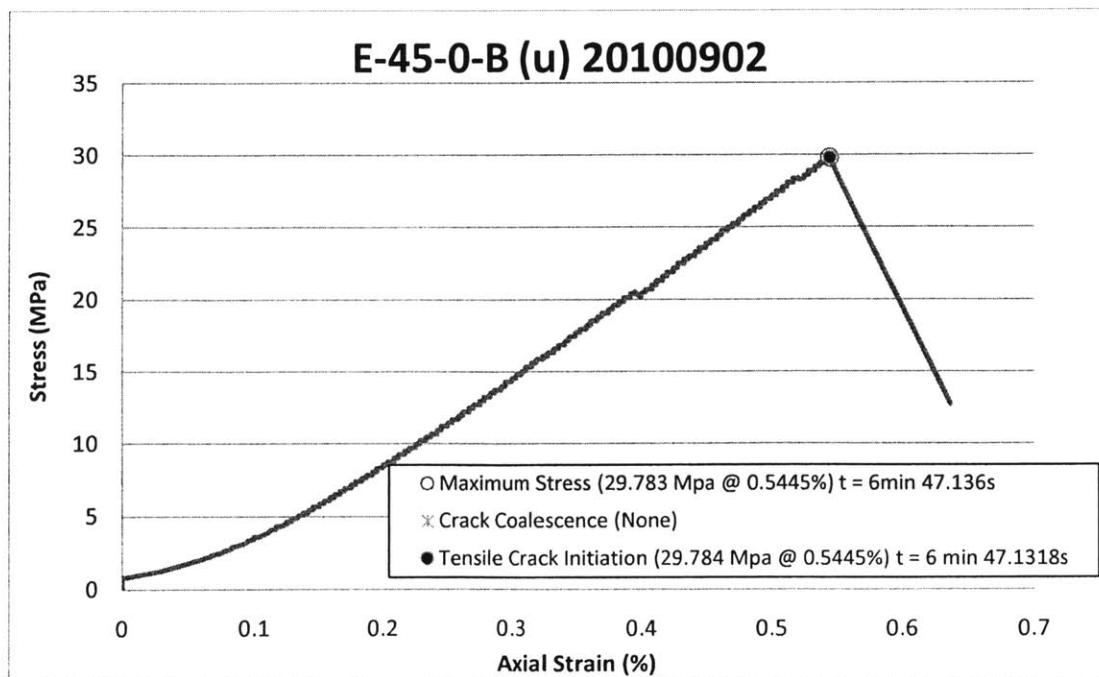
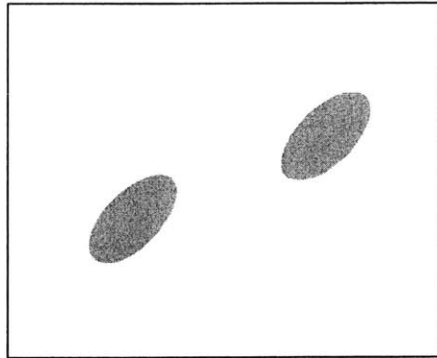
Frame 10 of the High Speed Camera footage.


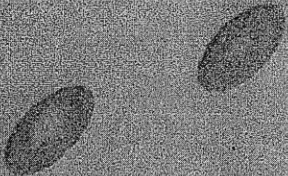
6

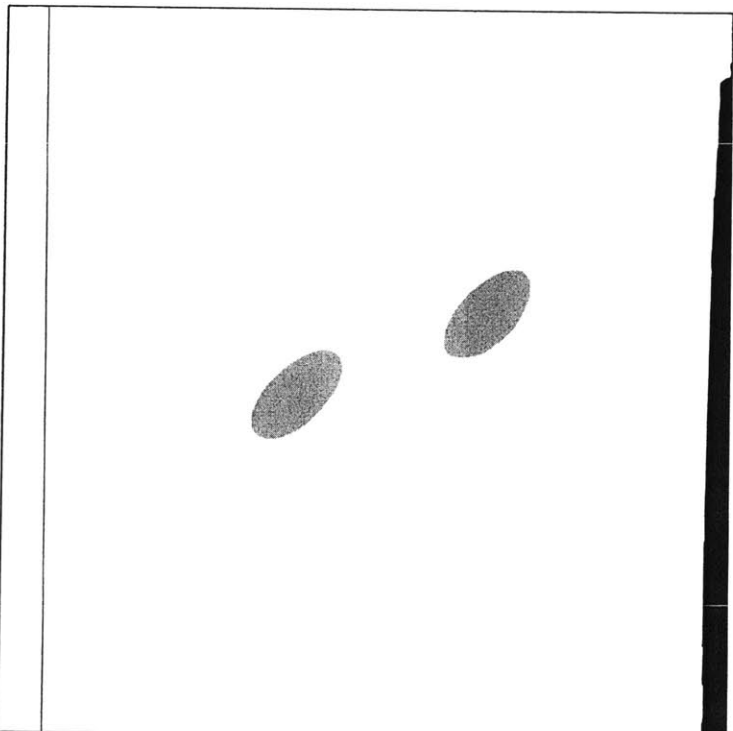
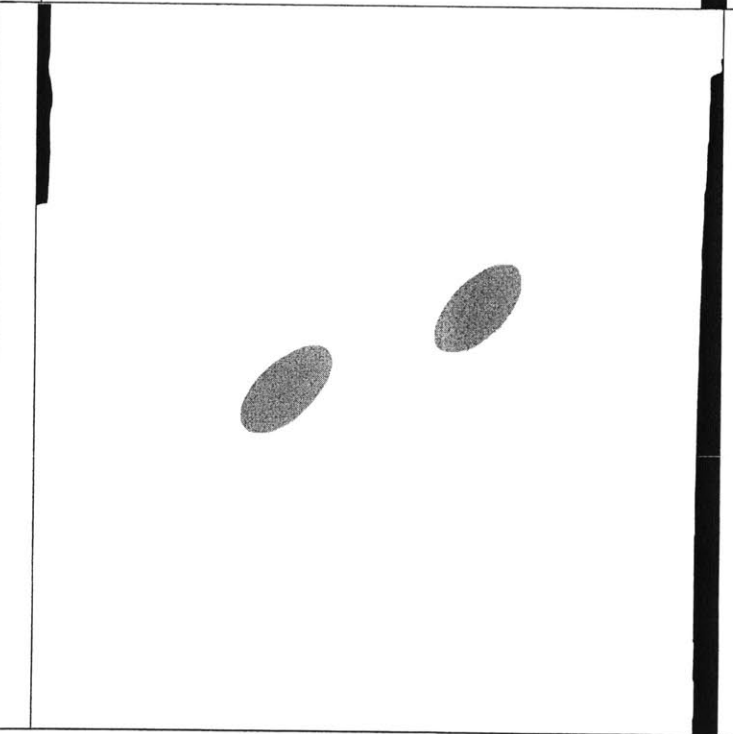
ULTRACAL

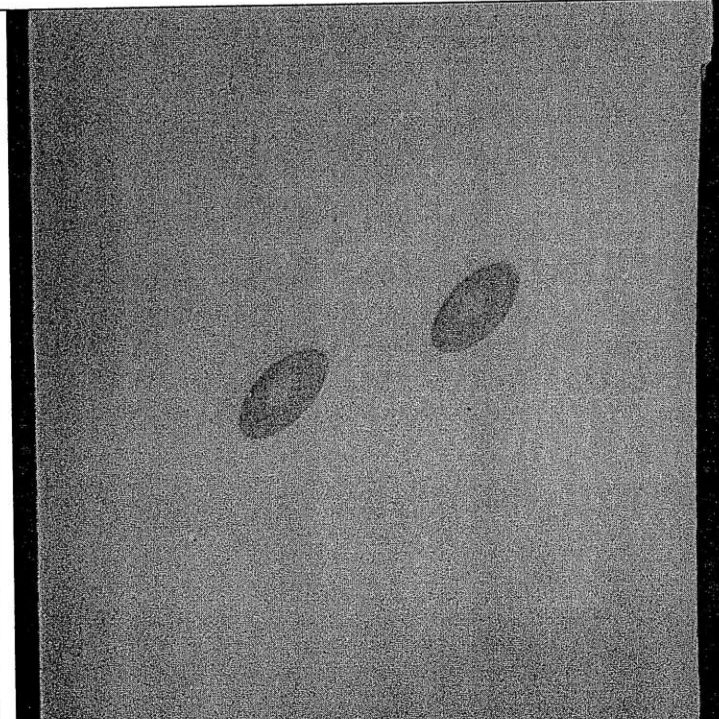
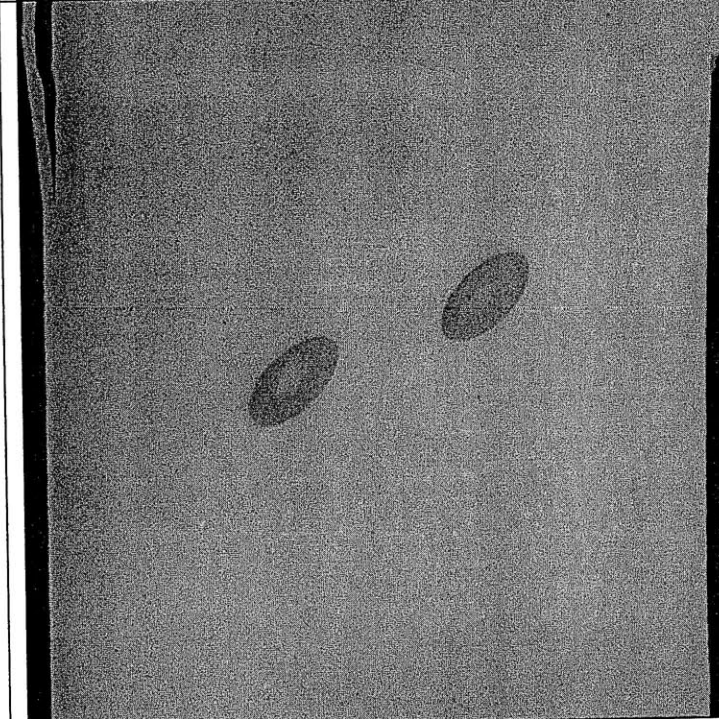
E-45-0-Bu

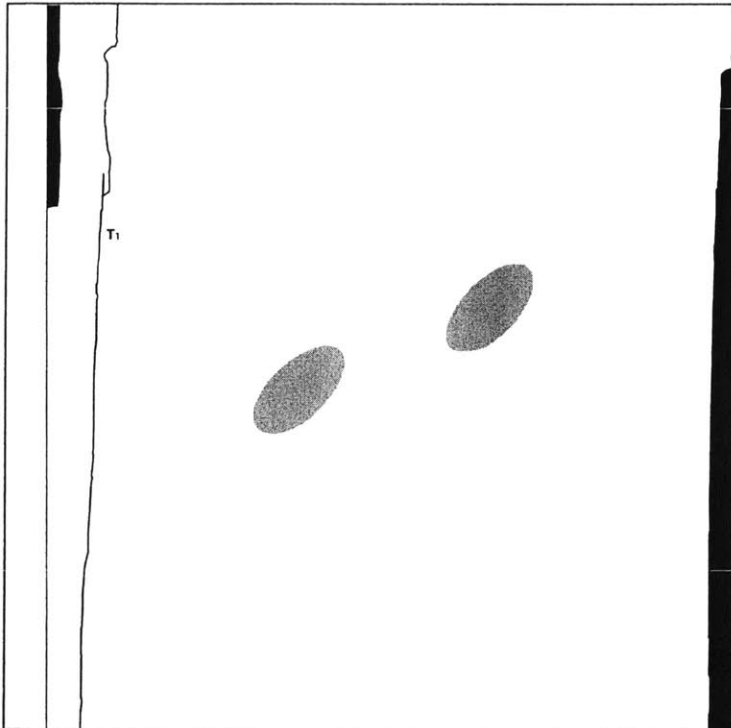
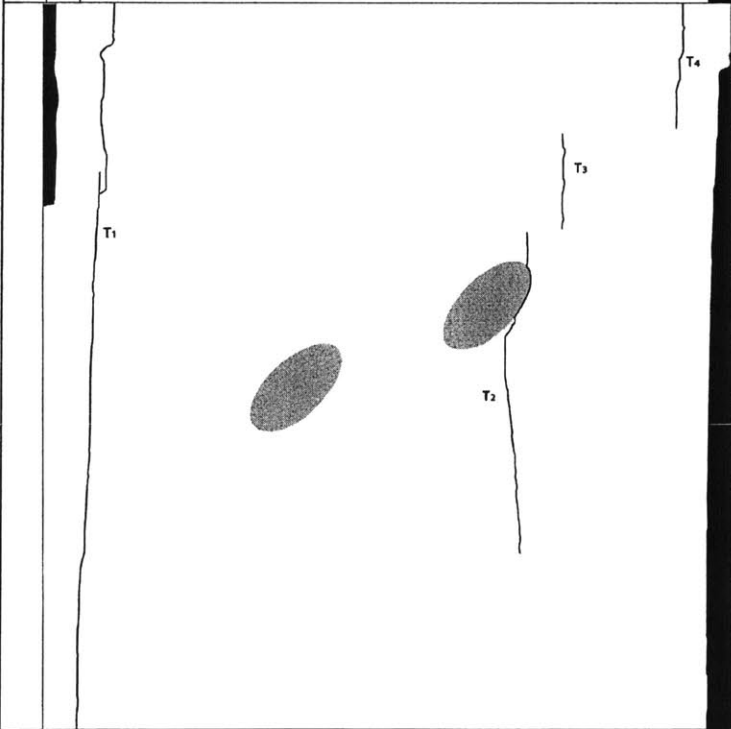
Shape = Ellipse
(Inclination = 45°
Bridging Angle = 0°
Test Repetition = B
Material = Ultracal
Size = 1/2"

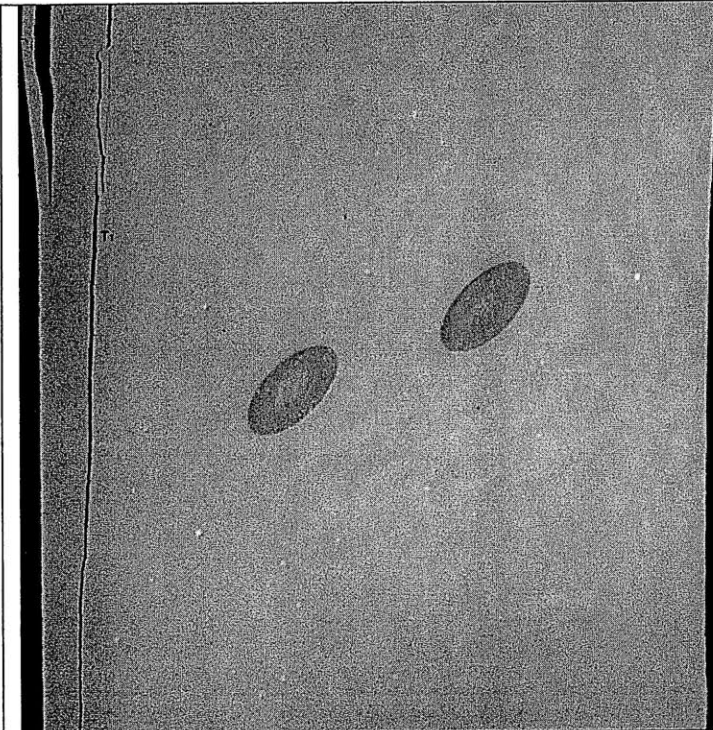


	<p>Time: 0m 0s σ: ~0 MPa</p> <p>Picture taken prior to testing.</p> <p style="text-align: right;">0</p>
	<p>Time: 0m 0s σ: ~0 MPa</p> <p>Picture taken prior to testing.</p> <p style="text-align: right;">0</p>

	<p>Time: 4m 29.478s σ: ~20.463 MPa</p> <p>Still image captured with High Speed Camera before High Speed Recording.</p> <p>A piece breaks off of the right side of the specimen.</p> <p style="text-align: right;">1</p>
	<p>Time: 6m 27.414s σ: ~28.453 MPa</p> <p>Still image captured with High Speed Camera before High Speed Recording.</p> <p>A small piece breaks off of the top left corner of the specimen.</p> <p style="text-align: right;">2</p>

	<p>Time: 4m 29.478s σ: ~20.463 MPa</p> <p>Still image captured with High Speed Camera before High Speed Recording.</p> <p>1</p>
	<p>Time: 6m 27.414s σ: ~28.453 MPa</p> <p>Still image captured with High Speed Camera before High Speed Recording.</p> <p>2</p>

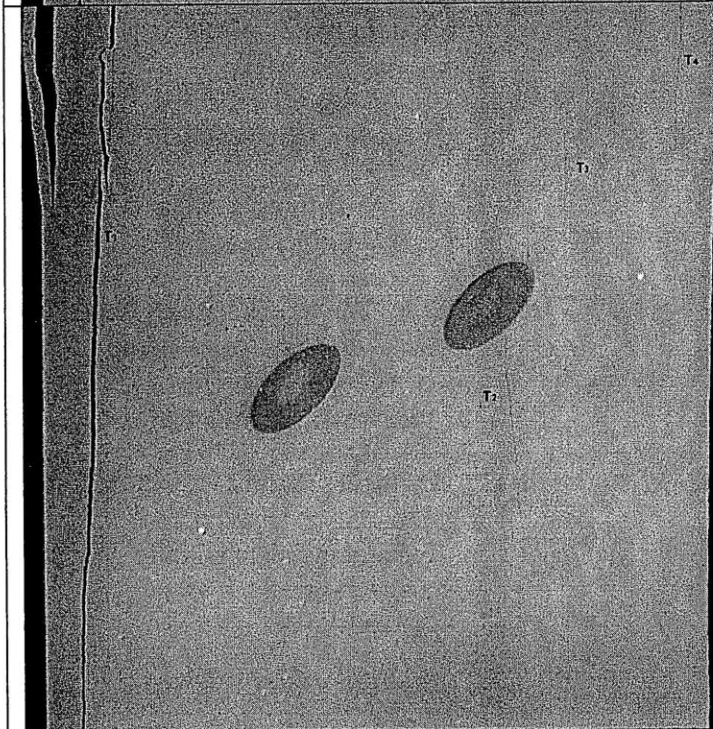
	<p>Time: 6m 47.049s σ: ~29.780 MPa</p> <p>Frame 663 of the High Speed Camera footage.</p> <p>Tension crack T_1 initiates from the top of the specimen and moves down to the bottom of the specimen (no interactions with the inclusions).</p> <p style="text-align: right;">3</p>
	<p>Time: 6m 47.1318s σ: ~29.784 MPa</p> <p>Tensile Crack Initiation</p> <p>Frame 251 of the High Speed Camera footage.</p> <p>T_2, T_3 and T_4 initiate on the same high speed frame (chronological order unknown). T_2 forms on the right side of the right inclusion (partial debonding). T_3 and T_4 form in the matrix in the top right-hand corner of the specimen.</p> <p style="text-align: right;">4</p>



Time: 6m 47.049s
 σ : ~29.780 MPa

Frame 663 of the High Speed Camera footage.

3

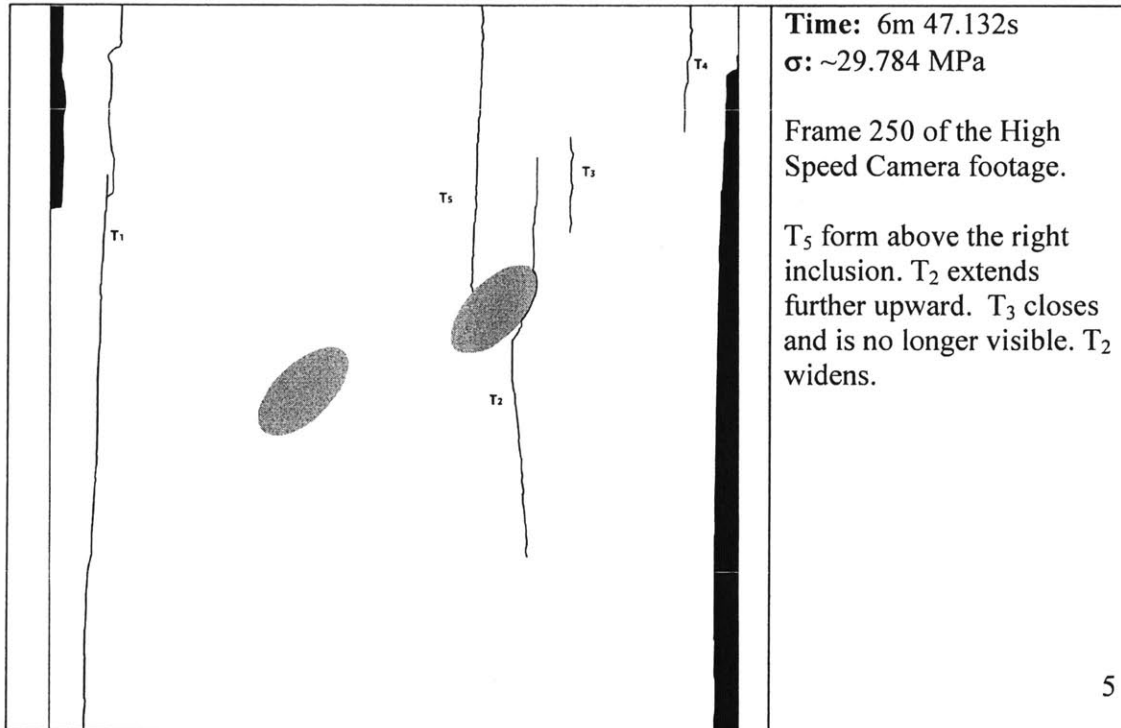


Time: 6m 47.1318s
 σ : ~29.784 MPa

Tensile Crack Initiation

Frame 251 of the High Speed Camera footage.

4

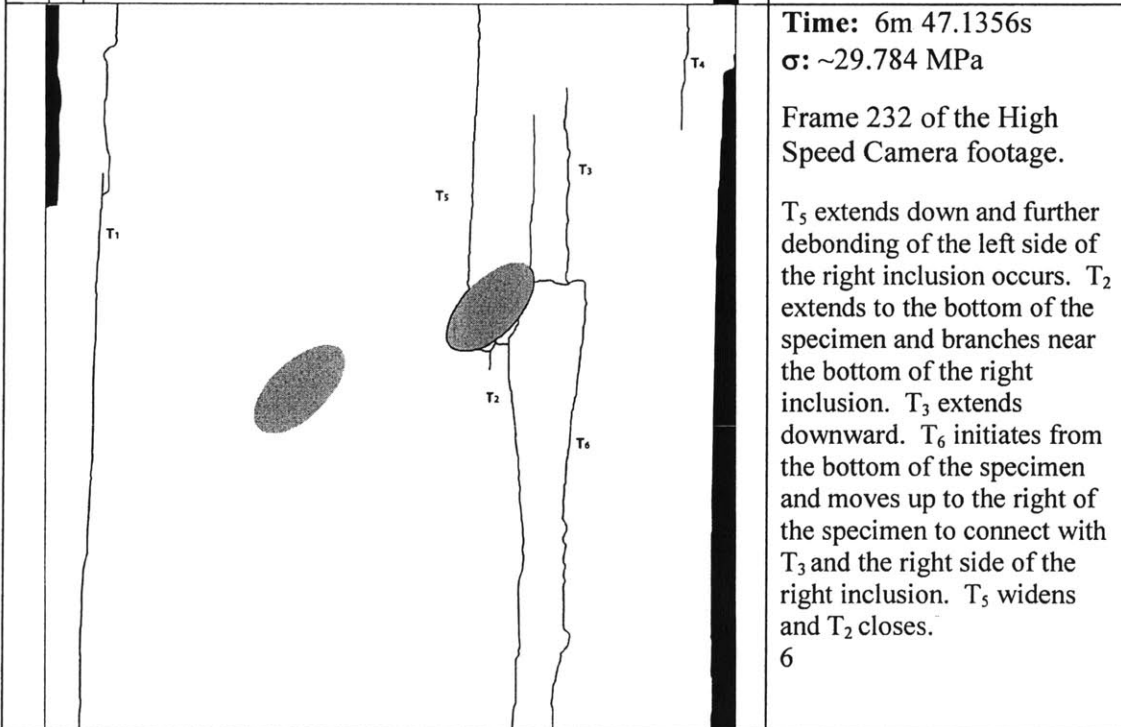


Time: 6m 47.132s
 σ : ~29.784 MPa

Frame 250 of the High Speed Camera footage.

T₅ form above the right inclusion. T₂ extends further upward. T₃ closes and is no longer visible. T₂ widens.

5

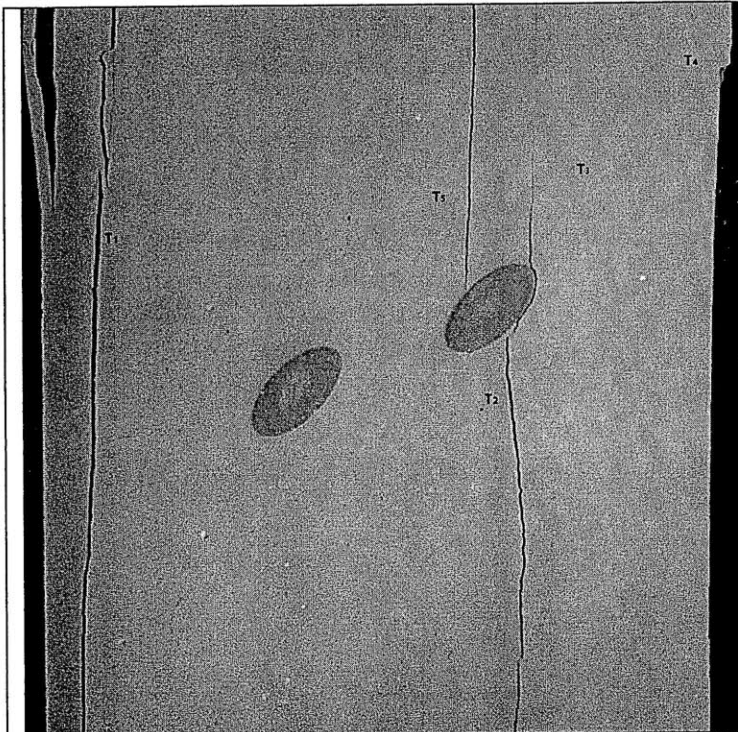


Time: 6m 47.1356s
 σ : ~29.784 MPa

Frame 232 of the High Speed Camera footage.

T₅ extends down and further debonding of the left side of the right inclusion occurs. T₂ extends to the bottom of the specimen and branches near the bottom of the right inclusion. T₃ extends downward. T₆ initiates from the bottom of the specimen and moves up to the right of the specimen to connect with T₃ and the right side of the right inclusion. T₅ widens and T₂ closes.

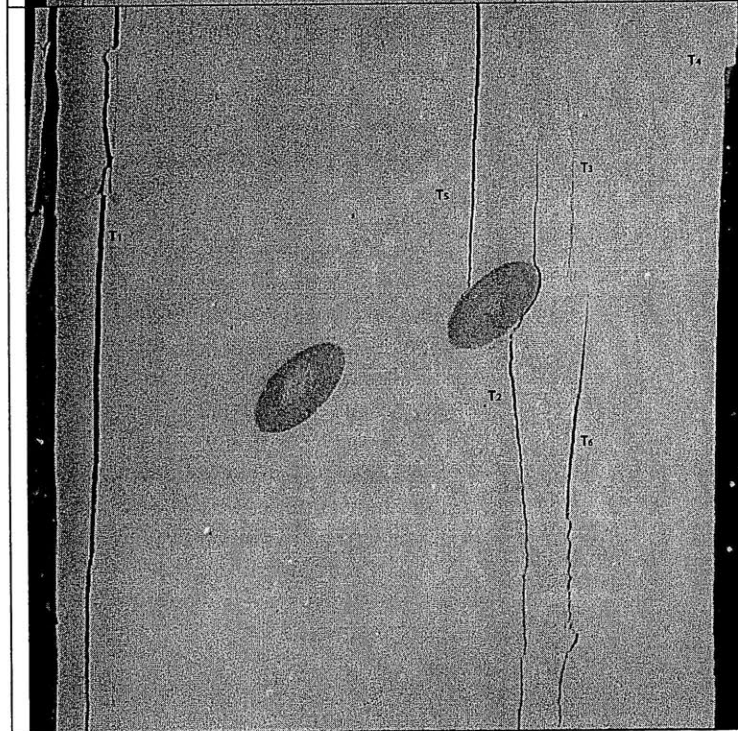
6



Time: 6m 47.132s
 σ : ~29.784 MPa

Frame 250 of the High Speed Camera footage.

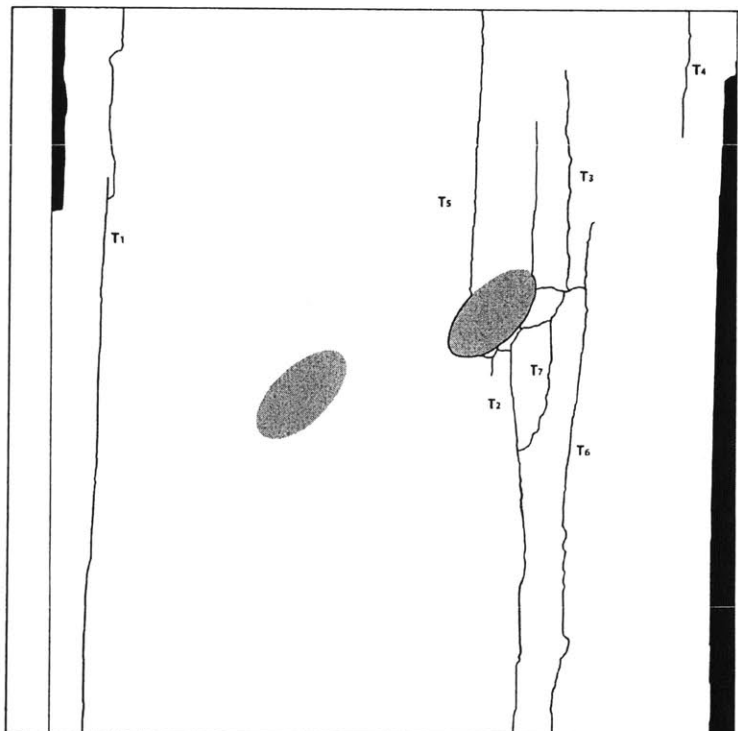
5



Time: 6m 47.1356s
 σ : ~29.784 MPa

Frame 232 of the High Speed Camera footage.

6



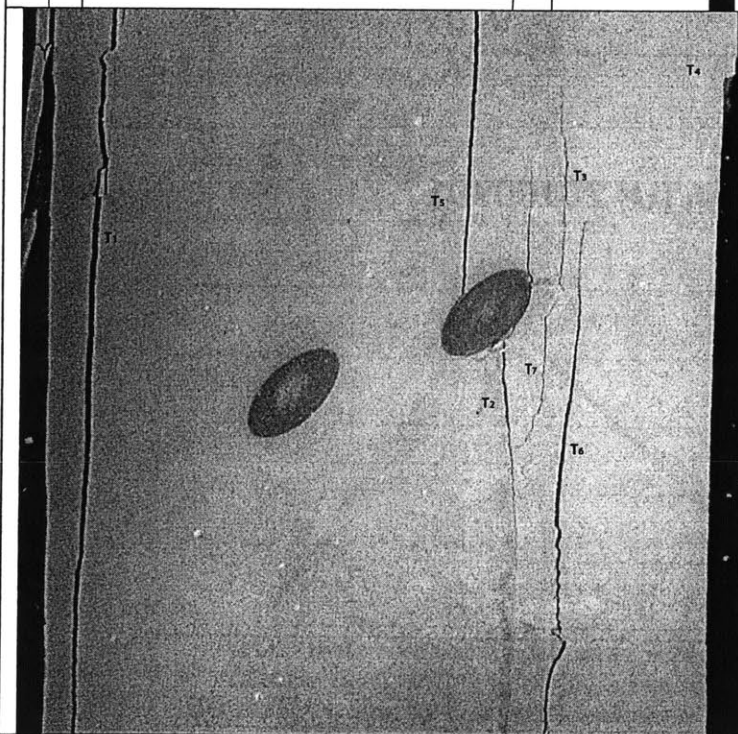
Time: 6m 47.1360s
 σ : ~29.784 MPa

FAILURE

Frame 230 of the High Speed Camera footage.

T₆ branches upward parallel to T₃, to the right of the right inclusion. T₇ forms between T₂ and T₆ and connects with T₂. T₅ and T₆ widen.

7



Time: 6m 47.1360s
 σ : ~29.784 MPa

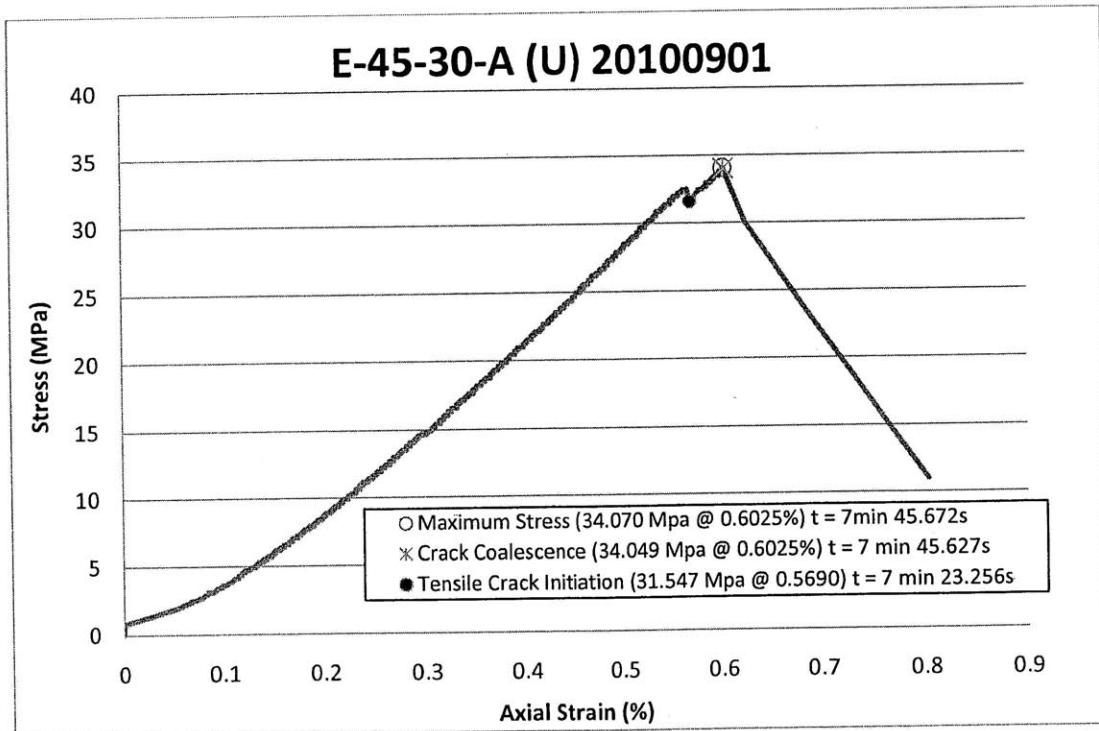
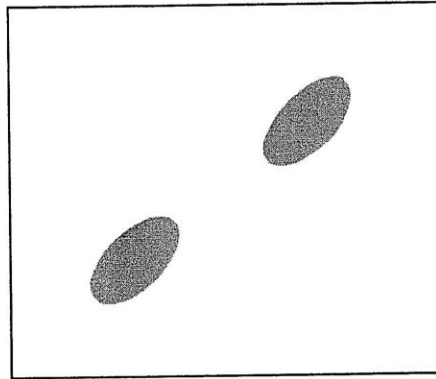
FAILURE

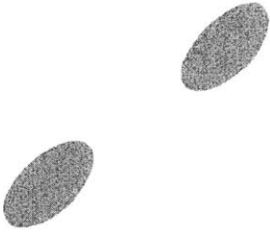
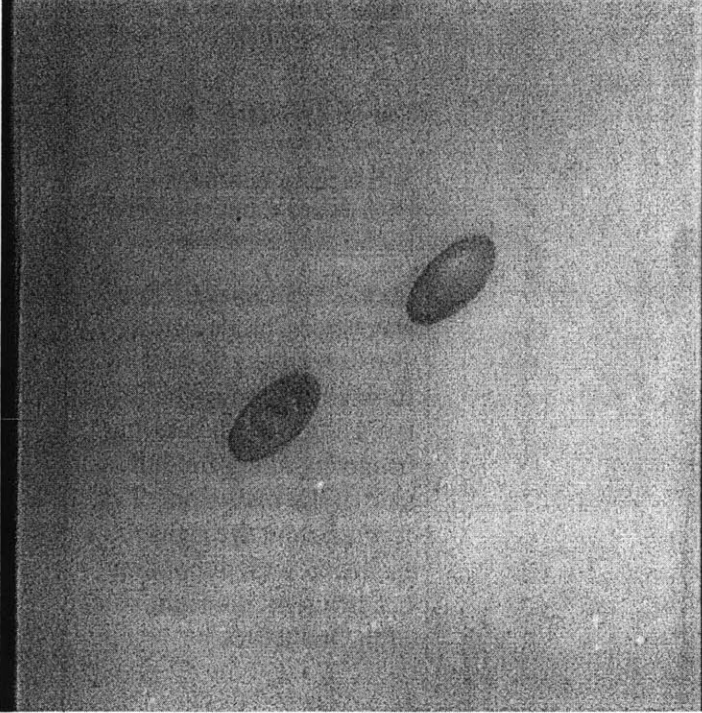
Frame 230 of the High Speed Camera footage.

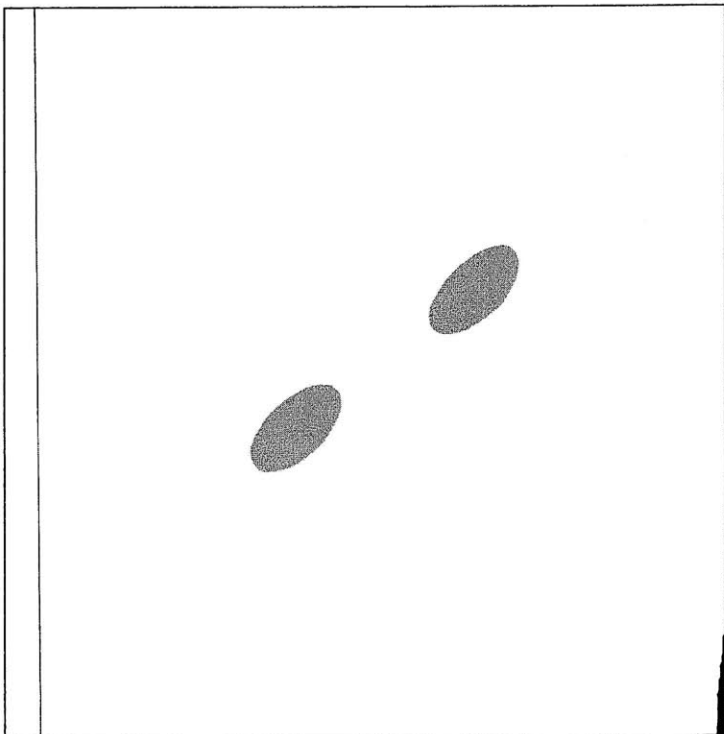
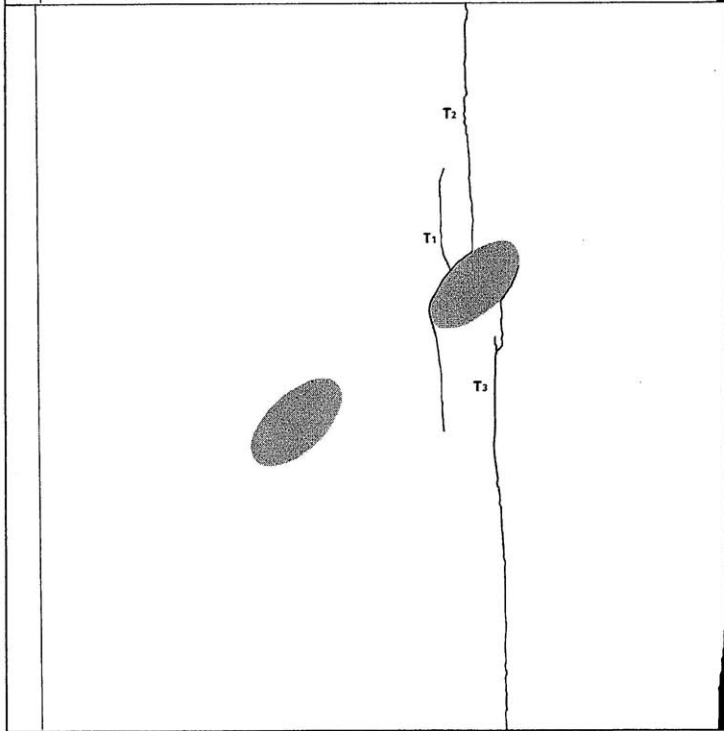
7

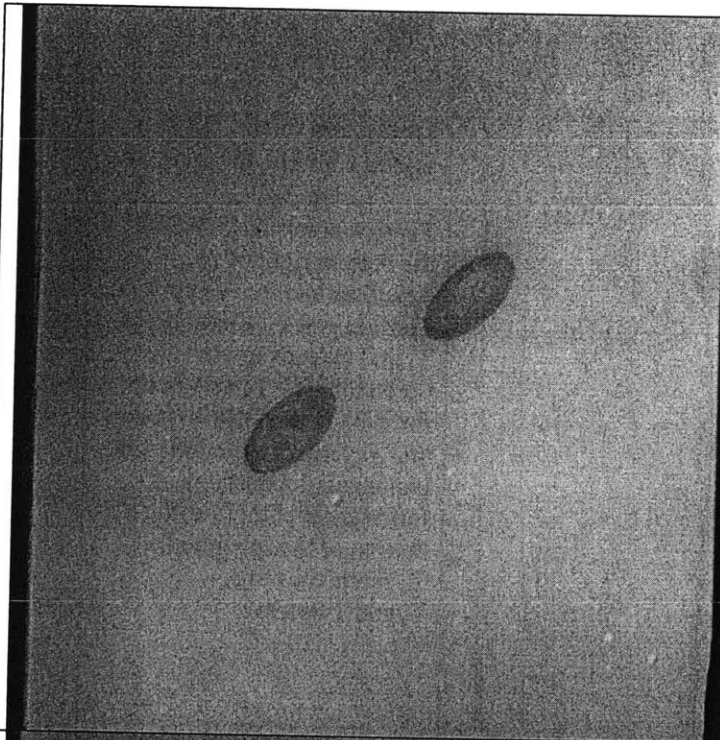
E-45-30-Au

Shape = Ellipse
(Inclination = 45°)
Bridging Angle = 30°
Test Repetition = A
Material = Ultracal
Size = 1/2"



	<p>Time: 0m 0s σ: ~0 MPa</p> <p>Picture taken prior to testing.</p> <p>0</p>
	<p>Time: 0m 0s σ: ~0 MPa</p> <p>Picture taken prior to testing.</p> <p>0</p>

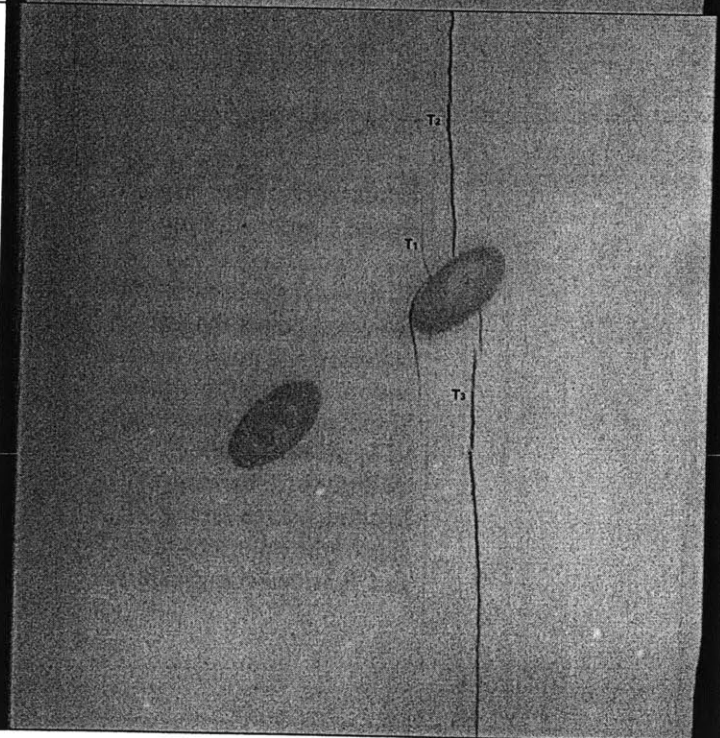
	<p>Time: 3m 4.872s σ: ~14.609 MPa</p> <p>Still image captured with High Speed Camera before High Speed Recording.</p> <p>A small piece breaks off of the bottom right corner of the specimen</p> <p style="text-align: right;">1</p>
	<p>Time: 7m 23.256 s σ: ~31.547 MPa</p> <p>Tensile Crack Initiation</p> <p>Still image captured with High Speed Camera before High Speed Recording.</p> <p>(Before High Speed – Not Numbered Chronologically) Tension cracks T_1 and T_2 form above the right inclusion with debonding occurring along the left side of the inclusion. T_3 forms below the right inclusion with debonding occurring on the right side of the inclusion.</p> <p style="text-align: right;">2</p>



Time: 3m 4.872s
 σ : ~14.609 MPa

Still image captured with
High Speed Camera before
High Speed Recording.

1



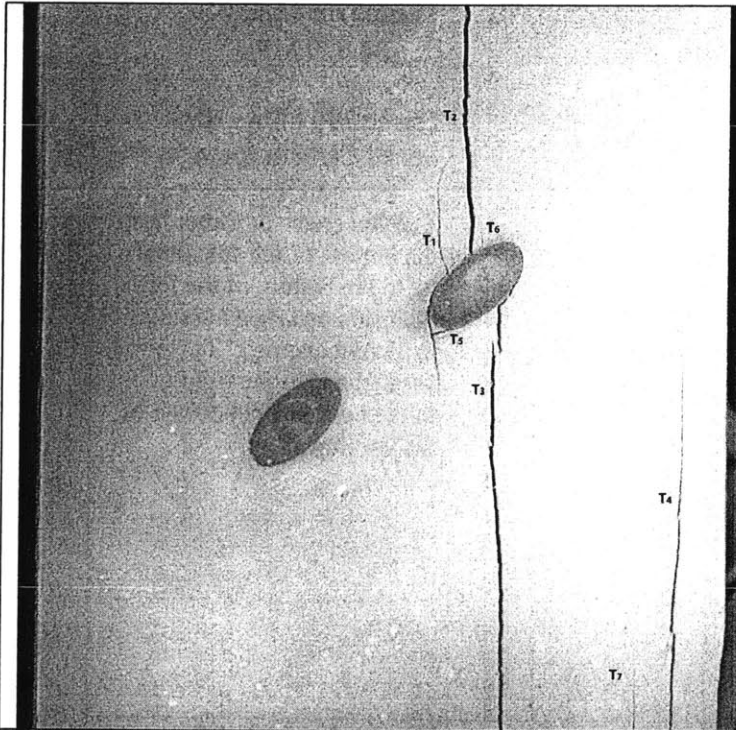
Time: 7m 23.256 s
 σ : ~31.547 MPa

Tensile Crack Initiation

Still image captured with
High Speed Camera before
High Speed Recording.

2

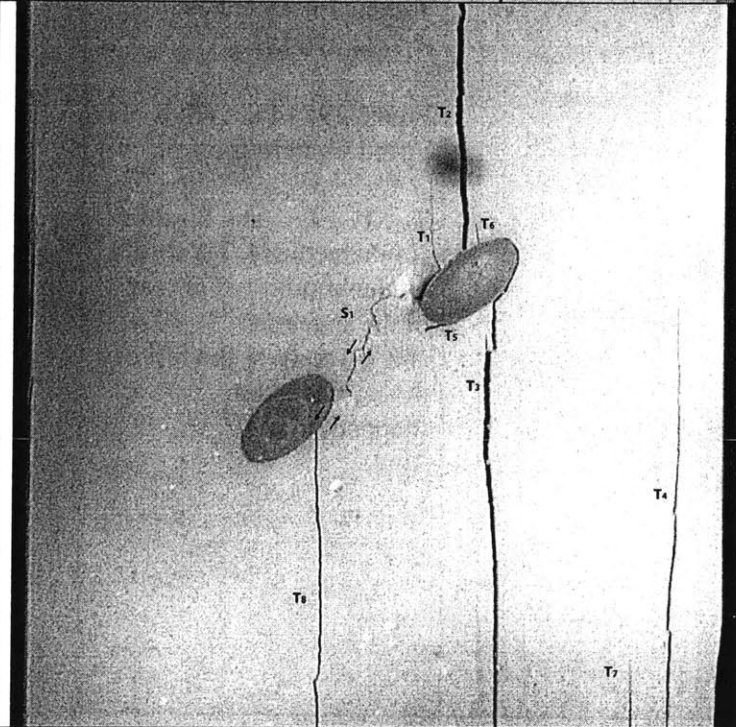
<p>The diagram shows a vertical specimen with two shaded oval inclusions. A central vertical crack is labeled T₁ at its top and T₅ at its bottom. To the right of the specimen, a vertical crack is labeled T₄. At the bottom of the specimen, a crack is labeled T₇. On the left side, a crack is labeled T₂. On the right side, a crack is labeled T₃. Above the right inclusion, a crack is labeled T₆. The top of the central crack is labeled T₁.</p>	<p>Time: 7m 45.579s σ: 34.049 MPa</p> <p>Frame 690 of the High Speed Camera footage.</p> <p>Tension crack T₄ forms on the bottom right of the specimen and moves upward. Tension crack T₅ initiates at T₁ and extends toward T₃ (debonding). T₃ moves up the right side of the inclusion and T₆ forms above the right inclusion (debonding). T₇ forms parallel to T₄ at the bottom of the specimen. T₁ extend upward. T₂ and T₃ widen.</p> <p style="text-align: right;">3</p>
<p>The diagram shows the specimen at a later stage. The central crack is now labeled T₁ at the top and T₅ at the bottom. A new crack T₈ has formed at the bottom left. A shear crack S₁ is shown between the two inclusions. The right inclusion is now surrounded by cracks T₅ and T₆. The left inclusion is surrounded by cracks T₁ and T₂. The right side of the specimen still shows cracks T₃ and T₄. The bottom crack is still labeled T₇.</p>	<p>Time: 7m 45.627s σ: ~34.049 MPa</p> <p>COALESCENCE</p> <p>Frame 449 of the High Speed Camera footage.</p> <p>T₈ forms at the bottom of the specimen below the left inclusion and moves up to the bottom of the left inclusion. Simultaneously shear crack S₁ forms between the inclusions (debonding). Spalling occurs on the left side of the right inclusion. T₂ and T₃ widen significantly.</p> <p style="text-align: right;">4</p>



Time: 7m 45.579s
 σ : 34.049 MPa

Frame 690 of the High Speed Camera footage.

3

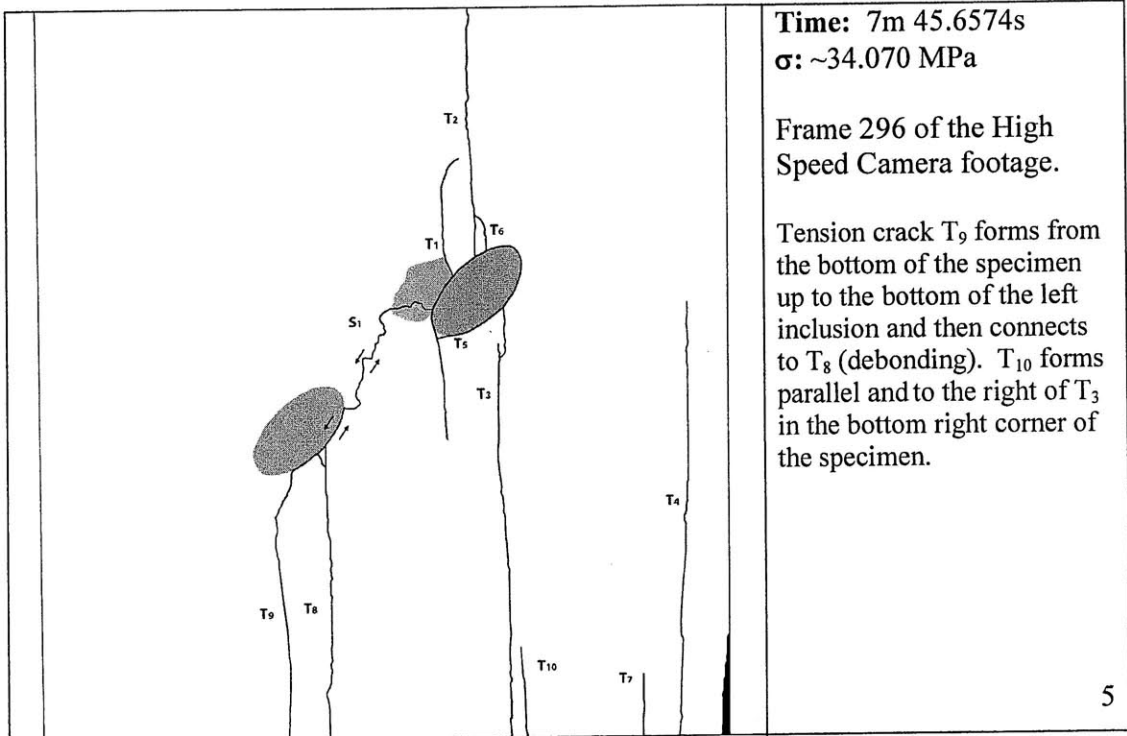


Time: 7m 45.627s
 σ : ~34.049 MPa

COALESCENCE

Frame 449 of the High Speed Camera footage.

4

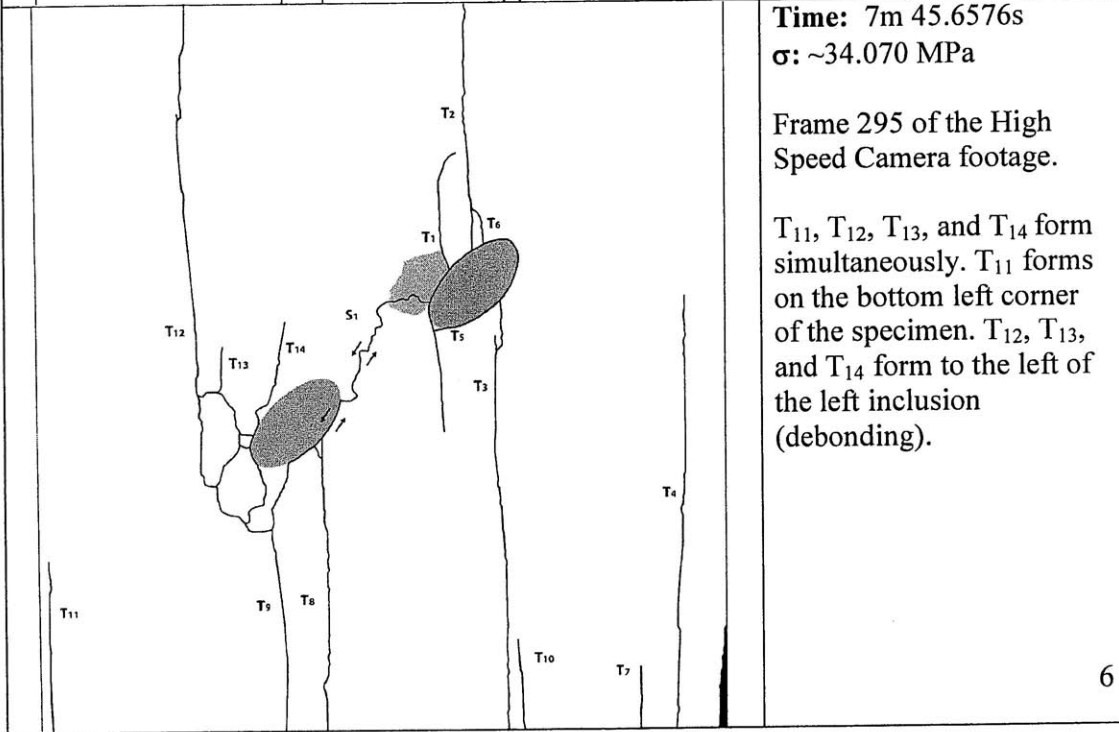


Time: 7m 45.6574s
 σ : ~34.070 MPa

Frame 296 of the High Speed Camera footage.

Tension crack T₉ forms from the bottom of the specimen up to the bottom of the left inclusion and then connects to T₈ (debonding). T₁₀ forms parallel and to the right of T₃ in the bottom right corner of the specimen.

5

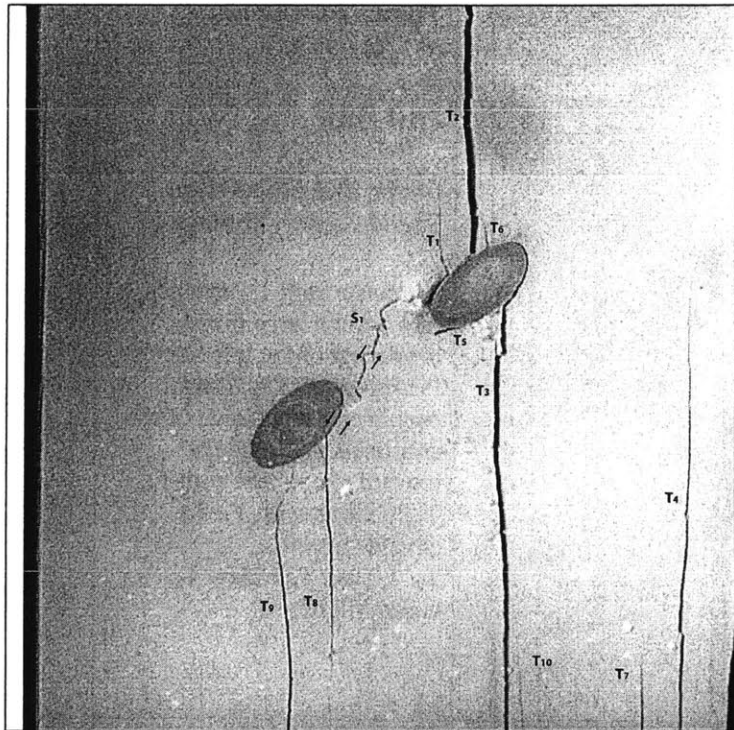


Time: 7m 45.6576s
 σ : ~34.070 MPa

Frame 295 of the High Speed Camera footage.

T₁₁, T₁₂, T₁₃, and T₁₄ form simultaneously. T₁₁ forms on the bottom left corner of the specimen. T₁₂, T₁₃, and T₁₄ form to the left of the left inclusion (debonding).

6

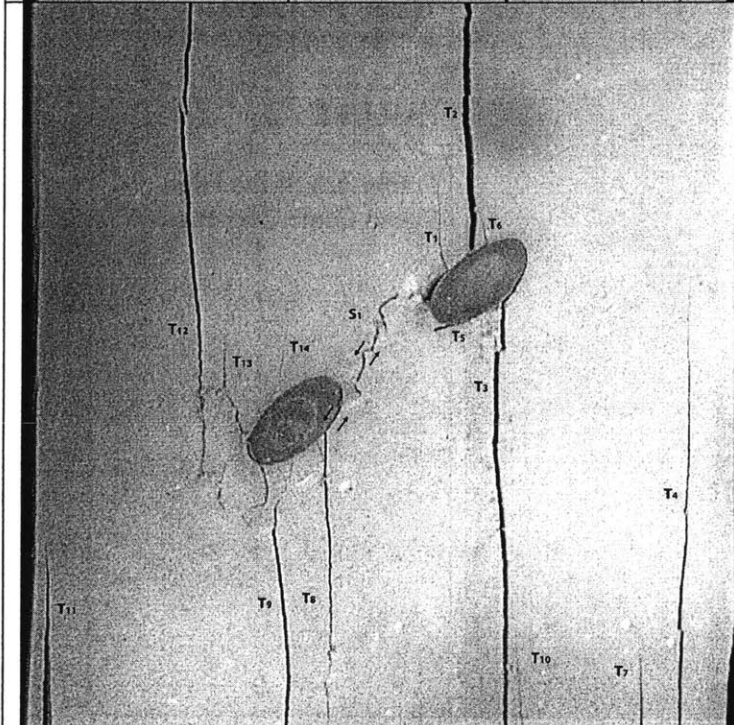


Time: 7m 45.6574s

σ : ~34.070 MPa

Frame 296 of the High Speed Camera footage.

5



Time: 7m 45.6576s

σ : ~34.070 MPa

Frame 295 of the High Speed Camera footage.

6



Time: 7m 45.672s
 σ : ~34.070 MPa

FAILURE

Frame 223 of the High Speed Camera footage.

A branch from T₁₂ extends down and a large piece breaks off of the left side of the specimen. Spalling occurs on the left side of the specimen. T₁₀ extends upward to connect with T₃. T₁ connects with T₂. T₄ extends upward. T₂, T₃, and T₉ widen. T₈ closes slightly.

7



Time: 7m 45.672s
 σ : ~34.070 MPa

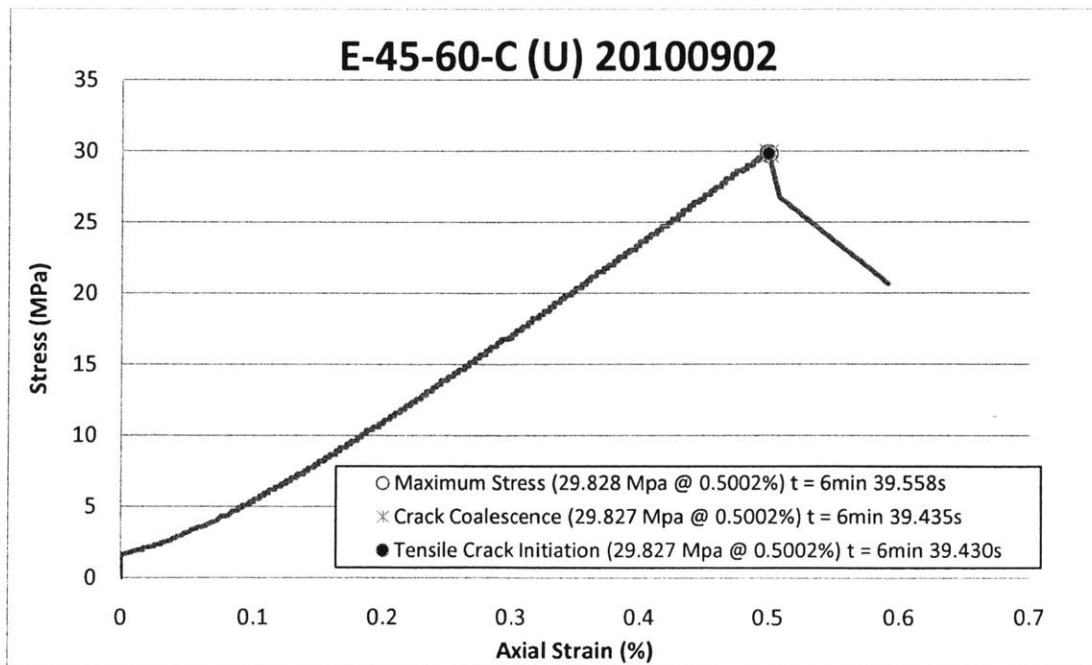
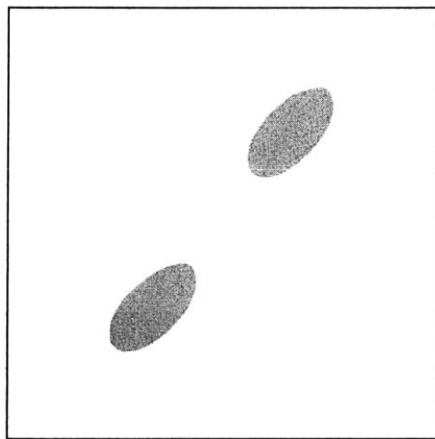
FAILURE

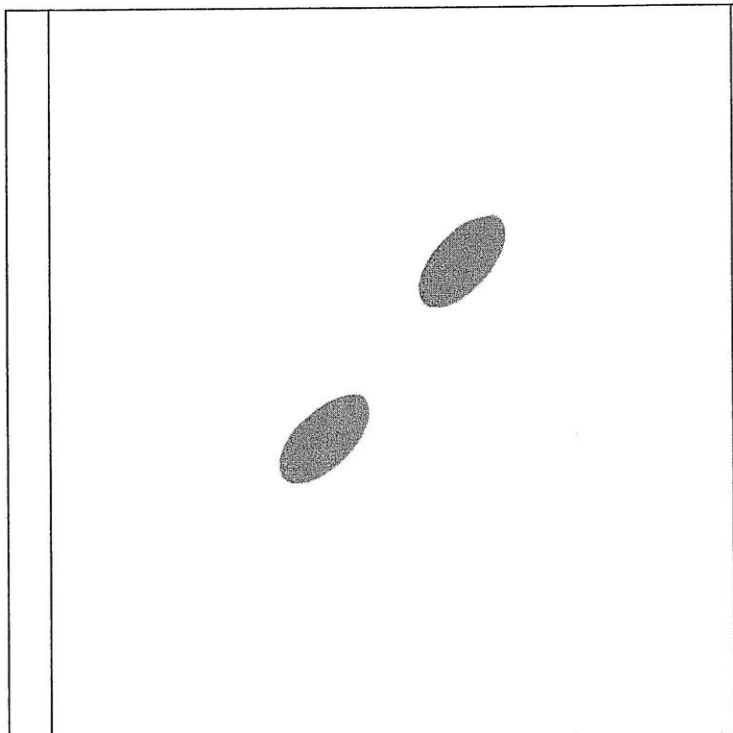
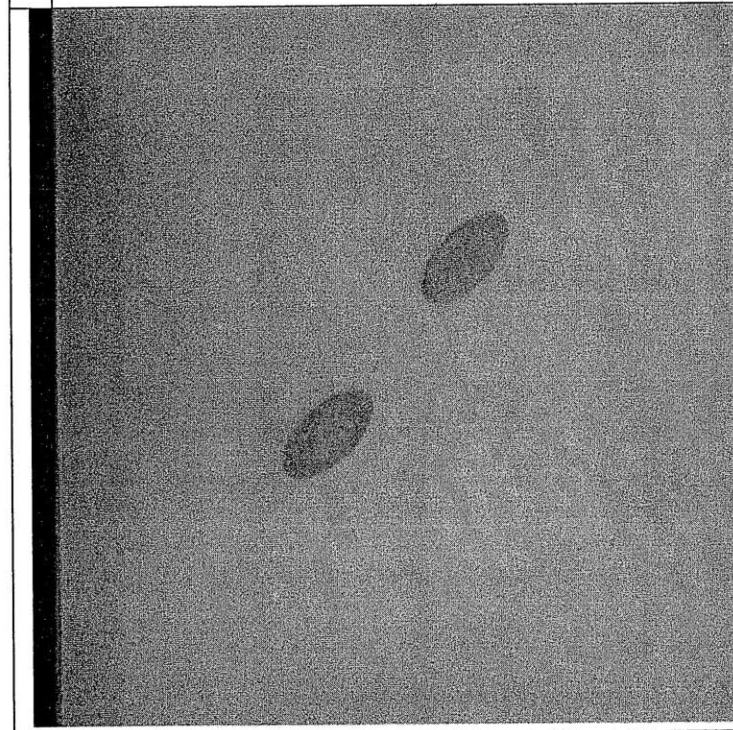
Frame 223 of the High Speed Camera footage.

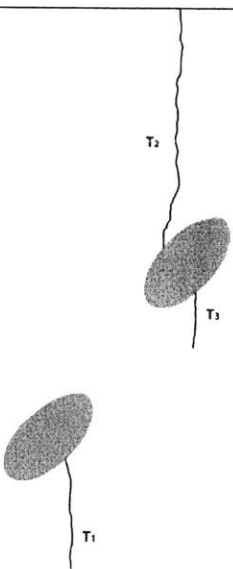
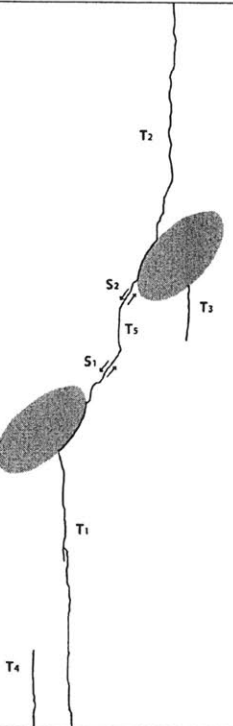
7

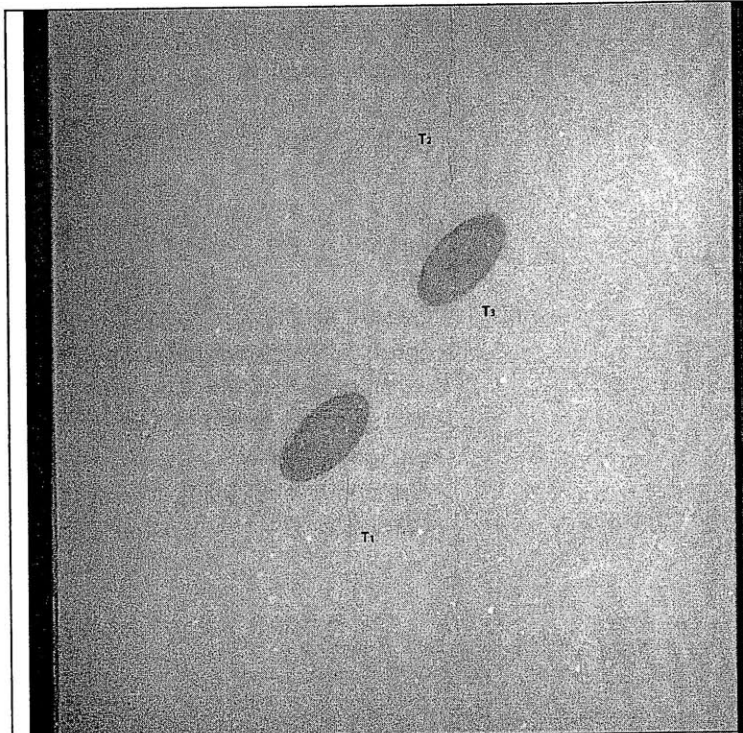
E-45-60-Cu

Shape = Ellipse
(Inclination = 45°)
Bridging Angle = 60°
Test Repetition = C
Material = Ultracal
Size = 1/2"



	<p>Time: 0m 0s σ: ~0 MPa</p> <p>Picture taken prior to testing.</p> <p>0</p>
	<p>Time: 0m 0s σ: ~0 MPa</p> <p>Picture taken prior to testing.</p> <p>0</p>

	<p>Time: 6m 39.430s σ: ~29.827 MPa</p> <p>Tensile Crack Initiation</p> <p>Frame 749 of the High Speed Camera footage.</p> <p>Tension cracks T_1, T_2 and T_3 form simultaneously. T_1 forms below the left inclusion. T_2 forms above the right inclusion. T_3 forms below the right inclusion.</p> <p style="text-align: right;">1</p>
	<p>Time: 6m 39.435s σ: ~29.827 MPa</p> <p>COALESCENCE</p> <p>Frame 724 of the High Speed Camera footage.</p> <p>T_4 forms at the bottom of the specimen boundary. T_1 extends down to the bottom of the specimen. T_1 extends upward along the right side of the left inclusions (debonding). T_2 extends downward along the left side of the right inclusions (debonding). S_1, S_2, and T_5 form simultaneously resulting in coalescence between the two inclusions. T_1 and T_2 widen. T_3 closes slightly.</p> <p style="text-align: right;">2</p>

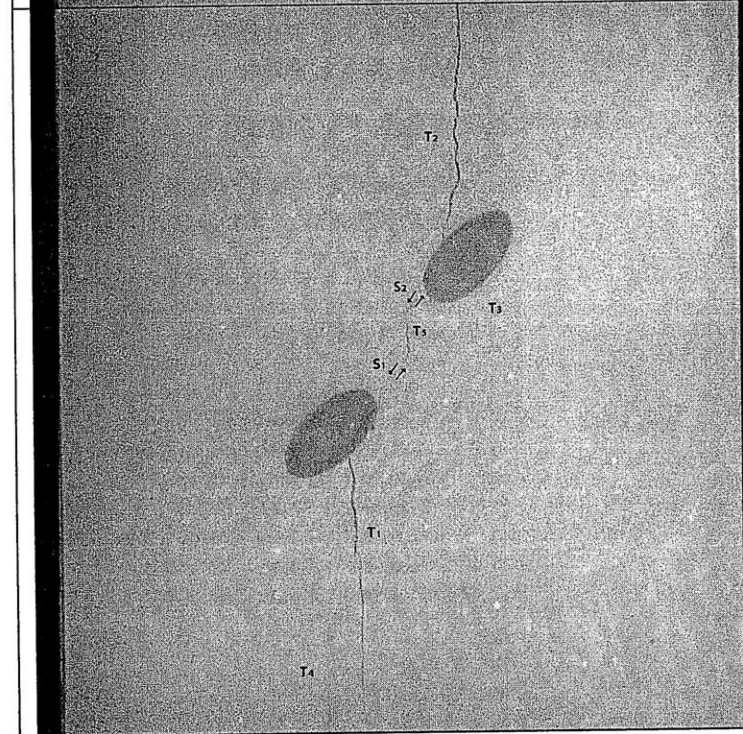


Time: 6m 39.430s
 σ : ~29.827 MPa

Tensile Crack Initiation

Frame 749 of the High Speed Camera footage.

1

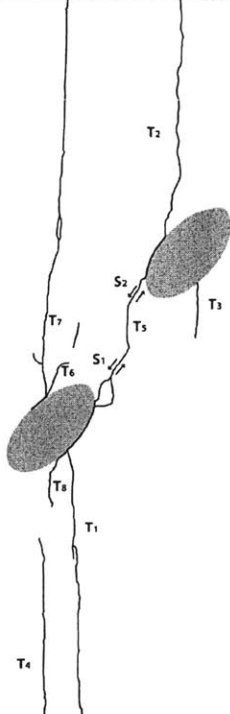
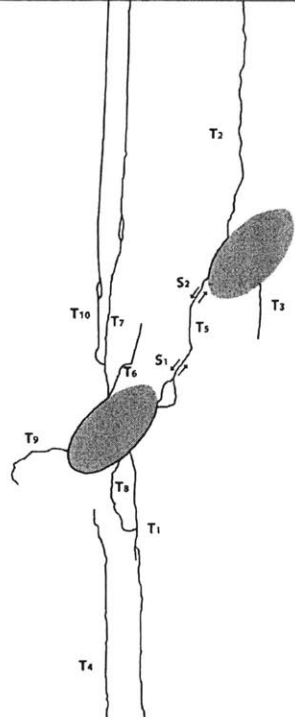


Time: 6m 39.435s
 σ : ~29.827 MPa

COALESCENCE

Frame 724 of the High Speed Camera footage.

2

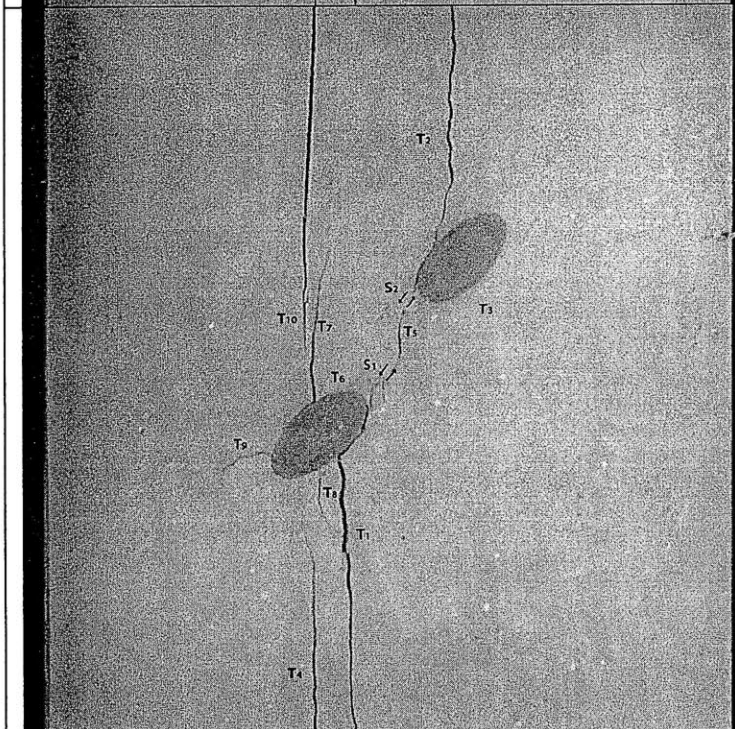
 <p>A schematic diagram of a crack network in a specimen. Two dark grey oval inclusions are shown. The left inclusion is larger and has a crack labeled T₆ extending upwards from its top edge. A crack labeled T₇ extends upwards from the top of the left inclusion. A crack labeled T₈ extends downwards from the bottom of the left inclusion. A crack labeled T₅ extends upwards from the right side of the left inclusion. A crack labeled T₃ extends upwards from the right side of the right inclusion. A crack labeled T₂ extends upwards from the top of the right inclusion. A crack labeled T₁ extends upwards from the bottom of the specimen. A crack labeled T₄ extends downwards from the bottom of the specimen. Two small cracks labeled S₁ and S₂ are shown near the top of the left inclusion.</p>	<p>Time: 6m 39.436s σ: ~29.827 MPa</p> <p>Frame 718 of the High Speed Camera footage.</p> <p>Tension crack T₆ forms in the matrix above the left inclusion. T₇ then forms at the top of the inclusion and extends to the top of the specimen (debonding). T₈ forms below the left inclusion and T₄ simultaneously extends upward. T₁ and T₂ widen.</p> <p style="text-align: right;">3</p>
 <p>A schematic diagram of a crack network in a specimen, similar to the one above. The left inclusion is larger and has a crack labeled T₉ extending upwards from its top edge. A crack labeled T₆ extends upwards from the top of the left inclusion. A crack labeled T₇ extends upwards from the top of the left inclusion. A crack labeled T₈ extends downwards from the bottom of the left inclusion. A crack labeled T₅ extends upwards from the right side of the left inclusion. A crack labeled T₃ extends upwards from the right side of the right inclusion. A crack labeled T₂ extends upwards from the top of the right inclusion. A crack labeled T₁ extends upwards from the bottom of the specimen. A crack labeled T₄ extends downwards from the bottom of the specimen. Two small cracks labeled S₁ and S₂ are shown near the top of the left inclusion. A crack labeled T₁₀ extends upwards from the left side of the left inclusion.</p>	<p>Time: 6m 39.515s σ: ~29.828 MPa</p> <p>Frame 323 of the High Speed Camera footage.</p> <p>T₆ extends upward above the left inclusion. T₉ forms on the left side of the left inclusion. T₁₀ forms to the left of T₇ and T₇ extends down the left side of the left inclusion (debonding). T₁ widens slightly. T₇ closes.</p> <p style="text-align: right;">4</p>



Time: 6m 39.436s
 σ : ~29.827 MPa

Frame 718 of the High Speed Camera footage.

3

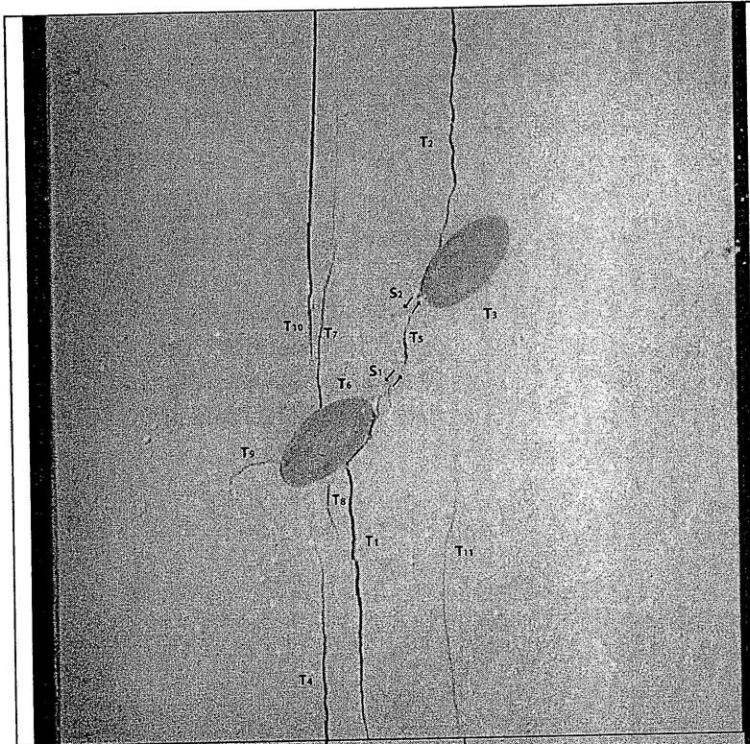


Time: 6m 39.515s
 σ : ~29.828 MPa

Frame 323 of the High Speed Camera footage.

4

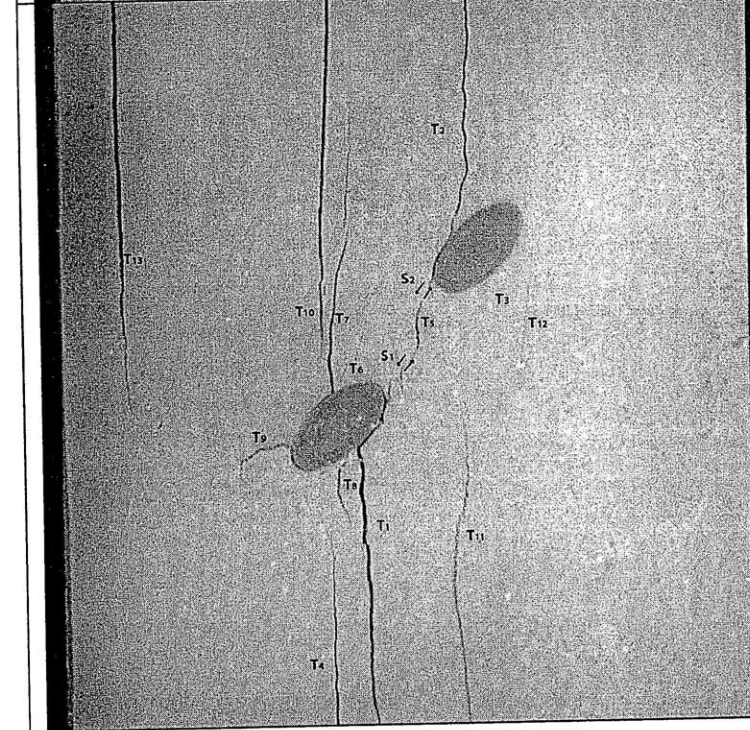
	<p>Time: 6m 39.519s σ: ~29.828 MPa</p> <p>Frame 307 of the High Speed Camera footage.</p> <p>T₁₁ forms at the bottom specimen boundary and propagates into the matrix below the right inclusion.</p> <p style="text-align: right;">5</p>
	<p>Time: 6m 39.538s σ: ~29.828 MPa</p> <p>Frame 212 of the High Speed Camera footage.</p> <p>T₁₂ forms in the matrix to below the right inclusion. T₁₃ forms at the top of the specimen and extends into the matrix to the left of the left inclusion.</p> <p style="text-align: right;">6</p>



Time: 6m 39.519s
 σ : ~29.828 MPa

Frame 307 of the High Speed Camera footage.

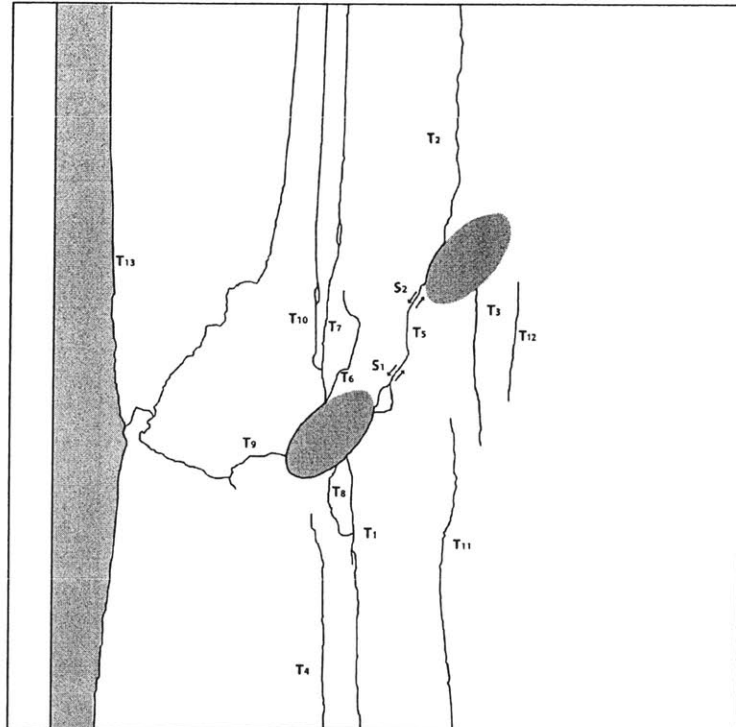
5



Time: 6m 39.538s
 σ : ~29.828 MPa

Frame 212 of the High Speed Camera footage.

6

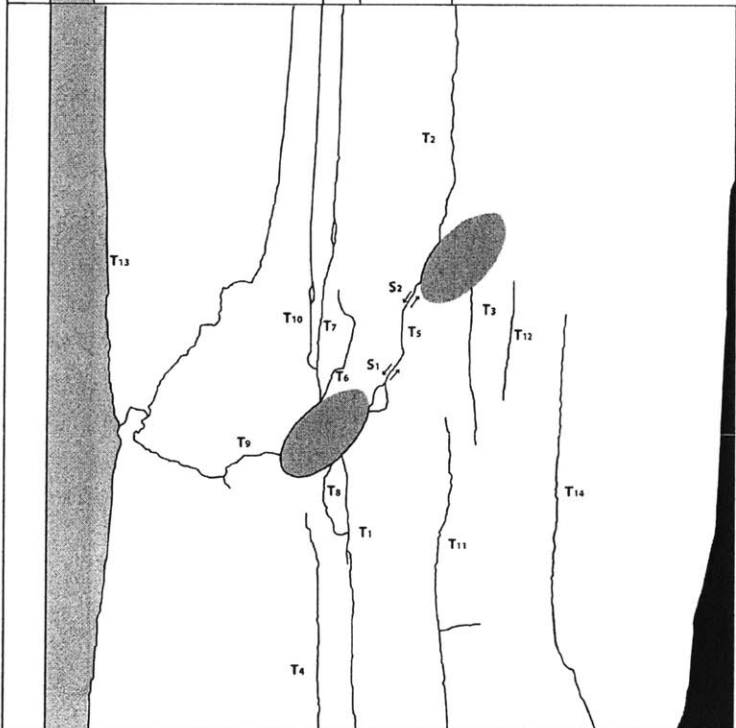


Time: 6m 39.550s
 σ : ~29.828 MPa

Frame 151 of the High Speed Camera footage.

T₁₃ extends down to the bottom of the specimen and a piece breaks off of the left side of the specimen. T₉ extends to the top of the specimen. T₆ extends upward and T₈ extends down to connect with T₁. T₁₀ closes.

7



Time: 6m 39.556s
 σ : ~29.828 MPa

Frame 121 of the High Speed Camera footage.

T₁₄ initiates from the bottom boundary of the specimen and propagates upward. A piece breaks off of the bottom right side of the specimen.

8



Time: 6m 39.550s
 σ : ~29.828 MPa

Frame 151 of the High Speed Camera footage.

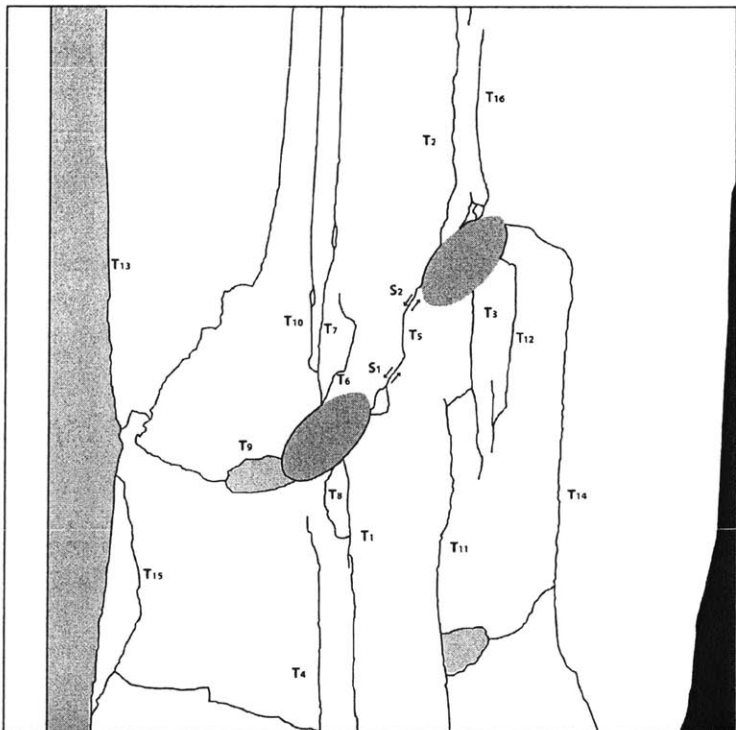
7



Time: 6m 39.556s
 σ : ~29.828 MPa

Frame 121 of the High Speed Camera footage.

8



Time: 6m 39.558s
 σ : ~29.828 MPa

FAILURE

Frame 110 of the High Speed Camera footage.

T₁₅ forms to the right of T₁₃. T₁₆ forms at the top of the right inclusion and extends upward (debonding). Spalling occurs at the left side of the left inclusion near the initiation point of T₉. T₁₁ extends upward to connect with T₃. T₁₂ and T₁₄ extend upward to connect at the right side of the right inclusion (debonding). T₁₀ and T₁₄ widen. T₁ and T₂ close.

9



Time: 6m 39.558s
 σ : ~29.828 MPa

FAILURE

Frame 110 of the High Speed Camera footage.

Frame 1924 of the High Speed Camera footage.

9